Evaluation of Motor Vehicle Fire Initiation and Propagation Part 13: Propagation of an Engine Compartment Fire in a 1998 Front-Wheel Drive Passenger Vehicle

Jeffrey Santrock
General Motors Corporation

ABSTRACT

This report describes a vehicle fire propagation test conducted pursuant to an agreement between GM and the United States Department of Transportation. The fire test described in this report was conducted on February 23, 1999. The test vehicle was a crash-tested 1998 Honda Accord. In the crash test, this vehicle was stationary and was struck in the left front corner (driver's side) by a moving barrier. A fire was observed in the windshield fluid reservoir of the test vehicle after this crash test [2]. This fire was caused by (1) autoignition of power steering fluid on the exhaust manifold and (2) ignition of methanol vapor in the windshield washer fluid reservoir by burning power steering fluid aerosol that entered the windshield washer fluid reservoir. The ignition protocol used in the fire test described in this report simulated this ignition scenario. The test vehicle was stationary during this fire test. A power steering fluid aerosol was sprayed from a hand-held oil mister through a flame of a propane torch toward openings in the windshield washer fluid reservoir of the test vehicle, and ignited methanol vapor in the windshield washer fluid reservoir. The windshield washer fluid reservoir started to burn between 4 and 6 minutes after ignition of the methanol vapor in the windshield washer fluid reservoir (post-ignition). Flames spread to the left front wheelhouse panel, the left front headlamp assembly, and the left front tire between 10 and 20 minutes post-ignition. Flames spread into the engine compartment of the test vehicle between 21 and 22 minutes post-ignition. Flames spread into the passenger compartment through the windshield and through pass-through openings in the dash panel between 22 and 27 minutes post-ignition. This test was ended at approximately 27 minutes post-ignition.

Table of Contents

Appendicies

List of Figures

Report

List of Figures

Appendicies

List of Tables

Report

List of Tables

Appendicies

1 Introduction and Test Summary

The work described in this report was conducted by General Motors (GM) pursuant to an agreement between GM and the United States Department of Transportation. According to this agreement, GM and the National Highway Traffic Safety Administration (NHTSA) jointly developed fifteen separate vehicle fire safety research projects. One of these projects, entitled "Fire Initiation and Propagation Tests", involves conducting 1) vehicle crash tests to investigate potential ignition events that occur in vehicle crashes, and 2) subsequent vehicle fire tests to characterize fire propagation in these crash-tested vehicles. The vehicle models to be tested, and the crash- and fire-test methods to be used for Project B.3 are described in another report [1]. The objectives of the fire tests are:

- To determine the principal fire paths and time-lines for flame propagation into the passenger compartment under the test conditions;
- To identify which components burn and to measure the thermal environments around those components associated with their ignition under the test conditions; and
- To measure air temperatures, heat fluxes, and combustion gas concentrations in the passenger compartment under the test conditions.

These tests were conducted under carefully designed test conditions noted throughout this and other reports. They cannot be relied upon to predict the specific nature and characteristics of actual post-collision fires in the field.

The test vehicle was a 1998 Honda Accord (VIN: 1HGCG5642WA003857) with the following options: 2.3 liter L4 engine, a 4-speed automatic transmission, air conditioning, a tilt steering wheel, and power seats. The test vehicle was crash tested on August 12, 1998 at the General Motors Proving Ground in Milford, Michigan [2]. In the crash test, the test vehicle was stationary and was struck in the left front (driver's side) by a moving barrier. The moving barrier had a deformable aluminum honeycomb face as described in FMVSS214 [3]. The test vehicle was parked with the brakes on and positioned at approximately a 21° angle relative to the velocity vector of the moving barrier. The barrier face struck the front left corner of the test vehicle. The mass of the test vehicle was 1738 kg (3,824 lbs.). The mass of the barrier was 1640 kg (3,608 lbs.). The barrier speed at impact was 104.1 km/h (64.7 mph). The change in velocity of the test vehicle was 53 kmh (33 mph) in the direction of the barrier's initial longitudinal axis. The maximum velocity change occurred approximately 53 msec after impact. A more detailed description of this test can be found in another report [2].

Figure 1 is a photograph of the test vehicle after the crash test. A fire was observed in the windshield fluid reservoir of the test vehicle after this crash test [2]. Figure 2 is a photograph of the windshield washer fluid reservoir in the test vehicle burning several minutes after Crash Test C12127. The following sequence of events was determined to have resulted in this fire. The power steering fluid reservoir, which was located in the left front quadrant of the engine compartment, was crushed during impact. Power steering fluid expelled from the power steering fluid reservoir ignited when it contacted the exhaust manifold. The windshield washer fluid reservoir, which was located in the left front fender forward of the left front wheel, also was crushed and split in several places during impact. The filler neck for the windshield washer fluid reservoir was severed. Most of the windshield washer fluid reservoir was expelled from the reservoir during impact. An undetermined volume of windshield washer fluid was observed in the bottom of the broken windshield washer fluid reservoir after this crash test. Burning power steering fluid aerosol entered the windshield washer fluid reservoir as the test vehicle rebounded

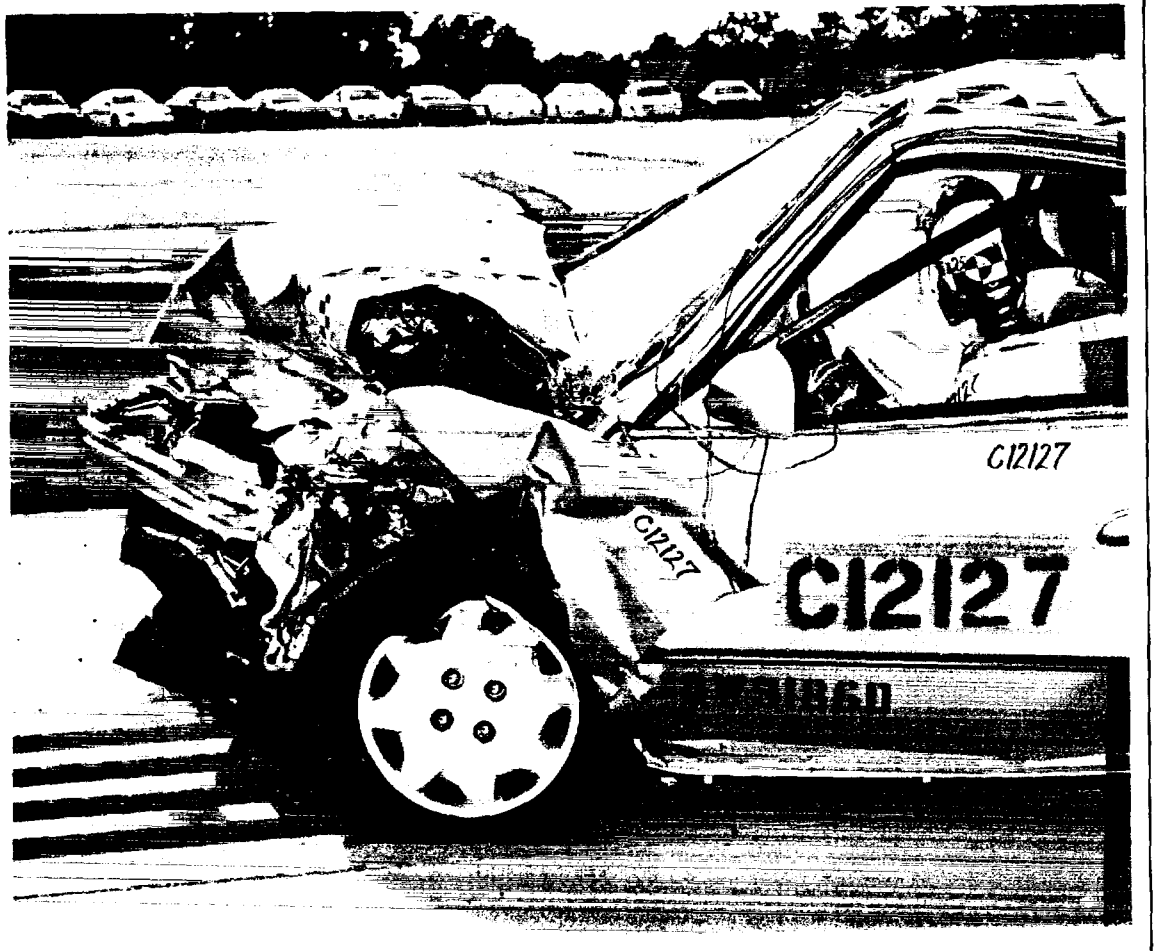

Figure 1. Fire Test F99030B. Photograph of the test vehicle after the crash test.

Figure 2. Fire Test F99030B. Photograph of the windshield washer fluid reservoir in the test vehicle burning several minutes after Crash Test C12127.

from the impacting barrier and ignited methanol vapor in the windshield washer fluid reservoir.[1] A detailed description of the analysis of the crash test data supporting this ignition scenario can be found in a report describing Crash Test C12127 [2].

The fire test described in this report was conducted on February 23, 1999. The ignition protocol used in this fire test simulated the ignition mechanism described above. Table 1 summarizes the timing of flame-spread in the test vehicle during this fire test.

[1] Replicate open-cup flash point tests indicated that the flash point of the windshield washer fluid in the test vehicle during this crash test was between 35 ± 2°C (mean ± SE). The ambient air temperature during this crash test was approximately 35°C. Temperatures of components within the engine compartment of the test vehicle, which were heated by the running engine, were higher than the ambient air temperature.

Table 1

Summary of Fire Development during in Fire Test F99030B

Time[1] (min)	Event
- 0.25	Burning power steering fluid aerosol was sprayed toward the windshield washer fluid reservoir in the test vehicle.
0	Ignition of methanol vapor in the windshield fluid reservoir was confirmed by observing temperature increase recorded from thermocouples in the windshield fluid reservoir.
4 – 6	The windshield washer fluid reservoir started to burn.
11 - 12	Flames spread from the windshield washer fluid reservoir to the left front inner fender panel.
15 - 16	Flames spread from the windshield washer fluid reservoir and the left front inner fender panel to the left front tire.
21 - 22	Flames spread across the hood insulator into the engine compartment.
22 - 24	Fames started to vent from the engine compartment along the rear edge of the hood and impinge onto the windshield.
25 - 26	Pieces of burning windshield started to fall inward into the passenger compartment.
26 - 27	The left front seat cushion, center console, and steering wheel were ignited by pieces of burning windshield.
27	Fire suppression began.

[1]Time after ignition of methanol vapor in the windshield washer fluid reservoir by a burning power steering fluid aerosol.

2 Vehicle Condition and Test Protocol

The fire test described in this report was conducted at the Factory Mutual Test Center in West Glocester, Rhode Island. The crash-tested vehicle was prepared for the fire tests at the General Motors Research and Development Center (GM R&D Center) in Warren, Michigan, and shipped to the Factory Mutual Test Center. The test vehicle was returned to the GM R&D Center after the fire test, where it was systematically disassembled to permit closer inspection of the fire damage and identification of fire spread paths that were not obvious during the tests.

A description of the video cameras used during this test is in **APPENDIX A**. A description of the infrared cameras used in this test is in **APPENDIX B**. A description of the thermocouples installed in the test vehicle and data from these thermocouples are in **APPENDIX C**. A description of the aspirated thermocouples used in this test and data from these aspirated thermocouples are in **APPENDIX D**. A description of the heat flux transducer/radiometer assemblies installed in the test vehicle and data from these devices are in **APPENDIX E**. A description of the pressure and airflow measurement equipment and analysis procedures, and data from these measurements are in **APPENDIX F**. A description of the Fire Products Collector (FPC) at the Factory Mutual Global Test Center and analysis procedures, and data from this device are in **APPENDIX G**. Descriptions of the Fourier Transform Infrared Gas Analysis System used during this test and results from this device are in **APPENDIX H**. A description of the Gas Chromatography/Mass Spectrometry equipment and analysis procedures, and the results of these analyses are in **APPENDIX I**. A description of the particulate sampling equipment and analysis procedures, and the results of these analyses are in **APPENDIX J**.

The vehicle was placed in a rectangular steel pan (length = 25 ft., width = 15 ft., height = 4 in.) to prevent spilled and leaking automotive fluids from spreading in the test facility. This fluid containment pan was fabricated from two sheets of carbon steel. Angle-braces were welded to the under-side of the pan to keep it from flexing under the weight of the vehicle. The corners of the support frame rested on load cells. Mass loss was determined from data acquired from the load cells during the test.

A layer of fiberglass-reinforced cement construction board (DuraRock, USG Corporation) was placed on bottom of the fluid containment pan. A thin layer of sand was used to level the concrete board so that the grade of the surface measured from the center to the edges along the major and minor axes was no greater than 1%. The joints between boards were sealed with latex caulking.

The test vehicle was placed in the center of the pan (Fig. 3). All doors were closed. The windshield and the glass in the left front door were broken in the crash test, and were not replaced for the fire test.

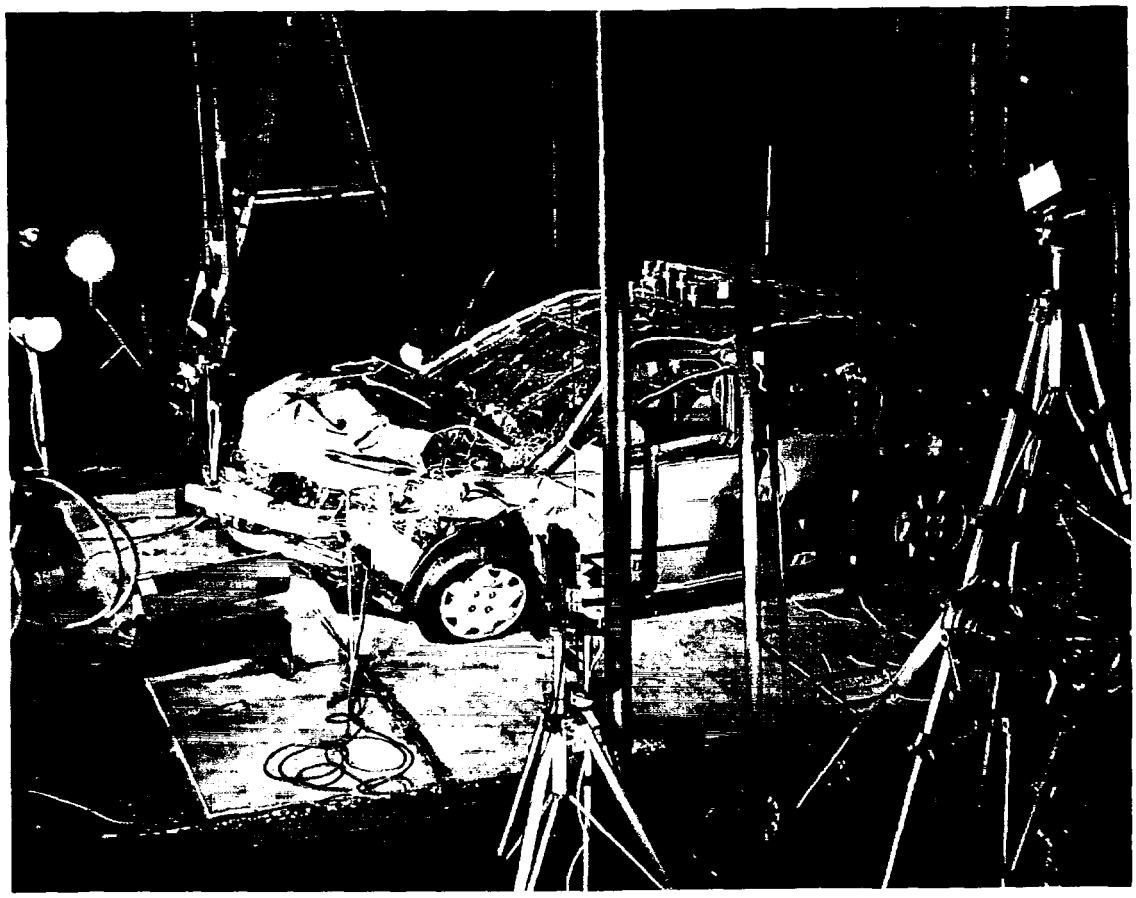

Figure 3. Fire Test F99030B. Photograph of the test vehicle before the start of this test showing a propane "torpedo" heater used to heat the windshield washer fluid reservoir.

The fire that occurred after the crash test damaged the windshield washer fluid reservoir and left front inner fender panel in the test vehicle. These components were replaced with service parts obtained from a Honda dealership. Holes were cut in the front and left side of the replacement windshield washer fluid reservoir to simulate damage to the original reservoir that occurred in the crash test.

To begin this fire test, approximately 2 L of a 1:1 mixture of antifreeze and water heated to a temperature of approximately 100°C was sprayed onto the hood insulator and allowed to drip into

the engine compartment. Windshield washer fluid heated to a temperature of approximately 50°C was added to the replacement windshield washer fluid reservoir in the test vehicle.[2] An insulated, hand-pump oiling can fitted with a misting nozzle was filled with power steering fluid heated to a temperature of approximately 85°C. Power steering fluid was sprayed toward the windshield washer fluid reservoir. A hand-held propane torch was used to ignite the power steering fluid so that a burning fluid aerosol impinged on and entered the windshield washer fluid reservoir.

To compensate for the low ambient temperatures in the test facility during this fire test and maintain the temperature of the windshield fluid in the windshield washer fluid reservoir above its flash point, the windshield washer fluid reservoir in the test vehicle were heated. A propane space heater was used to heat the windshield washer fluid reservoir and adjacent components in the left front corner of the test vehicle (Fig. 3). The air temperature in the windshield washer fluid reservoir was approximately 40°C at the start of this test.

To synchronize the various data systems used in this test with ignition of the methanol vapor in the windshield washer fluid reservoir, an air horn was used to signal the following two events: (1) sustained combustion of methanol vapor in the windshield washer fluid reservoir after ignition by burning power steering fluid aerosol and (2) the end of the test. The air horn was audible on the videotapes and infrared imaging systems. One channel of the data acquisition system for vehicle instrumentation monitored a normally open switch, which was depressed at each sounding of the air horn. The time delay between the sounding of the air horn and depression of this switch was estimated to be between 1 and 2 seconds. The real-time clock in the FTIR data system was synchronized to the real-time clock in the vehicle instrumentation data system.

A fine water mist was used to extinguish the fire in the test vehicle. After the signal to end the test was sounded, the water mist was directed into the passenger compartment through the left side window to extinguish flames in the interior of the vehicle first. The water mist was then directed toward the engine compartment to extinguish flames outside of the passenger compartment.

[2] The ambient air temperature in the test facility during this test was approximately 10°C. The windshield washer fluid was heated to approximately 50°C so that the temperature of this fluid would be greater than its flash point at the time of ignition and would remain greater than its flash point until the windshield washer fluid reservoir ignited.

3 Ignition

Figures 4 through 6 show video stills from Cameras 1, 3, and 4 show heated power steering fluid aerosol being sprayed toward the windshield washer fluid reservoir and ignited by the flame from a propane torch at the start of this test.

Figure 7 shows plots of temperature data recorded from Thermocouple A4, located in the windshield washer fluid reservoir. The origin of the abscissa in this plot was determined from the timing of the first air horn signal. The plot in Figure 7 shows temperature data recorded from 30 seconds before to 30 seconds after the first sounding of the air horn (– 30 to + 30 sec). Analysis of video from Camera 3 indicated a 14 second delay from the time burning power steering fluid aerosol entered the windshield washer fluid reservoir to the first sounding of the air horn audible in this video. Temperature data recorded from Thermocouple A7 started to increase from ambient levels between 15 and 16 seconds before the timing signal (Fig. 7

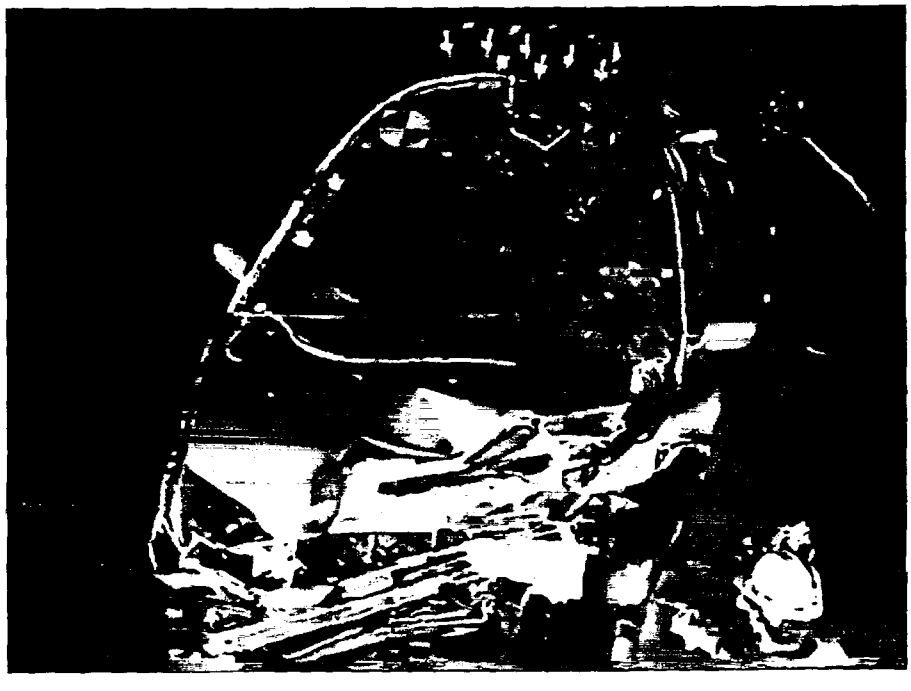

Figure 4. Fire Test F99030B. Video still from Camera 4 approximately 1 second before burning power steering fluid aerosol ignited methanol vapor in the windshield washer fluid reservoir.

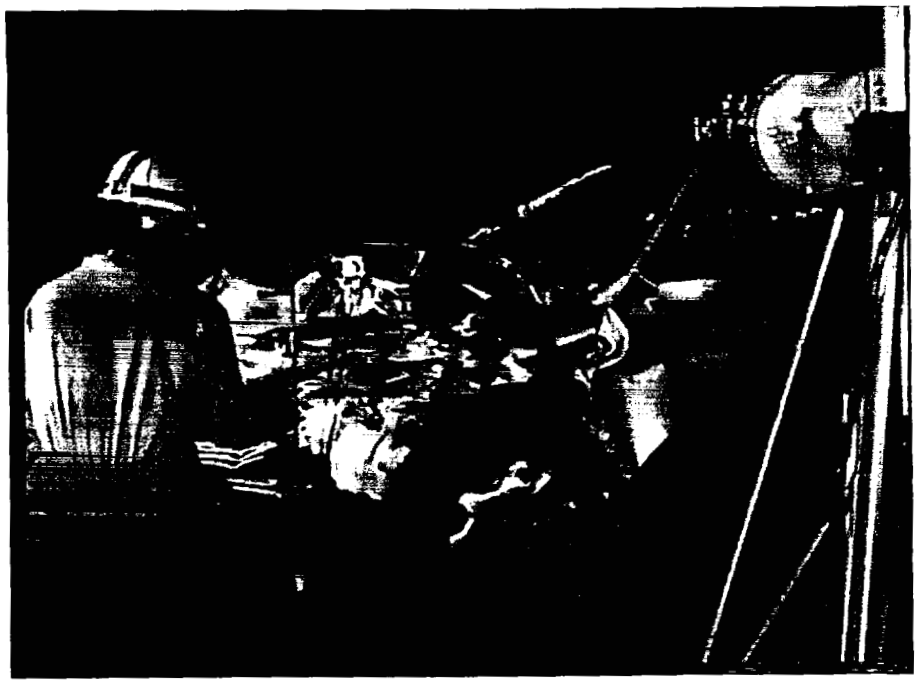

Figure 5. Fire Test F99030B. Video still from Camera 3 approximately 1 second before burning power steering fluid aerosol ignited methanol vapor in the windshield washer fluid reservoir.

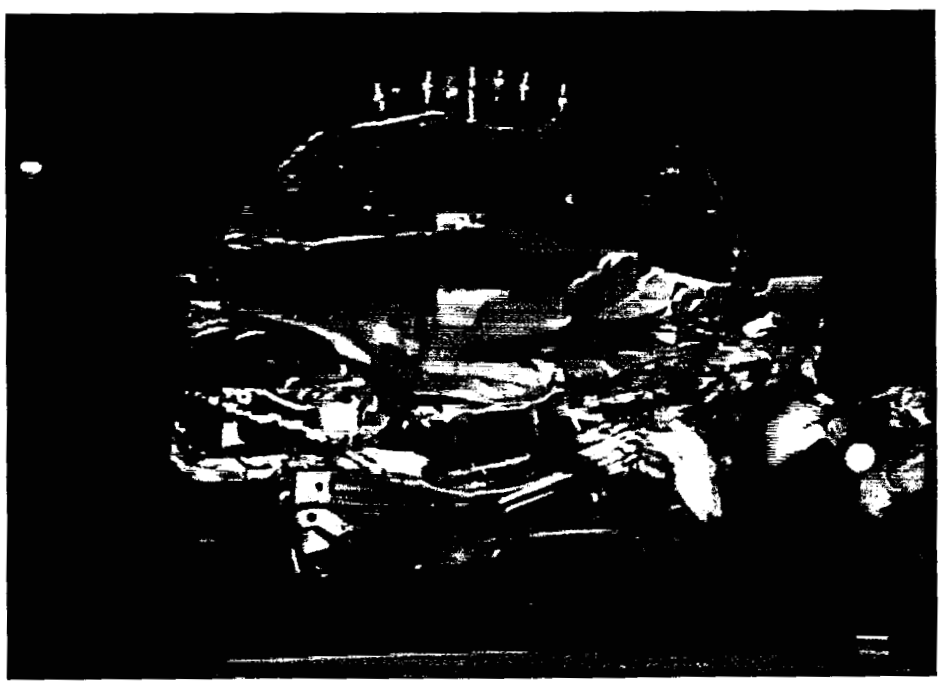

Figure 6. Fire Test F99030B. Video still from Camera 1 approximately 1 second before burning power steering fluid aerosol ignited methanol vapor in the windshield washer fluid reservoir.

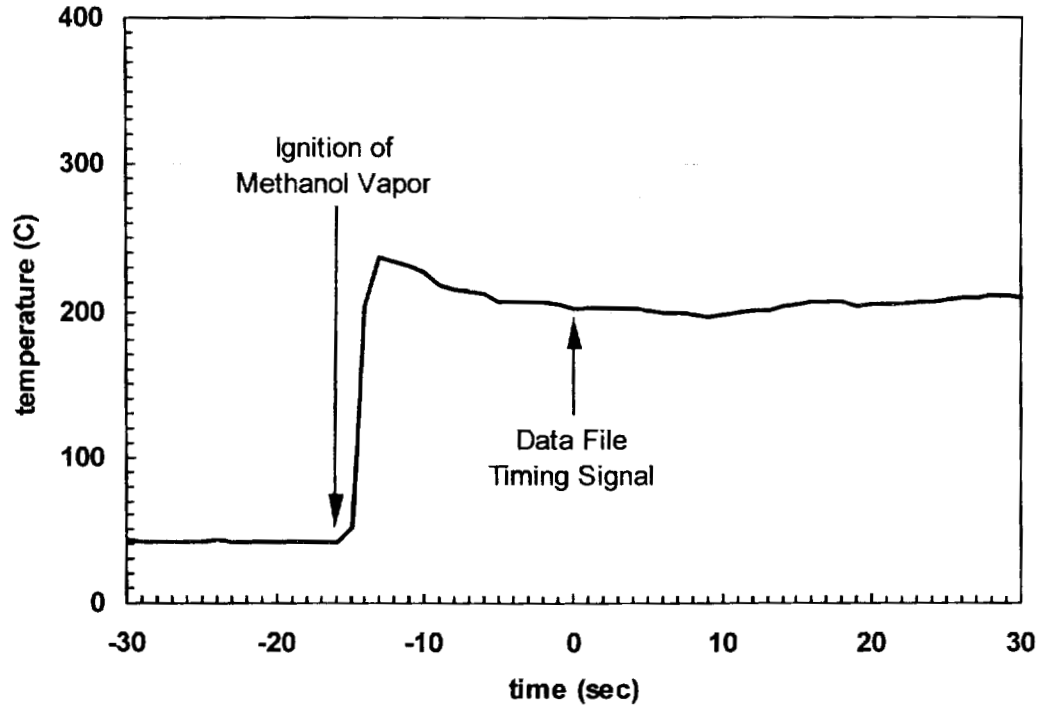

Figure 7. Fire Test F99030B. Plot of temperature data recorded from Thermocouple A4.

The 16-second interval between ignition of methanol vapor in the windshield fluid reservoir and the timing signal in the data file is consistent with a 14 second time interval from entry of burning power steering fluid aerosol into the windshield washer fluid reservoir to the first sound of the air horn and an estimated 1 to 2 seconds delay for manually depressing the timing switch on the thermocouple data acquisition system after hearing the air horn. All discussions of the timing of flame-spread in this report are relative to the time of ignition of methanol vapor in the windshield washer fluid reservoir, which occurred approximately 16 seconds prior to the timing signal in the data files.

4 Flame-Spread in the Engine Compartment

Burning methanol vapor ignited the windshield washer fluid reservoir between 4 and 6 minutes post-ignition.[3] Flames spread from the windshield washer fluid reservoir to the left front inner fender panel, the left headlamp assembly, and the left front tire. Flames entered the engine compartment through the gap between the deformed hood and the left front fender.

4.1 Ignition of the Windshield Washer Fluid Reservoir and Flame-Spread to the Left Front Inner Fender Panel and Left Front Tire

Methanol vapor burned for approximately 5 minutes before there was visual indication of fire in the windshield fluid reservoir. For example, temperatures recorded from Thermocouple A4 were between 200 and 250°C from the time of ignition through about 5 minutes post-ignition (Fig. 8).

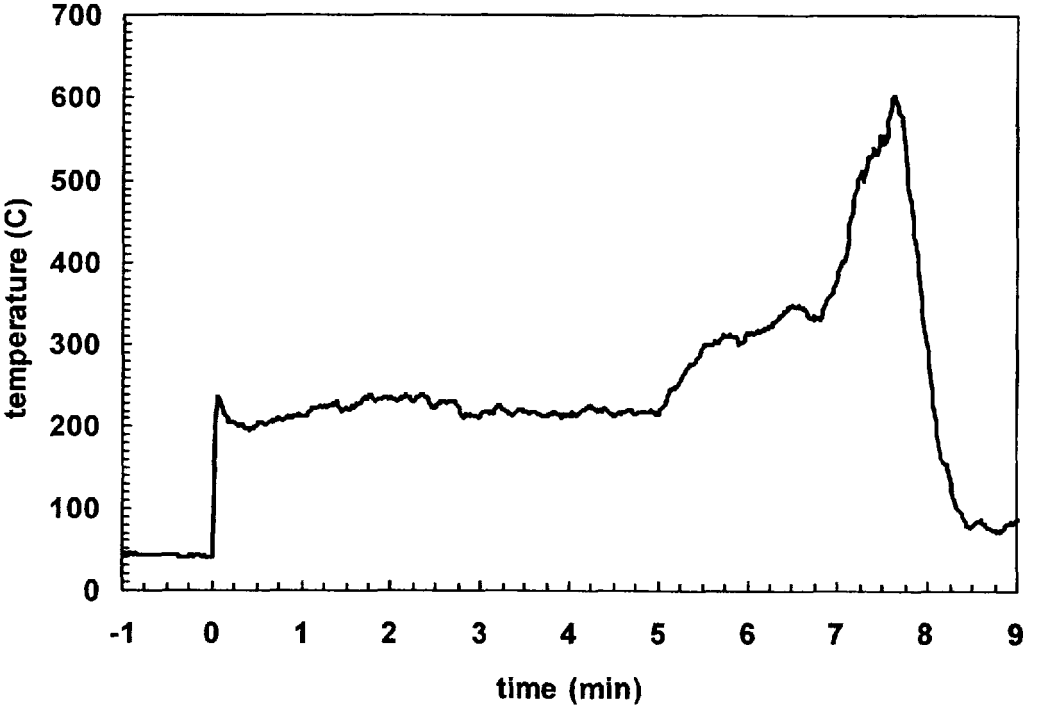

Figure 8. Fire Test F99030B. Plot of temperature data recorded from Thermocouple A4. The abscissa has been shifted +16 seconds to compensate for the delay between ignition and the timing signal recorded in the thermocouple data files.

[3] The windshield washer fluid reservoir in the test vehicle was poly(ethylene).

Methanol vapor typically burns with a low luminosity flame in the visible region. Even though temperature data from Thermocouple A4 indicated combustion inside the windshield washer fluid reservoir continuously from the time of ignition of the methanol vapor with the burning power steering fluid aerosol, no visual evidence of combustion such as a glow inside the reservoir was observed until about 5 minutes post-ignition. Figures 9 through 26 show video stills from Cameras 1 and 3 at 1-minute intervals between 5 and 22 minutes post-ignition. Visual evidence of fire, such as flames or smoke, is not observed before 7 minutes post-ignition (Fig.'s 9 through 11). A faint glow inside the windshield washer fluid reservoir was first detected at about 5 minutes post-ignition. This increased luminosity in the visible region probably was the result of combustion of thermal decomposition products from poly(ethylene) caused by heat transfer from the burning methanol vapor to the walls of the windshield washer fluid reservoir.

Continued heating caused a section of the wall of the windshield washer fluid reservoir to soften and ignite. The rate of thermal decomposition of poly(ethylene) on the inner surface of the wall would have increased as the temperature of the wall increased, resulting in an increase in the temperature and luminosity of the flame inside the windshield washer fluid reservoir and eventually flame attachment to the wall. Temperature data recorded from Thermocouple A4 increased from about 220 to 600°C between 5 and 7½ minutes post-ignition (Fig. 8). A section of the outer wall of the windshield washer fluid reservoir ignited between 7 and 8 minutes post-ignition (lower video stills, Fig.'s 11 and 12). The decrease in the temperature data recorded from Thermocouple A4 after 7½ minutes post-ignition appeared to have been caused by movement of the thermocouple junction out of the flame when the section of the windshield washer fluid wall it was attached to softened and sagged.

Flames spread upward and forward on the outer wall of the windshield washer fluid reservoir (Fig.'s 13 through 17). A section of the left front inner fender panel[4] appears to have ignited between 11 and 12 minutes post-ignition (Fig.'s 15 and 16) and self-extinguished by 16 minutes post-ignition (Fig. 20). By 14 minutes post-ignition, poly(ethylene) from the windshield washer fluid reservoir, poly(propylene) from the left front inner fender panel, and pieces of the broken left front headlamp assembly[5] had fallen onto the ground in front of the left front tire and were burning (Fig. 18). The inner sidewall of the left front tire ignited between 15 and 16 minutes post-ignition (Fig.'s 19 and 20). Over the next 5 minutes, flames spread upward along the inner sidewall of the tire and re-ignited the left front inner fender panel (Fig.'s 17 through 21). As the height of the flames grew, a portion of the fire plume was deflected by the left edge of the deformed hood into the engine compartment.

[4] The left front inner fender panel was poly(propylene).
[5] The left front headlamp assembly was poly(methyl methacrylate).

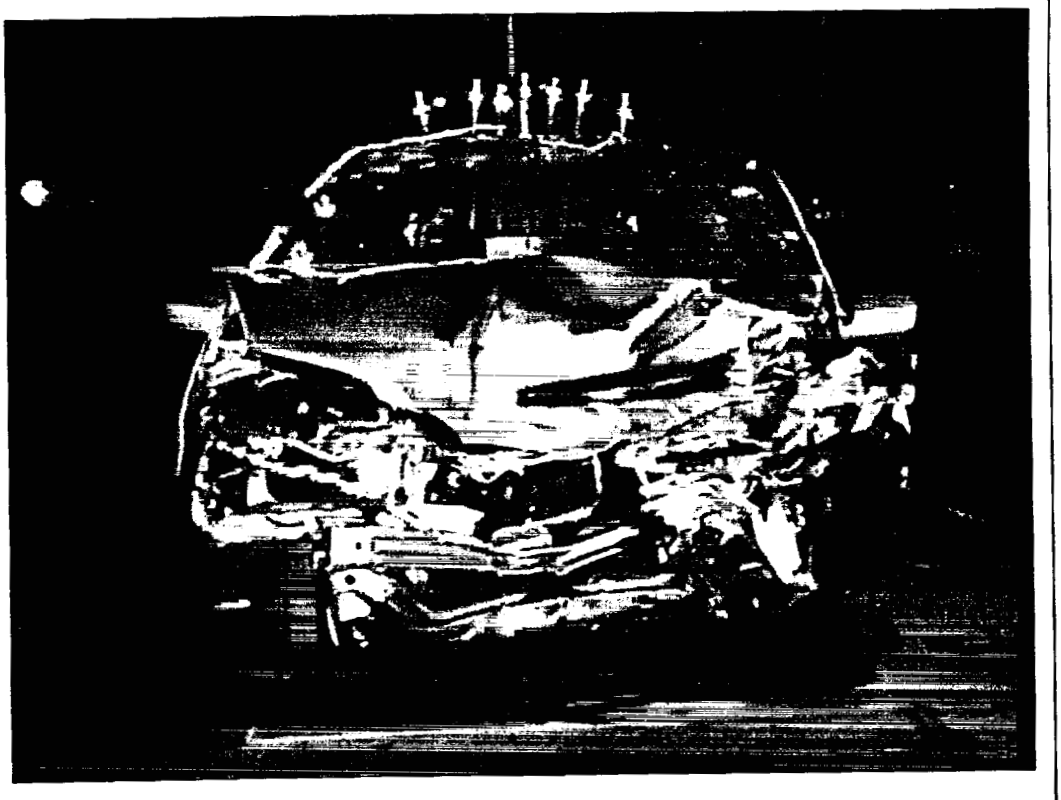

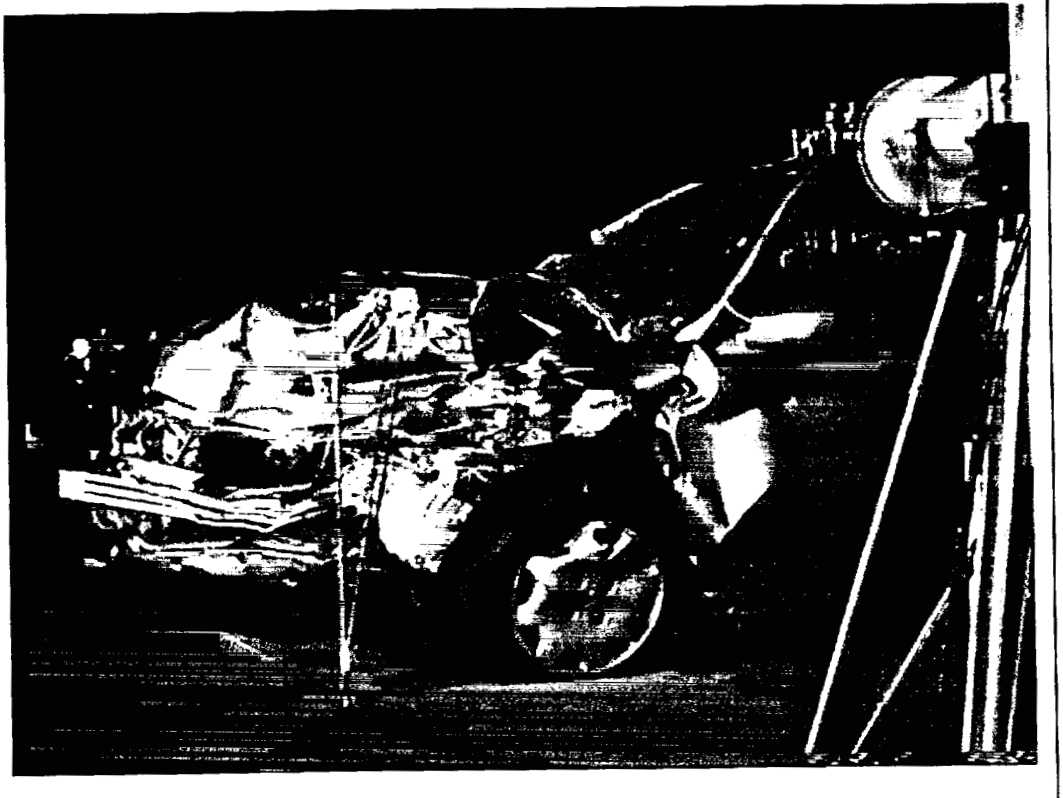

Figure 9. Fire Test F99030B. Video stills from Camera 1 (upper) and Camera 3 (lower) at 5 minutes post-ignition.

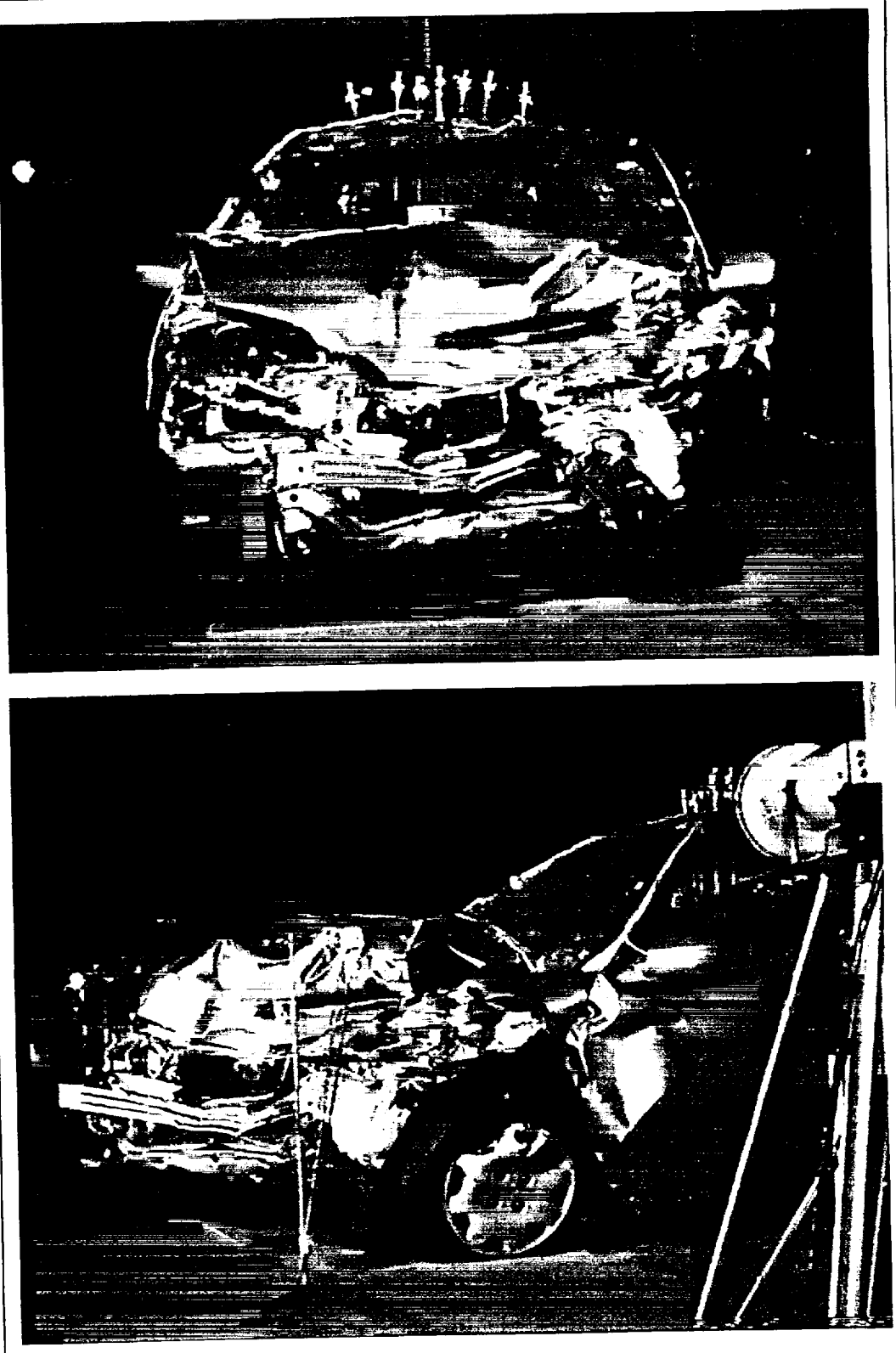

Figure 10. Fire Test F99030B. Video stills from Camera 1 (upper) and Camera 3 (lower) at 6 minutes post-ignition.

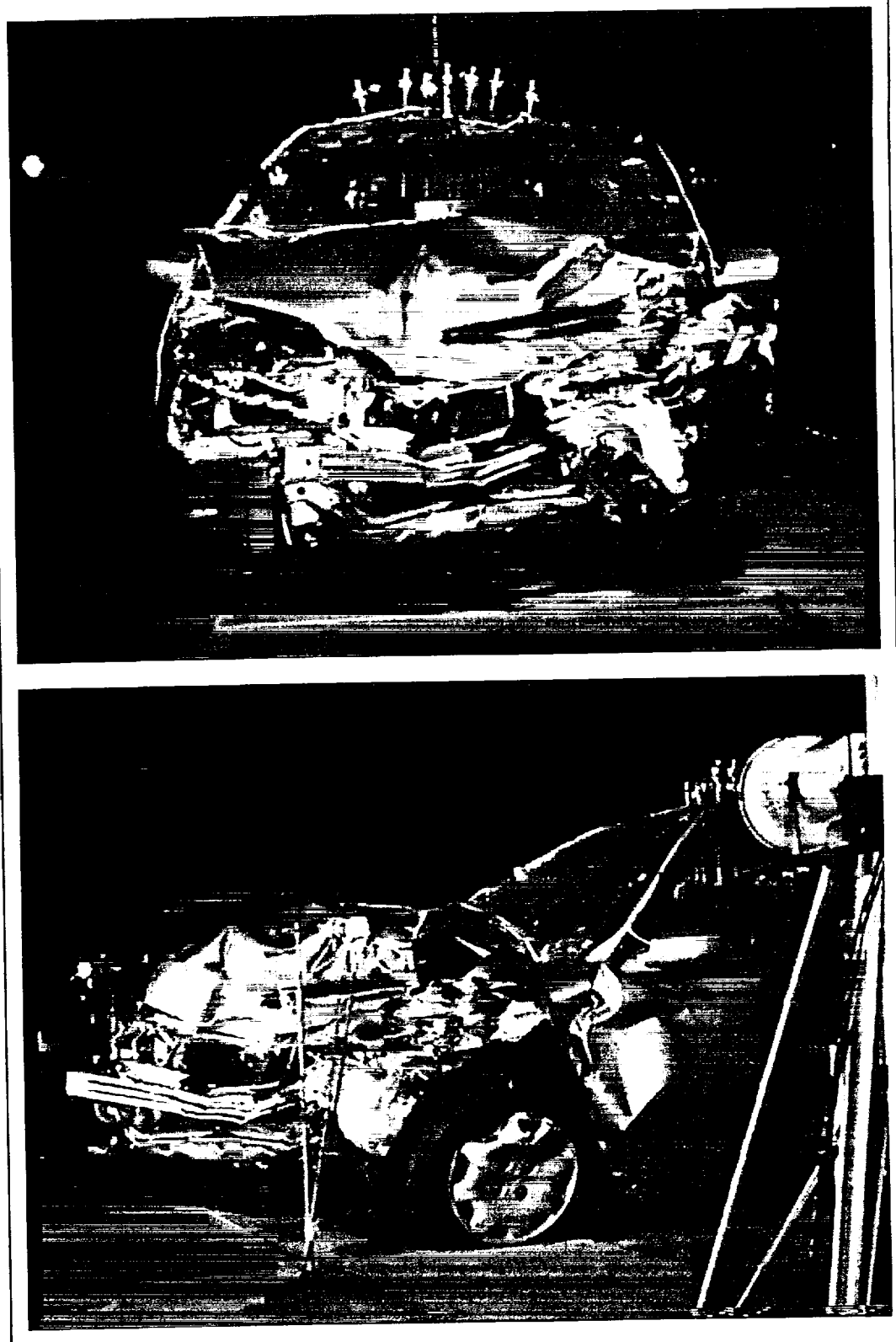

Figure 11. Fire Test F99030B. Video stills from Camera 1 (upper) and Camera 3 (lower) at 7 minutes post-ignition.

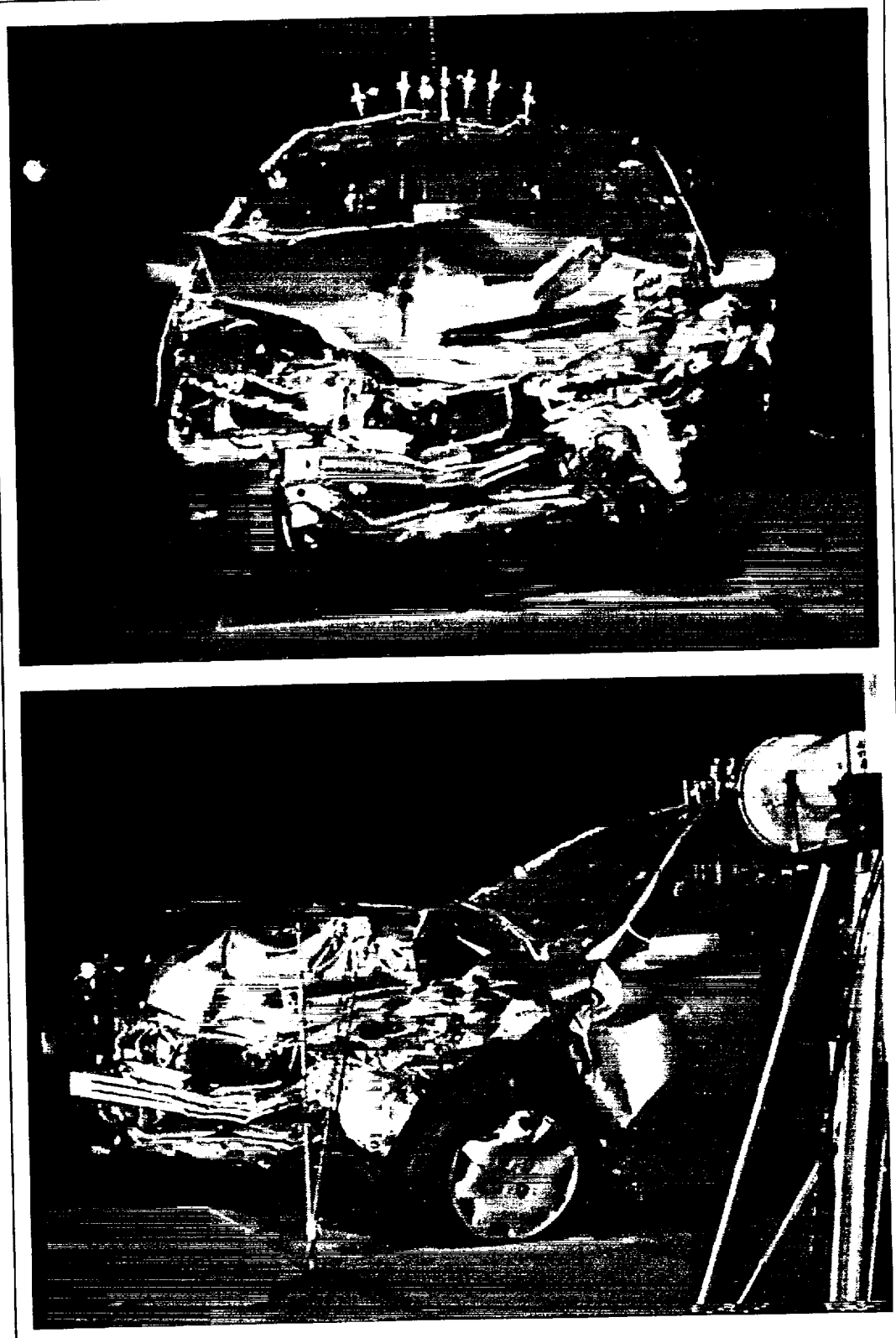

Figure 12. Fire Test F99030B. Video stills from Camera 1 (upper) and Camera 3 (lower) at 8 minutes post-ignition.

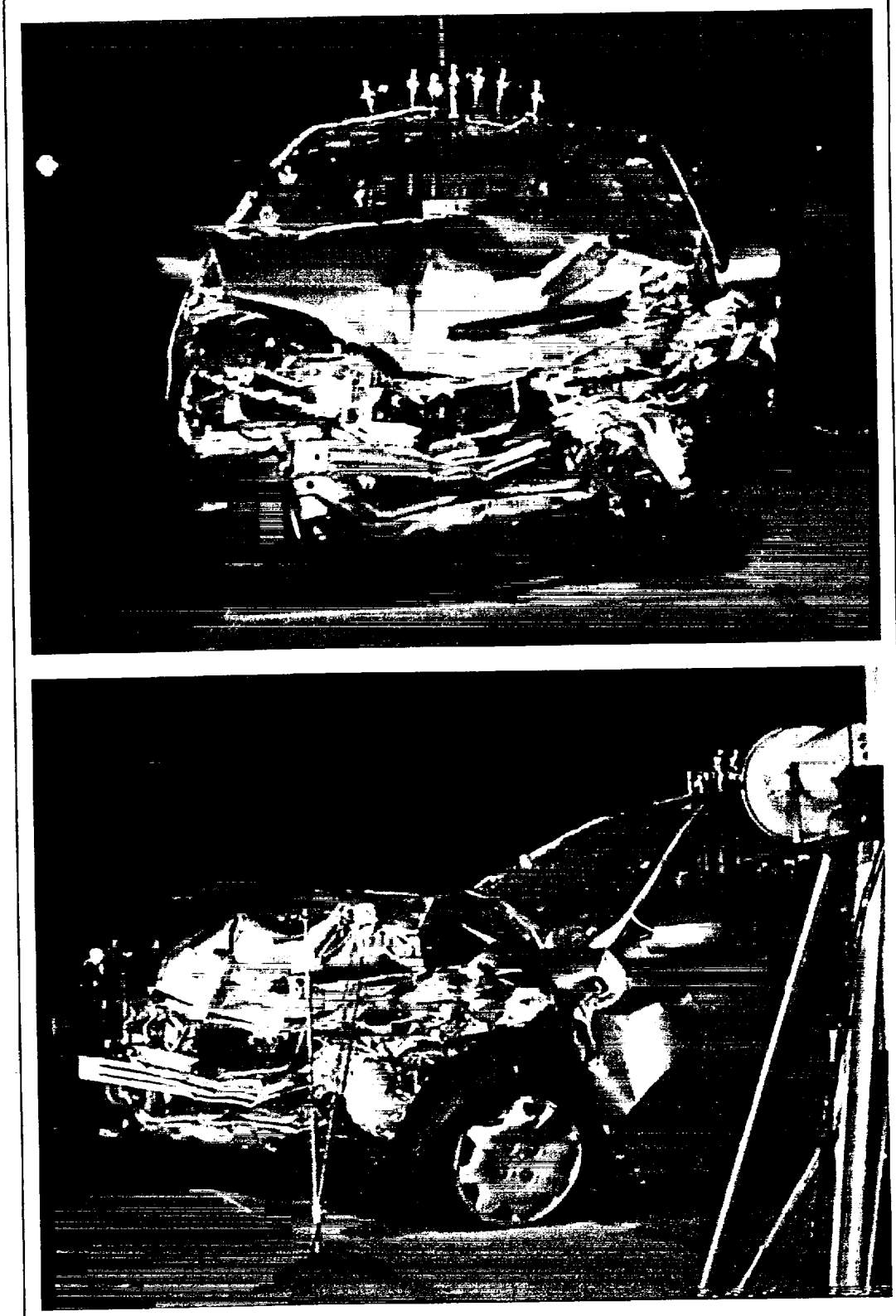

Figure 13. Fire Test F99030B. Video stills from Camera 1 (upper) and Camera 3 (lower) at 9 minutes post-ignition.

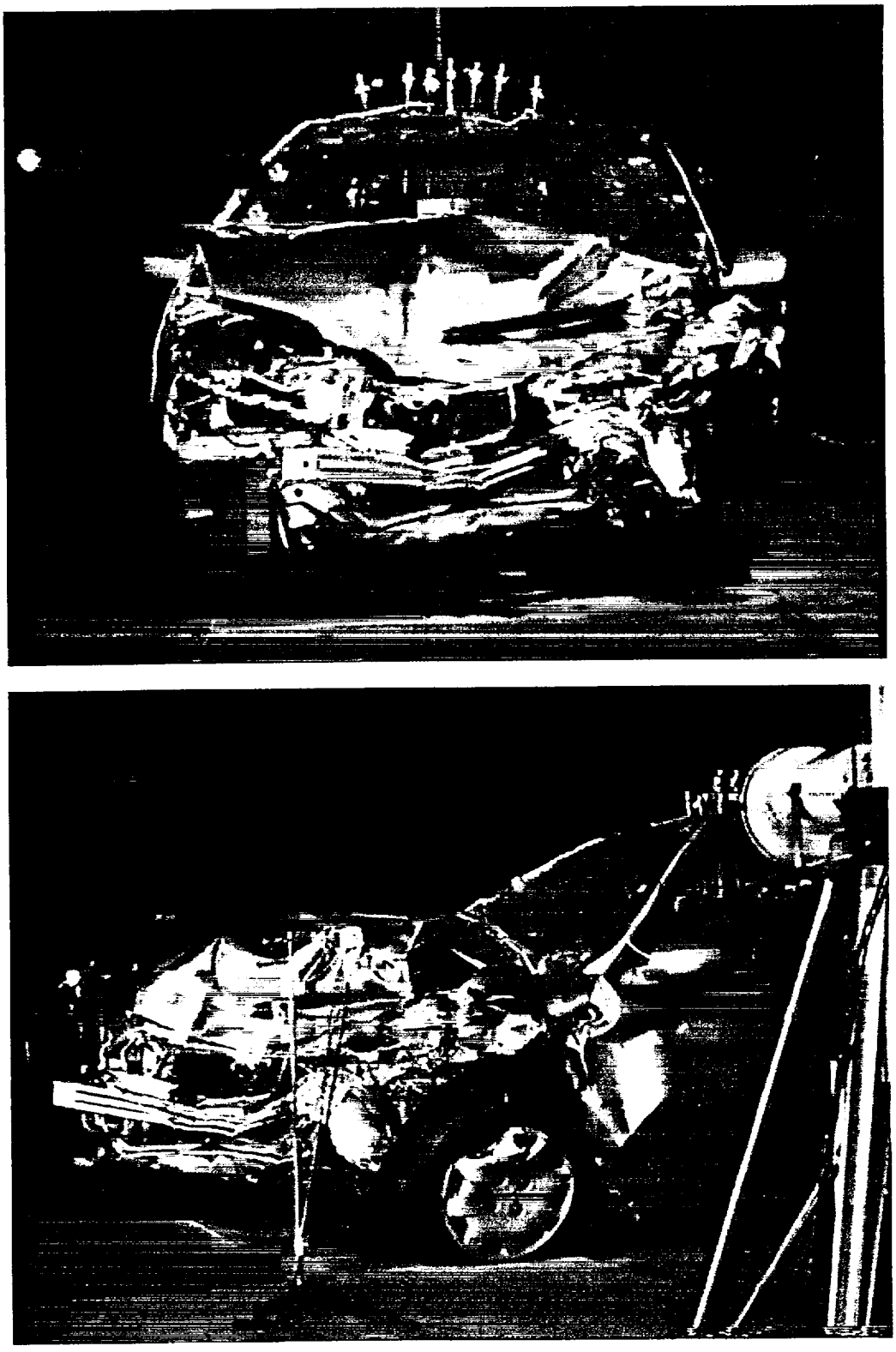

Figure 14. Fire Test F99030B. Video stills from Camera 1 (upper) and Camera 3 (lower) at 10 minutes post-ignition.

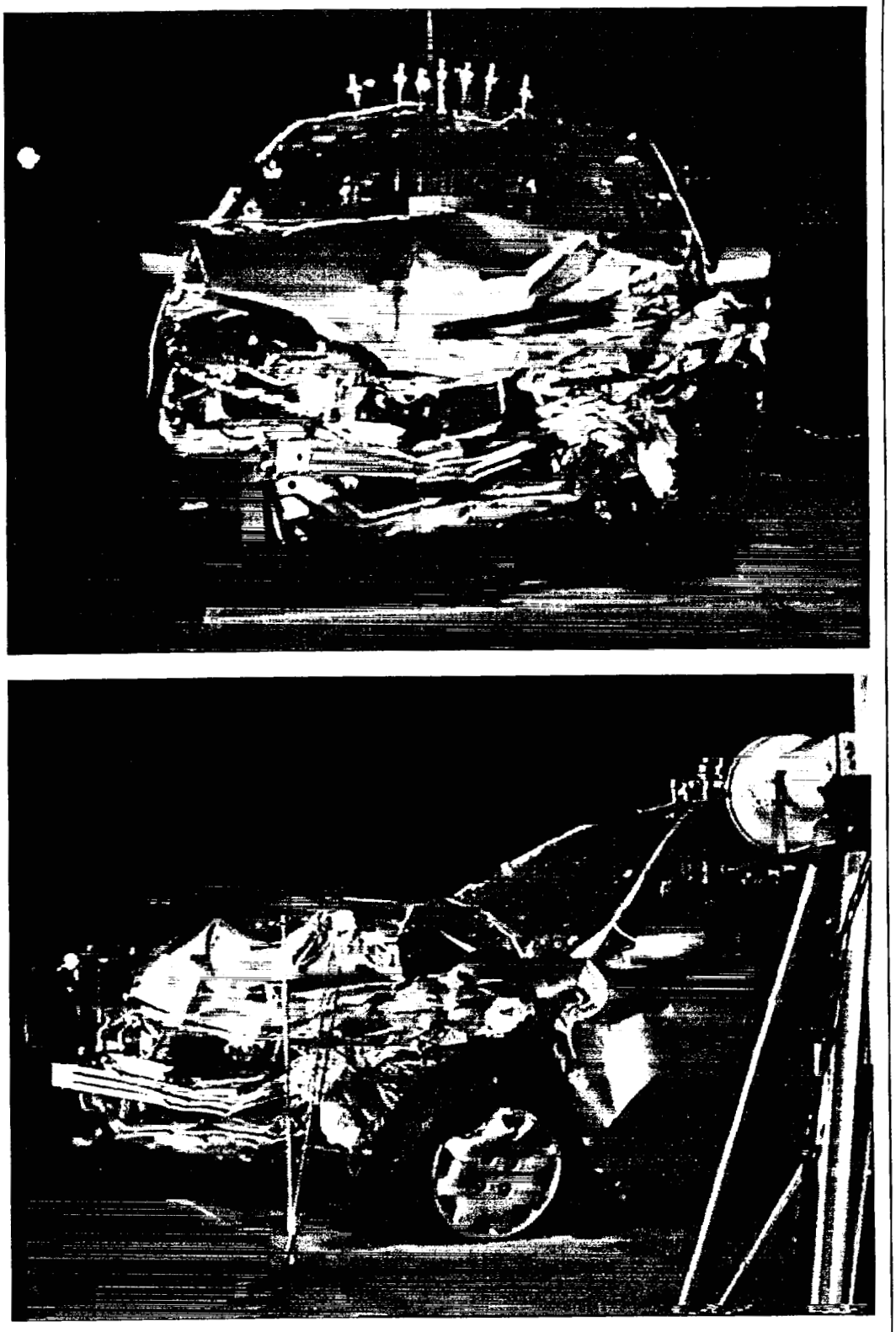

Figure 15. Fire Test F99030B. Video stills from Camera 1 (upper) and Camera 3 (lower) at 11 minutes post-ignition.

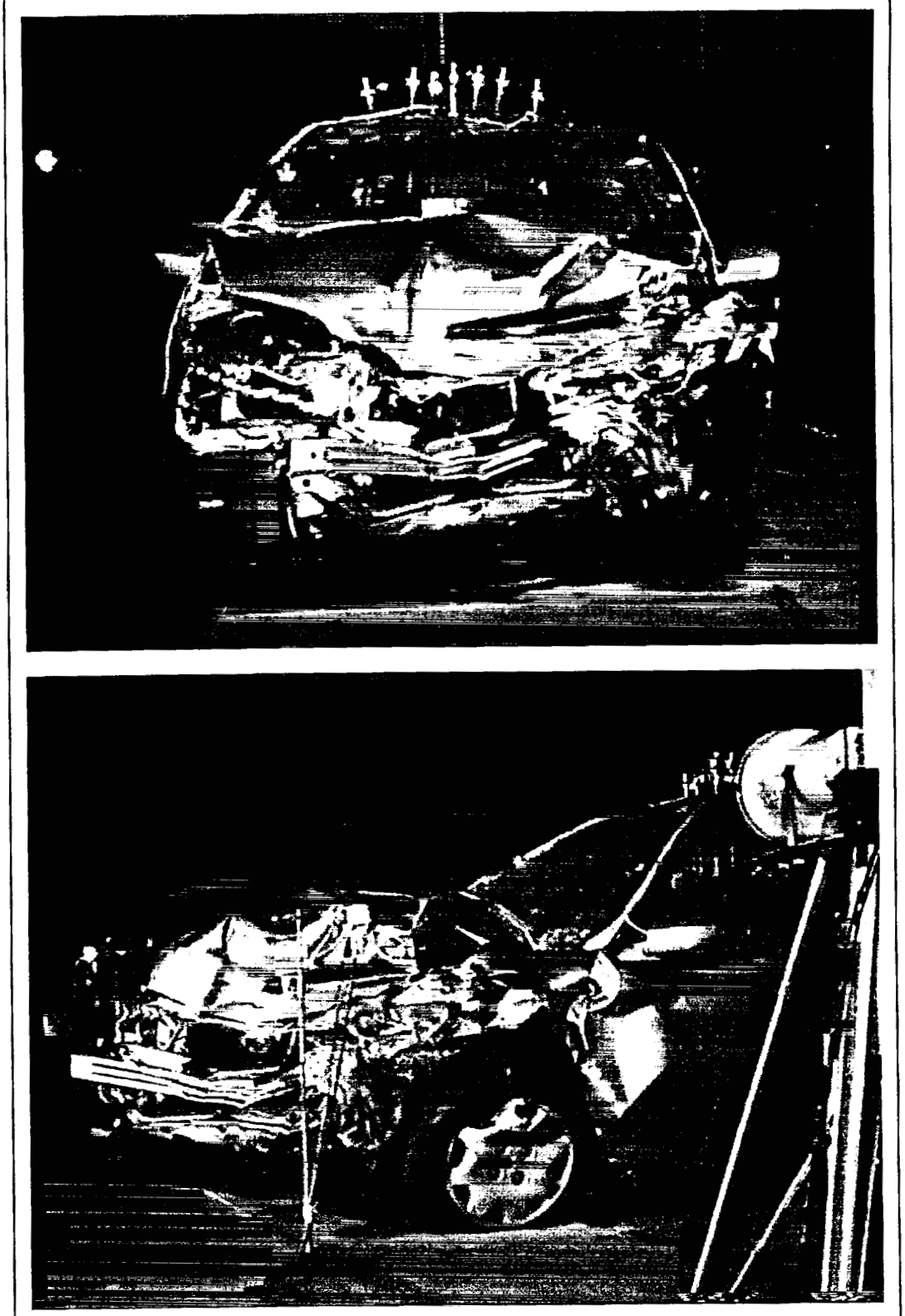

Figure 16. Fire Test F99030B. Video stills from Camera 1 (upper) and Camera 3 (lower) at 12 minutes post-ignition.

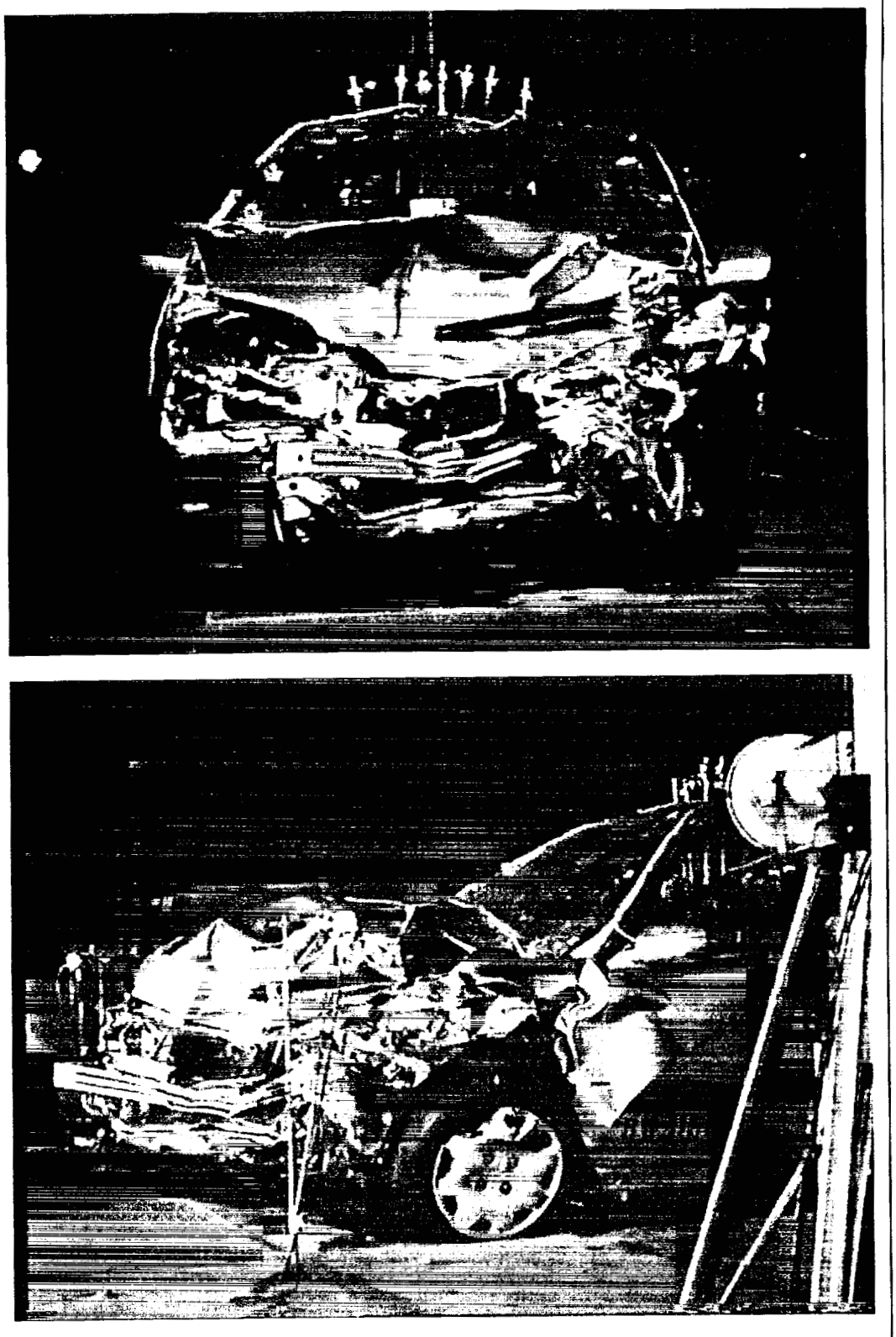

Figure 17. Fire Test F99030B. Video stills from Camera 1 (upper) and Camera 3 (lower) at 13 minutes post-ignition.

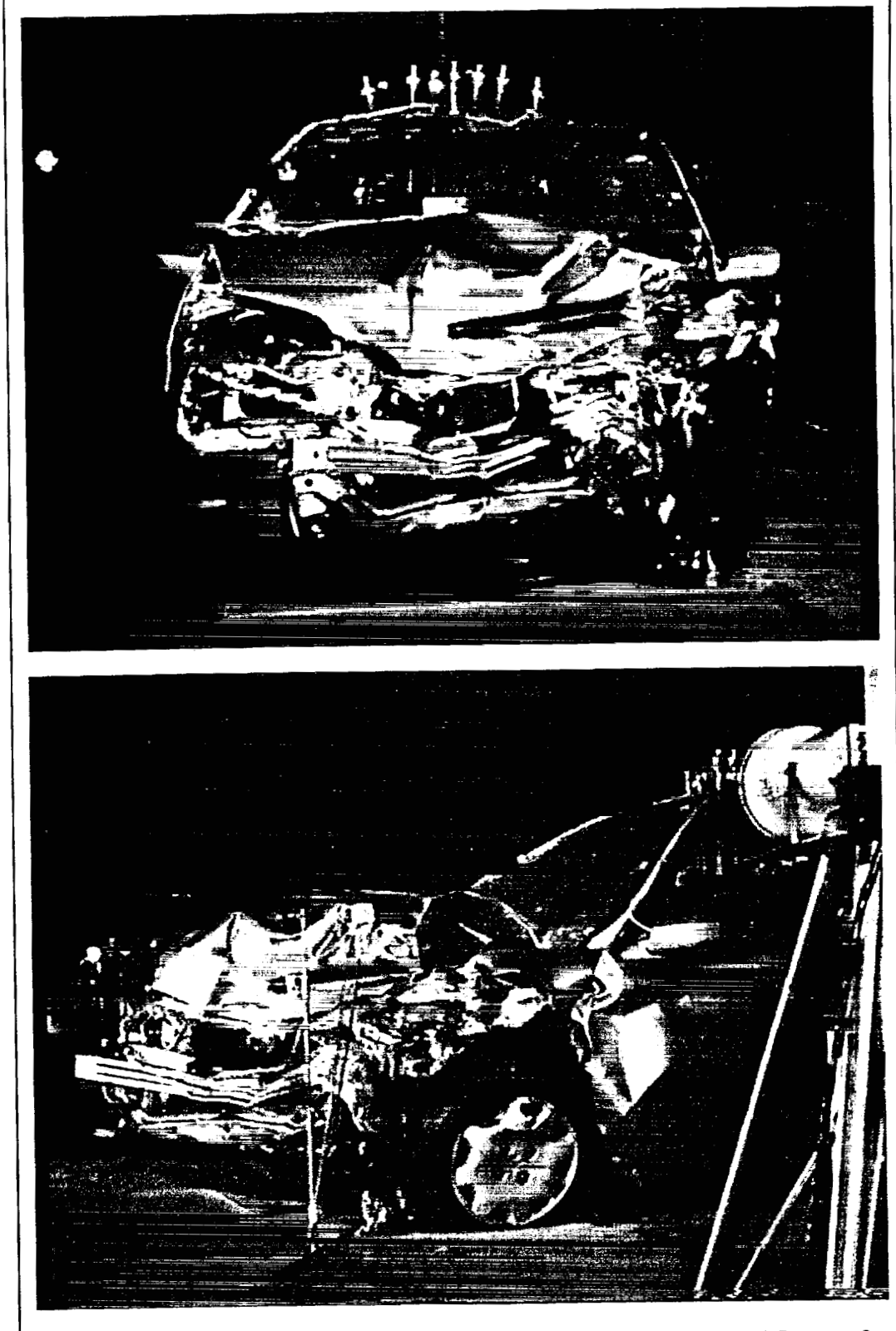

Figure 18. Fire Test F99030B. Video stills from Camera 1 (upper) and Camera 3 (lower) at 14 minutes post-ignition.

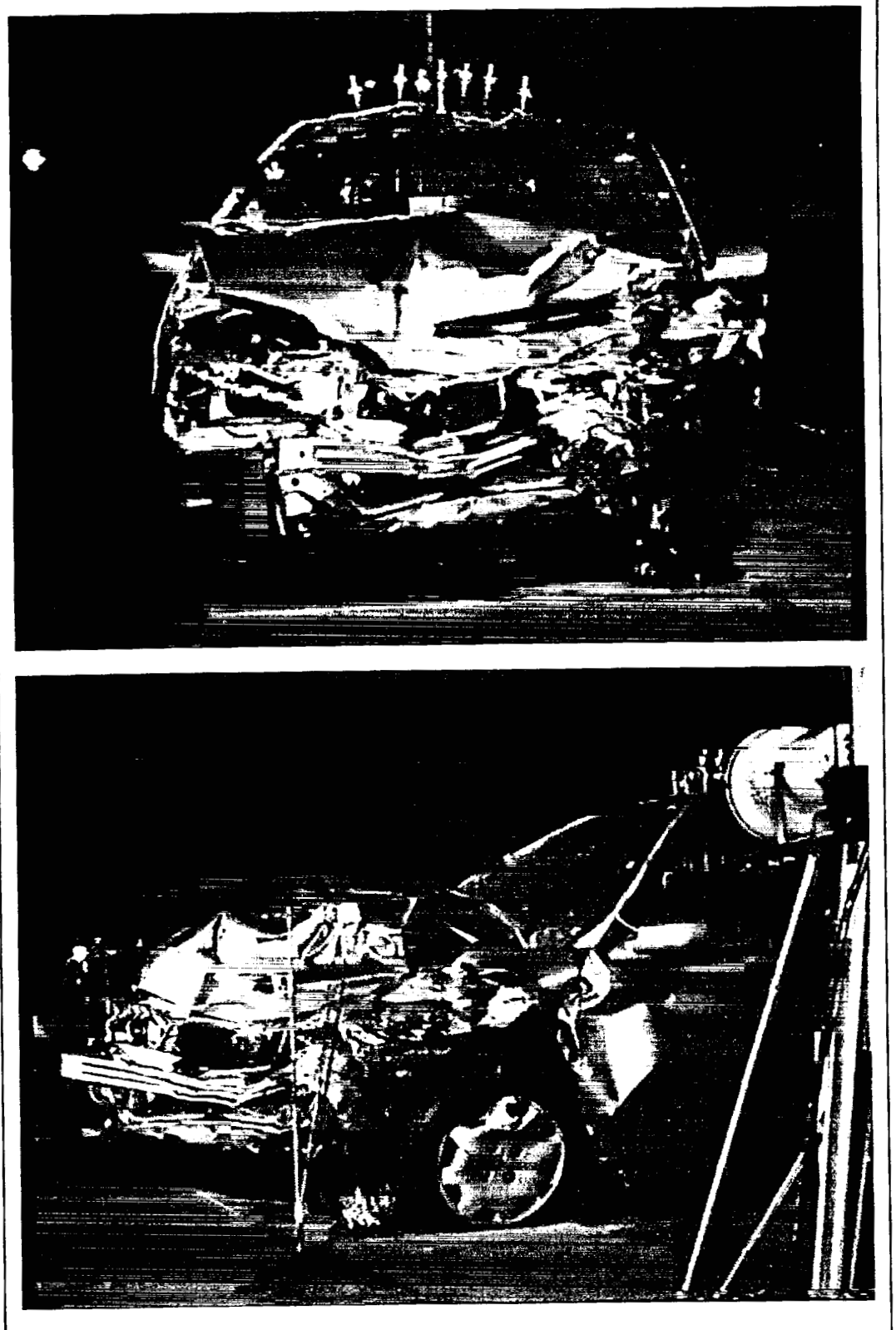

Figure 19. Fire Test F99030B. Video stills from Camera 1 (upper) and Camera 3 (lower) at 15 minutes post-ignition.

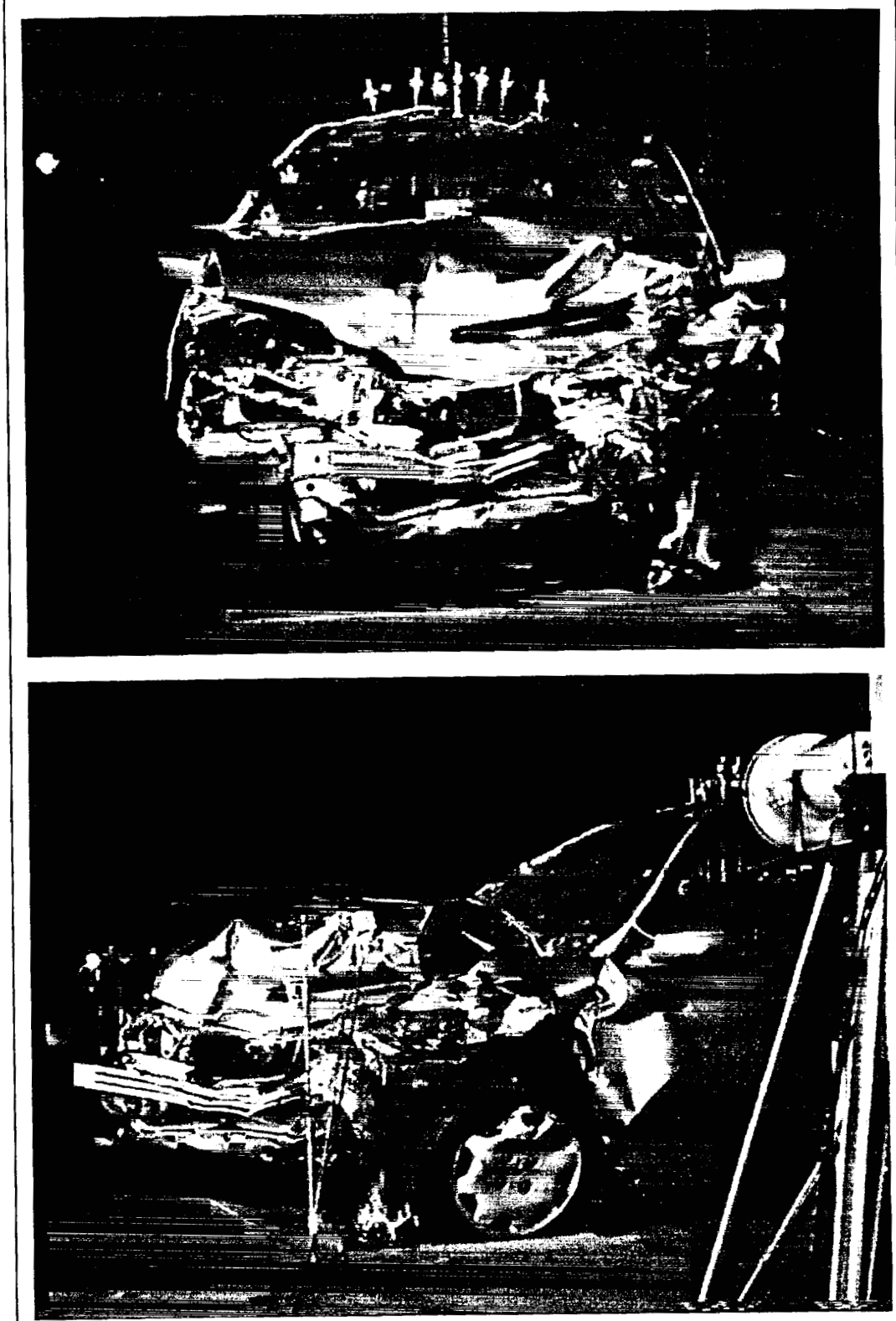

Figure 20. Fire Test F99030B. Video stills from Camera 1 (upper) and Camera 3 (lower) at 16 minutes post-ignition.

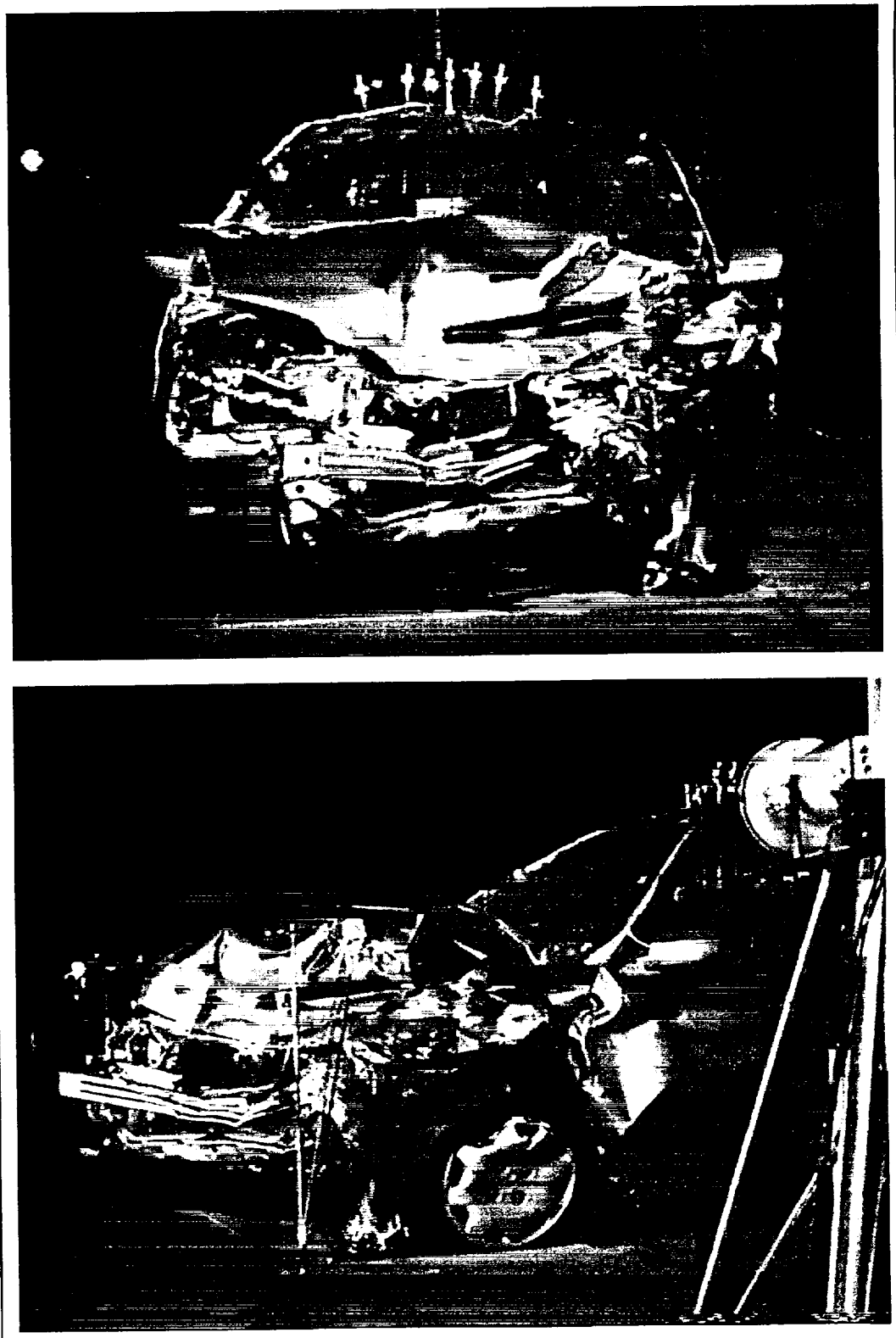

Figure 20. Fire Test F99030B. Video stills from Camera 1 (upper) and Camera 3 (lower) at 16 minutes post-ignition.

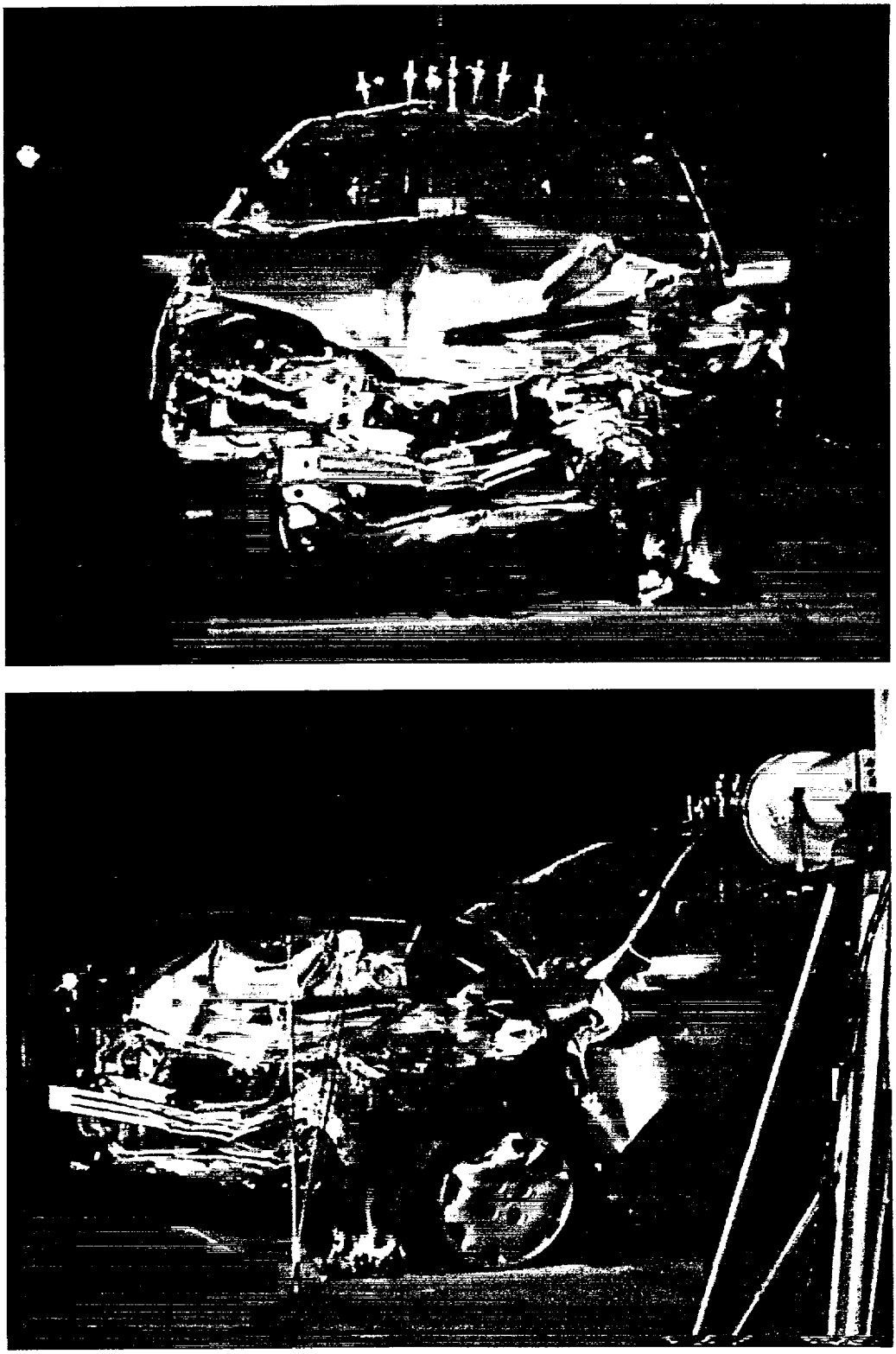

Figure 21. Fire Test F99030B. Video stills from Camera 1 (upper) and Camera 3 (lower) at 17 minutes post-ignition.

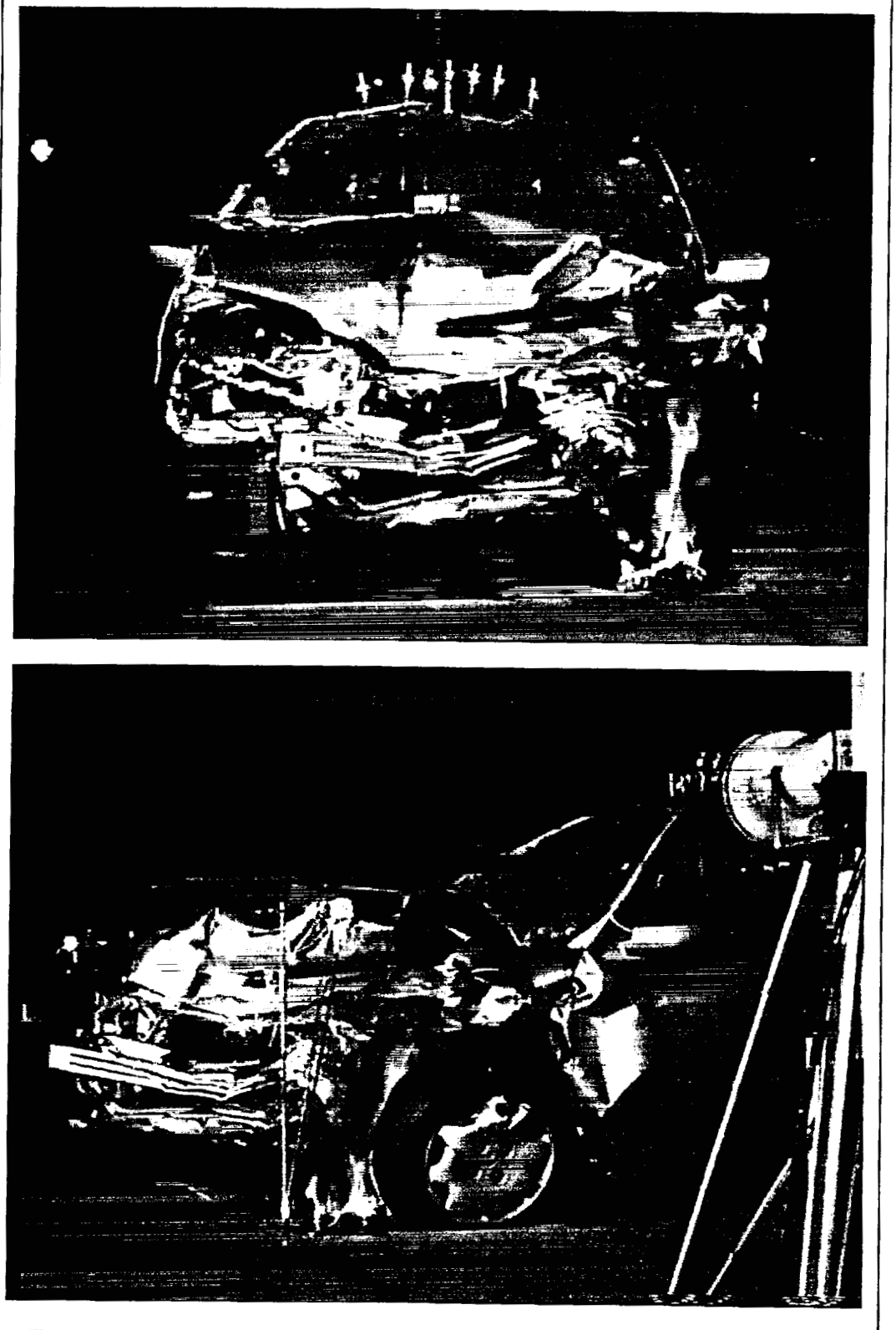

Figure 22. Fire Test F99030B. Video stills from Camera 1 (upper) and Camera 3 (lower) at 18 minutes post-ignition.

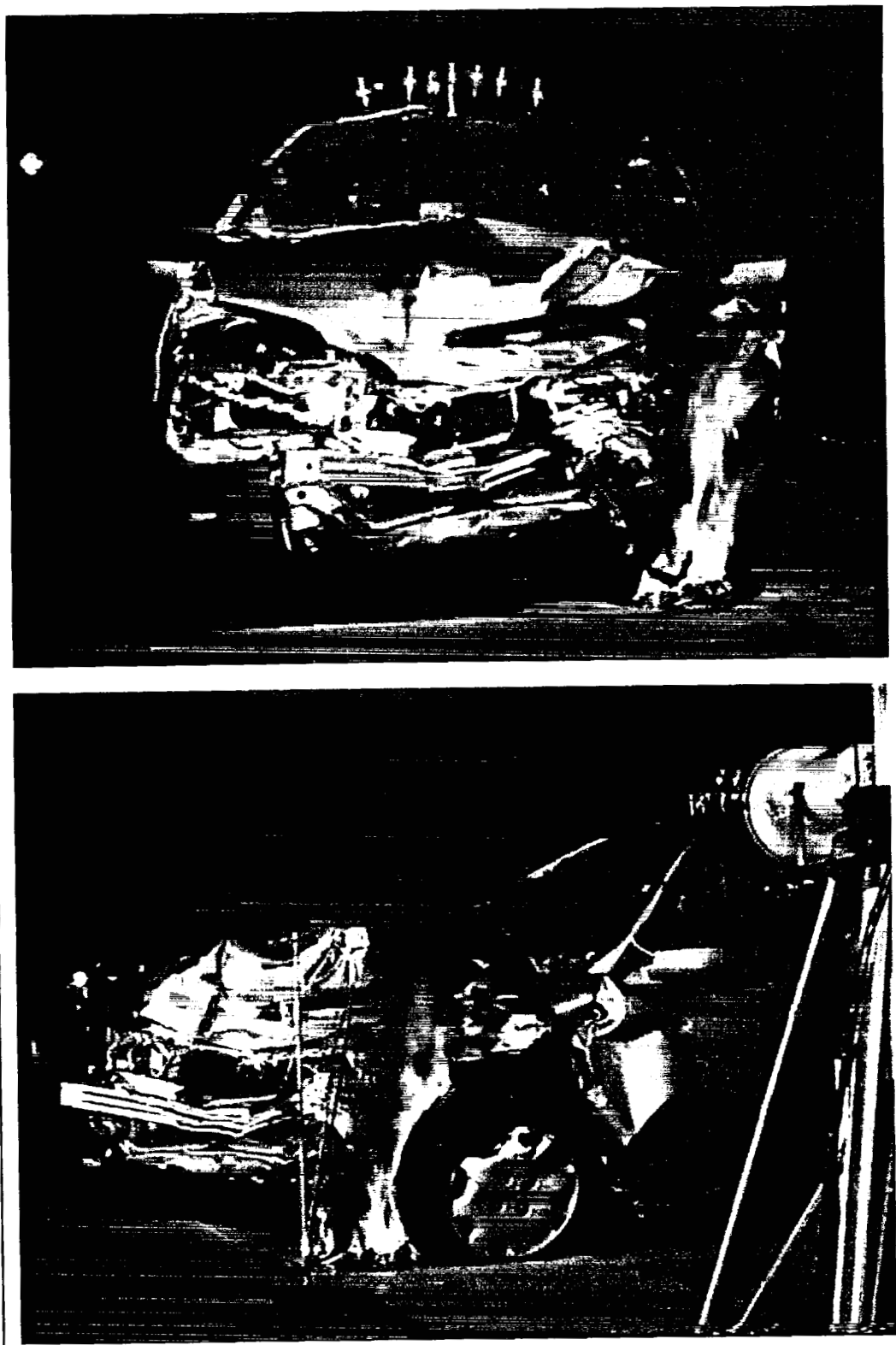

Figure 23. Fire Test F99030B. Video stills from Camera 1 (upper) and Camera 3 (lower) at 19 minutes post-ignition.

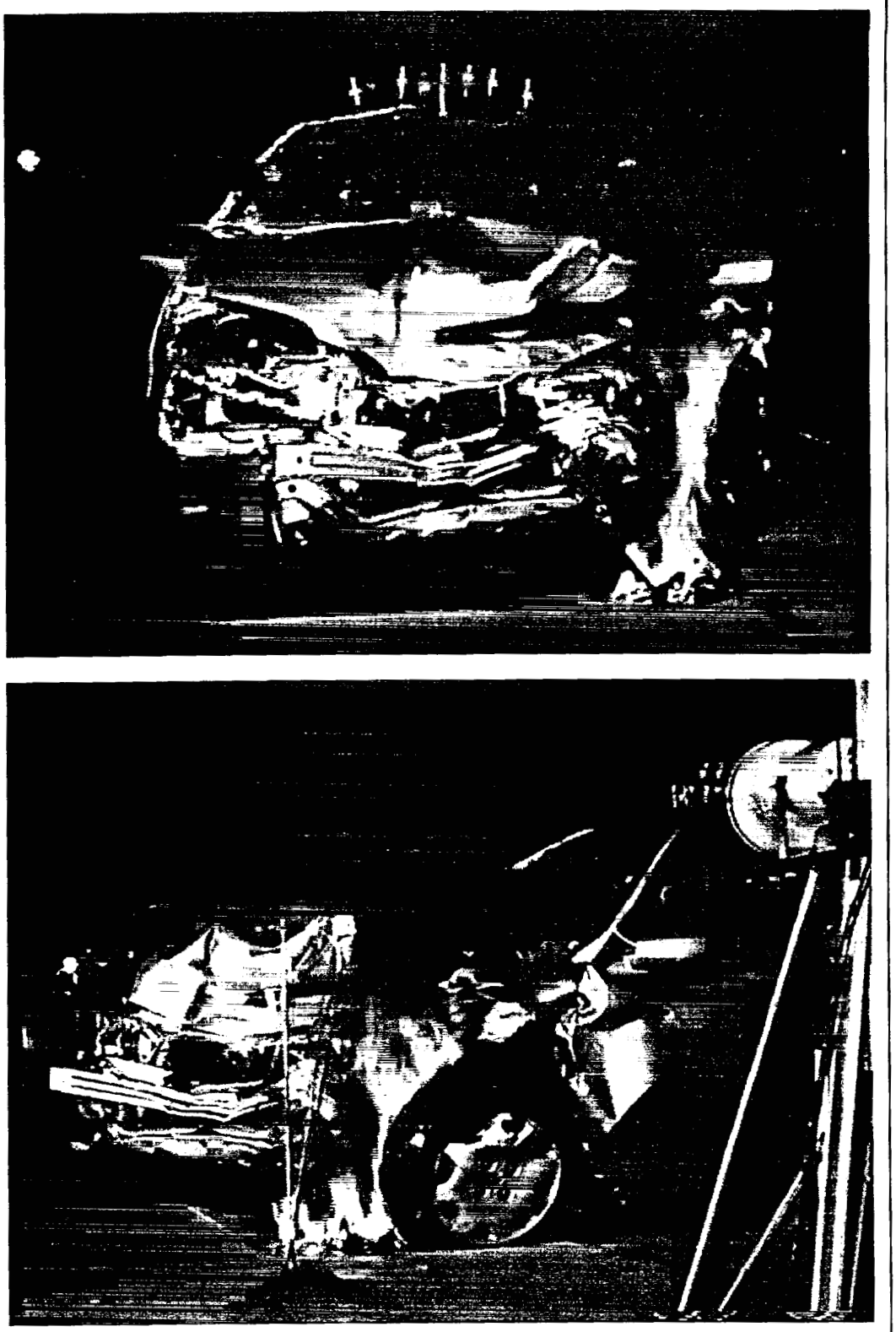

Figure 25. Fire Test F99030B. Video stills from Camera 1 (upper) and Camera 3 (lower) at 20 minutes post-ignition.

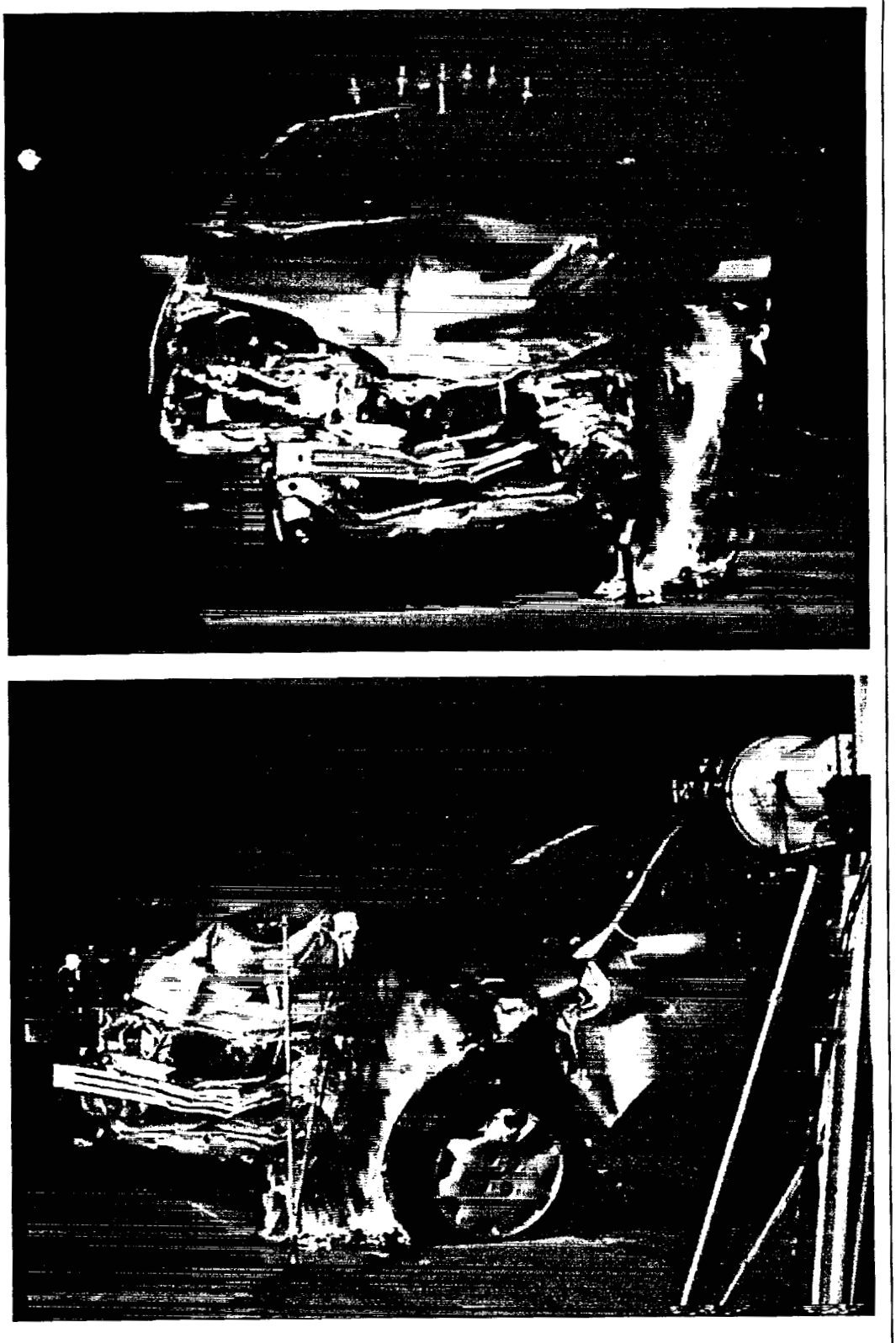

Figure 25. Fire Test F99030B. Video stills from Camera 1 (upper) and Camera 3 (lower) at 21 minutes post-ignition.

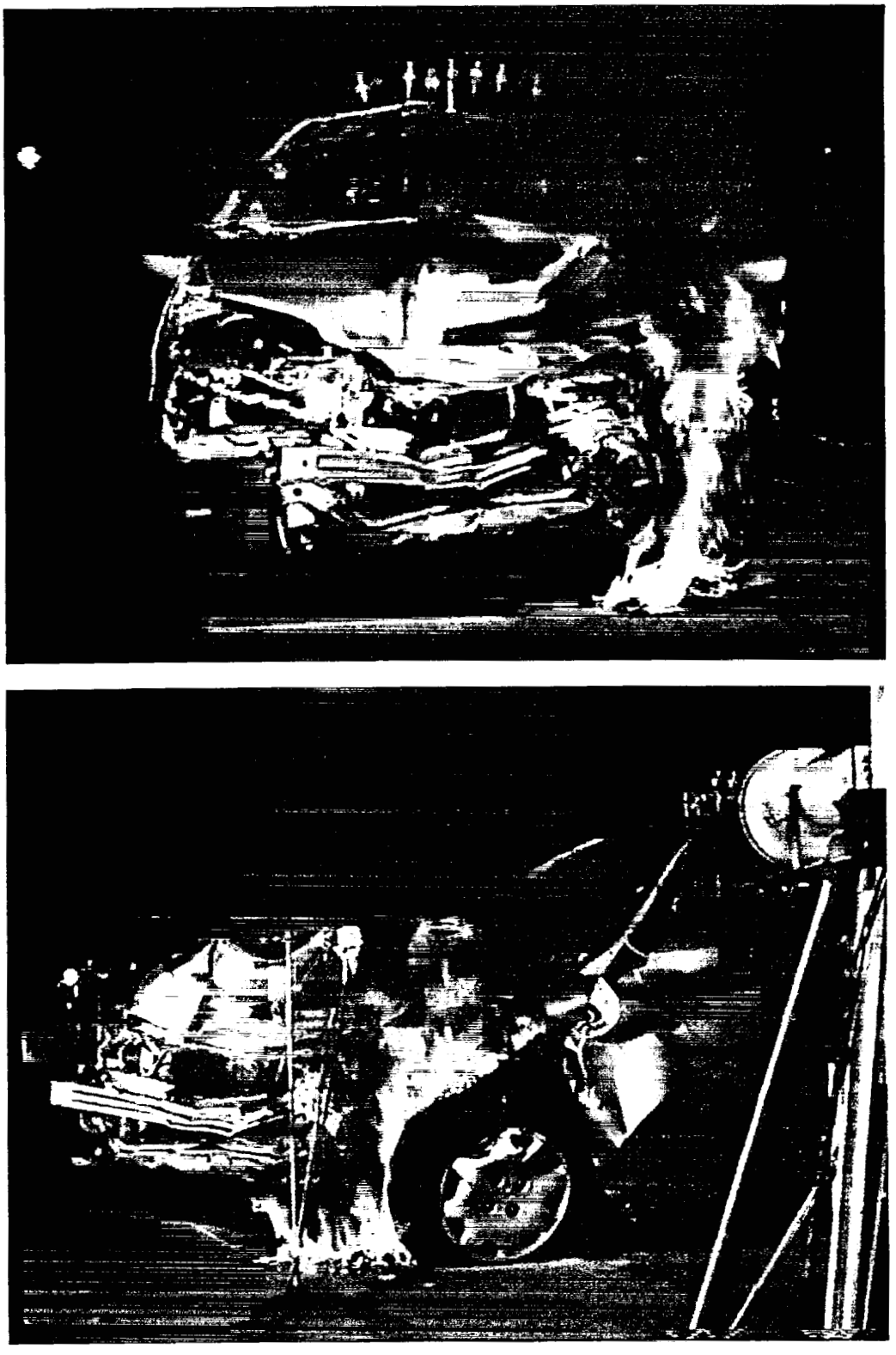

Figure 26. Fire Test F99030B. Video stills from Camera 1 (upper) and Camera 3 (lower) at 22 minutes post-ignition.

4.2 Flame-Spread in the Engine Compartment

Cameras 2 and 8 provided limited views of the engine compartment from the right side of the test vehicle. Figures 27 through 30 show video stills from Cameras 2 and 8 at 21, 22, 23, and 24 minutes post-ignition. These video stills show that flames first entered the engine compartment between 21 and 22 minutes post-ignition (Fig.'s 27 and 28). Flames had spread toward the right on the hood lining panel and to combustible materials in the left side of the engine compartment by 24 minutes post-ignition (Fig. 30). However, unambiguous determination of the location of the flame front and what objects were burning as flames spread to the right in the engine compartment was not possible by analysis of the videos from these cameras alone. Temperature data from thermocouples in the engine compartment of the test vehicle also was used to determine the timing of flame spread in the engine compartment in this test.

Figure 32 shows estimated isothermal contours along the lower surface of the hood (left diagram) and in the upper engine compartment (right diagram) of the test vehicle at 18, 19, 20, 21, 22, 23, 24, 25, 26, and 27 minutes post-ignition[3]. These estimated isothermal contour plots indicated that heated gases entered the left side of the engine compartment and flowed from left to right along the lower surface of the deformed hood between 18 and 21 minutes post-ignition. Temperatures recorded from thermocouples along the lower surface of the hood were 75 to 150°C greater than temperatures recorded from thermocouples in the upper engine compartment. These data indicate that a vertical temperature gradient of 2 – 4°C/cm existed in the space between components in the engine compartment and the hood for at least 3 to 4 minutes before flames entered the engine compartment.

Video stills from Cameras 2 and 8 show flames on the lower surface of the hood insulator at 22 minutes post-ignition (Fig. 28). At 22 minutes post-ignition temperatures along the left side of the hood were between 500 and 600°C while temperatures on the right side of the hood insulator were < 200°C (Fig. 32). Temperatures were slightly lower than the 600°C threshold used to indicate the presence of flames in previous reports.[4] The hood insulator consisted of glass fibers

[3] Isothermal contours of the temperature below the lower surface of hood insulator panel were estimated from the temperature data recorded from Thermocouples H1, H2, H3, H4, H5, H6, H7, and H8. Isothermal contours of the temperature in the upper engine compartment were estimated from the temperature data recorded from Thermocouples A7, A11, A12, A13, A14, A16, A17, C1, C2, C3, C4, and C5. A three-dimensional interpolation algorithm available in SigmaPlot for Windows Version 4.00 used to calculate the estimated isothermal contour data [4]. This algorithm uses an inverse distance method to interpolate temperature values for points on a uniformly spaced Cartesian grid from the [x,y,t] triple data from these thermocouples. Refer to **APPENDIX C** for the approximate locations of these thermocouples.

[4] A value of 600°C was used in previous reports as the threshold to indicate the presence of flame. Using this criterion, the 600°C isothermal contour indicated the approximate boundary of the flame front in the engine compartment.

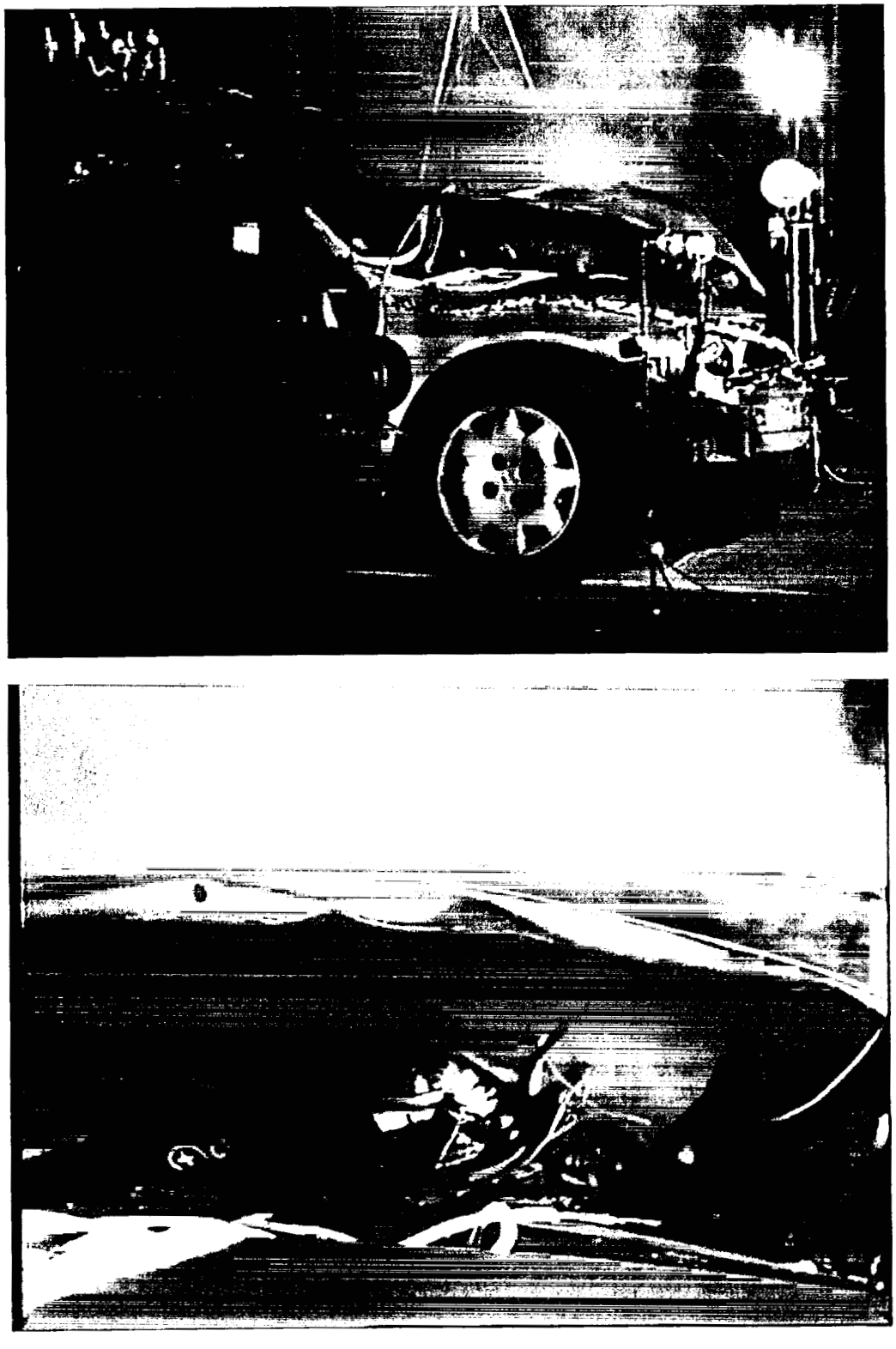

Figure 27. Fire Test F99030B. Video stills from Camera 2 (upper) and Camera 8 (lower) at 21 minutes post-ignition.

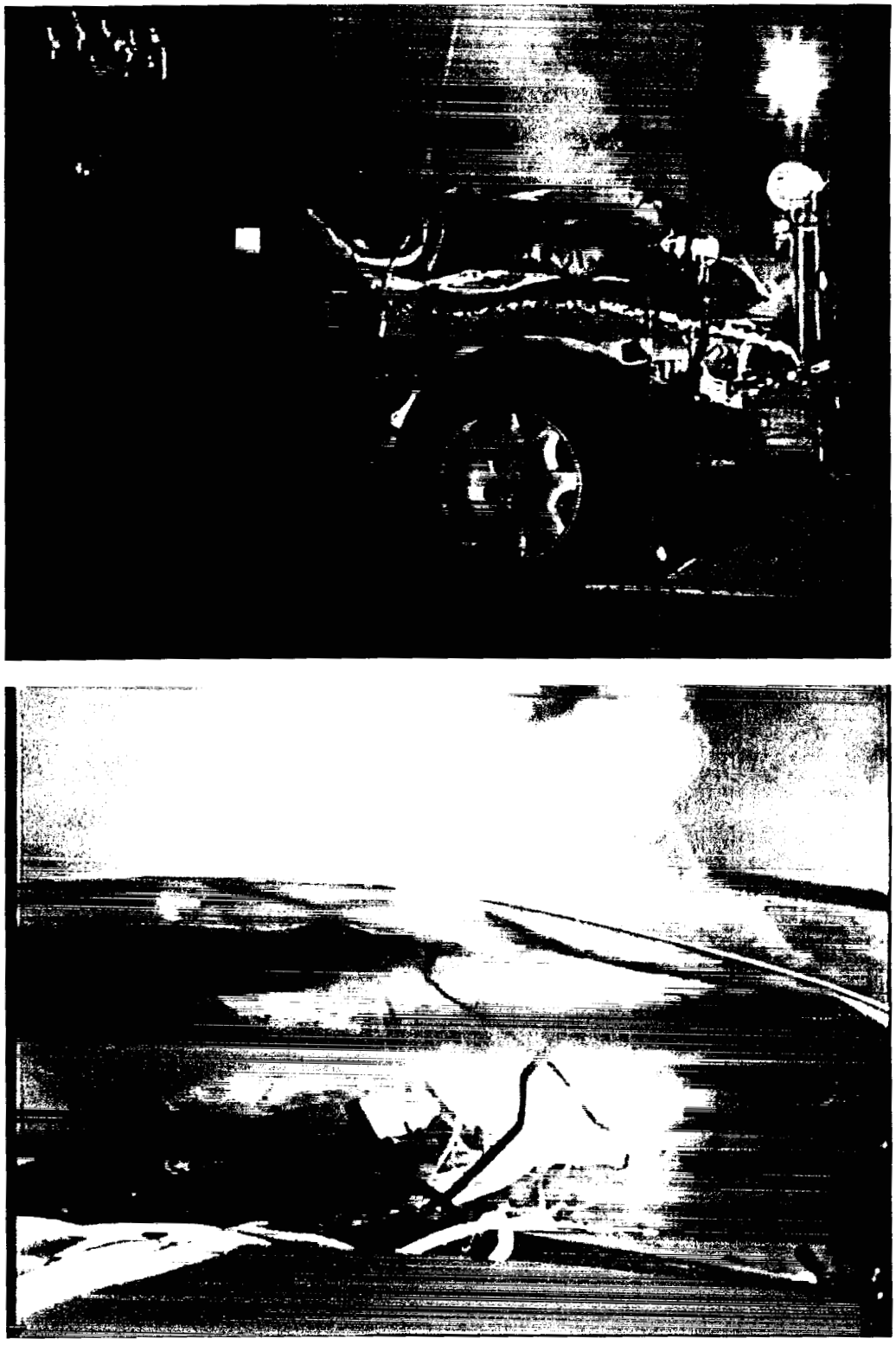

Figure 28. Fire Test F99030B. Video stills from Camera 2 (upper) and Camera 8 (lower) at 22 minutes post-ignition.

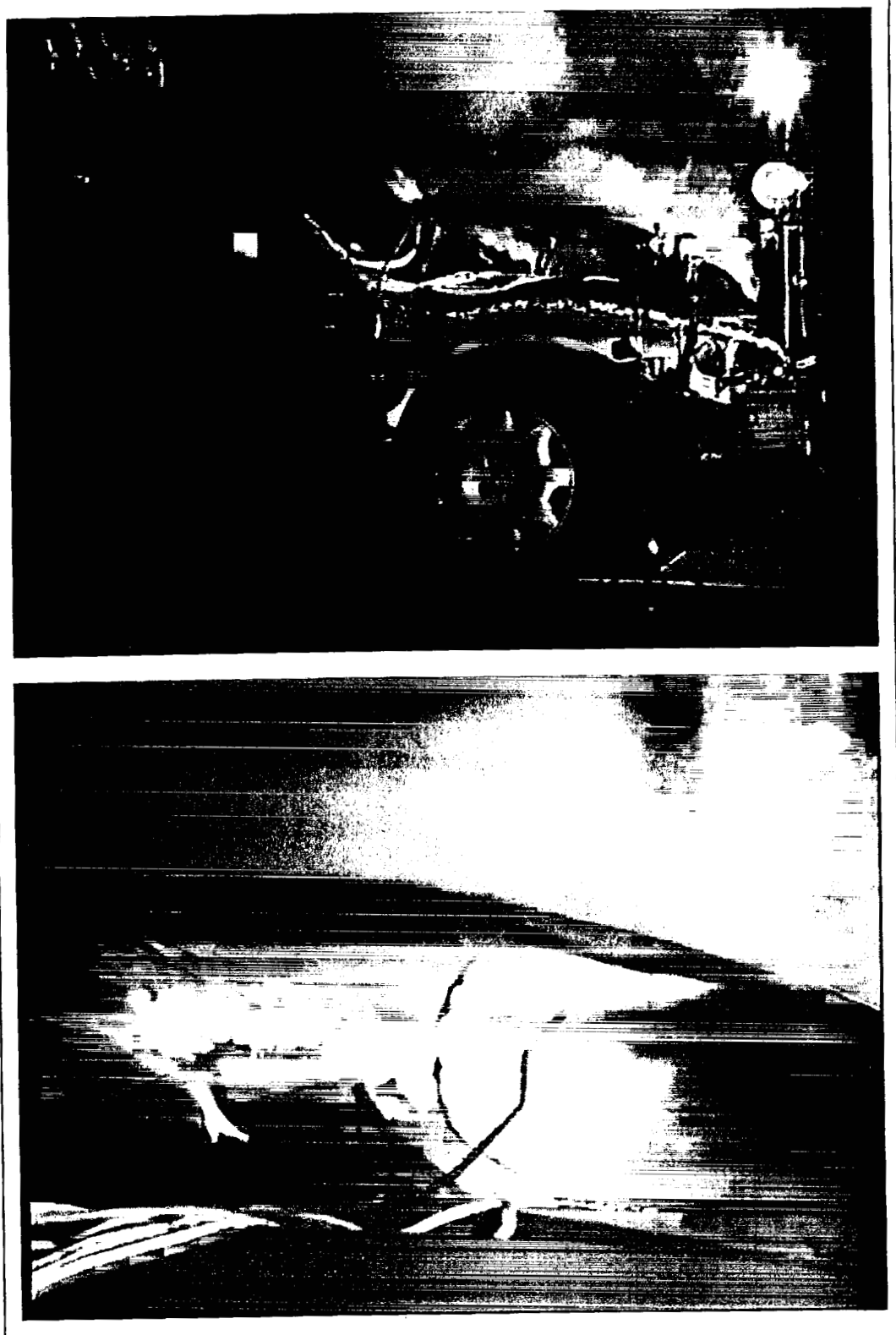

Figure 29. Fire Test F99030B. Video stills from Camera 2 (upper) and Camera 8 (lower) at 23 minutes post-ignition.

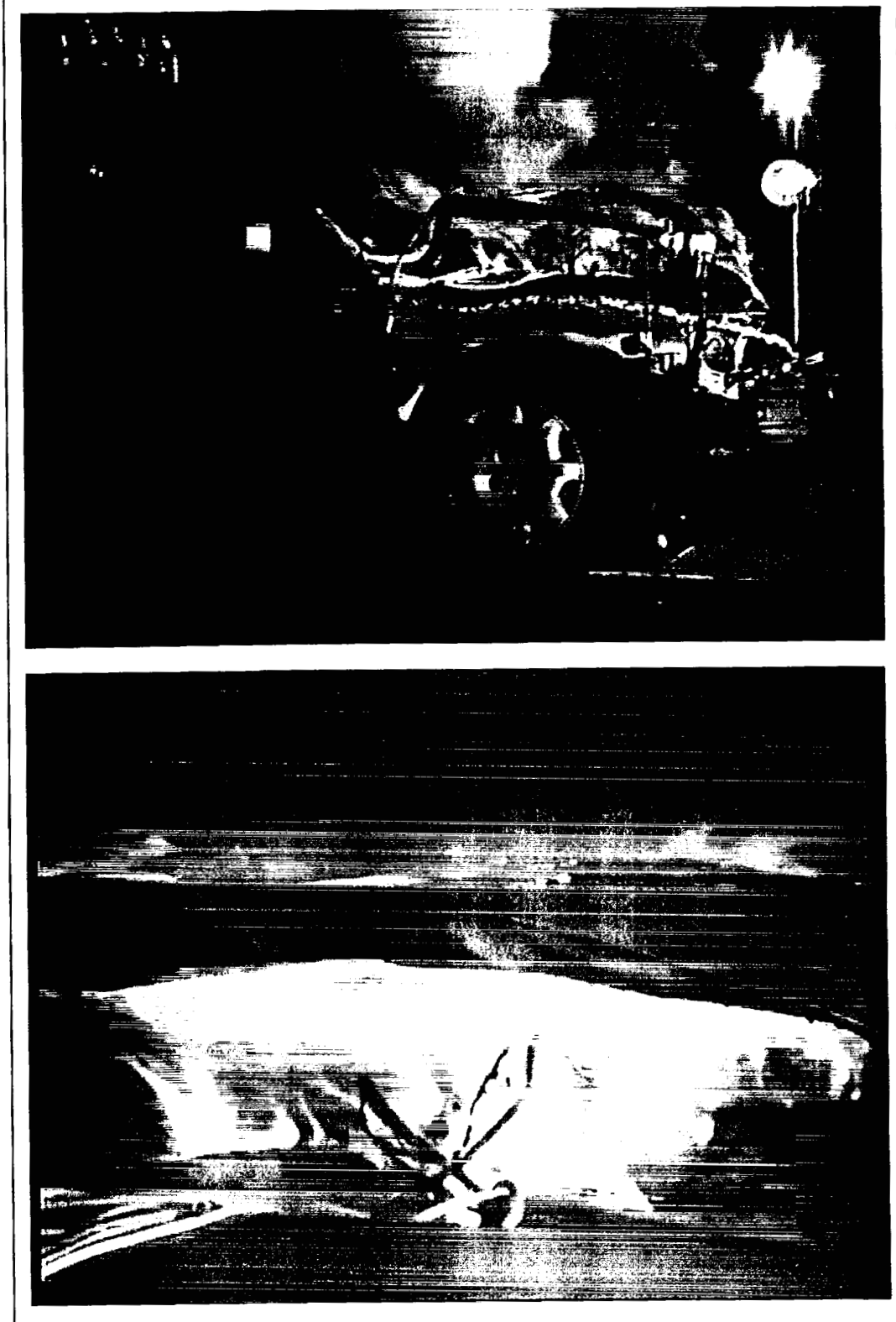

Figure 30. Fire Test F99030B. Video stills from Camera 2 (upper) and Camera 8 (lower) at 24 minutes post-ignition.

Figure 31. Fire Test F99030B. Video stills from Camera 2 (upper) and Camera 8 (lower) at 25 minutes post-ignition.

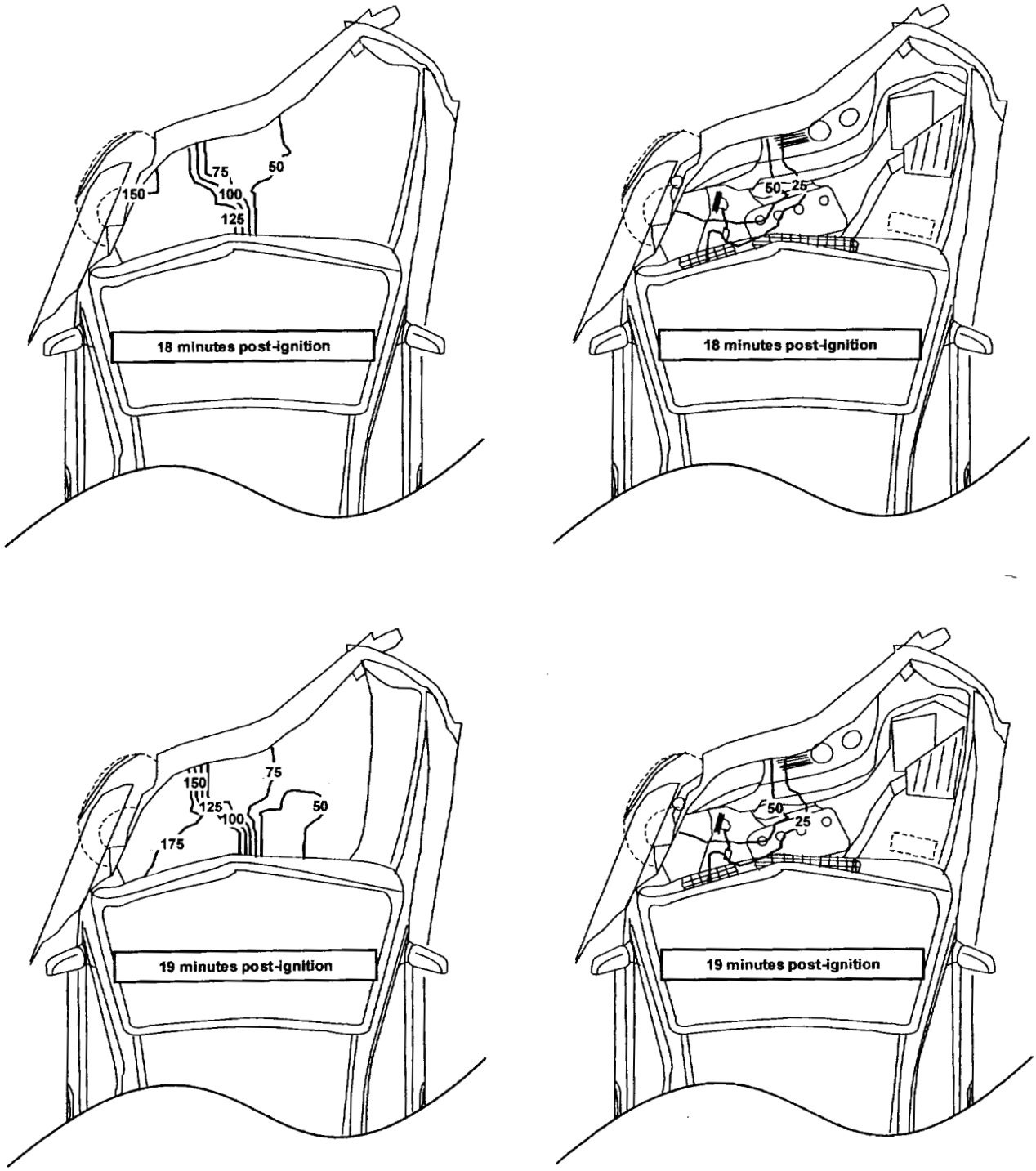

Figure 32. Fire Test F99030B. Isothermal contour plots of estimated temperatures along the lower surface of the hood (left) and in the upper engine compartment (right) of the test vehicle at 18, 19, 20, 21, 22, 23, 24, 25, 26, and 27 minutes post-ignition.

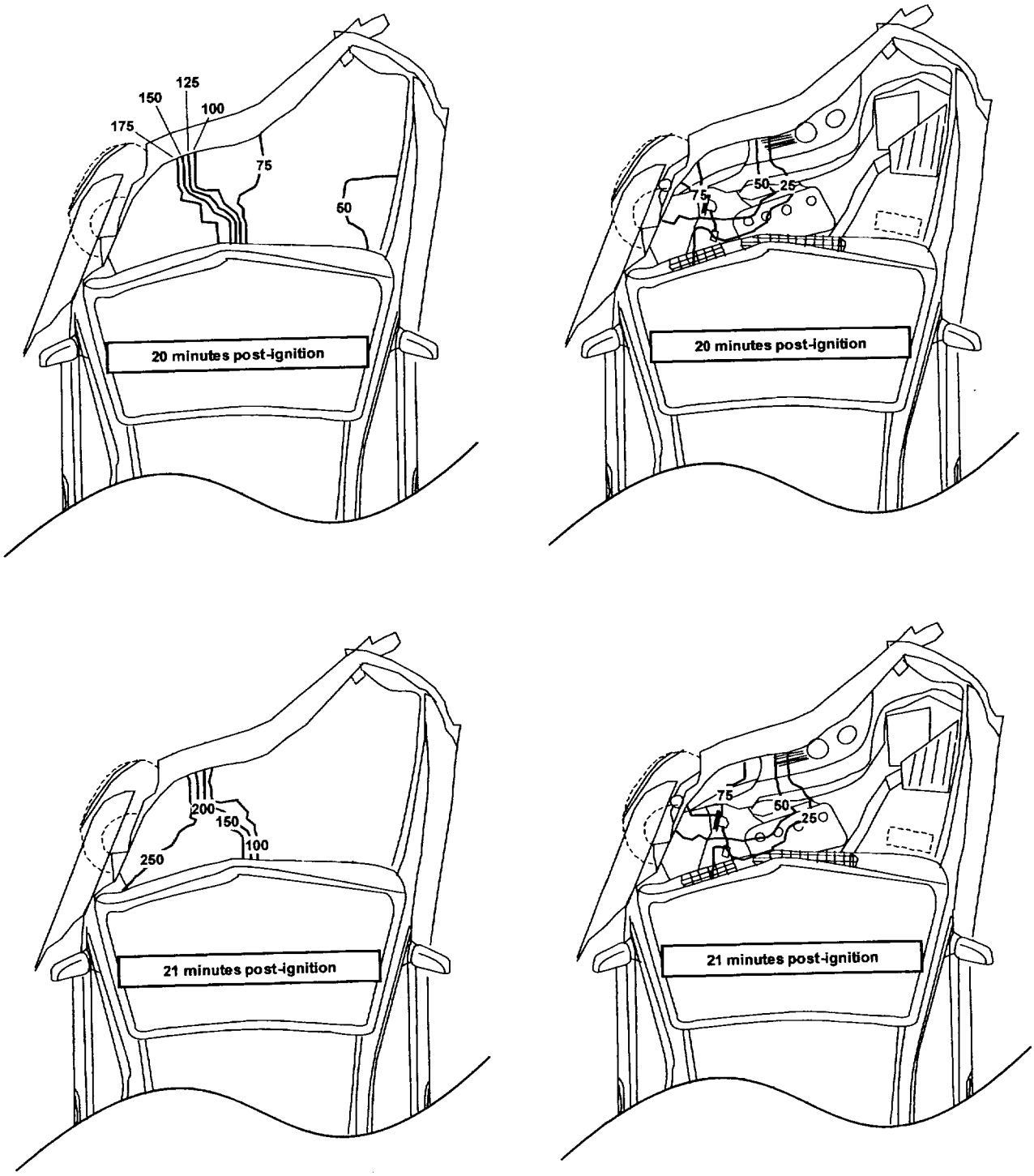

Figure 32, continued. Fire Test F99030B. Isothermal contour plots of estimated temperatures along the lower surface of the hood (left) and in the upper engine compartment (right) of the test vehicle at 18, 19, 20, 21, 22, 23, 24, 25, 26, and 27 minutes post-ignition.

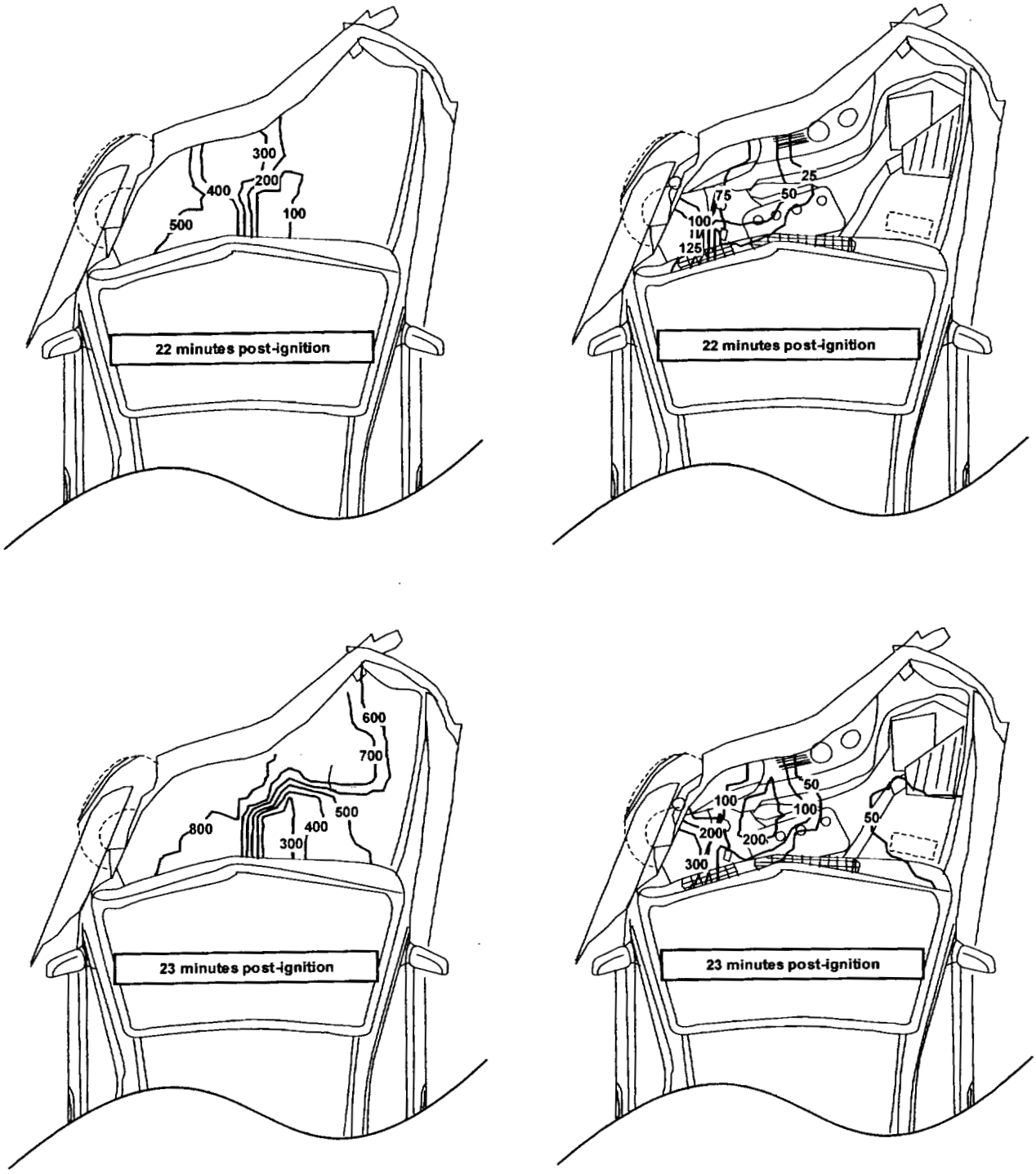

Figure 32, continued. Fire Test F99030B. Isothermal contour plots of estimated temperatures along the lower surface of the hood (left) and in the upper engine compartment (right) of the test vehicle at 18, 19, 20, 21, 22, 23, 24, 25, 26, and 27 minutes post-ignition.

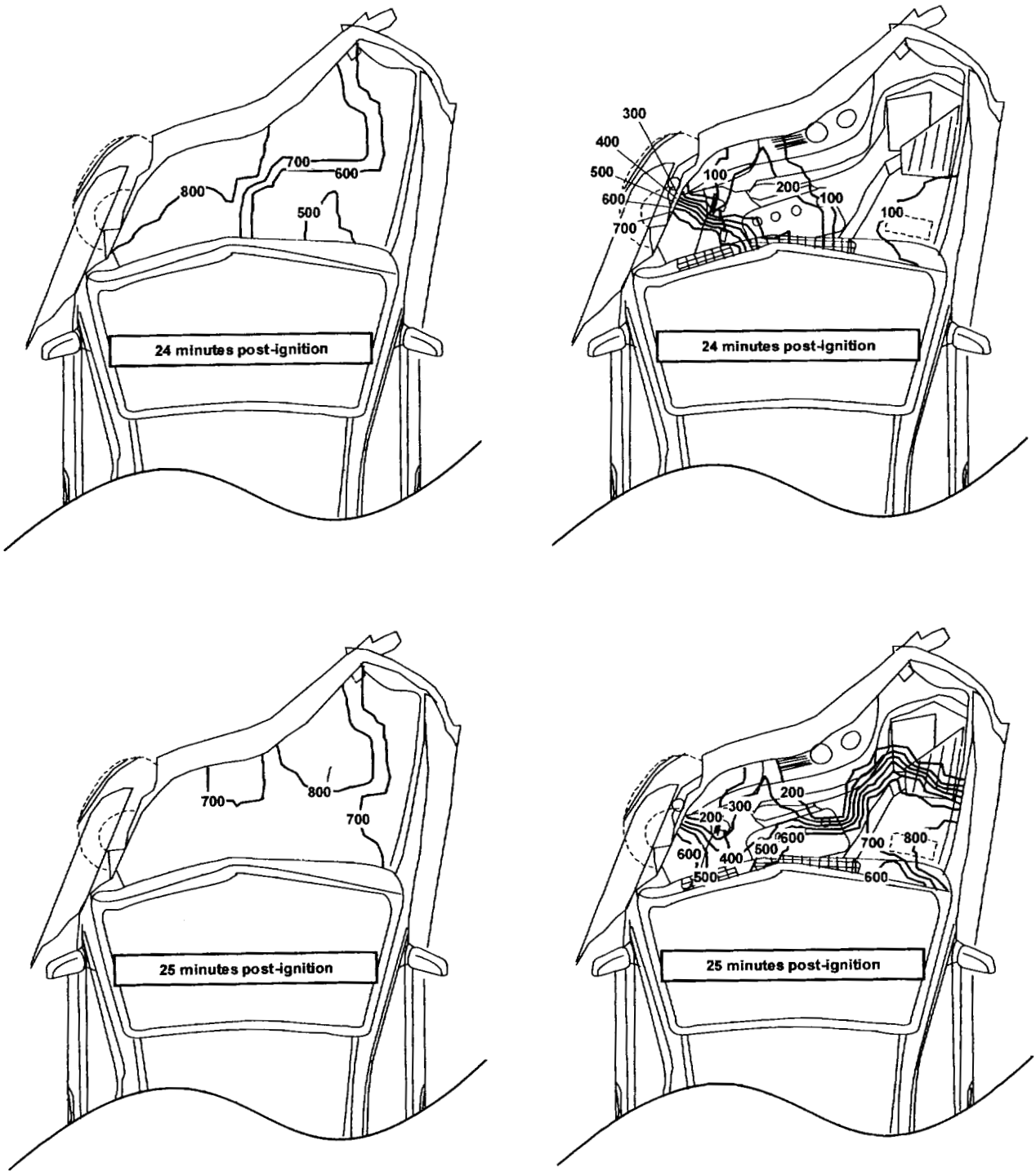

Figure 32, continued. Fire Test F99030B. Isothermal contour plots of estimated temperatures along the lower surface of the hood (left) and in the upper engine compartment (right) of the test vehicle at 18, 19, 20, 21, 22, 23, 24, 25, 26, and 27 minutes post-ignition.

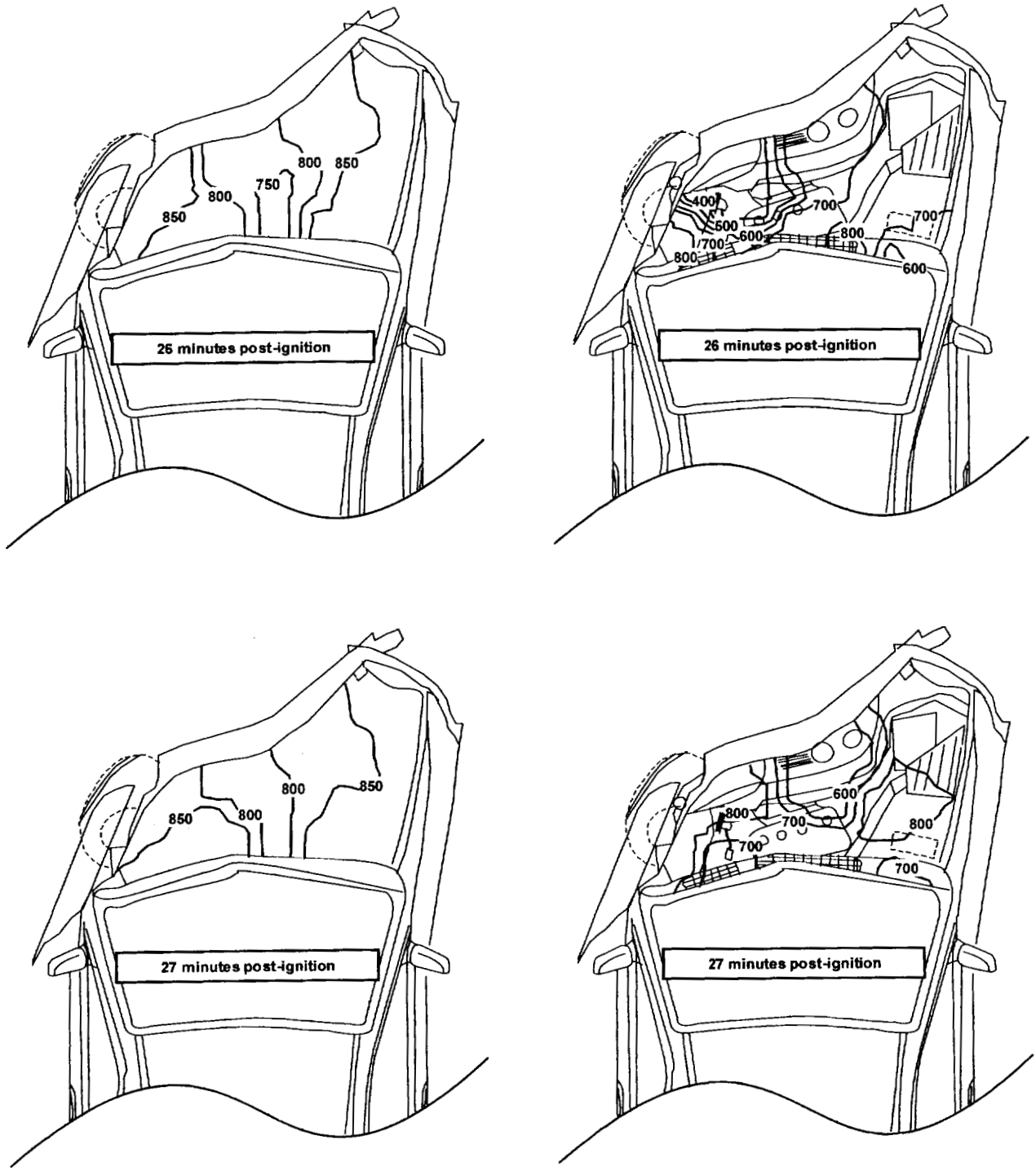

Figure 32, continued. Fire Test F99030B. Isothermal contour plots of estimated temperatures along the lower surface of the hood (left) and in the upper engine compartment (right) of the test vehicle at 18, 19, 20, 21, 22, 23, 24, 25, 26, and 27 minutes post-ignition.

held together with an organic binder. The low organic (binder) content of this material may explain the low temperatures observed on the right side of the hood insulator during the early stages of ignition of the hood insulator just after flames entered the engine compartment.

The video stills from Cameras 2 and 8 appear to show flames on the entire width of the hood insulator and attached to components in the left side of the engine compartment by 24 minutes post-ignition (Fig. 30). Temperature data recorded from thermocouples in the hood insulator and in the engine compartment are consistent with this assessment, showing temperatures greater than 600°C along most of the hood insulator and in the left rear section of the engine compartment (Fig. 32). By 25 minutes post-ignition, flames were observed venting from the engine compartment along the right side of the deformed hood (upper video still, Fig. 31), and temperatures on the hood insulator were > 600°C on the entire lower surface of the hood insulator (Fig. 32). Estimated isothermal contours in the engine compartment indicted that only components in the rear of the engine compartment had ignited (Fig. 32), while temperatures in the front of the engine compartment were less that 200°C at this time (Fig. 32). Between 25 and 27 minutes post-ignition, flames spread forward in the engine compartment so that estimated temperatures in the engine compartment were > 600°C except in an area near the center of the upper radiator cross-member (Fig. 32).

5 Flame-Spread into the Passenger Compartment

Flames spread into the passenger compartment through the windshield and through pass-through openings in the left side of the dash panel. Flames entering the passenger compartment through pass-through openings in the dash panel ignited components in the left side of the instrument panel. Flame-spread through the windshield progressed by (1) flame-spread rearward along the top of the instrument panel and (2) ignition of interior components by pieces of windshield with the inner layer burning and falling into the passenger compartment.

5.1 Flame-Spread into the Passenger Compartment Through the Windshield

The lower left corner of the windshield in the test vehicle was exposed to heated gases from the fire starting at about 7 minutes post-ignition. A section of the windshield in front of the left front seat was exposed to flames from the burning HVAC air intake cowl starting at about 22 minutes post-ignition. A hole developed in the lower left side of the windshield in front of the steering wheel between 22 and 24 minutes post-ignition. Flames from the engine compartment entered the passenger compartment through this hole and spread upward along the interior surface of the windshield, igniting the windshield inner-layer around this hole and in an area where pieces of glass were dislodged from the windshield and the inner-layer was exposed. Pieces of windshield with the inner-layer burning started to fall into the passenger compartment between 23 and 23½ minutes post-ignition. A section of the windshield sagged onto the left side of the instrument panel between 24½ and 25 minutes post-ignition.

Figure 33 shows plots of temperature data recorded from thermocouples located on the lower exterior surface of the windshield in the test vehicle. These data indicate that the extreme left side of the windshield was exposed to heated gases from the fire starting at about 7 minutes post-ignition. The fire remained outside the engine compartment until between 21 and 22 minutes post-ignition. Thermocouple W1 was located on the left corner of the windshield which is normally rearward of the hood. However, because the front section of the test vehicle was displaced to the right during the crash test, Thermocouple W1 was located outboard of the left side of the engine compartment, allowing heated gases from the burning windshield washer fluid reservoir and left front tire to flow upward onto this section of the windshield. Temperatures recorded from Thermocouple W1 increased from an ambient temperature of about 24°C before 7 minutes post-ignition to approximately 175°C by 20 minutes post-ignition (Fig. 33), while temperatures recorded from Thermocouples W2, W3, W4, and W5 remained at pre-ignition levels during this time (Fig. 33).

As flames spread into the left side of the engine compartment, a section on the lower left side of the windshield that was rearward of the engine compartment was exposed to flames venting from the rear edge of the deformed hood. This is seen in the increases in temperatures recorded from Thermocouple W2 from approximately 30°C at 21½ minutes post-ignition to 770°C by 23 minutes post-ignition (Fig. 33). Temperatures recorded from Thermocouples W3, W4, and W5 indicate that the center and right side of the windshield were exposed to flames venting from the rear edge of the hood as fire propagated to the right in the engine compartment (Fig. 33).

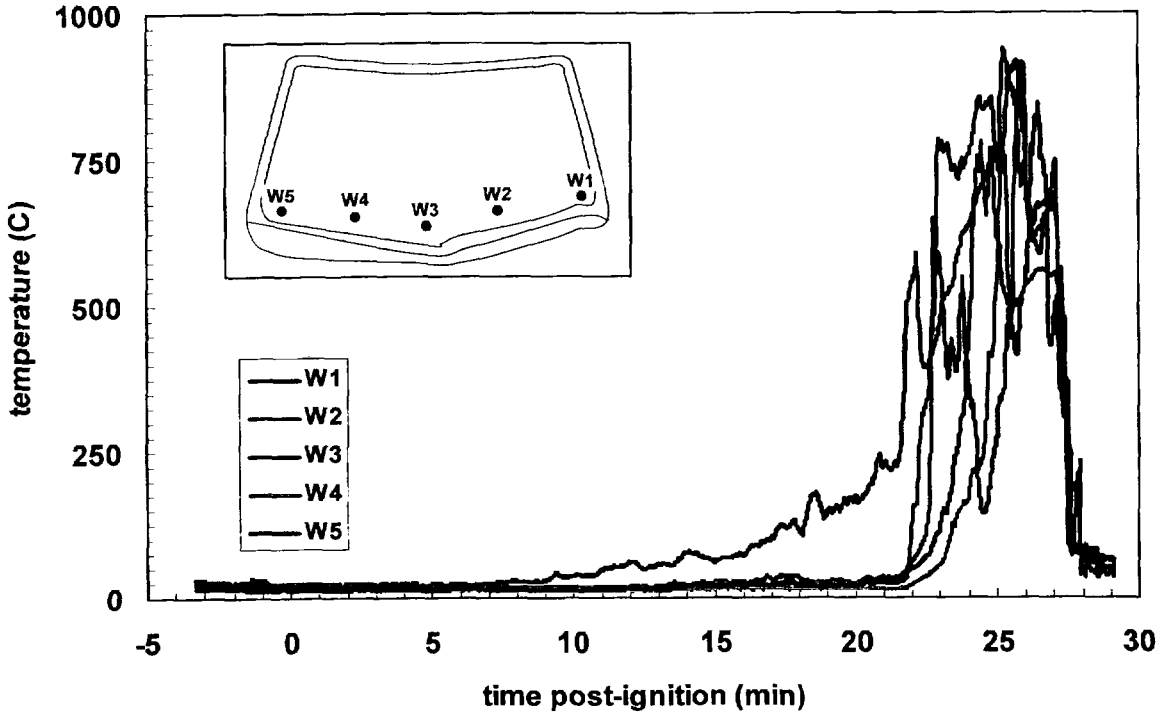

Figure 33. Fire Test F99030B. Temperature data from Thermocouples W1, W2, W3, W4, and W5 located on the exterior surface of the windshield. The insert shows the approximate locations of these thermocouples on the windshield.

Data recorded from a heat flux transducer in the left side of the windshield indicated that the heat flux to the lower left of the windshield rearward of the engine compartment increased as fire propagated into the left side of the engine compartment (Fig. 34). Heat transfer to the windshield resulted in increases in the temperature of both the exterior and interior glass outer-layers in this section of the windshield. For example, at 20 minutes post-ignition, the exterior surface of the windshield was exposed to heated gases flowing from the objects burning in the left front fender. The heat flux to this section of the windshield was approximately 3 kW/m^2 and the temperatures of the exterior and interior glass outer-layers were approximately 65 and 50°C, respectively (Fig. 34). At 23 minutes post-ignition, this area of the windshield was exposed to flames (Fig. 33). The

heat flux to this section of the windshield was 33 kW/m^2 and the temperatures of the exterior and interior glass outer-layers were approximately 260°C and 100°C (Fig. 34).

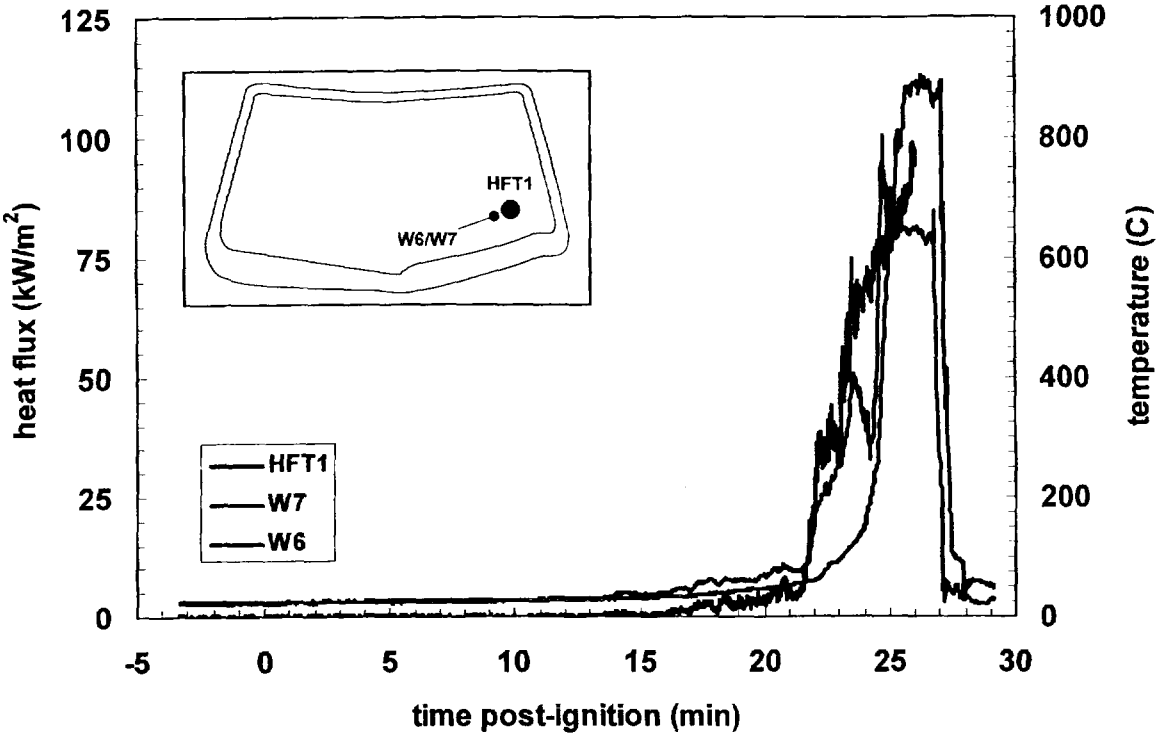

Figure 34. Fire Test F99030B. Heat flux data from HFT1 and temperature data from Thermocouples W6 and W7 located on left section of the windshield in the test vehicle. Heat flux data from HFT1 was invalid after about 26 min, and therefore not shown in this plot, minutes post-ignition because this exceeded its upper temperature limit at this time.

The glass outer-layers of the windshield were broken during the crash test of the test vehicle. The edges of the windshield remained attached to the metal frame of the windshield opening and most of the fragments of the glass outer-layers remained attached to the windshield inner-layer.[5] As the temperature of the windshield increased, the windshield inner-layer softened and the windshield sagged under the weight of the glass. As the windshield inner-layer liquefied, pieces of windshield to fall into the passenger compartment. Figures 35 through 38 show a series of video stills from Camera 9 at 22, 23, 24, and 25 minutes post-ignition. These video stills show a view of the lower left side of the interior of the windshield through the left front door window.

[5] Motor vehicle windshields are laminated structures consisting of two glass outer-layers adheared to a polymer inner-layer. The windshield inner-layer in the test vehicle was a (vinyl butural/vinyl alcohol) copolymer. Laboratory tests not reported here indicate that the glass transition temperature (Tg) of this polymer is between 70 and 80°C, and it starts to undergo thermal decomposition (loses mass) when heated to temperatures greater than about 350°C.

Figure 35. Fire Test F99030B. Video still from Camera 9 at 22 minutes post-ignition.

Figure 36. Fire Test F99030B. Video still from Camera 9 at 23 minutes post-ignition.

Figure 37. Fire Test F99030B. Video still from Camera 9 at 24 minutes post-ignition.

Figure 38. Fire Test F99030B. Video still from Camera 9 at 25 minutes post-ignition.

These video stills show that two holes developed in the lower edge of the windshield in front of the left front seat between 22 and 23 minutes post-ignition (Fig.'s 35 and 36). A section of windshield sagged onto the top of the instrument panel between 23 and 25 minutes post-ignition (Fig.'s 36, 37, and 38).

The temperature of the windshield inner-layer was not measured in this test. However, temperatures recorded from thermocouples attached to the glass outer-layers (Fig. 34) can be used to estimate the temperature gradient through the lower left side of the windshield, and the temperature of the windshield inner-layer was between the temperatures of the glass outer-layers. Table 2 contains estimates of the temperature of the windshield inner-layer at the location of Thermocouples W6 and W7 assuming a linear temperature gradient through the windshield.

Table 2
Estimates of the Temperature of the Windshield Inner Layer

Time Post-Ignition (min)	Temperature (C)
20	57
20½	63
21	67
21½	70
22	100
22½	145
23	180
23½	255

The estimates in Table 2 indicate that the temperature of the inner-layer in this area of the windshield exceeded the glass transition temperature of this material between 21½ and 22 minutes post-ignition. The windshield inner-layer would have been expected to soften and start to sag under the weight of the glass fragments at this time. These estimates indicate that the temperature of the windshield inner-layer was greater than its glass transition temperature between 1 and 2 minutes before holes were observed developing in the windshield.

Pieces of the broken windshield continued to fall into the passenger compartment until the test was ended at about 27 minutes post-ignition. Inspection of the test vehicle after this test showed that sections of the instrument panel and deployed passenger side airbag were charred where pieces of the windshield fell onto these objects (Fig. 39). Fragments of the windshield, where the inner-layer appeared to have liquefied and flowed out around the perimeter of the broken glass, ignited and burned, were embedded in the top of the instrument panel.

Figure 39. Fire Test F99030B. Photograph of the instrument panel of the test vehicle after this test.

5.1.1 Flame-Spread Rearward Along the Top of the Instrument Panel

Figure 40 shows isothermal contour plots of temperatures on the top of the instrument panel and deployed passenger side air bag of the test vehicle at ½-minute intervals between 23 and 27½ minutes post-ignition.[6]

[6] Isothermal contours of the temperature on the top of the instrument panel were estimated from the temperature data recorded from Thermocouples I1, I2, I3, I4, I5, I6, I7, I8, I9, and I10. A three-dimensional interpolation algorithm available in SigmaPlot for Windows Version 4.00 used to calculate the estimated isothermal contour data [4]. This algorithm uses an inverse distance method to interpolate temperature values for points on a uniformly spaced Cartesian grid from the [x,y,t] triple data from these thermocouples. Refer to **APPENDIX C** for the approximate locations of these thermocouples.

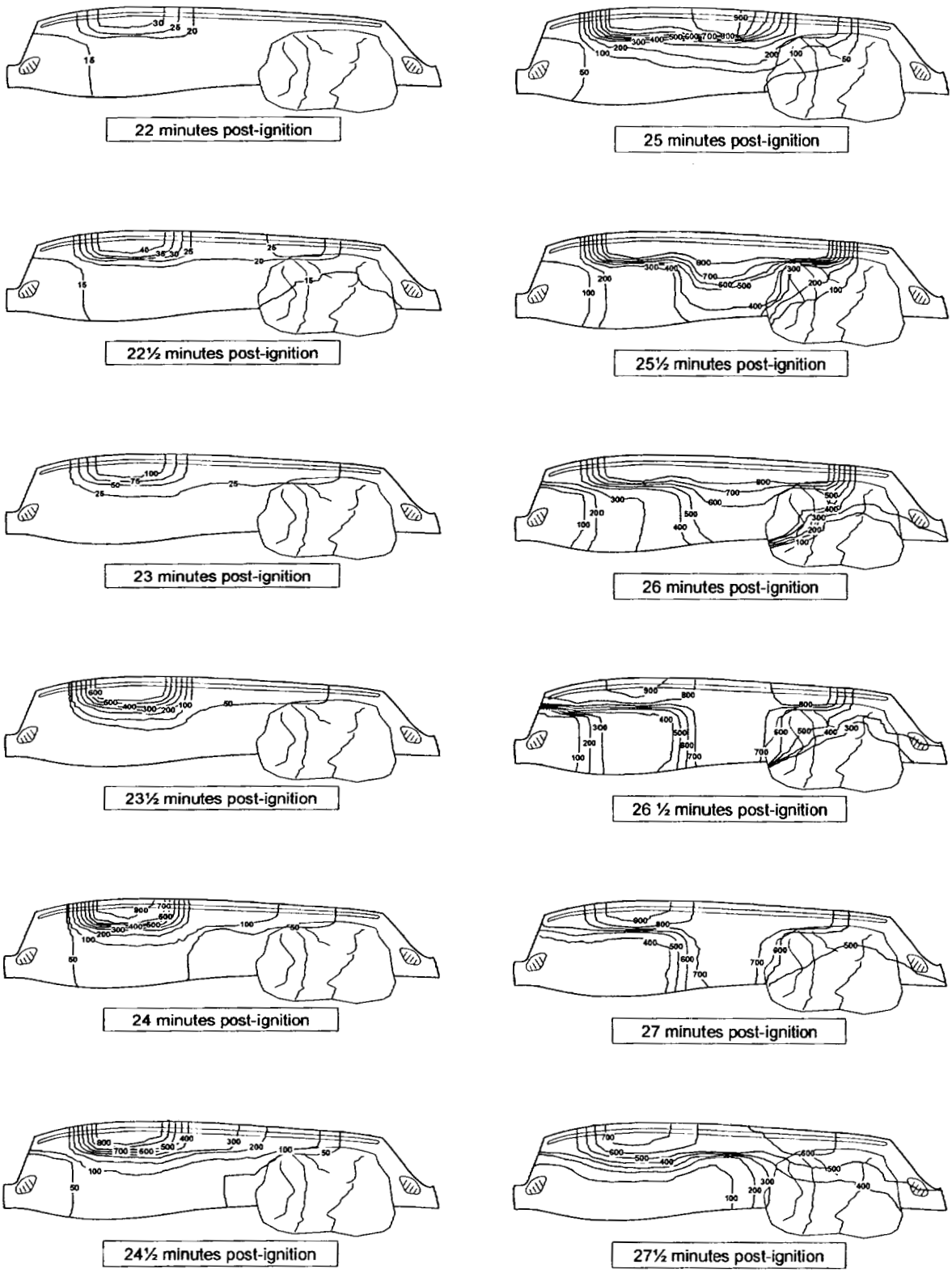

Figure 40. Fire Test F99030B. Plots of estimated temperatures on the top of the instrument panel of the test vehicle at 22, 22½, 23, 23½, 24, 24½, 25, 25½, 26, 26½, 27, and 27½ minutes post-ignition.

Temperature plots in Figure 40 indicate that a section of the forward edge of the left side of the instrument panel ignited between 23 and 23½ minutes post-ignition (Fig 40). This occurred in the same area where holes developed along the lower edge of the windshield between 22 and 24 minutes post-ignition (Fig.'s 35 through 38), and suggests that flames venting from the engine compartment along the rear edge of the left side of the deformed hood ignited the top of the instrument panel as sections of the windshield fell onto the instrument panel. Flames spread to the right across the front of the instrument panel between 23½ and 25 minutes post-ignition and, coincident with the timing of holes developing in the center of the windshield, rearward on the center of the instrument panel between 25 and 27 minutes post-ignition (Fig. 40). Flames spread to the right on the forward section of the instrument panel between 25½ and 26 minutes post-ignition and ignited the deployed passenger side air bag (Fig. 40).

Inspection of the test vehicle after this test showed that fire damage to the top of the instrument panel extended from the left A-pillar to the deployed passenger air bag (Fig. 41). The areas around the side window defroster vents were not burned (Fig. 41). The area that showed evidence of fire damage after this test (Fig. 41) was greater that the area of the instrument panel where estimated temperatures were > 600°C (Fig. 40).

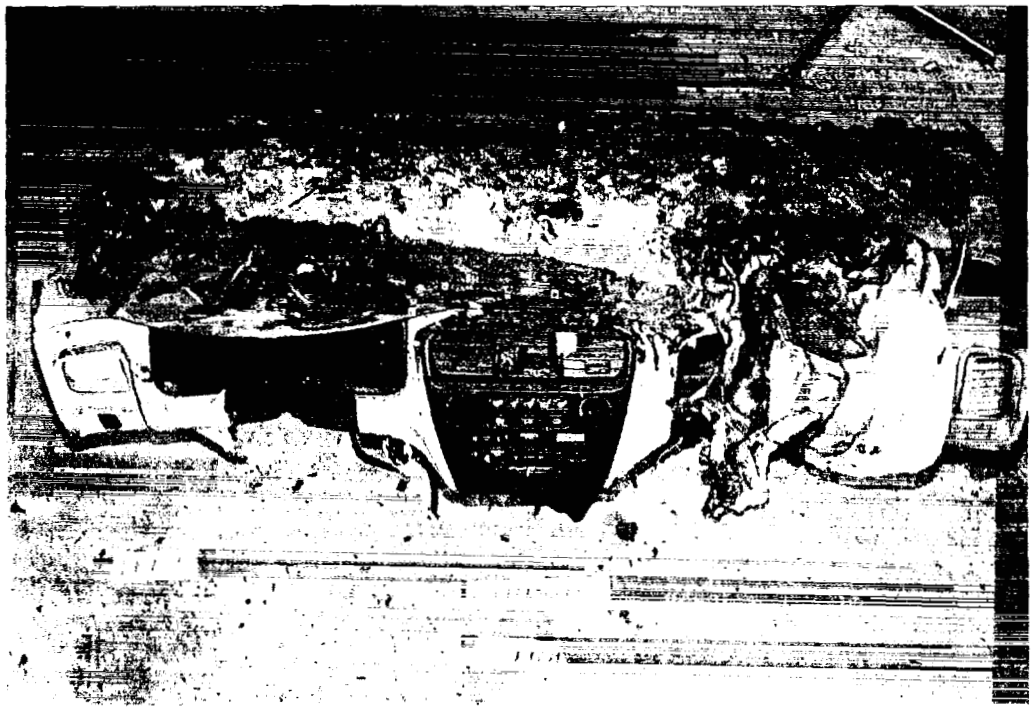

Figure 41. Fire Test F99030B. Photograph of the instrument panel removed from the test vehicle after this test.

One possible explanation for this apparent discrepancy between the observed fire damage and the 600°C flame temperature used here is that fragments of the windshield covered some of the thermocouples on the instrument panel upper trim panel. Temperature data recorded from thermocouples insulated from the flames in this manner would reflect the temperature of the materials they were in contact with, rather than flame temperature. If this is the case, then the estimated temperature profiles in Figure 40 are not a completely accurate representation of the distribution of flames on top of the instrument panel.

5.1.2 Ignition of the Front Seats, Center Console, and Steering Wheel

Pieces of windshield in which the windshield inner-layer had ignited and was burning fell into the passenger compartment and ignited the deployed passenger side air bag, the floor carpet in front of the right front seat, the front seat cushions, the steering wheel cover, and the center console. Figure 42 is a video still from Camera 6 at 27 minutes post-ignition showing a piece of windshield that fell onto the left front seat cushion and ignited the seat cushion and the steering wheel cover.

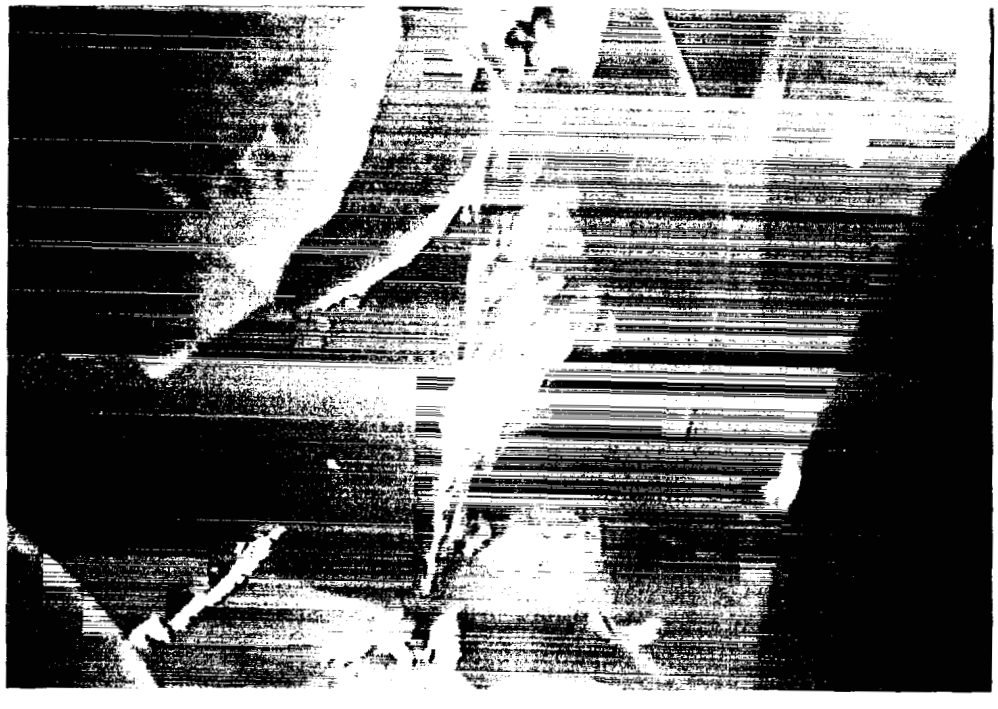

Figure 42. Fire Test F99030B. Video still from Camera 6 at 27 minutes post-ignition.

Inspection of the test vehicle after this test showed that debris from the windshield was observed on both front seat cushions, and the floor in front of both front seats, and on the center console (Fig. 43). Areas of the covers on both front seat cushions were burned, exposing the foam pad (Fig. 43). The passenger side air bag was burned and charred (Fig. 43). The shift lever and areas of the center console around the shift lever were burned and charred (Fig. 43). Areas of the floor carpet in front of the right front seat were burned and charred (Fig. 43).

Figure 43. Fire Test F99030B. Photograph of the front seats in the test vehicle after this test.

5.2 Flame-Spread into the Passenger Compartment Through the Left Inner Hinge Pillar

Systematic disassembly of the test vehicle after this test showed that the upper left corner of the insulation on the interior of the dash panel was burned and charred (Fig. 44), and soot was deposited on the upper left corner of the dash panel and on the right side of the dash panel above the HVAC module in the area of the HVAC air intake (Fig. 45). In contrast to this evidence of flame-spread into the left side of the instrument panel, there was no evidence of flame-spread into the instrument panel on the right side of the test vehicle around the HVAC module (Fig.'s 44 and 45) .

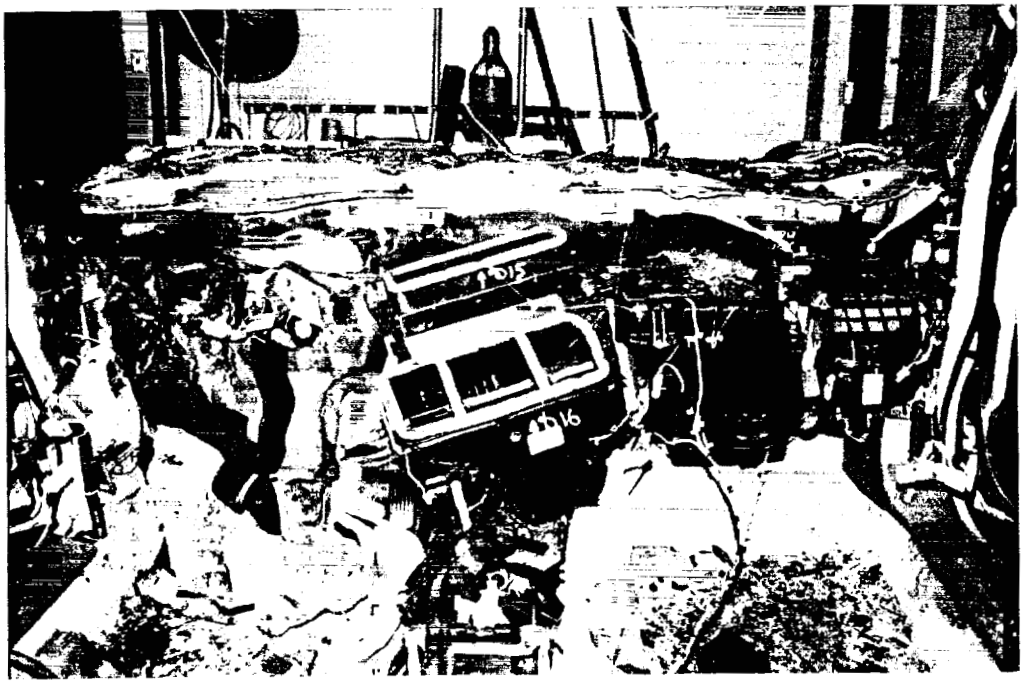

Figure 44. Fire Test F99030B. Photograph of the front of the passenger compartment of test vehicle with the instrument panel and front seats removed.

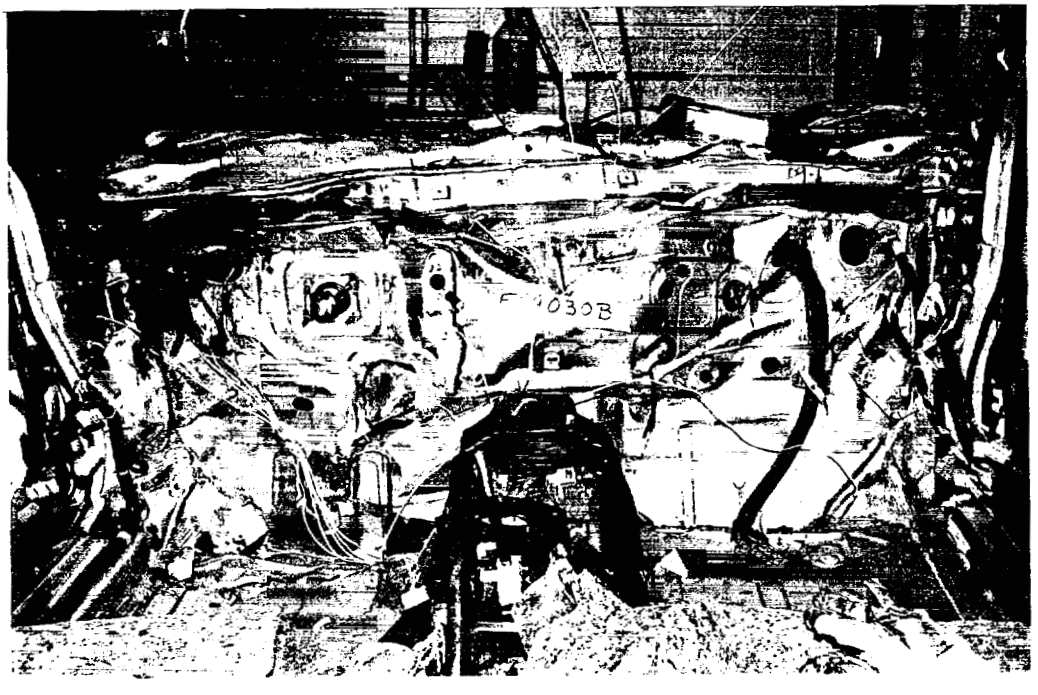

Figure 45. Fire Test F99030B. Photograph of the front of the test vehicle with HVAC module and dash insulation removed.

The dash panel and hinge pillar panels contained a number of pass-through and other openings with elastomer and polymer closures. Some of these openings were in an area of the test vehicle that was inside the rear of the left front fender, and would have been exposed to a portion of the fire plume from the burning windshield washer fluid reservoir, left front tire, and left front inner fender panel that was channeled rearward by the deformed left outer fender panel. Two of the pass-through closures in the upper part of the left hinge pillar (A and B) had burned through during this test (Fig. 46). An electrical pass-through closure in the upper left of the dash panel was charred (C), but did not appear to have burned through during this test (Fig. 46).

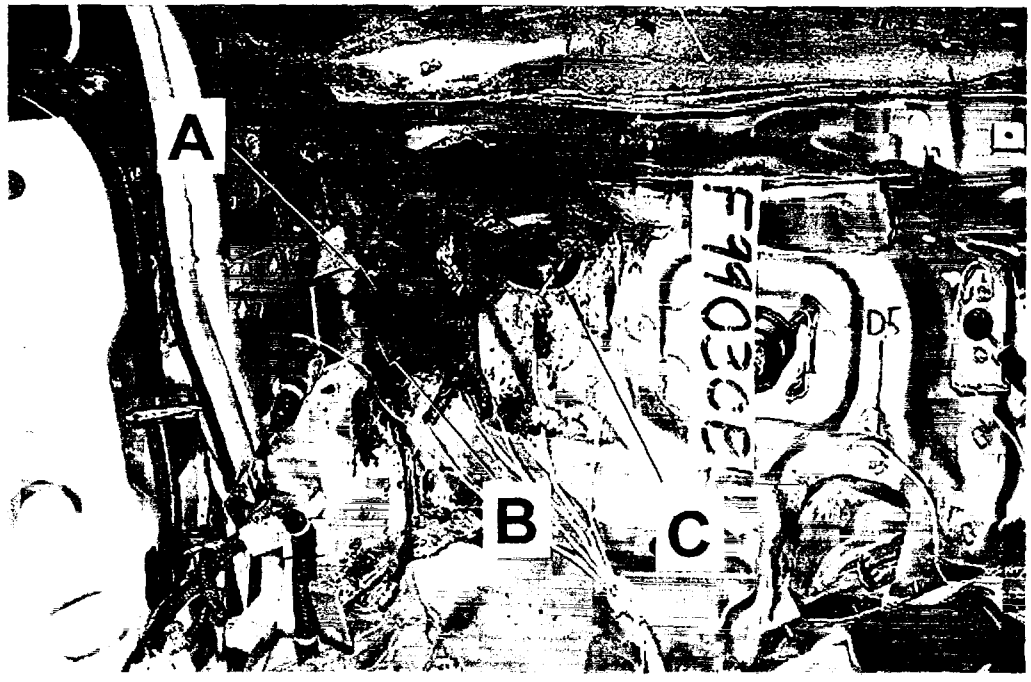

Figure 46. Fire Test F99030B. Photograph of the left side of the dash panel and left inner hinge pillar panel in the test vehicle.

Consistent with the visual inspection of the test vehicle after this test, temperature data recorded from thermocouples on the interior surfaces of these pass-through closures indicate that flames burned through the upper closure in the left hinge pillar (A, Fig. 46) at about 25 minutes post-ignition (D10, Fig. 47) and through the lower closure in the left hinge pillar (B, Fig 46) at about 25½ minutes post-ignition (D11, Fig. 47). These temperature data indicated that flames did not burn through the electrical pass-through closure in the upper left part of the dash panel (C, Fig 46) at any time during this test (D3, Fig. 47).

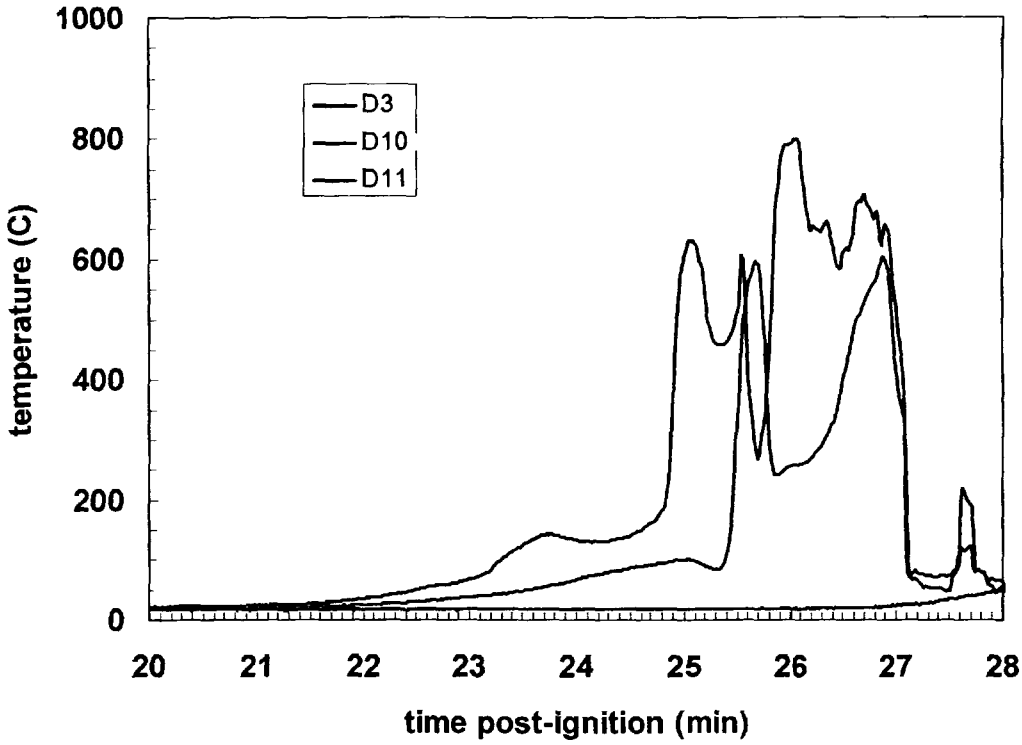

Figure 47. Fire Test F99030B. Plots of temperature data recorded from thermocouples D3, D10, and D11. Thermocouple D3 was located on the interior surface of the Electrical Pass-Through Closure C in Figure 46. Thermocouple D10 was located on the interior surface of Closure A in Figure 46. Thermocouple D11 was located on the interior surface of Closure B in Figure 46.

Observation of soot and residue of burned and charred polymeric material on the left end of the instrument panel support indicated that flames entering the openings in the left hinge pillar ignited components in the interior of the left side of the dash panel (Fig. 48). Transient increases and decreases plots of the temperature data recorded from thermocouples D10 and D11 between 25½ and 27 minutes post-ignition (Fig. 48) suggest that flaming inside of the instrument panel was intermittent. One possible explanation for this phenomenon is that the closed structure of the instrument panel restricted airflow into this space, creating a condition where the rate of oxygen consumption by flames in the interior of the instrument panel was greater than the rate of replenishment. If this were the case, then intermittent depletion of oxygen in this space would be expected to result in intermittent flaming in the instrument panel, and possibly intermittent flame-spread through the openings in the left hinge panel.

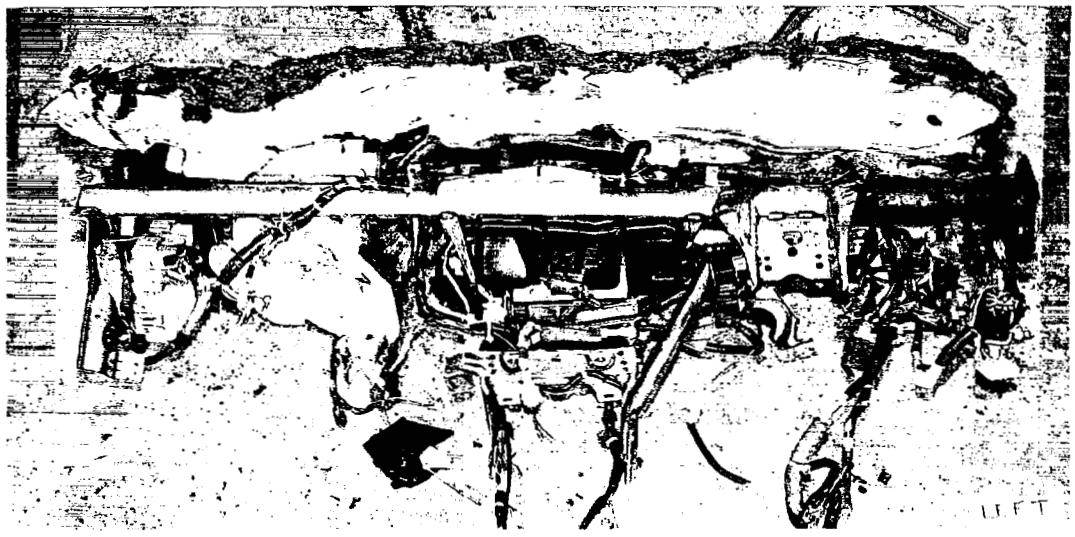

Figure 48. Fire Test F99030B. Photograph of the side of the interior of the instrument panel. This photograph has been inverted so that the left side of the view is from the perspective of looking rearward into the instrument panel from the front of the test vehicle so that the left side of the instrument panel is on the right side of this photograph.

5.3 Heat and Fire Damage to the Headlining Panel and Front Seats

The pattern of heat and fire damage to the roof trim panel, estimated temperature profiles along the lower surface of the headlining panel, and data recorded from the aspirated thermocouple assembly located in the passenger compartment indicate that a burning upper layer did not develop in the passenger compartment during this test. Except for a section of the fabric covering on the roof trim panel and a section of the fabric covering on the left sun visor, the roof trim panel showed no evidence of being exposed to heat and flames during this test (Fig. 49).

Temperature data recorded by thermocouples on the lower surface of the roof trim panel indicate that heated gases started to accumulate along the roof of the test vehicle between 22½ and 23 minutes post-ignition. Figure 50 shows isothermal contour plots[7] superimposed on diagrams of the test vehicle at ½-minute intervals between 23 and 27½ minutes post-ignition.

[7] The isothermal contour plots in Figure 50 were estimated from recorded temperature data using a three-dimensional interpolation algorithm available in SigmaPlot for Windows Version 4.00 [4]. This algorithm uses an inverse distance method to generated temperature values for points on a uniformly spaced Cartesian grid from input [x,y,t] triple data. Data recorded from Thermocouples R1 through R12 were used to calculate the isothermal contour plots in Figure 50.

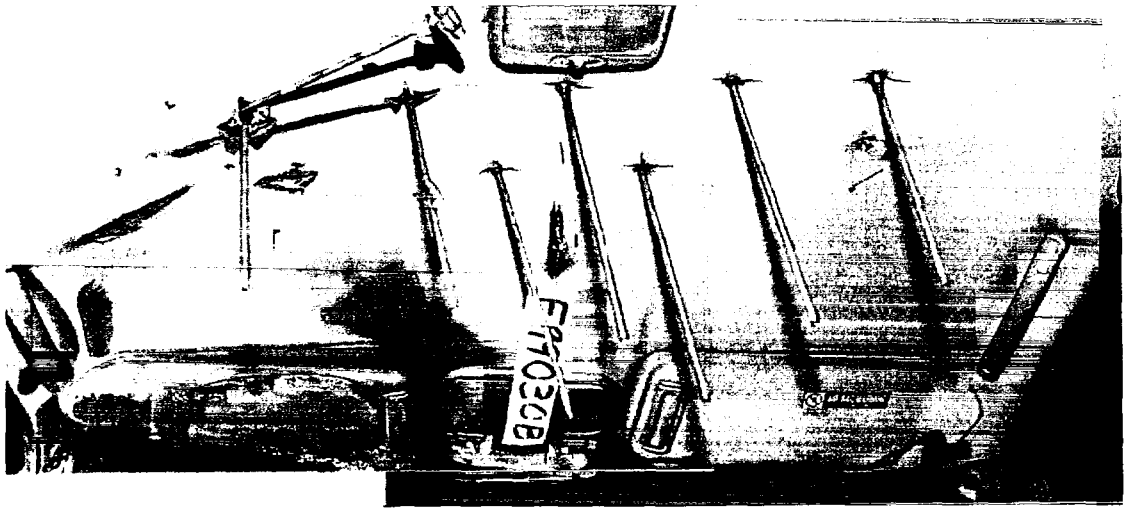

Figure 49. Fire Test F99030B. Composite of photographs of the forward section of the roof trim panel in the test vehicle after this test.

These estimated temperature profiles indicate that temperatures along the lower surface of the roof trim panel started to increase from ambient levels at about the time holes first developed in the windshield. The estimated temperature profiles in Figures 40 and 50 suggest that the fire plume from flames on the top of the instrument panel rose upward through openings in the windshield as flames first spread rearward on the instrument panel. For example, the front of the instrument panel in the center and left of the test vehicle had ignited by 25 minutes post-ignition (Fig. 40). Temperatures along the lower surface of the roof trim panel were < 200°C at this time (Fig. 50), indicating that only a small fraction of the heated gases from the fire plume flowed into the passenger compartment. Development of higher temperatures along sections of the roof trim panel (Fig. 50) coincided with the timing of pieces of burning windshield falling into the passenger compartment and igniting the steering wheel cover (Fig. 42). The area where the fabric cover on the left visor is burned (Fig. 49) is above the right side of the steering wheel that ignited between 26 and 27 minutes post-ignition (Fig. 42).

Air temperature data recorded from an aspirated thermocouple probe located between the front seats also indicates that a burning upper layer did not develop in the passenger compartment of the test vehicle during this test. The air temperature just below the roof trim panel in this area was approximately 20°C (ambient) from the time of ignition through 22 minutes post-ignition, increased to 125°C at 25 minutes post-ignition 225°C at 27 minutes post-ignition (Fig. 51).

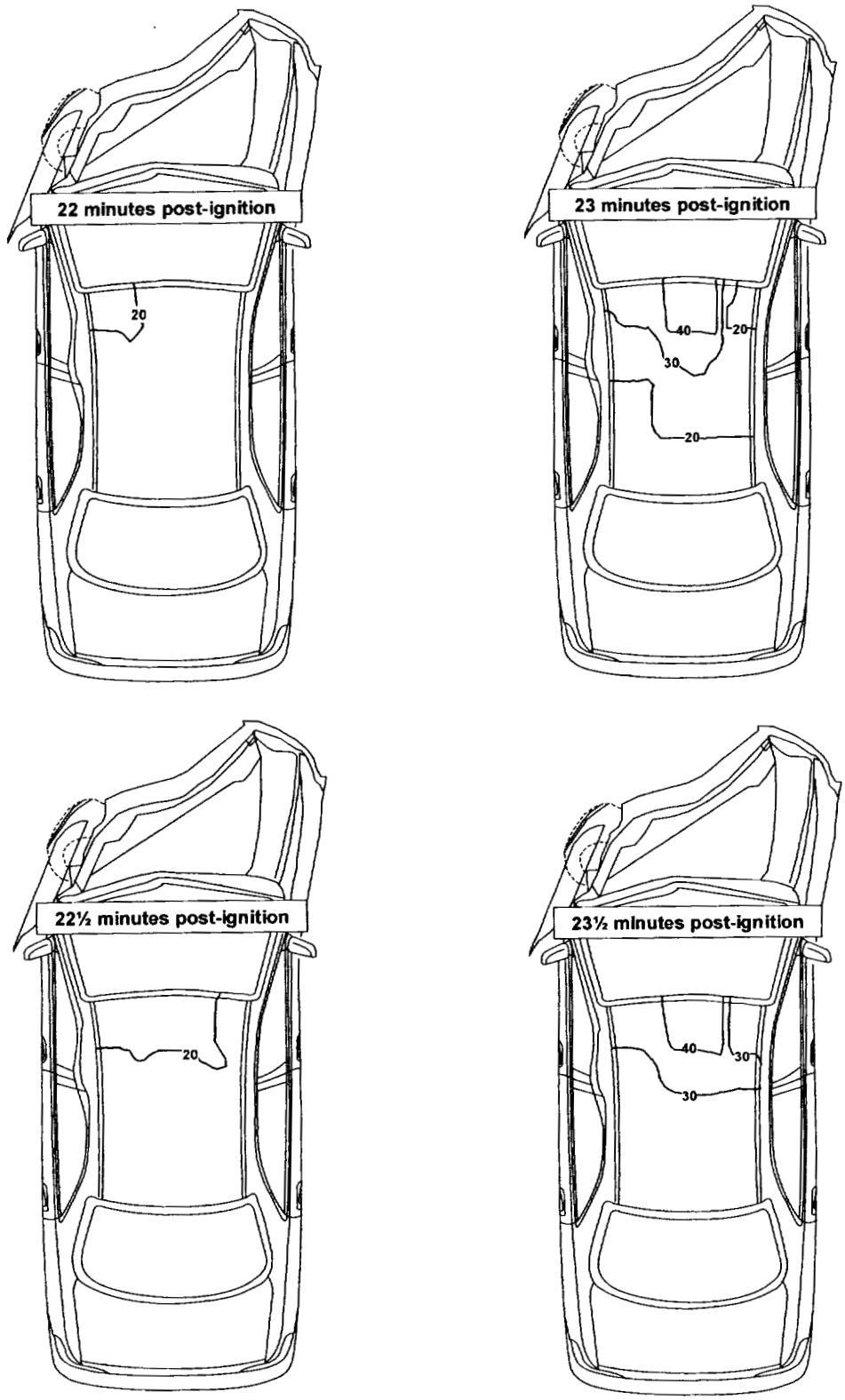

Figure 50. Fire Test F99030B. Plots of estimated temperatures on the roof trim panel at 22, 22½, 23, 23½, 24, 24½, 25, 25½, 26, 26½, 27, and 27½ minutes post-ignition.

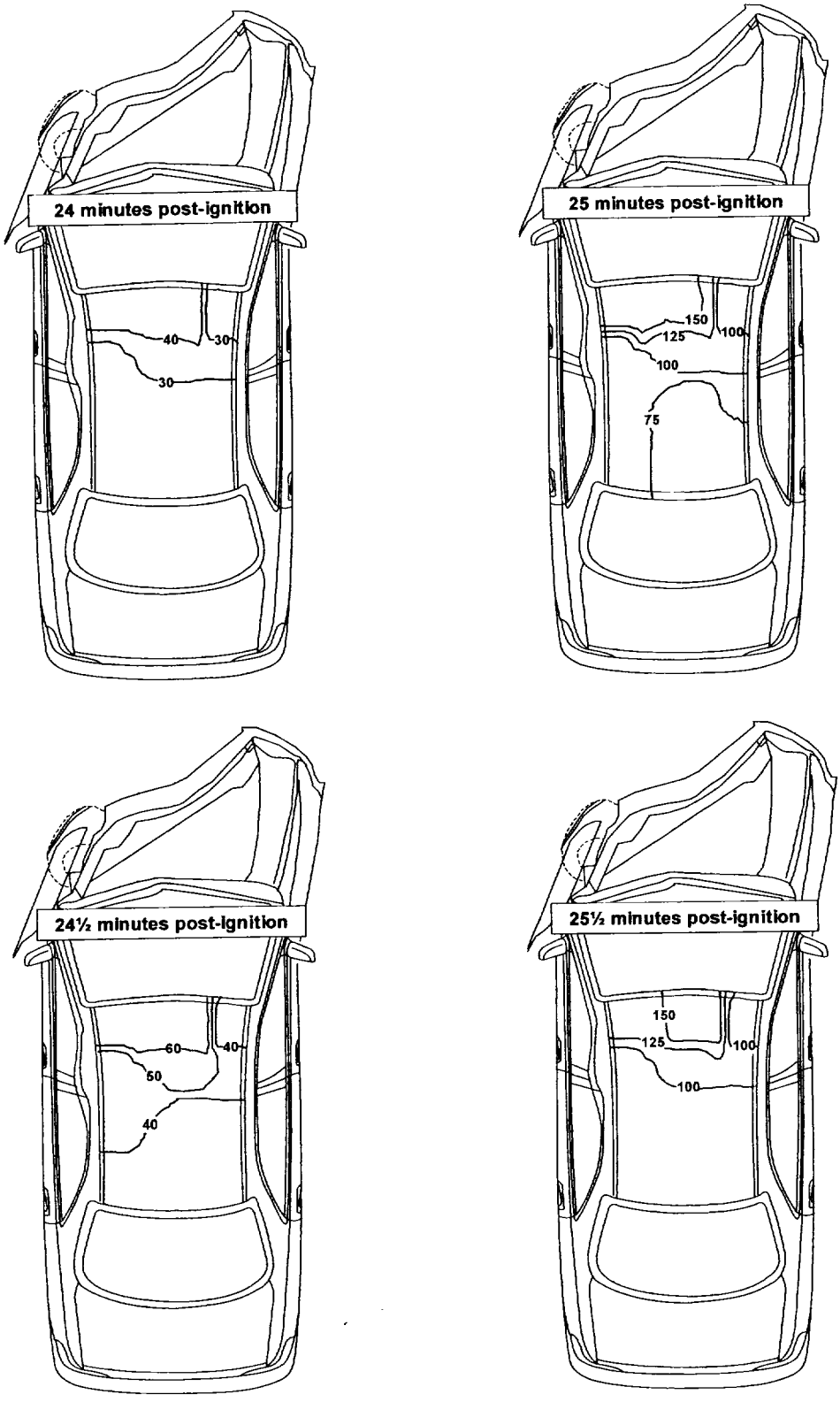

Figure 50, continued. Fire Test F99030B. Plots of estimated temperatures on the roof trim panel at 22, 22½, 23, 23½, 24, 24½, 25, 25½, 26, 26½, 27, and 27½ minutes post-ignition.

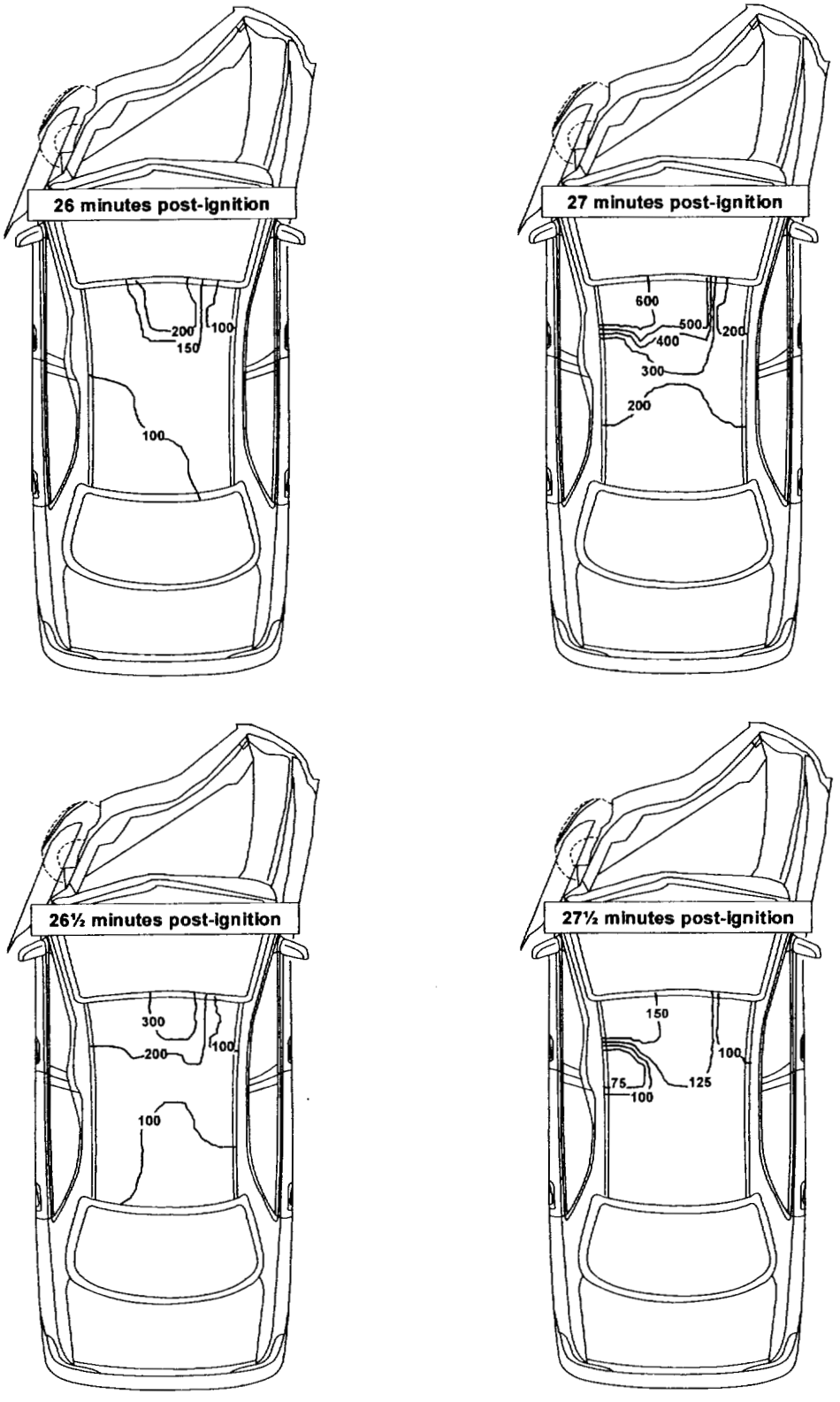

Figure 50, continued. Fire Test F99030B. Plots of estimated temperatures on the roof trim panel at 22, 22½, 23, 23½, 24, 24½, 25, 25½, 26, 26½, 27, and 27½ minutes post-ignition.

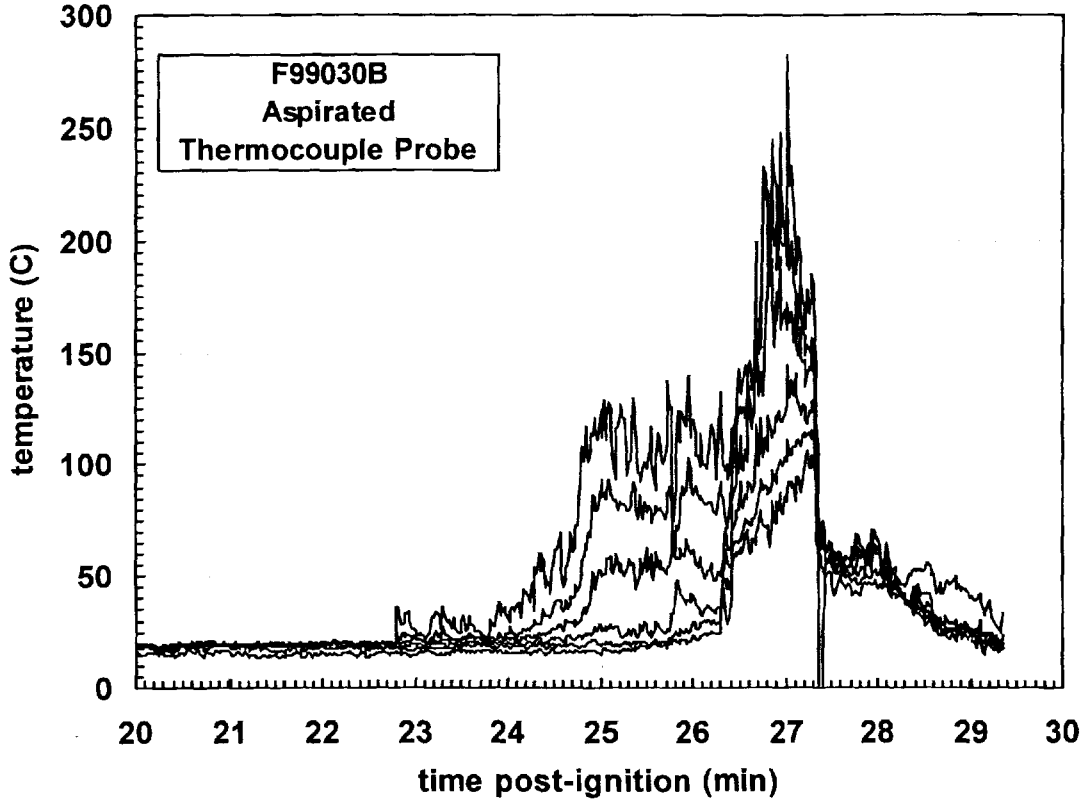

Figure 51. Fire Test F99030B. Plots of air temperature recorded from thermocouples in an aspirated thermocouple probe located between the front seats of the test vehicle.

The aspirated thermocouple probe used in this test contained six aspirated thermocouples spaced vertically at 75 cm intervals starting just below the roof trim panel. The temperature data recorded from the thermocouples in the aspirated thermocouple shows that the air temperature in the passenger compartment of the test vehicle decreased at increasing distance below the lower surface of the roof trim panel (Fig. 51). At 27 minutes post-ignition, the vertical temperature gradient in the passenger compartment between the front seats was approximately 3.7°C/cm.

6 Combustion Conditions

The output of combustion products from a fire depends on the material burning and on the supply of air to the flame. A well-ventilated fire is one in which the air supplied to the flames is sufficient for complete combustion. In partially enclosed spaces, such as an engine compartment or passenger compartment, airflow to the flames may be inadequate for complete combustion. In this case, called a ventilation-controlled or under-ventilated fire, the supply of air limits both the heat released by the fire and oxidation (combustion) of the gaseous fuel in the fire zone. As ventilation decreases, the output of carbon monoxide, hydrocarbons, smoke, and other products of incomplete combustion increase. The chemical composition of these gases depends on the chemical compositions of the materials burning and on the burning conditions, primarily ventilation. For fires in an enclosed space, heated buoyant gases can accumulate below the ceiling or roof of the enclosed space, forming what is called the upper layer. The upper layer can be ignited by flames from burning objects (piloted ignition) or can ignite spontaneously (autoignition) when the temperature of the gases exceeds a minimum threshold temperature (autoignition temperature), which depends on the chemical composition and the fuel/oxygen ratio of the gaseous upper layer. Once ignited, radiation from the burning upper layer transfers heat downward, and may ignite combustible materials below the burning upper layer. Ventilation of the flames affects the chemical composition of the gases produced in a fire.

The equivalence ratio is a quantitative measure of the amount of oxygen consumed during combustion, and is defined as follows:

$$\Phi = \frac{\left[fuel/O_2\right]_{fire}}{\left[fuel/O_2\right]_{stoichiometric}}$$

where Φ is the equivalence ratio, $[fuel/O_2]_{fire}$ is the fuel-to-oxygen ratio in the fire, and $[fuel/O_2]_{stoichiometric}$ is the fuel-to-oxygen ratio required for complete (stoichiometric) combustion. Combustion product concentration data, oxygen concentration data, gas temperature data, and airflow data are typically used to calculate a value of the equivalence ratio in laboratory tests [5]. In most instances, the equivalence ratio is not determined for large-scale tests where objects made of different materials may burn in different physical environments. Ventilation and thus the equivalency ratio may be different in each environment. Since it was not possible to isolate and measure the fire products produced by each of the materials burning or to measure airflow into each of the unique environments that existed during this test, the equivalence ratio was not determined here.

Air temperature and gas concentration data collected during this test were used to estimate derived parameters that are related to ventilation. Air temperature and gas concentration data from the Fire Products Collector at the test facility were used to estimate the ratios $[G_{CO}]/[G_{CO2}]$ and $[G_{HC}]/[G_{CO2}]$. Air temperature data from the aspirated thermocouples in the passenger compartment and gas concentration data from the FTIR gas analysis of air in the passenger compartment were used to estimate the ratios $[C_{CO} \times d_{CO}]/[C_{CO2} \times d_{CO2}]$, $[C_{HC} \times d_{HC}]/[C_{CO2} \times d_{CO2}]$, $[C_{CO2} \times d_{CO2}]/[t_{air} \times Cp]$, $[C_{CO} \times d_{CO}]/[t_{air} \times Cp]$, and $[C_{CO2} \times d_{CO2}]/[t_{air} \times Cp]$. Ventilation was assessed by comparing the values of these derived parameters estimated from the test data to reference values obtained during the testing of individual materials in small-scale flammability tests,[3] where the equivalence ratio was measured precisely [5]. The reference parameters used in this comparison include $Y(CO)/Y(CO_2)$, $Y(HC)/Y(CO_2)$, $Y(CO_2)/\Delta H_{CON}$, $Y(CO)/\Delta H_{CON}$, $Y(HC)/\Delta H_{CON}$ (Table 3).

Table 3

Fire Products for Well-ventilated Fires[1,2]

material	$Y(CO)/Y(CO_2)$ (g/g)	$Y(HC)/Y(CO_2)$ (g/g)	$Y(CO_2)/\Delta H_{CON}$ (g/kJ)	$Y(CO)/\Delta H_{CON}$ (g/kJ)	$Y(HC)/\Delta H_{CON}$ (g/kJ)
poly(ethylene)	0.0087	0.0025	0.13	0.0011	0.00032
poly(propylene)	0.0086	0.0022	0.12	0.0011	0.00027
poly(styrene)	0.026	0.0060	0.21	0.0054	0.00127
polyester	0.05	0.019	0.15	0.0065	0.00185
Nylon	0.018	0.0078	0.13	0.0035	0.00098
Flexible urethane foams	0.006 - 0.027	0.0013 - 0.0033	0.15 - 0.21	0.0012 - 0.0055	0.00023 - 0.00069
Rigid urethane foams	0.015 - 0.046	0.006 - 0.036	0.17 - 0.23	0.0028 - 0.0081	0.00011 - 0.00070

[1]Values reported in Table 3 were calculated from data reported in Table 3-4.11 in reference 5.

[2]Y(CO) is the mass-yield of carbon monoxide (g). $Y(CO_2)$ is the mass-yield of carbon dioxide (g). Y(HC) is the mass-yield of gaseous hydrocarbons (g). $Y(CO_2)/\Delta H_{con} = (C_{CO_2}/c_p\Delta T)(\rho_{CO_2}/\rho_{air})$, $Y(CO)/\Delta H_{con} = (C_{CO}/c_p\Delta T)(\rho_{CO}/\rho_{air})$, and $Y(HC)/\Delta H_{con} = (C_{HC}/c_p\Delta T)(\rho_{HC}/\rho_{air})$. ΔH_{CON} is the convective heat of combustion per unit fuel vaporized (kJ/g). The C_j are the gas-phase concentrations (volume fraction) of carbon dioxide, carbon monoxide, and total hydrocarbons. The ρ_j are the gas-phase densities (g/m^3) of carbon dioxide, carbon monoxide, total hydrocarbons, and air. c_p is the heat capacity of air (kJ/g-K). ΔT is the difference between the gas temperature and the temperature of the ambient air (K).

[3] Small-scale flammability tests to determine combustion properties of materials were conducted in the Factory Mutual Research Corporation Flammability Apparatus is a small-scale test apparatus (see Reference 5).

The values of these parameters in Table 3 were determined for well-ventilated combustion of poly(ethylene), poly(propylene), poly(styrene), polyester, Nylon, a group of flexible urethane foams, and a group of rigid urethane foams in controlled small-scale laboratory tests.[4]

An analysis of combustion conditions based on data from the Fire Products Collector was not done because the carbon monoxide release rate data collected during this test was unreliable (see **Appendix H**).

An analysis of combustion conditions based on air temperature and gas concentration data from the passenger compartment is shown in Figures 42 through 56. Air temperature and gas concentration data from the passenger compartment were used to determine $[C_{CO} \times d_{CO}]/[C_{CO2} \times d_{CO2}]$, $[C_{HC} \times d_{HC}]/[C_{CO2} \times d_{CO2}]$, $[C_{CO2} \times d_{CO2}]/[t_{air} \times Cp]$, $[C_{CO} \times d_{CO}]/[t_{air} \times Cp]$, and $[C_{HC} \times d_{HC}]/[t_{air} \times Cp]$. The ratios $[C_{CO} \times d_{CO}]/[C_{CO2} \times d_{CO2}]$, $[C_{HC} \times d_{HC}]/[C_{CO2} \times d_{CO2}]$, $[C_{CO2} \times d_{CO2}]/[t_{air} \times Cp]$, $[C_{CO} \times d_{CO}]/[t_{air} \times Cp]$, and $[C_{HC} \times d_{HC}]/[t_{air} \times Cp]$ are equivalent to $Y(CO)]/[Y(CO_2)$, $Y(HC)]/[Y(CO_2)$, $Y(CO_2)/\Delta H_{CON}$, $Y(CO)/\Delta H_{CON}$, and $Y(HC)/\Delta H_{CON}$, respectively, in Table 2. In these formulas, C_j is the gas-phase concentration of species j, d_j is the density of species j, t_{air} is the air temperature, and C_p is the heat capacity of air. The product $[C_j \times d_j]$ equals the mass-concentration of species j in passenger compartment. The concentrations of the gaseous combustion products (C_j) were determined by Fourier Transform Infrared Spectrometry (**APPENDIX I**). Air temperature data from the aspirated thermocouple assemblies in the passenger compartment (**APPENDIX D**) was used to determine t_{air}. Air temperature and the concentrations of carbon monoxide, carbon dioxide, and hydrocarbons in the passenger compartment remained at pre-test levels from the time of ignition through about 22 minutes post-ignition. Thus, the plots in Figures 42 through 56 start at 22 minutes post-ignition.

Trends in $[C_{CO} \times d_{CO}]/[C_{CO2} \times d_{CO2}]$, $[C_{HC} \times d_{HC}]/[C_{CO2} \times d_{CO2}]$, $[C_{CO2} \times d_{CO2}]/[t_{air} \times Cp]$, $[C_{CO} \times d_{CO}]/[t_{air} \times Cp]$, and $[C_{HC} \times d_{HC}]/[t_{air} \times Cp]$ appear to have been related to flame-spread into the passenger compartment between 25 and 27 minutes post-ignition. Before combustible materials in the passenger compartment ignited, gases detected in the passenger compartment were either from products of combustion from materials in the engine compartment entering the passenger compartment through the windshield and pass-through openings in the left inner hinge pillar panel or from thermal decomposition (pyrolysis) of materials in the passenger compartment. Thermal decomposition of materials in the test vehicle generally yields organic gaseous hydrocarbons and does not yield appreciable amounts of carbon dioxide, carbon monoxide, and heat.

[4] The compositions and physical properties such as density, thermal conductivity, and heat capacity of these materials were not specified in Reference 5.

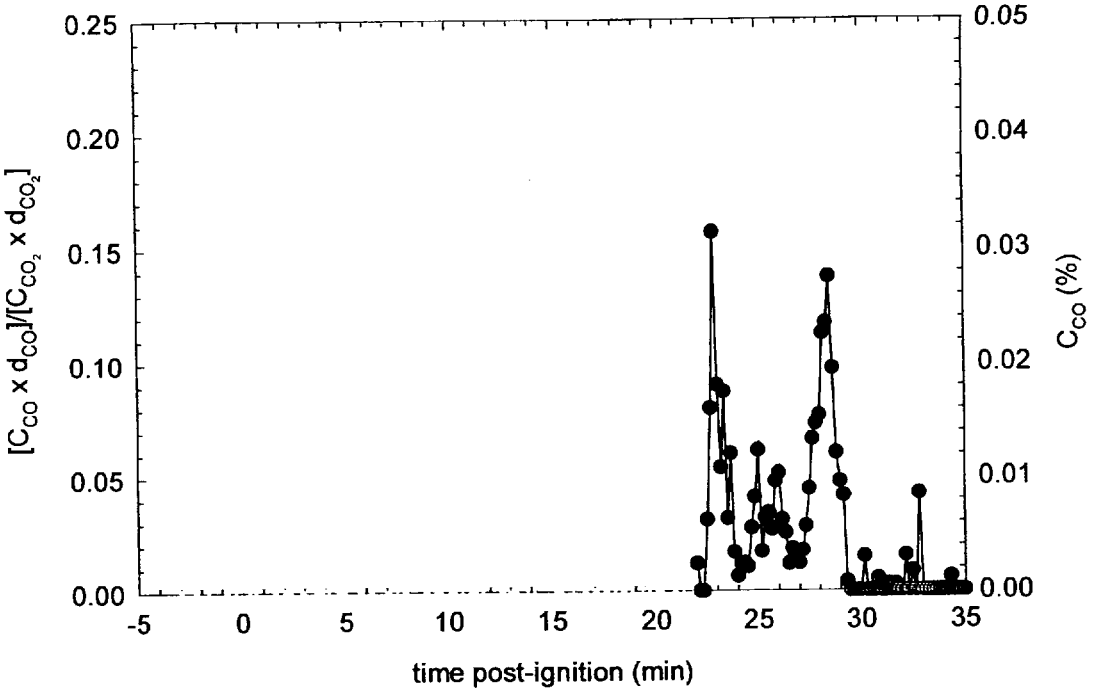

Figure 52. Fire Test F99030B. Plots of $[C_{CO} \times d_{CO}]/[C_{CO2} \times d_{CO2}]$ (—●—, left axis) and the concentration of carbon monoxide (—, right axis) in the passenger compartment.

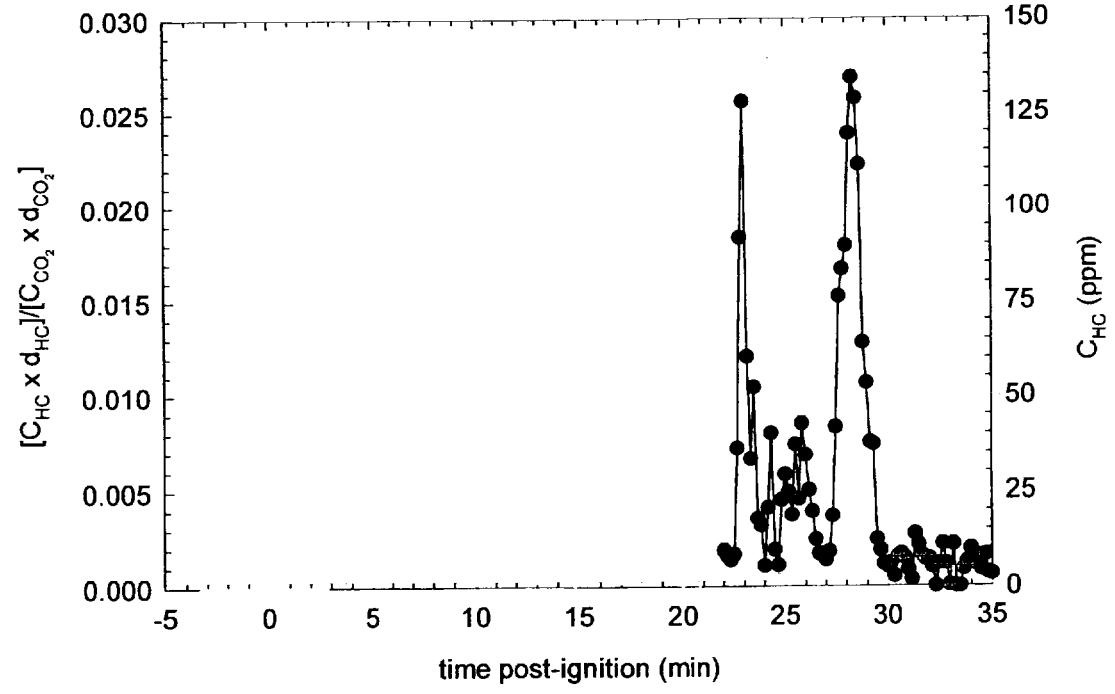

Figure 53. Fire Test F99030B. Plots of $[C_{HC} \times d_{HC}]/[C_{CO2} \times d_{CO2}]$ (—●—, left axis) and the concentration of total hydrocarbons (—, right axis) in the passenger compartment.

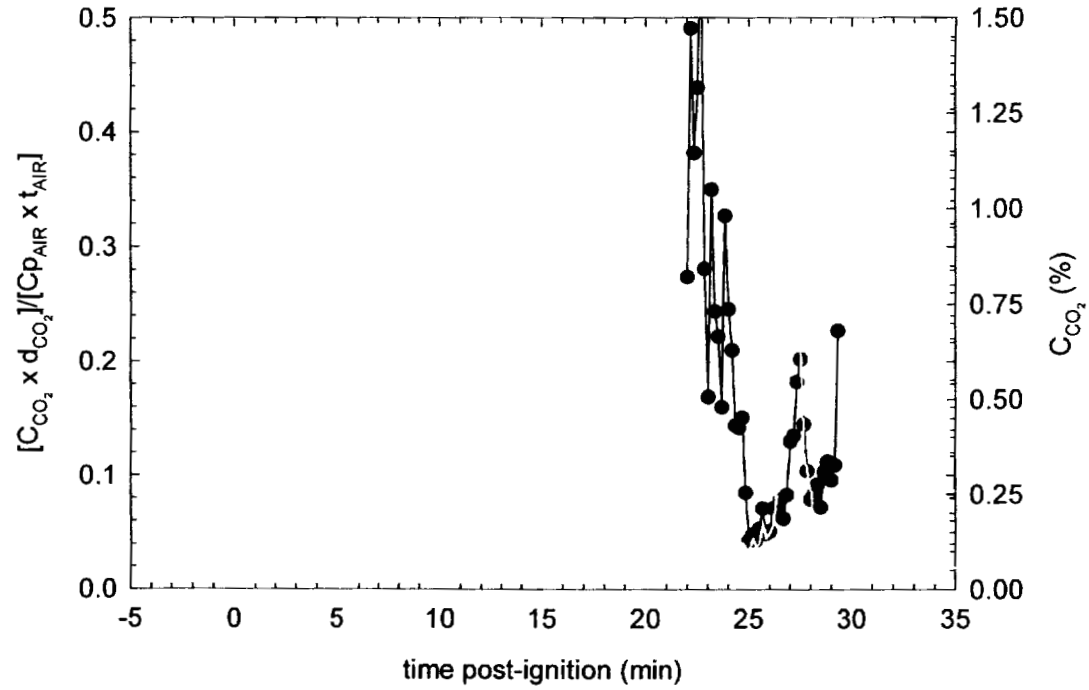

Figure 54. Fire Test F99030B. Plots of $[C_{CO2} \times d_{CO2}]/[t_{air} \times Cp]$ (—●—, left axis) and the concentration of carbon dioxide (—, right axis) in the passenger compartment.

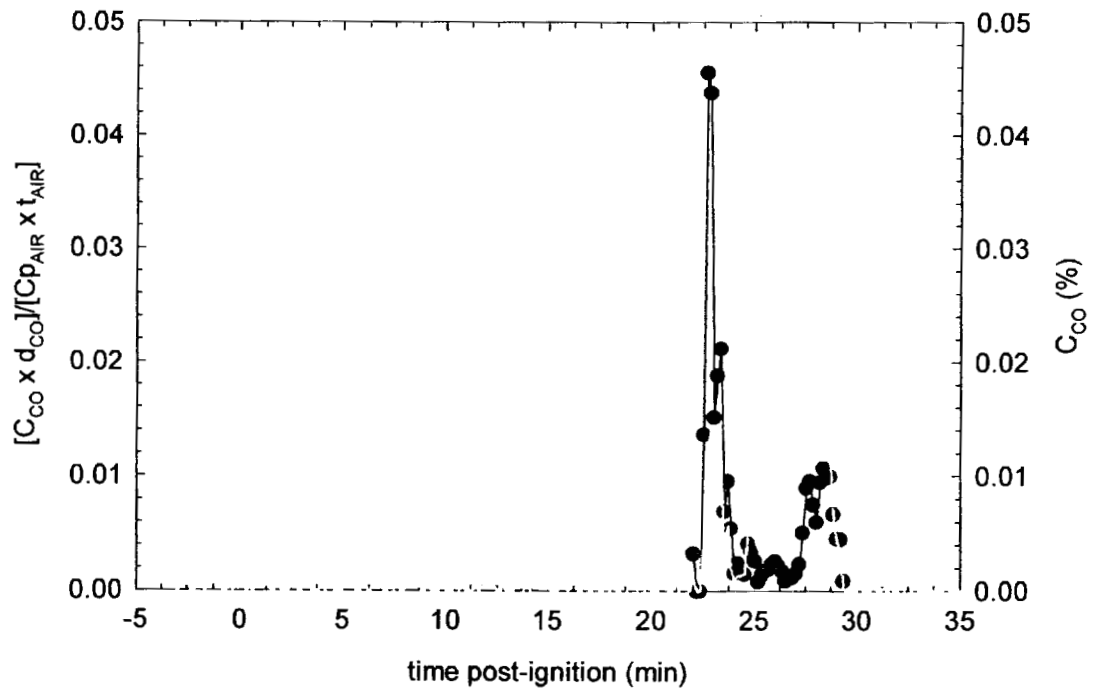

Figure 55. Fire Test F99030B. Plots of $[C_{CO} \times d_{CO}]/[t_{air} \times Cp]$ (—●—, left axis) and the concentration of carbon monoxide (—, right axis) in the passenger compartment.

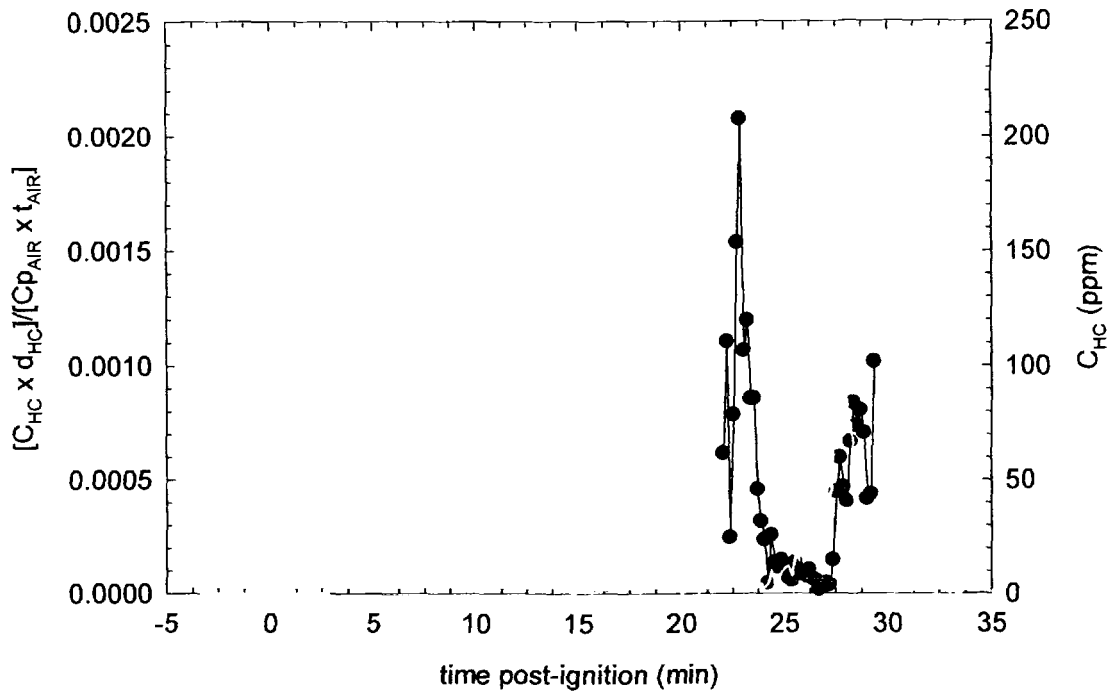

Figure 56. Fire Test F99030B. Plots of $[C_{HC} \times d_{HC}]/[t_{air} \times Cp]$ (—●—, left axis) and the concentration of hydrocarbons (—, right axis) in the passenger compartment.

Based on these considerations, values of $[C_{CO} \times d_{CO}]/[C_{CO2} \times d_{CO2}]$, $[C_{HC} \times d_{HC}]/[C_{CO2} \times d_{CO2}]$, $[C_{CO2} \times d_{CO2}]/[t_{air} \times Cp]$, $[C_{CO} \times d_{CO}]/[t_{air} \times Cp]$, and $[C_{HC} \times d_{HC}]/[t_{air} \times Cp]$ would be expected to be greater than the respective reference values for well-ventilated combustion of in Table 2 as materials in the passenger compartment started to thermally decompose as a result of exposure to flames from the engine compartment entering the passenger compartment, and decrease as these materials ignited.

The plots of Figures 52 through 56 show three distinct regions. The first region occurred between 22 and 23 minutes post-ignition. The concentrations of carbon monoxide and hydrocarbons in the passenger compartment started to increased above pre-test, while the concentration of carbon dioxide and air temperature remained at approximately pre-test levels. The plots of $[C_{CO} \times d_{CO}]/[C_{CO2} \times d_{CO2}]$, $[C_{HC} \times d_{HC}]/[C_{CO2} \times d_{CO2}]$, $[C_{CO2} \times d_{CO2}]/[t_{air} \times Cp]$, $[C_{CO} \times d_{CO}]/[t_{air} \times Cp]$, and $[C_{HC} \times d_{HC}]/[t_{air} \times Cp]$ in Figures 28 through 52 increased during this time, and the values of each of these parameters were greater than their respective reference values for well-ventilated combustion of materials similar to those used in interior components in the test vehicle (Table 3). These results could have been caused by one or both of two phenomena: an influx into the passenger compartment of combustion products from under-ventilated combustion in the engine compartment and accumulation in the passenger compartment of gaseous thermal

decomposition products from interior materials that were heated by radiation from flames at the rear of the engine compartment as holes in the windshield developed.

The second region occurred between 23 and 27 minutes post-ignition. Air temperature and the concentrations of carbon dioxide, carbon monoxide, and hydrocarbons in the passenger compartment increased during this time. The plots of $[C_{CO} \times d_{CO}]/[C_{CO2} \times d_{CO2}]$, $[C_{HC} \times d_{HC}]/[C_{CO2} \times d_{CO2}]$, $[C_{CO2} \times d_{CO2}]/[t_{air} \times Cp]$, $[C_{CO} \times d_{CO}]/[t_{air} \times Cp]$, and $[C_{HC} \times d_{HC}]/[t_{air} \times Cp]$ in Figures 52 through 56 decreased, approaching their respective reference values for well-ventilated combustion of shown in Table 3. This behavior is consistent with accumulation of products of well-ventilated combustion in the passenger compartment as flames spread rearward on the top of the instrument panel, flames spread into the left side of the instrument panel, and the center console and steering wheel were ignited by pieces of burning windshield falling into the passenger compartment.

The third region occurred after about 27 minutes post-ignition and corresponds to the time when flames in the passenger compartment were being extinguished. Air temperature and the concentrations of carbon dioxide, carbon monoxide, and hydrocarbons in the passenger compartment started to decrease at about 27 minutes post-ignition. The plots of $[C_{CO} \times d_{CO}]/[C_{CO2} \times d_{CO2}]$, $[C_{HC} \times d_{HC}]/[C_{CO2} \times d_{CO2}]$, $[C_{CO2} \times d_{CO2}]/[t_{air} \times Cp]$, $[C_{CO} \times d_{CO}]/[t_{air} \times Cp]$, and $[C_{HC} \times d_{HC}]/[t_{air} \times Cp]$ in Figures 52 through 56 increased between 27 and 28 minutes post-ignition, then decreased after about 28 minutes post-ignition. This behavior suggests that the efficiency of combustion decreased for a period of approximately 1 minute as flames in the passenger compartment were extinguished. After 29 minute post-ignition, flames in the passenger compartment were extinguished. Air temperature and the concentrations of carbon dioxide, carbon monoxide, and hydrocarbons in the passenger compartment were at pre-test levels. Thus, the plots of $[C_{CO} \times d_{CO}]/[C_{CO2} \times d_{CO2}]$, $[C_{HC} \times d_{HC}]/[C_{CO2} \times d_{CO2}]$, $[C_{CO2} \times d_{CO2}]/[t_{air} \times Cp]$, $[C_{CO} \times d_{CO}]/[t_{air} \times Cp]$, and $[C_{HC} \times d_{HC}]/[t_{air} \times Cp]$ in Figures 52 through 56 do not tell anything about combustion conditions in the passenger compartment after about 29 minutes post-ignition.

7 Estimation of Skin Temperature Profiles from Measured Heat Flux Data, Fractional Equivalent Dose Parameters from Measured Gas Concentration Data, and Thermal Damage to the Respiratory Tract from Measured Air Temperature Data

The mathematical model "BURNSIM: A Burn Hazard Assessment Model" [6] was used to estimate the time and depth of burns to exposed skin. The inputs to this model were heat fluxes derived from the directional flame thermometer measurements and air temperatures measured using the aspirated thermocouple probe.

Two models were used to estimate the potential for toxicity from exposure to the combustion gases measured in the passenger compartment. The Federal Aviation Administration (FAA) Combined Hazard Survival Model [7] was used to estimate the time to incapacitation and the time to lethality. A model described by Purser [8] also was used to estimate the time to incapacitation. Both models estimate the risk from exposure to hot air, reduced oxygen, carbon monoxide, carbon dioxide, hydrogen cyanide, hydrogen chloride, hydrogen fluoride, hydrogen bromide, acrolein, and nitrogen dioxide. Both models also account for the physiological effect of carbon dioxide-induced hyperventilation, which increases the respiratory uptake.

7.1 The BURNSIM Model

The computer model BURNSIM was the analytical tool chosen to estimate skin temperature depth profiles from the heat flux data in **APPENDIX G**. The BURNSIM model divides the skin into a series of ten layers, with a uniform thickness of 0.2 mm per layer. The top layer was divided into 8 layers each with a uniform thickness of 0.025 mm to better account for the non-instantaneous heat transfer from the epidermal surface into the first layer.

Skin Model of BURNSIM

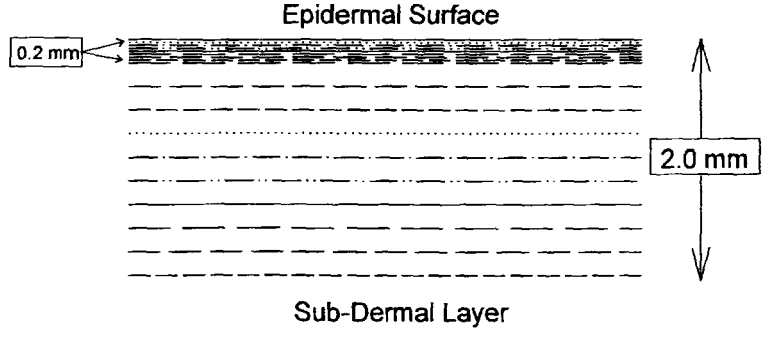

The BURNSIM analysis used here incorporated the following assumptions to estimate skin temperature profiles. The absorbtivity of exposed skin was assumed to be 0.60 (i.e., the skin

absorbs 60% of the radiation incident upon the epidermal surface). The absorbtivity of surface hair was assumed to be 0.05 (i.e., surface hair absorbs 5% of the incident radiation before it reached the skin). Exposed skin was assumed to absorb 100% of the measured convective heat flux to its surface. The temperature of each layer was estimated as a function of the time of exposure to an external heat flux. A portion of the absorbed heat is removed from the skin by the circulatory system. In the BURNSIM model, thermal damage results when the temperature of that layer exceeds 45°C.

In estimating skin temperature, the analysis presented in this paper using BURNSIM did not account for the presence of facial or head hair, or clothing covering the skin, all of which may block direct heat transfer to the skin. This analysis also did not account for variations in skin thickness among individuals, or variations in skin thickness at different parts of the body on the same individual. For example, skin thickness can vary from 1 to 5 mm with body location. This analysis also did not account for the effect of skin pigmentation on absorbtivity. In using the radiative and convective heat flux estimates shown in **APPENDIX G** to estimate skin temperature profiles, this analysis assumed that the location and orientation of the skin was identical to that of the HFT/RAD transducer assemblies used to measure heat flux. Small changes in position or angle of the surface can result in large differences between in the incident heat flux to the surface (see below). Based on the currently available information and data, the accuracy of the estimated skin temperature depth profiles in humans exposed to heat flux levels from fire such as measured in this test obtained using BURNSIM has not been determined.

7.1.1 Estimation of Skin Temperature Profiles using BURNSIM

The absorbed heat flux at each of the HFT/RAD assembly locations was estimated from the data recorded from HFT/RAD 10 through HFT/RAD 15. Estimates of absorbed heat flux obtained by analysis of the data recorded from these transducers were input into the BURNSIM model to estimate skin temperature profiles for exposed skin at these locations. The BURNSIM calculations were performed using data recorded between 20:00 and 27:20 min:sec post-ignition. The resulting estimated temperature profiles are shown in Figures 57 through 62.

The timing and magnitude of changes in the estimated skin temperature profiles correlated with the recorded convective and radiative heat flux data used in these calculations, which was dependent on the location and orientation of the HFT/RAD assemblies in the test vehicle. For example, HFT/RAD 10 was located above the left front seat cushion facing upward (**APPENDIX E**) and responded to convection and downward radiation from heated gases flowing into the passenger compartment along the roof trim panel (**Section 5.3**).

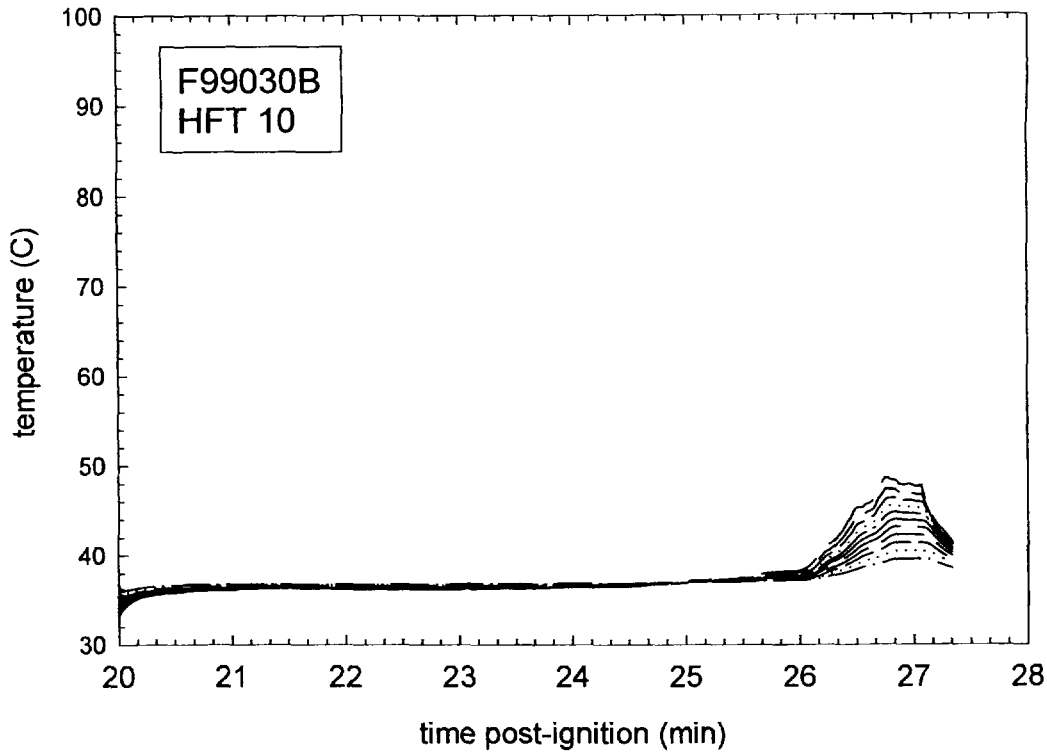

Figure 57. Fire Test F99030B. Skin temperature profiles estimated from heat flux data recorded from HFT/RAD Assembly 10 (**APPENDIX E**, Plots E2 and E3).

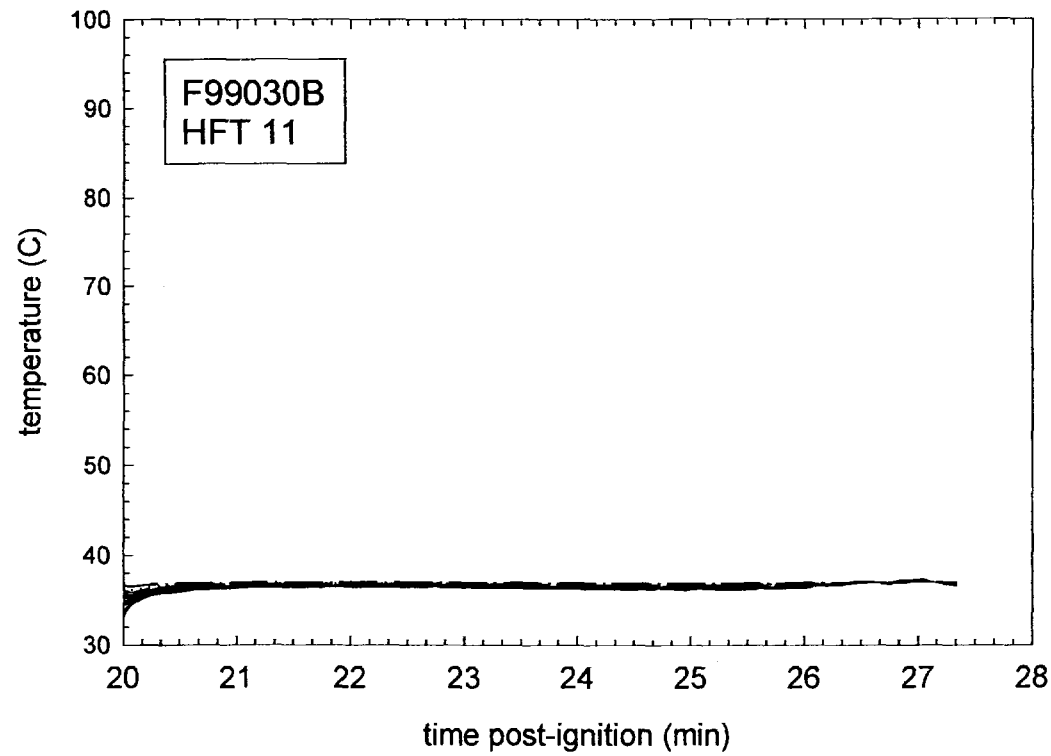

Figure 58. Fire Test F99030B. Skin temperature profiles estimated from data recorded from HFT/RAD Assembly 11 (**APPENDIX E**, Plots E4 and E5).

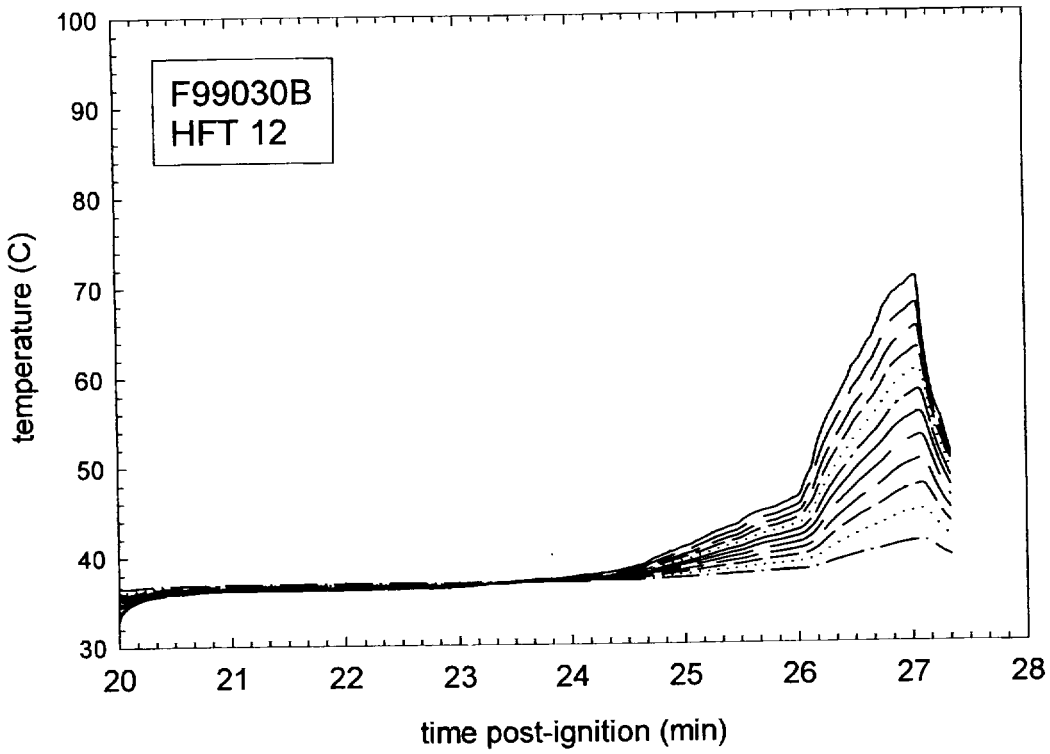

Figure 59. Fire Test F99030B. Skin temperature profiles estimated from data recorded from HFT/RAD Assembly 12 (**APPENDIX E**, Plots E6 and E7).

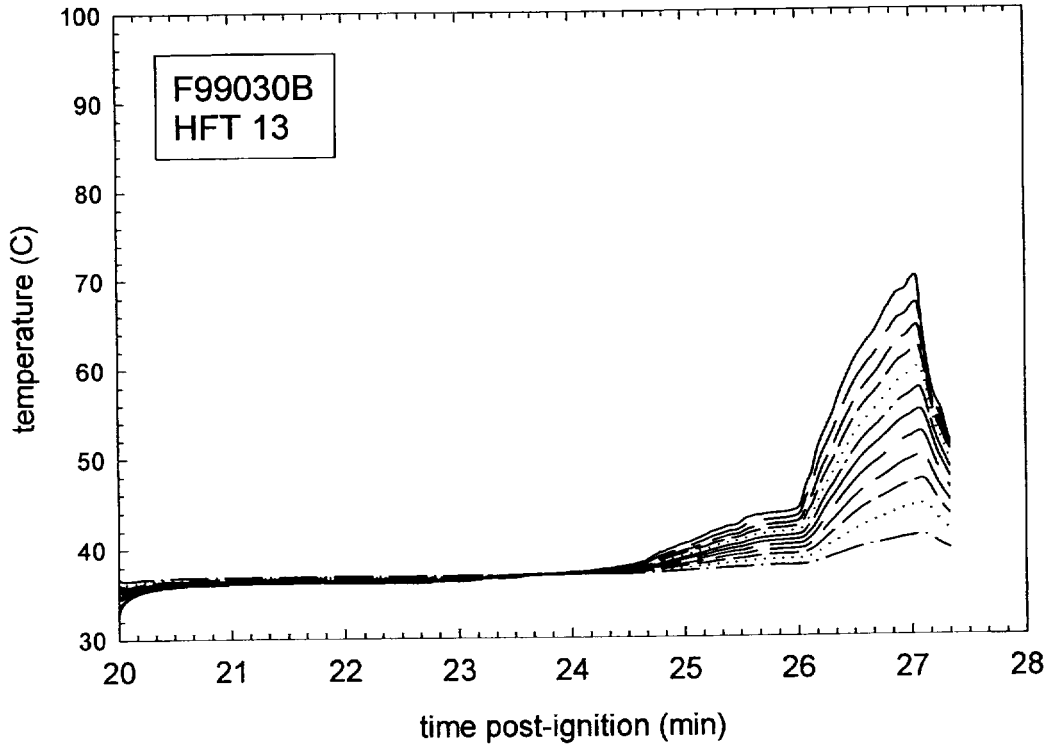

Figure 60. Fire Test F99030B. Skin temperature profiles estimated from data recorded from HFT/RAD Assembly 13 (**APPENDIX E**, Plots E8 and E9).

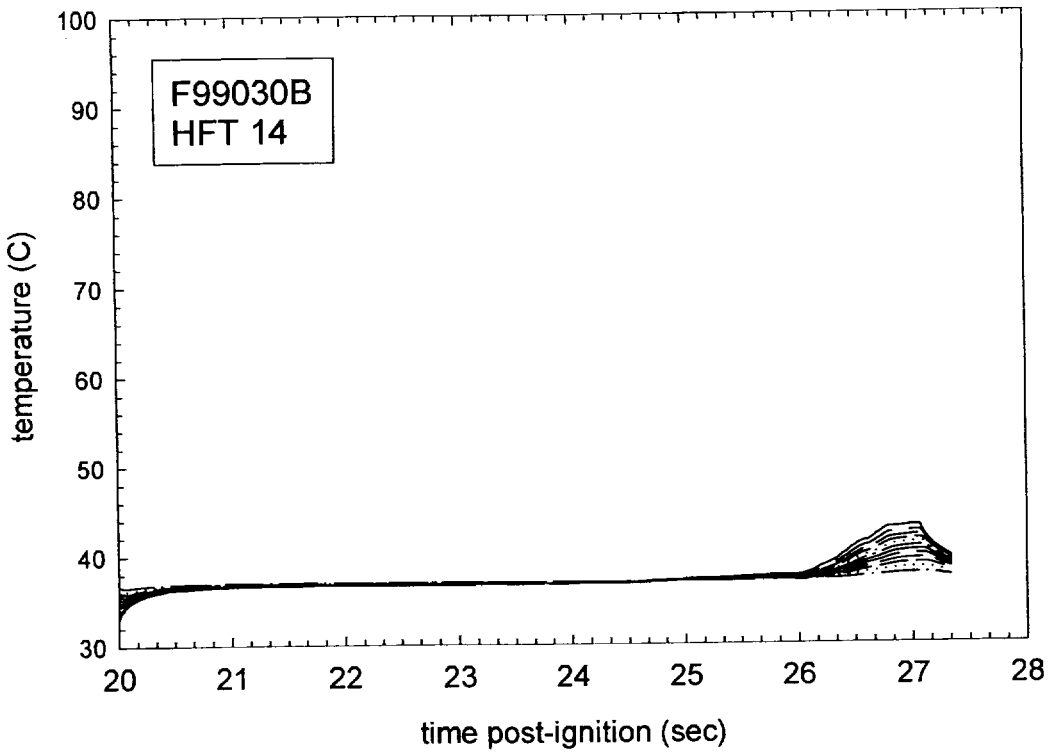

Figure 61. Fire Test F99030B. Skin temperature profiles estimated from data recorded from HFT/RAD Assembly 14 (**APPENDIX E**, Plots E10 and E11).

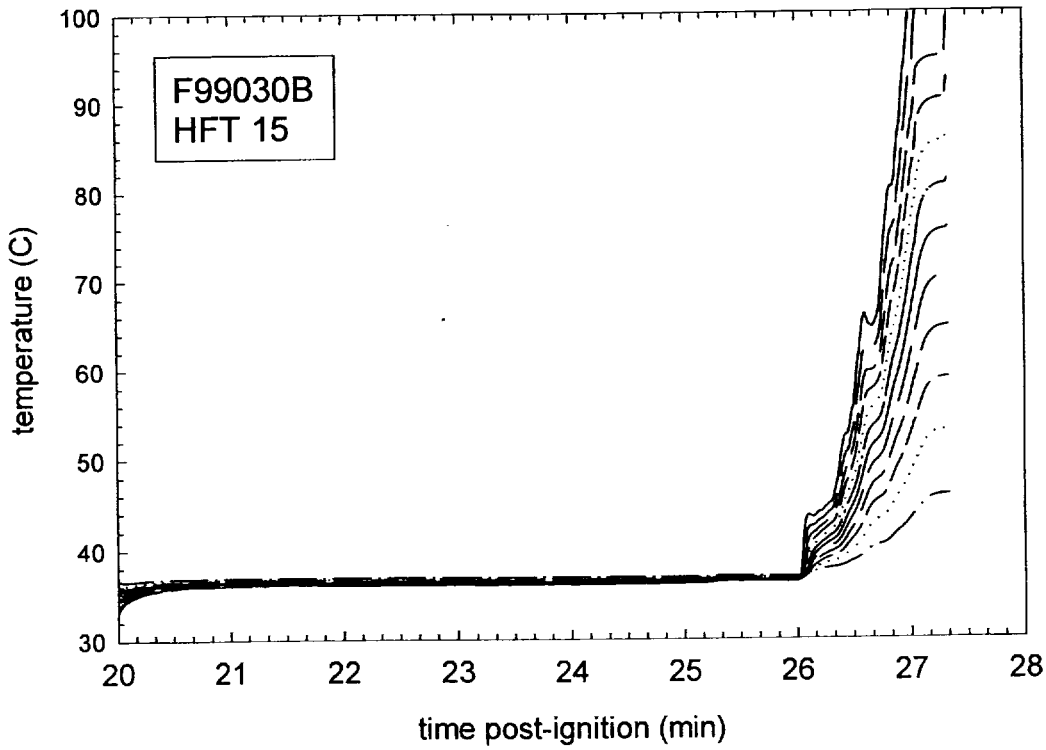

Figure 62. Fire Test F99030B. Skin temperature profiles estimated from data recorded from HFT/RAD Assembly 15 (**APPENDIX E**, Plots E12 and E13).

The peak heat flux to HFT/RAD 10 started to increase at about 25½ minutes post-ignition and peaked at approximately 6 kW/m^2 at between 26½ and 27 minutes post-ignition (**APPENDIX E**). Epidermal temperatures estimated using data from HFT/RAD 10 started to increase between 25 and 26 minutes post-ignition and peaked at approximately 29°C at about 27 minutes post-ignition (Fig. 57).

HFT/RAD 11 was located on the left front seat cushion facing forward (**APPENDIX E**) and indicated no heat flux to this transducer during this test (**APPENDIX E**). Epidermal temperatures estimated using data from HFT/RAD 11 did not increase between 20:00 and 27:20 min:sec post-ignition (Fig. 58).

HFT/RAD 12 was located above the left front seat cushion facing forward (**APPENDIX E**) and responded to radiation from flames in the engine compartment after holes developed in the windshield between 24 and 25 minutes post-ignition (**Section 5.1**). The heat flux to HFT/RAD 12 started increase between 24 and 25 minutes post-ignition and peaked at approximately 16 kW/m^2 between 26½ and 27 minutes post-ignition (**APPENDIX E**). Epidermal temperatures estimated using data from HFT/RAD 12 started to increase between 24 and 25 minutes post-ignition and peaked at approximately 70°C at 27 minutes post-ignition (Fig. 59).

HFT/RAD 13 was located above the right front seat cushion facing forward (**APPENDIX E**) and responded to radiation from flames in the engine compartment after holes developed in the windshield (**Section 5.1**). The heat flux to HFT/RAD 13 started increase between 24 and 25 minutes post-ignition and peaked at approximately 16 kW/m^2 between 26½ and 27 minutes post-ignition (**APPENDIX E**). Epidermal temperatures estimated using data from HFT/RAD 13 started to increase between 24 and 25 minutes post-ignition and peaked at approximately 70°C at 27 minutes post-ignition (Fig. 60).

HFT/RAD 14 was located above the right front seat cushion facing upward (**APPENDIX E**) responded to convection and downward radiation from heated gases flowing into the passenger compartment along the roof trim panel starting between 24 and 25 (**Section 5.3**). The heat flux to HFT/RAD 14 started to increase at about 24½ minutes post-ignition and peaked at approximately 2 kW/m^2 between 26½ and 27 minutes post-ignition (**APPENDIX E**). Epidermal temperatures estimated using data from HFT/RAD 14 started to increase at about 25½ minutes post-ignition and peaked at approximately 43°C at 27 minutes post-ignition (Fig. 61).

HFT/RAD 15 was located on the right front seat cushion facing forward (**APPENDIX E**) and responded to convection and radiation from the burning deployed passenger side airbag (**Section 5.1.1**). The heat flux to HFT/RAD 15 started to increase at about 26 minutes post-ignition and peaked at approximately 45 kW/m^2 between 26½ and 27 minutes post-ignition (**APPENDIX E**). Epidermal temperatures estimated using data from HFT/RAD 16 started to increase just after 26 minutes post-ignition and peaked at > 100 43°C between 27 and 28 minutes post-ignition (Fig. 62).

7.2 The FAA Combined Hazard Survival Model and Purser's Model of Combustion Gas Toxicity

The FAA Combined Hazard Survival Model and Purser's model utilize the concept of a Fractional Effective Dose [FED] to estimate the cumulative effects of exposure to a mixture of gases produced by burning materials. For exposure to a single gas with an unchanging concentration in air, the Fractional Effective Dose for Incapacitation [FED(I)] is defined as the product of the gas-phase concentration and the time of exposure ($C \times t$) normalized to the concentration-time product that results in incapacitation of 50% of an exposed population [7, 8]. Similarly, the Fractional Effective Dose for lethality [FED(L)] is defined as the product of the gas-phase concentration and the time of exposure normalized to the concentration-time product that results in the death of 50% of an exposed population [see references in 7 and 8]. The estimates of FED(I) and FED(L) obtained using the FAA Combined Hazard Survival Model or Purser's model of combustion gas toxicity and presented in this report cannot be used to predict precisely when the gas concentrations measured in this test would have resulted in incapacitating narcosis or death for a vehicle occupant. Whether exposure to these gases results in toxicity depends on a number of complex physical and physiological variables.

Some of the physical variables include the exact chemical composition of the gaseous mixture, the concentration of each component of the gaseous mixture, and the time of exposure. Exposure to these gases in a burning vehicle can be highly variable, and depend on factors such as elevation in the passenger compartment and airflow through the passenger compartment. As mentioned in the previous section, combustion gases are hotter than the ambient air and form an upper-layer. As both heat and mass are conserved in a fire, the existence of a steep vertical air-temperature gradient implies the existence of similarly steep vertical concentration gradients for gaseous combustion products accumulating in the passenger compartment. The location of the head and nose in the passenger compartment will effect the exposure concentration. An occupant whose head was located below the level where gases were measured, such as an

occupant bent over in the seat, would have been exposed to lower concentrations of combustion gases than those shown in **APPENDIX H**. Airflow through the passenger compartment will dilute or remove these gases.

Uncertainties in the responses of humans exposed to these gases also complicate the determination of when and whether toxicity occurs. The mathematical equations for the calculation of FED(I) and FED(L) were derived by analysis of data from controlled experiments in which different species of laboratory animals were exposed to a range of concentrations of each gas. In using data from these laboratory animal experiments to define FED(I) and FED(L), both models implicitly assume that humans respond the same as laboratory animals to exposure to these gases – an assumption that is largely untested and may not be accurate. For example, except for incapacitation from exposure to carbon dioxide, none of the model predictions using either the FAA Combined Hazard Survival Model or Purser's model have been validated for humans. That is, the accuracy of FED(I) and FED(L) in predicting human responses to exposure to the combustion gases measured in this test has not been determined. Consequently, there is a high degree of uncertainty as to the effect exposure to these levels of combustion gases would actually have on a human vehicle occupant. In addition, neither of these models accounts for variation in individual responses to these gases nor the effect of trauma suffered during the crash on an occupant's response to these gases.

The equations presented in both the FAA Combined Hazard Survival Model and in Purser's model divide the exposure into one-minute intervals when the concentration of the gaseous species changes with time. In this test, Fourier Transform Infrared spectra were obtained at seven-second intervals to characterize the changing gas concentrations observed in the passenger compartment. The equations presented in the FAA Combined Hazard Survival Model and in Purser's model were modified to account for the faster sampling times used in this test. These modified equations are shown below and were used to derive the estimated of FED(I) and FED(L) shown in **SECTION 7.2.1.**

Carbon dioxide-induced hyperventilation can increase the respiratory uptake of airborn combustion products. The FAA Combined Hazard Survival Model uses a multiplication factor to account for the increased respiratory uptake of gaseous combustion products because of exposure to elevated levels of carbon dioxide [V_{CO2}]:

$$V_{CO_2} = \frac{\exp(1.9086 + 0.2496 \times C_{CO_2})}{6.8} \qquad (1)$$

where the units of C_{CO2} are %. This equation was not modified for the analysis presented in **SECTION 7.2.1**.

The Fractional Effective Doses for Incapacitation from exposure to carbon dioxide, carbon monoxide, hydrogen chloride, hydrogen cyanide and decreased oxygen were calculated using the following equations modified to account for sampling intervals of less than 1 minute:

$$FED(I)_{CO_2} = \left(\frac{t}{60}\right) \times \sum \left\{ \frac{1}{2193.8 - \left(311.6 \times C_{CO_2}\right)} \right\} \tag{2}$$

when $5.5 \leq C_{CO2} \leq 7.0\%$,

$$FED(I)_{CO_2} = \left(\frac{t}{60}\right) \times \sum \left\{ \frac{1}{\exp\left(6.1623 - \left(0.5189 \times C_{CO_2}\right)\right)} \right\} \tag{3}$$

when $C_{CO2} > 7.0\%$,

$$FED(I)_{CO} = \left(\frac{t}{60}\right) \times \left(\frac{1}{3.4250}\right) \times \sum \left\{ V_{CO_2} \times C_{CO} \right\} \tag{4}$$

when $V_{CO2} \times C_{CO} > 0.01\%$,

$$FED(I)_{HCl} = \left(\frac{t}{60}\right) \times \sum \left\{ \frac{1}{3 + \frac{336{,}000}{\left(V_{CO_2} \times C_{HCl}\right) - 300}} \right\} \tag{5}$$

when $V_{CO2} \times C_{HCl} > 300$ ppm;

$$FED(I)_{HCN} = \left(\frac{t}{60}\right) \times \left(\frac{1}{564}\right) \times \sum \left\{ \left(V_{CO_2} \times C_{HCN}\right) - 63 \right\} \tag{6}$$

when $V_{CO2} \times C_{HCN} > 63$ ppm; and

$$FED(I)_{O_2} = \left(\frac{t}{60}\right) \times \sum \left\{ \frac{1}{\exp\left(8.55 - \left(0.511 \times \left(20.9 - C_{O_2}\right)\right)\right)} \right\} \tag{7}$$

when $C_{O2} < 11\%$. The value of t in these equations was the time in seconds between acquisition of FTIR spectra. The overall Fractional Effective Dose for Incapacitation was calculated by summing the terms in equations 2 through 7:

$$FED(I)_{TOTAL} = FED(I)_{CO_2} + FED(I)_{CO} + FED(I)_{HCl} + FED(I)_{HCN} + FED(I)_{O_2} \quad (8)$$

The Fractional Effective Doses for Lethality from exposure to carbon monoxide and hydrogen cyanide were calculated using the following equations modified to account for sampling intervals of less than 1 minute:

$$FED(L)_{CO} = \left(\frac{t}{60}\right) \times \sum \left\{ \frac{1}{\exp\left(5.85 - \left(0.00037 \times V_{CO_2} \times C_{CO}\right)\right)} \right\} \quad (9)$$

when $2000 \leq V_{CO2} \times C_{CO} \leq 9000$ ppm,

$$FED(L)_{CO} = \left(\frac{t}{60}\right) \times \sum \left\{ \frac{1}{0.4 + \left(\frac{58{,}000}{V_{CO_2} \times C_{CO}}\right)} \right\} \quad (10)$$

when $V_{CO2} \times C_{CO} > 9000$ ppm, and

$$FED(L)_{HCN} = \left(\frac{t}{60}\right) \times \left(\frac{1}{2586}\right) \times \sum \left\{ \left(V_{CO_2} \times C_{HCN}\right) - 43.2 \right\} \quad (11)$$

when $V_{CO2} \times C_{HCN} > 43.2$ ppm;

The overall Fractional Effective Dose for Lethality was calculated by summing the terms in equations 8 through 10:

$$FED(L)_{TOTAL} = FED(L)_{CO} + FED(L)_{HCN} \quad (12)$$

The model described by Purser also uses a multiplication factor to account for the enhanced respiratory uptake of toxic gases because of exposure to elevated levels of carbon dioxide:

$$V_{CO_2} = \frac{\exp(1.9086 + (0.2496 \times C_{CO_2}))}{6.8} \quad (13)$$

The Fractional Effective Doses for Incapacitation from exposure to carbon monoxide and hydrogen cyanide were calculated using the following equations modified to account for sampling intervals of less than 1 minute:

$$FED(I)_{CO_2} = \left(\frac{t}{60}\right) \times \sum \left\{ \frac{1}{\exp(6.1623 - (0.5189 \times C_{CO_2}))} \right\} \quad (14)$$

when $C_{CO2} > 5\%$,

$$FED(I)_{CO} = \left(\frac{t}{60}\right) \times V_{CO_2} \times \sum \left\{ \frac{0.00082925 \times C_{CO}}{30} \right\} \quad (15)$$

where the units of C_{CO} are ppm,

$$FED(I)_{HCN} = \left(\frac{t}{60}\right) \times V_{CO_2} \times \sum \left\{ \frac{4.4}{185 - C_{HCN}} \right\} \quad (16)$$

when $80 \leq C_{HCN} \leq 180$ ppm,

$$FED(I)_{HCN} = \left(\frac{t}{60}\right) \times V_{CO_2} \times \sum \left\{ \frac{1}{\exp(5.396 - (0.023 \times C_{HCN}))} \right\} \quad (17)$$

when $C_{HCN} > 180$ ppm; and

$$FED(I)_{O_2} = \left(\frac{t}{60}\right) \times \sum \left\{ \frac{1}{\exp(8.13 - (0.54 \times (20.9 - C_{O_2})))} \right\} \quad (18)$$

when $C_{O2} < 11.3\%$.

As in the FAA model, the value of t in these equations was the time in seconds between acquisition of FTIR spectra. The overall Fractional Effective Dose for Incapacitation was calculated by summing the terms in equations 14 through 18:

$$FED(I)_{TOTAL} = FED(I)_{CO_2} + FED(I)_{CO} + FED(I)_{HCN} + FED(I)_{O_2} \quad (19)$$

Both the FAA Combined Hazard Survival model and Purser's model predict that 50% of an exposed population would experience incapacitating narcosis (*i.e.*, an occupant loses

consciousness and would be unable to exit a vehicle without assistance) when $FED(I)_{TOTAL} = 1.0$. Similarly, both of these models predict that 50% of an exposed population would die when $FED(L)_{TOTAL} \geq 1.0$.

7.2.1 Estimation of Fractional Equivalent Dose Parameters

Results of analysis of combustion products toxicity following procedures described in the FAA Combined Hazard Survival Model and Purser's model are shown in Figures 63 through 68. These analysis yielded estimates of $FED(I)_{co}$ only. The concentrations of carbon dioxide, hydrogen chloride, and hydrogen cyanide did not exceed the respective threshold concentrations for calculation of FED(I) at any time during this test. Therefore, these models did not yield estimates of $FED(I)_{CO2}$, $FED(I)_{HCN}$, and $FED(I)_{HCL}$. Other gaseous species included in these models, such as O_2, were not measured during this test, and values of FED(I) or FED(L) were not estimated for these gases.

Plots of the $FED(I)_{co}$ parameters estimated using both models are shown in Figure 64. The equations presented in the Purser model for computation of $FED(I)_{co}$ include a term for respiratory minute volume. Minute volumes corresponding to respiration during rest (8.5 L/min) and light activity (25 L/min) were used in these calculations [8]. Purser's model also accounts for the effect of exposure to carbon dioxide on respiratory rate.

The FAA Combined Survival Hazard Model computes only one estimate of $FED(I)_{co}$, which accounts for the effect of exposure to carbon dioxide on respiratory rate [7]. Both models yielded estimates of $FED(I)_{co} < 0.05$ throughout this test. The estimates of $FED(I)_{co}$ derived using the FAA model, and Purser's model with a respiratory minute volumes of 8.5 and 25 L/min reached maximum values of about 0.012, 0.014, and 0.023, respectively, at 27 minutes post-ignition, the time when fire suppression began, and 0.029, 0.030, and 0.040 at 29 minutes post-ignition.

The concentrations of carbon dioxide, carbon monoxide, hydrogen chloride, and hydrogen cyanide did not exceed the respective threshold concentrations for calculation of FED(L) at any time during this test. Therefore, the FAA Combined Survival Hazard Model did not yield estimates of $FED(L)_{CO}$, $FED(L)_{HCN}$, $FED(L)_{HCl}$, $FED(L)_{TOTAL}$ (Fig. 68).

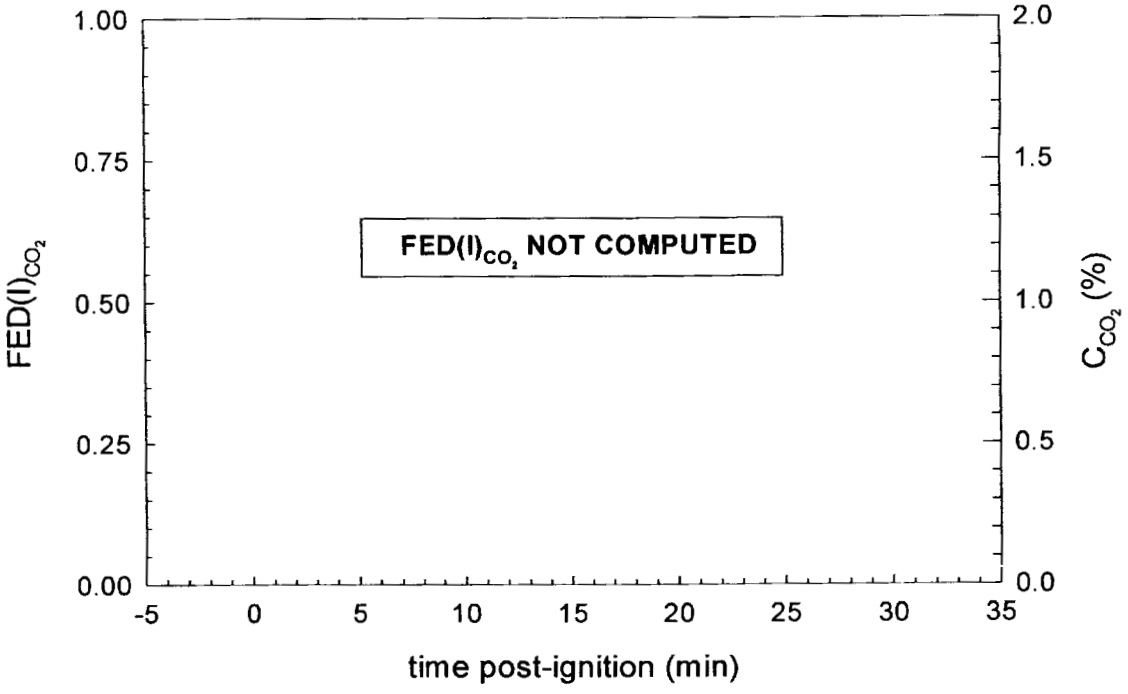

Figure 63. Fire Test F99030B. C_{CO2} did not exceed the threshold concentrations for calculation of $FED(I)_{CO2}$ at any time during this test. A plot of C_{CO2} (——) is shown for reference.

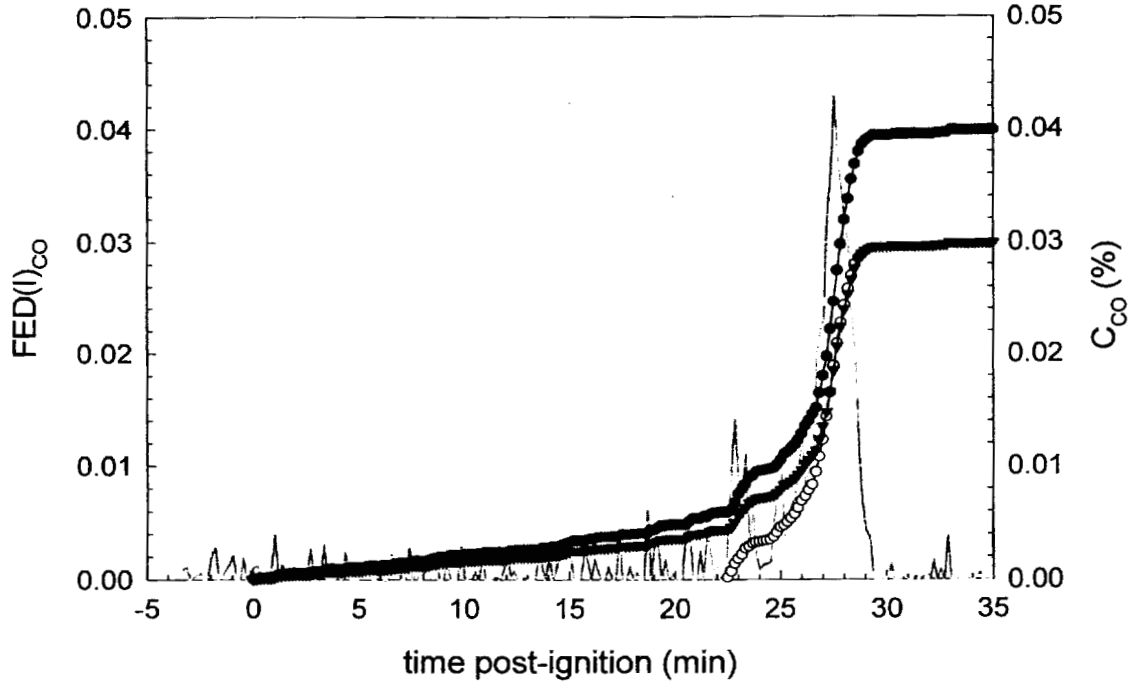

Figure 64. Fire Test F99030B. Plots of estimates of $FED(I)_{CO}$ versus time post-ignition computed using the FAA Combined Hazard Survival Model (—○—), the Purser model with a respiratory minute volume of 8.5 L/min (—▼—), and the Purser model with a respiratory minute volume of 25 L/min (—●—). A plot of C_{CO} (——) is shown for reference.

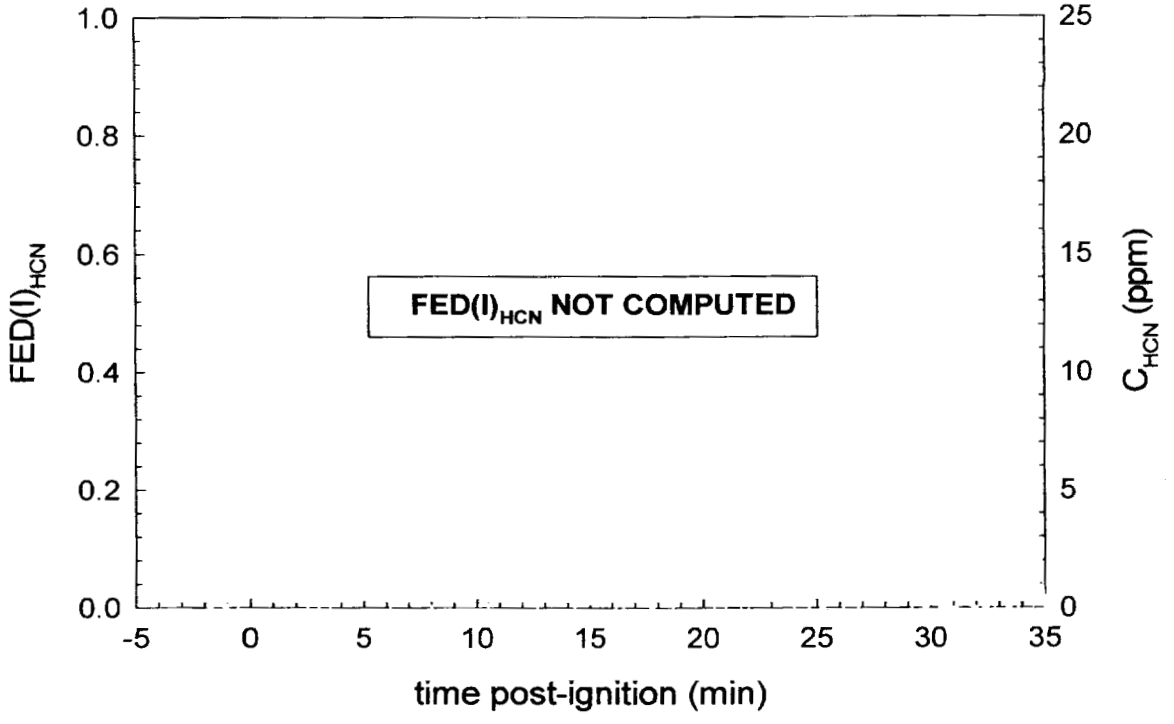

Figure 65. Fire Test F99030B. C_{HCN} did not exceed the threshold concentrations for calculation of $FED(I)_{HCN}$ at any time during this test. A plot of C_{HCN} (——) is shown for reference.

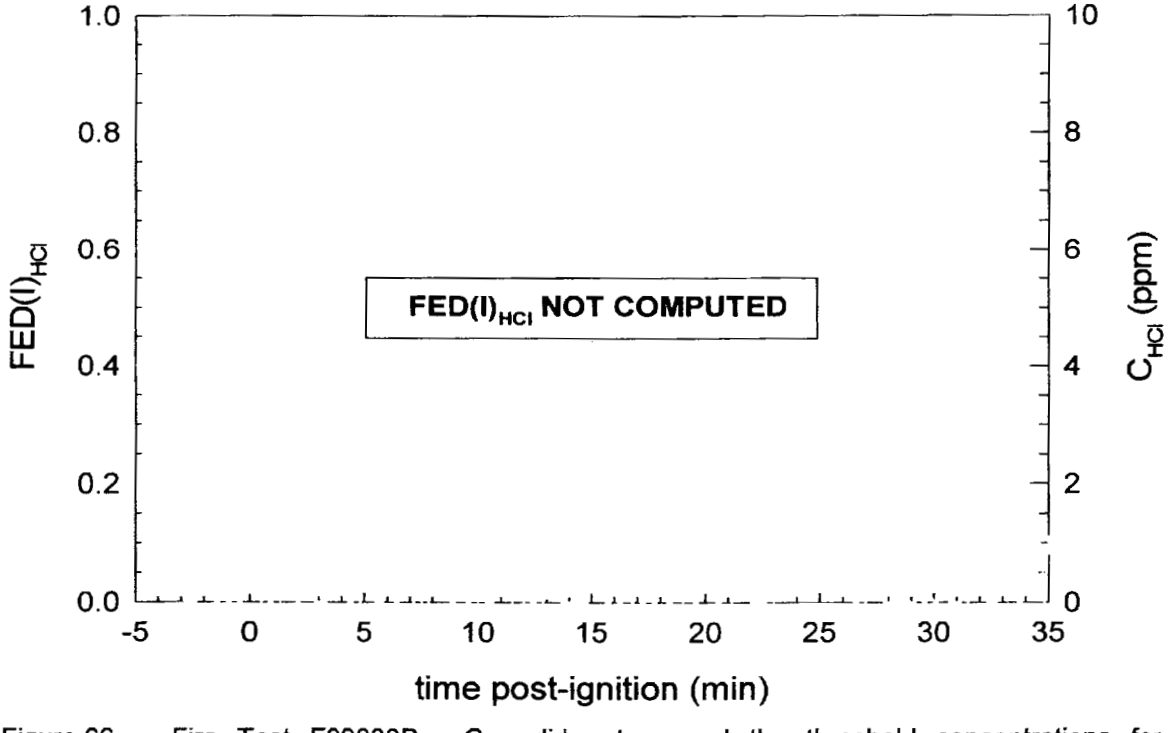

Figure 66. Fire Test F99030B. C_{HCl} did not exceed the threshold concentrations for calculation of $FED(I)_{HCL}$ at any time during this test. A plot of C_{HCl} (——) is shown for reference.

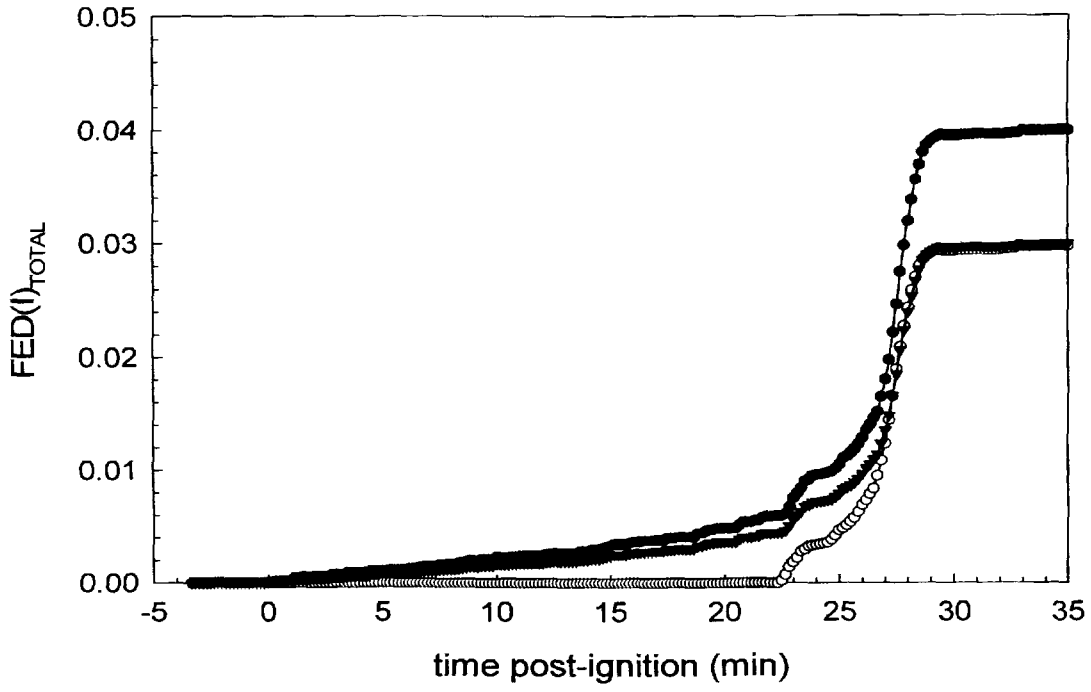

Figure 67. Fire Test F99030B. Plots of $FED(I)_{TOTAL}$ versus time post-ignition: FAA Combined Hazard Survival Model (—O—); Purser's model with RMV = 8.5 L/min (—▼—); and Purser's model with RMV = 25 L/min (—●—).

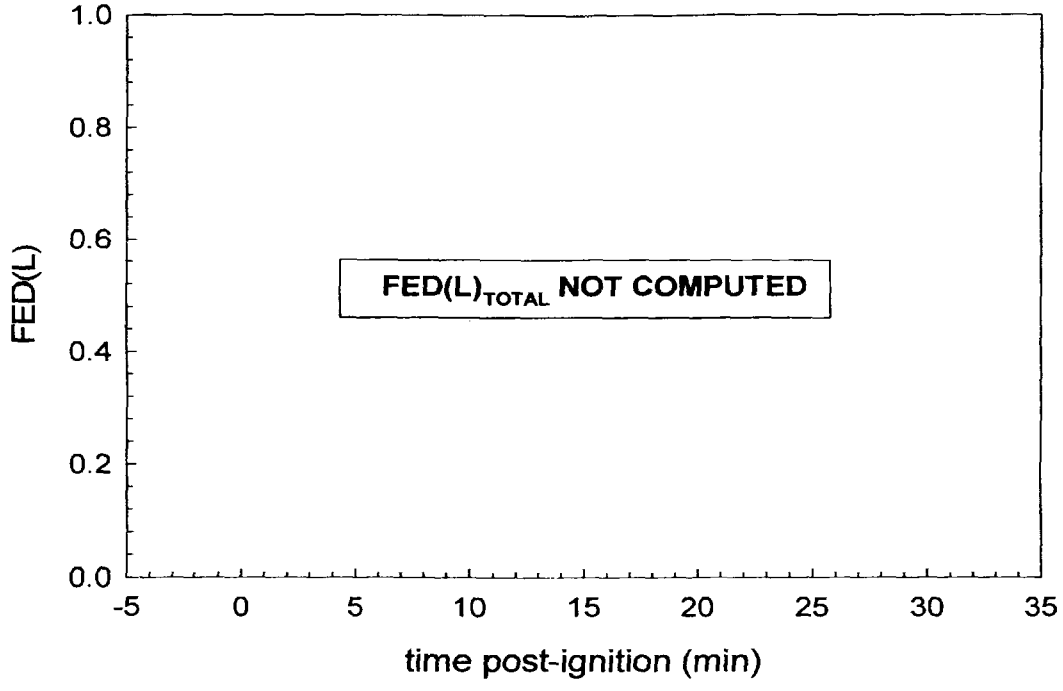

Figure 68. Fire Test F99030B. C_{CO2} , C_{HCN} , and C_{HCl} did not exceed the threshold concentrations for calculation of $FED(L)_{CO}$, $FED(L)_{HCN}$, and $FED(L)_{HCl}$ at any time during this test. Therefore, $FED(L)_{TOTAL}$ was not computed.

The estimates of FED(I) obtained using the FAA Combined Hazard Survival Model and Purser's model of combustion gas toxicity cannot predict precisely when exposure to the gas concentrations measured in this test would have resulted in incapacitating narcosis or death. This is especially true for prediction of lethality, where the mathematical relationships in these models were derived from experiments using laboratory animals or accidental, uncontrolled human exposures [7, 8]. Variation in susceptibility to these hazards among the human population also will contribute to the uncertainty in these predictions. In addition, the effect of trauma caused by the crash on an occupant's tolerance to these toxic gases is impossible to quantify.

Another variable that may affect an occupant's susceptibility to the combustion products is the location of the head. The data from the aspirated thermocouples indicated that a steep air-temperature gradient developed in the front of the passenger compartment during this test (see below). As both heat and mass are conserved in a fire, the existence of a steep vertical air-temperature gradient implies the existence of a similarly steep vertical concentration gradient for combustion products accumulating in the passenger compartment. The inlet to the gas sampling tube in the passenger compartment was in the breathing zone of that of a six-foot tall adult male sitting upright in either the driver's or front passenger's seat. An occupant whose head was located below the level where gases were sampled would have been exposed to lower concentrations of combustion gases than those shown in **APPENDIX H**. And, the estimated values of FED(I) and FED(L) for this occupant would have been lower than those shown in Figures 64 through 69.

7.3 Estimation of Burn-Injury to the Respiratory Tract

As discussed in Section 5.3, heated gases started to flow into the passenger compartment along the roof trim panel between 22 and 23 minutes post-ignition (Fig. 47). A vertical temperature gradient existed in the passenger compartment and the air temperatures measured by the aspirated thermocouple probes depended on the distance form the roof because of the test vehicle during this test. At 27 minutes post-ignition, the vertical temperature gradient was approximately 3.7°C/cm (**Section 5.3**) and linear from the lower surface of the roof trim panel to 40 cm below the lower surface of the roof trim panel (Fig. 69). Thus, the temperatures just below the roof trim panel was approximately 280°C at 27 minutes post-ignition and the air temperature 40 cm below the roof trim panel was approximately 85°C (Fig. 69).

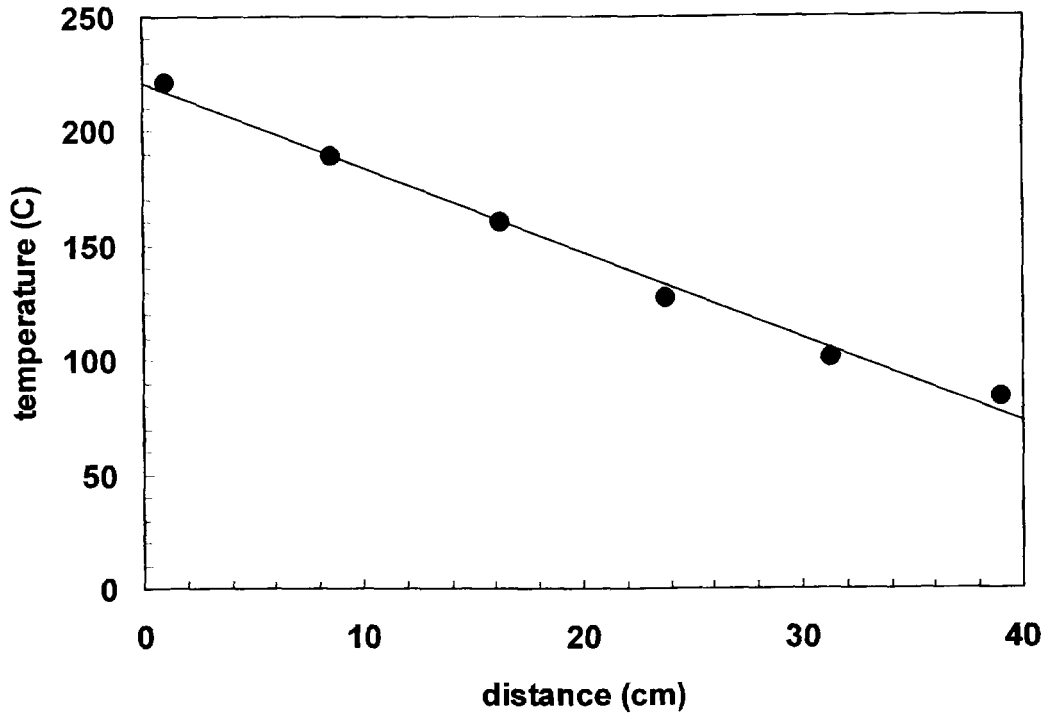

Figure 69. Fire Test F99030B. Plot of air temperature as a function of distance below the roof trim panel at 27 minutes post-ignition.

It is not possible to estimate the potential for burn injury to the respiratory tract caused by inhalation of hot air by relying solely on air temperature data. Water and particulate produced by the fire increase the heat capacity of the air. The concentrations of these species in the inhaled air have been shown to affect both the severity and depth of burn injury in the respiratory system [see references in 8]. Neither the water- nor the particulate-concentrations of air in the passenger compartment were measured in this test. Purser states that a robust quantitative relationship between the temperature, water-content, and particulate-content of inhaled air and subsequent burn injury to respiratory airways has not been established [8]. A few controlled animal studies indicate that inhalation of steam at 100°C caused burns to the larynx and trachea similar to those produced by inhalation of dry air at 350°C or flames at 500°C [see references in 8]. In these controlled animal studies, death was not immediate, but resulted from obstructive edema in the burned airways a few to twenty-four hours after the exposure. As the concentration of water vapor in the air sampled from the passenger compartment was not measured during this test, the potential for burn injury to the respiratory airways from inhalation of hot gas cannot be determined accurately from the air temperature data shown. Moreover, as the discussion above shows, the measured air temperature in the passenger compartment was dependent on the height of the thermocouple, specifically the distance below the roof. As small changes in vertical distance

resulted in relatively large chances in air temperature, the temperature of inhaled air depends on the height of the breathing zone in the passenger compartment.

ACKNOWLEDGEMENTS

Dr. Thomas Ohlemiller and Thomas Cleary of the Building and Fire Research Laboratory, National Institute of Standards and Technology were responsible for video taping this fire test, and provided an initial analysis of the test data for fire propagation. Dr. Archibald Tewarson of Factory Mutual Research Corporation provided the data from the Fire Products Collector at the test facility that was collected during this test.

REFERENCES

1. Jack L. Jensen and Jeffrey Santrock. Evaluation of Motor Vehicle Fire Initiation and Propagation. Part 1: Vehicle Crash Test and Fire Propagation Test Program. Submitted to the National Highway Transportation Safety Administration pursuant to the Settlement Agreement between General Motors and the Department of Transportation. Submitted July 31, 1997.

2. Jack L. Jensen and Jeffrey Santrock. Evaluation of Motor Vehicle Fire Initiation and Propagation. Part 11: Crash Tests on a Front-Wheel Drive Passenger Vehicle. Submitted to the National Highway Transportation Safety Administration pursuant to the Settlement Agreement between General Motors and the Department of Transportation. Submitted May 7, 2002.

3. Federal Safety Standards. Motor Vehicle Safety Standard No. 214 Side Impact Protection - Passenger Cars, Trucks, Buses & Multipurpose Passenger Vehicles with GVWR of 10,000 Pounds or Less. 60FR57838-39 (November 22, 1995).

4. SigmaPlot® 4.0 for Windows®, SPSS Inc., 444 North Michigan Avenue, Chicago, IL 60611. Copyright © 1997 by SPSS Inc..

5. Archibald Tewarson. "Generation of Heat and Chemical Compounds in Fires" Section 3/Chapter 4, SFPE Handbook of Fire Protection Engineering, 2nd Edition, 1995, pp. 3:53-124.

6. F. S. Knox III, Dena Bonetti, and Chris Perry. User's Manual for BRNSIM/BURNSIM: A Burn Hazard Assessment Model. United States Army Aeromedical Research Laboratory Report No. 93-13. Fort Rucker, Alabama 36362-5292. February 1993.

7. L. C. Speitel. Toxicity Assessment of Combined Gases and Development of a Survival Model. DOT/FAA/AR-95-5. July 1995.

8. David A. Purser. "Toxicity Assessment of Combustion Products" Section 2/Chapter 8, SFPE Handbook of Fire Protection Engineering, 2nd Edition, 1995, pp. 2:85-146.

APPENDIX A
VIDEO CAMERA SET-UP

Scientific and technical personnel from the Building and Fire Research Laboratory, National Institute of Standards and Technology were primarily responsible for obtaining a video record of this test. Seven video cameras were used in this test. Figure A1 shows the approximate locations of the video cameras relative to the test vehicle during this test.

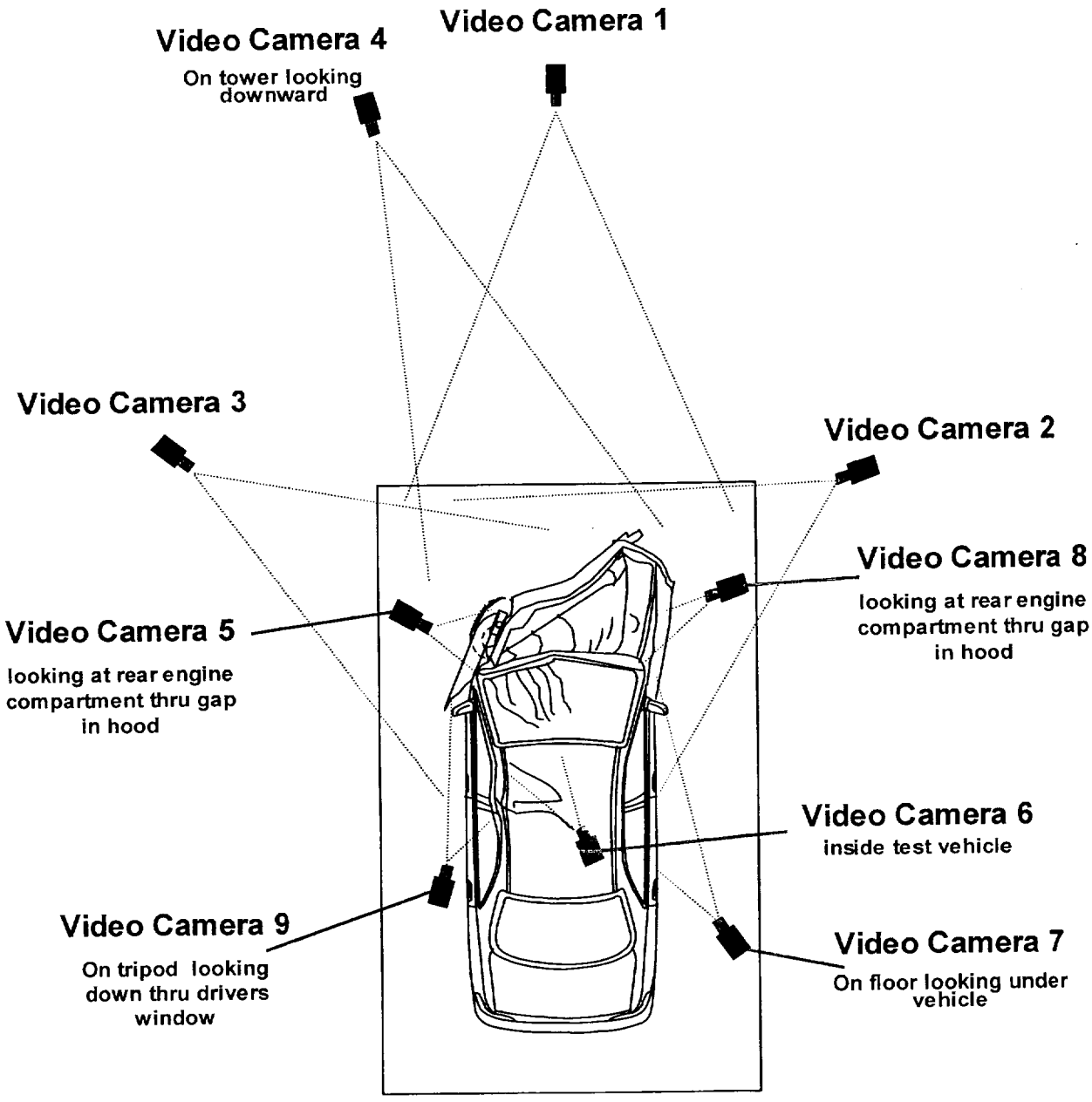

Figure A1. Fire Test F99030B. Diagram showing the approximate locations of the video cameras during this test. Distances in this figure are not to scale in this diagram.

Camera 1 was a Hi-8 camcorder mounted on a tripod. It had a field-of-view that included the full height and width of the front of the test vehicle. Camera 2 was a Hi-8 camcorder mounted on a tripod. It had a field-of-view that included the left side of the test vehicle from about the B pillar to beyond the front bumper. Camera 3 was a Hi-8 camcorder mounted on a tripod. It had a field-of-view that included the right side of the test vehicle from about the rear edge of the B pillar to beyond the front bumper. Camera 4 was a Hi-8 camcorder mounted on a tower approximately 3 meters above the test vehicle. Its field-of-view included the front of the test vehicle. Camera 5 was a black-and-white CCD camera mounted on a stand on the test surface. Its field of view included the area between the hood and fender looking toward the rear of the engine compartment on the left side. Camera 6 was a black-and-white CCD camera installed in the interior of the test vehicle. It had a field of view that included the front corner of the left front seat cushion from top of instrument panel to floor. Camera 7 was a Camcorder resting on the cement board surface in the fluid containment pan. Its field of view included the area between the vehicle underbody and the test surface under the front of the test vehicle. Camera 8 was a black-and-white CCD camera mounted on a stand on resting on the cement board surface in the fluid containment pan. It was focused through a gap between the right side of the deformed hood and right front fender and its field of view included the right side of the engine compartment. Camera 9 was mounted on a tripod located on the cement board surface in the fluid containment pan. Its field of view included the left front window from the A-pillar to just behind the B-pillar.

All video cameras were started before the test. A microphone on each camera recorded air horn signals indicating that spraying of a flaming aerosol of power steering fluid toward the windshield washer fluid reservoir and the end of the test.

Quartz-halogen floodlights were used to illuminate the exterior of the vehicle. The level of illumination provided by these lamps was insufficient to balance the intensity of light reflecting from the vehicle surfaces with the brightness of the flames. To compensate for this imbalance, the light sensitivity adjustments on the Hi-8 camcorders were set to the manual position so that the apparent brightness of the vehicle surfaces did not change as the fire developed. As a result, the flames were overexposed, in some cases causing them to appear more opaque than they actually were.

APPENDIX B
INFRARED THERMOGRAPHY

Infrared thermal imaging radiometers were used to help determine fire propagation, flame, and surface temperatures during this test. These imaging systems measure thermal radiation within a definite waveband, over a variable field of view. The data obtained from these measurements can be analyzed to produce a two-dimensional map of apparent temperature called a thermogram.

Thermal imaging systems produce a spatially resolved map of surface temperatures from the radiant energy emitted in the field of view. The response time of these systems is nanoseconds, giving them the capability to acquire over 1 million discrete measurements per second. The capability of high-speed data acquisition is advantageous in that it can provide a tremendous amount of thermal data during a vehicle fire test, which can be over in only a few minutes. Thermal imaging radiometers can be used concurrently as a vision system and a measurement system. However, the thermal sensitivity, scan speed, and spatial resolution must be optimized for a particular application.

B.1 Infrared Camera Location

Eight thermal imaging systems were used in this test. Figure B1 shows the approximate locations of the infrared cameras relative to the test vehicle during this test.

IR Camera 1 was an Inframetrics Model 760 long wavelength system (Inframetrics Inc, Billerica, MA). It was focused through the left front door glass opening downward onto the area of the instrument panel around the steering wheel. IR Camera 2 was an Agima model 900 long wavelength system. It was focused downward through the window opening in the left front door. IR Camera 3 was an Inframetrics Model 760 long wavelength system. It was focused downward through window opening in the left front door. IR Camera 4 was an Inframetrics Model 760 system. It was focused through the left front window opening of the test vehicle. IR Camera 5 was a Thermovision Model 570 system. It had a field-of-view that included the left front side of the test vehicle from the A-Pillar to the front of the hood and from the top of the hood to just above the left front tire. IR Camera 6 was a Thermovision Model 570 system. It had a field of view that included the entire front of the test vehicle. IR Camera 7 was an Inframetrics Model 760 long wavelength system. It had a field-of-view that included the windshield of the test vehicle. IR Camera 8 was located inside the test vehicle. It had a field of view that included the left half of the windshield from the header to approximately the midline of steering wheel.

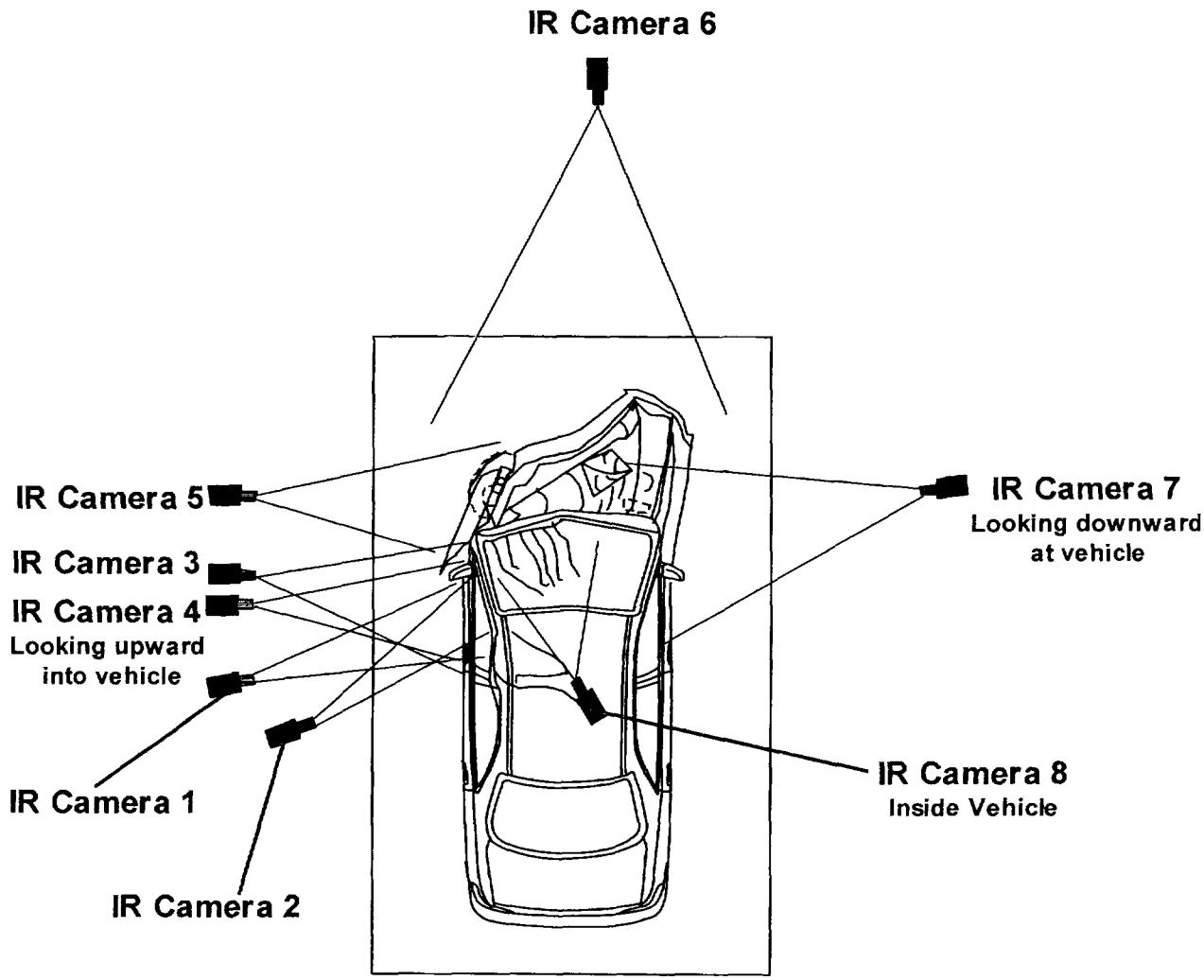

Figure B1. Fire Test F99030B. Diagram showing the approximate locations of infrared cameras around the test vehicle during this test. This diagram is approximate and not drawn to scale in this diagram.

B.2 Data Analysis

Thermal imaging systems measure infrared radiation within a certain spectral band and must be calibrated to convert radiant intensity in that spectral band to temperature. Due to variations in system response, every system has to be calibrated. Calibration curves for the basic thermal imaging radiometers are measured at the factory and stored in read-only memory or in analysis software programs. Additional calibrations are needed for the optical filters. These calibrations are stored in the analysis software programs. Since thermal imaging radiometers are AC coupled devices, they measure differences in thermal radiation. To get absolute temperatures, there must be a reference to provide DC restoration. In these instruments, the reference is an internal blackbody reference source that is viewed periodically by the detector.

The general radiometric equation was used to convert radiant energy to temperature:

$$I = [E_t \times F(T_t)] + [(1 - E_t) \times F(T_b)] - [E_r \times F(T_r)] - [(1 - E_r) \times F(T_b)] \qquad \text{(B1)}$$

Where I is the difference in radiance between the target and a reference surface; E_t is the emittance of the target surface, generally unknown; E_r is the emittance of the reference surface, T_t is the temperature of the target surface; T_b is the temperature of background surfaces (i.e., ambient temperature), or other emitters such as flames reflected from the target; T_r is the temperature of the reference surface; $F(T_t)$ is the radiance from an ideal emitting surface (i.e., black body) at the temperature of the target surface (T_t); $F(T_r)$ is the radiance from an ideal emitting surface at the temperature of the reference (T_r); and $F(T_b)$ is the radiance from the background relative to the radiance value from the reference surface when $E_r = 1$. Factors other than temperature determine the emittance of an object. These factors include the type of material, the texture of the surface, the wavelength of the detector, and the view-angle. In determining temperatures from the radiant energy from an object, the operator can set the emittance of an unknown target surface to a value of between .01 and 1.0.

Radiant intensity measured by the thermal imaging system is converted to a gray-scale value. An 8 bit system provides gray scale values from 0 to 255 for the radiant energy at each pixel in the instantaneous field of view. A 12 bit system provides gray scale values from 0 to 4095. As the radiometer scans the image, each pixel is assigned a gray scale value, and the gray scale image is stored either in a computer memory or onto videotape. When stored in computer memory, a single frame (1 thermogram) can contain up to 68,000 pixels (discrete measurements) with an assigned 8 bit or 12 bit value. Videotape provides a temporal resolution of 30 frames per second. Depending on the thermal range of the thermal imaging radiometer, a temperature value was

assigned to each pixel using either the factory calibration curves accompanying each instrument, or calibration curves stored in IR analysis software.

Separation of the apparent temperatures of various surfaces on and inside a burning vehicle from the captured data is not a trivial task. The data represent a complex combination of emitted infrared energy from those surfaces as well as reflected infrared energy from the flames, and reflected infrared energy from high intensity lights used to illuminate the vehicle for visual data capture. In addition, the flames themselves were emitting infrared radiation due to their sooty content, some part of which was captured by the infrared thermal imaging systems. Also, some of the infrared radiation being emitted by the vehicle surfaces had to pass through flames containing soot from incomplete combustion of synthetic polymers or through clear (clean) flames where more complete combustion was occurring, and/or a combination of both types of flames. In all of these cases, gases in the flame absorbed some of the infrared radiation emitted by objects behind the flame.

The following steps were taken to minimize the impact of unwanted infrared radiation being captured by the thermal imaging systems.

- Anti-reflection tapes, paint, and glazes were applied to highly reflective surfaces on the test vehicle to minimize interference from reflections of the video floor and spot lights on the test vehicle.
- The thermal imaging systems were located in the shadows of the vehicle to block the video lights from shining directly into the radiometer.
- In some cases, flame filters (3.9 μm) were used in an attempt to screen out a portion of the infrared radiation from flames.

Despite these precautions, accurate surface temperatures could not be determined for areas of the vehicle blocked by intense flame. As a result, only surface temperatures determined to be reliable by the IR analysts are reported here. In some cases, specialized data analysis techniques were used to obtain reliable surface temperatures from areas in close proximity to, but not shielded by flame. Where possible, temperature data were reported from areas that lie in the shadow of the flames, which comes from highly emissive surfaces not affected by the flame radiation, and/or is deemed reliable based on the experience of the analysts. Data from nearby thermocouples were compared to IR temperature readings for a more comprehensive analysis.

During the data analysis, the videotapes were reviewed frame-by-frame to observe the burn sequence. The analyst captured images from selected frames on a video board. The image was

processed to produce a digitized gray scale value for each element in the pixel matrix utilizing the camera settings automatically documented between video frames on the videotape during data acquisition. Thermograms were produced from the digitized image matrix using a commercial software package (Thermogram Pro V1.3, sold by Inframetrics, Inc., Billerica, MA). This software utilized the NIST traceable calibration tables supplied by the manufacturer with each thermal imaging system.

APPENDIX C
THERMOCOUPLE DATA

The thermocouples used in this test were type-N thermocouples fabricated by Medtherm Corporation (Huntsville, AL). Each thermocouple consisted of an ungrounded thermocouple junction (30 AWG thermocouple wire) enclosed in an Inconel 600 sheath insulated with magnesium oxide (o.d. = 0.040 in. (1 mm), length = 50 ft. (15.2 m)). A transition was made through a stress-relief bushing to a duplex thermocouple extension cable (24 AWG) with fiberglass insulation and a stainless steel over-braid (length = 1 ft. (0.28 m)). Each thermocouple wire terminated in a grounded, compensated Type-N thermocouple plug. The thermocouples were connected to the data acquisition system using Type-N thermocouple extension cables (length = 50 ft. (15.2 m)).

The data acquisition system consisted of a PC (75 MHz Pentium Processor, 16 MB RAM, an 814 MB hard disk, and a 16-bit, Model BG45-AP5CP, ACER Inc., Taiwan R. O. C.) with a 100 kHz I/O board with 16 analog input channels (DaqBoard 200A, IOTech, Inc., Cleveland, OH). Thermocouple multiplex expansion cards (DBK-19, IOTech, Inc., Cleveland, OH) were used for data acquisition from the thermocouples. The expansion cards were mounted in an electronics cabinet and hard-wired to a panel containing compensated Type-N thermocouple jacks.

To reduce electronic noise on the thermocouples, the ground leads from each thermocouple jack was connected to the electronic chassis ground of the thermocouple mutliplex extension cards. The vehicle chassis was connected to the electronic chassis ground by a large-gauge cable. The electronic chassis ground was connected to an isolated earth ground.

The data acquisition software (DASYLab, Daten System Technik GmbH, Mönchengladbach, Germany) was configured to sample each channel at a rate of 10 Hz and store the data in 10-point block averages.

Figures C1 through C9 show the approximate locations of thermocouples in the test vehicle. Plots C1 through C93 show plots of the temperature data recorded from these thermocouples during this test.

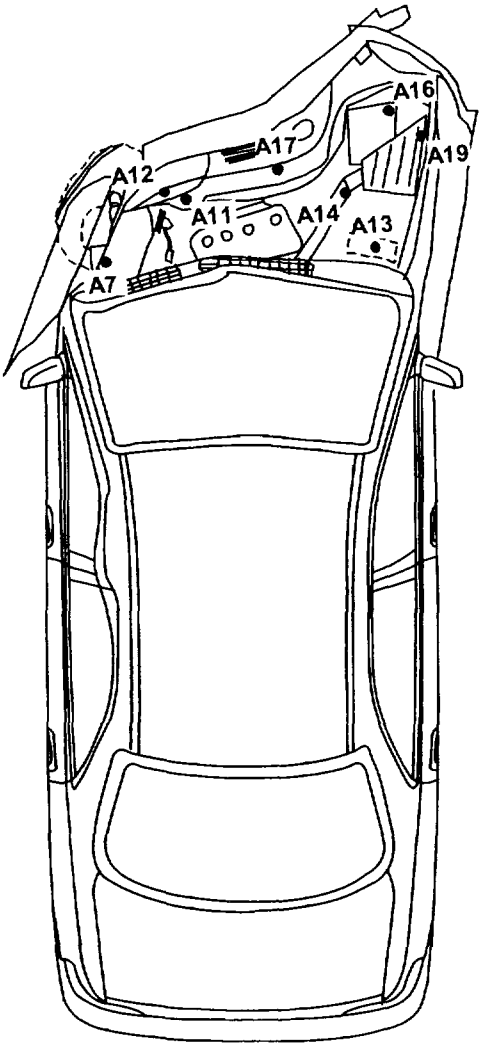

Figure C1. Fire Test F99030B. Diagram showing the approximate locations of thermocouples in the engine compartment of the test vehicle. Thermocouple A7 was located on the right front wheelhouse panel. Thermocouples A11 and A12 were located adjacent to the power steering fluid pump. Thermocouple A13 was located on the upper surface of the underhood fuse/relay box cover. Thermocouple A14 was located on the intake air tube. Thermocouple A16 was located on the battery. Thermocouple A17 was located on the radiator fan shroud. Thermocouple A19 was located on a piece of the air cleaner housing cover.

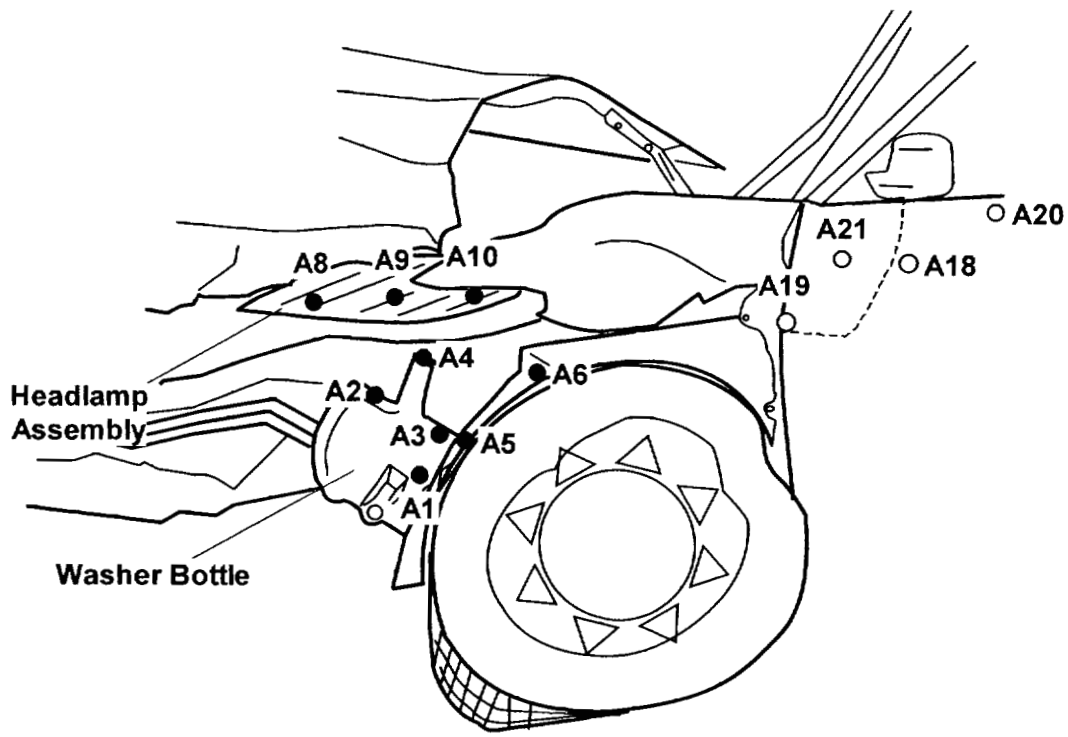

Figure C2. Fire Test F99030B. Diagram showing the approximate locations of thermocouples in the windshield washer fluid reservoir, right front wheelhouse panel, right headlamp assembly, and right front door of the test vehicle. Thermocouples A1, A2, A3, and A4 were located inside the windshield washer fluid reservoir. Thermocouples A5 and A6 were located on the right front wheelhouse panel. Thermocouples A8, A9, and A10 were located on the right headlamp lens. Thermocouples A18, A19, A20, and A21 were located inside the right front door.

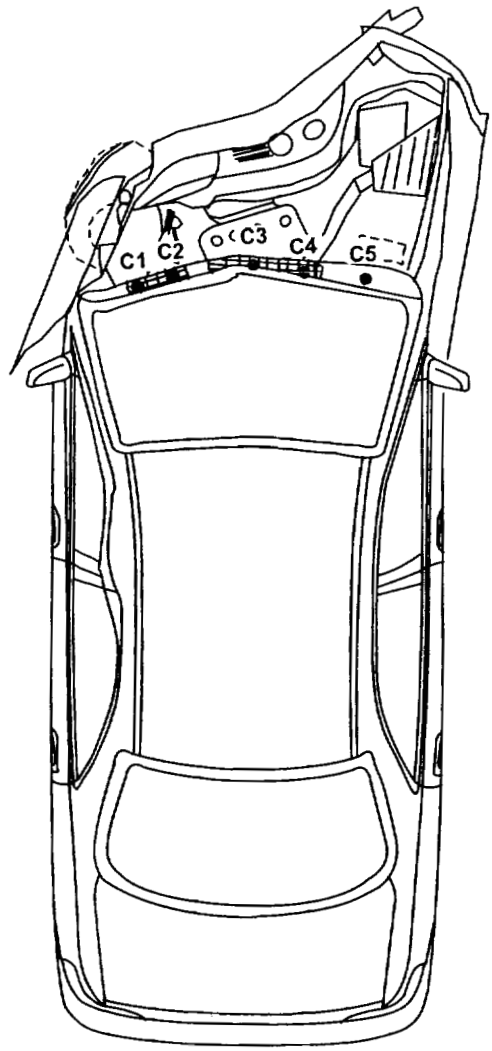

Figure C3. Fire Test F99030B. Diagram showing the approximate locations of thermocouples on the HVAC air intake cowl in the test vehicle. Thermocouples C1, C2, C3, C4, and C5 were located approximately 1 cm below the lower surface of the HVAC air intake cowl.

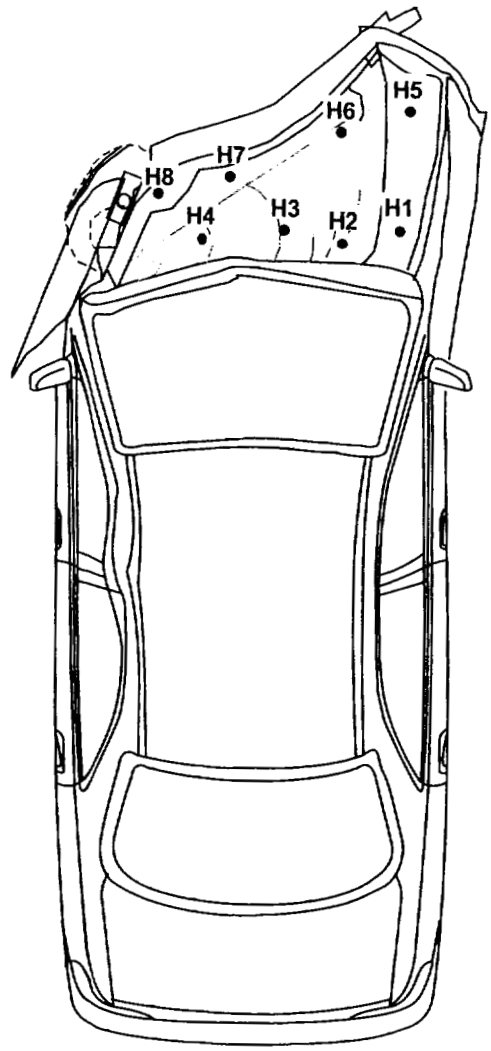

Figure C4. Fire Test F99030B. Diagram showing the approximate locations of thermocouples on the hood of the test vehicle. Thermocouples H1, H2, H3, H4, H5, H6, H7, and H8 were located approximately 1 cm below the lower surface of the hood insulator.

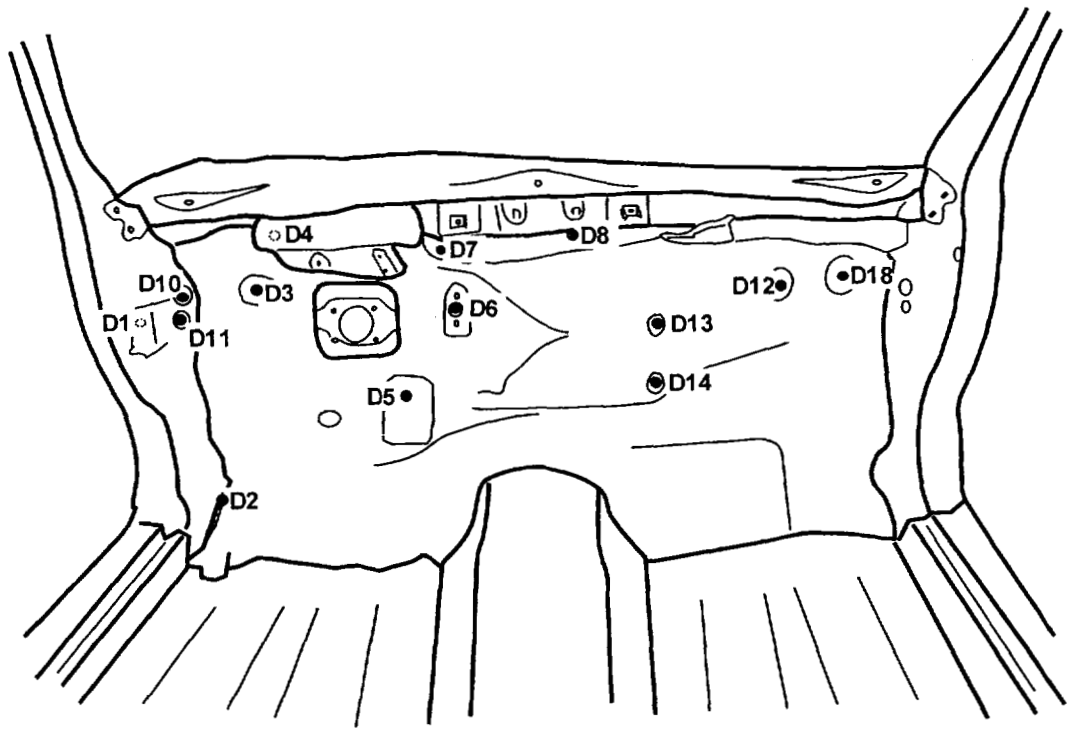

Figure C5. Fire Test F99030B. Diagram showing the approximate locations of thermocouples in the dash panel of the test vehicle. Thermocouple D1 was located inside the left A-pillar. Thermocouple D2 was located in a crash-induced seam opening between the floor panel and the inner rocker panel. Thermocouples D3, D12, and D18 were located on the interior surface of an electrical pass-through closure in the dash panel. Thermocouples D4, D7, and D8 were located in a crash-induced seam between the lower and upper dash panels. Thermocouple D5 was located in the steering column pass-through. Thermocouple D6 was located on the interior surface of the throttle linkage pass through closure. Thermocouples D10 and D11 were located on closures in the left A-Pillar. Thermocouples D13 and D14 were located in the heater hose pass-throughs.

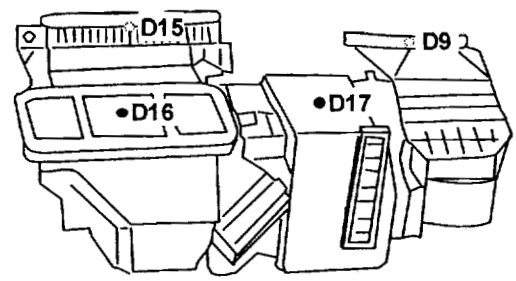

Figure C6. Fire Test F99030B. Diagram showing the approximate locations of thermocouples in the HVAV module and ducts of the test vehicle. Thermocouple D9 was located in the HVAC air intake lumen. Thermocouple D15 was located in the defroster duct limen. Thermocouple D16 was located in the air mixing duct. Thermocouple D17 was located on the upper evaporator housing.

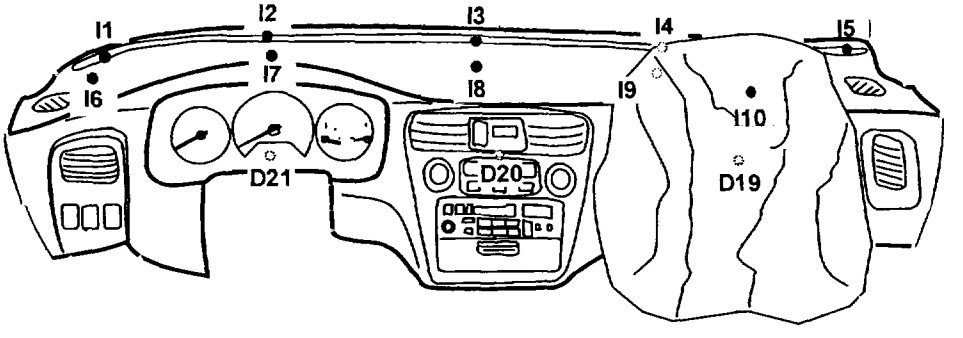

Figure C7. Fire Test F99030B. Diagram showing the approximate locations of thermocouples in the instrument panel of the test vehicle. Thermocouples I1, I2, I3, I4, and I5 were located along the forward edge of the instrument panel. Thermocouples I6, I7, I8, I9, and I10 were located along the approximate lateral centerline of the upper surface of the instrument panel. Thermocouple I10 was located on the surface of the deployed passenger airbag. Thermocouples D19, D20, and D21 were located in the instrument panel on the instrument panel cross member.

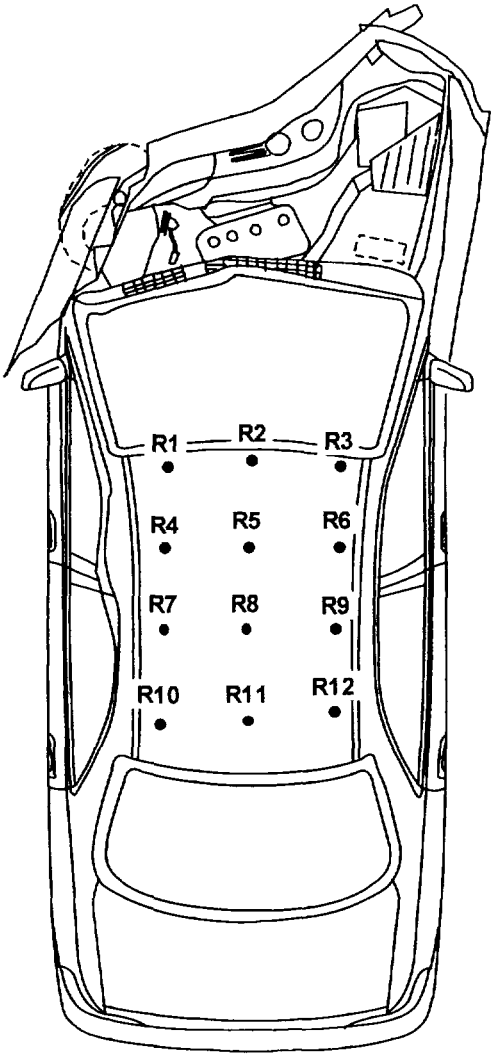

Figure C8. Fire Test F99030B. Diagram showing the approximate locations of thermocouples on the roof of the test vehicle. Thermocouples R1, R2, R3, R4, R5, R6, R7, R8, R9, R10, R11, and R12 were located approximately 1 cm below the lower surface of the roof trim panel.

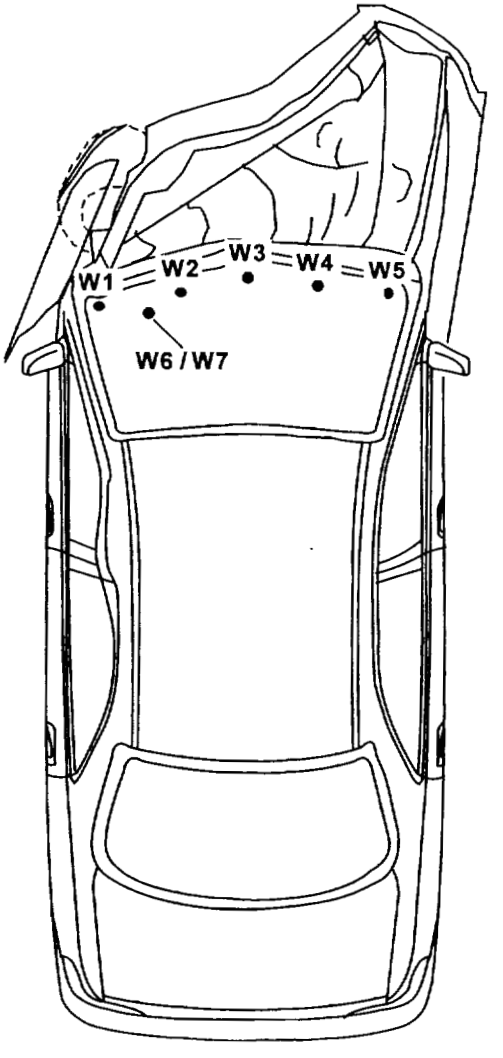

Figure C9. Fire Test F99030B. Diagram showing the approximate locations of thermocouples on the windshield of the test vehicle. Thermocouples W1, W2, W3, W4, and W5 were located approximately 1 cm forward of the exterior glass outer layer in the windshield. Thermocouple W6 was attached to the exterior glass outer layer with thermally conducting cement. Thermocouple A7 was attached to the interior glass outer layer with thermally conducing cement.

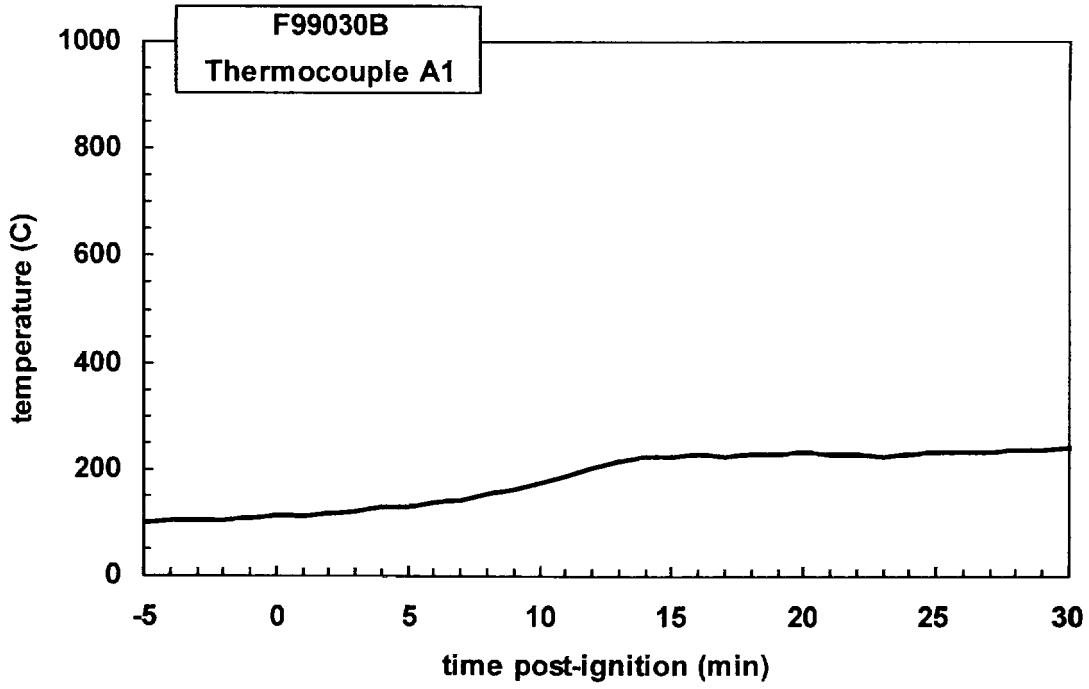

Plot C1. Fire Test F99030B. Data plot from thermocouple A 1.

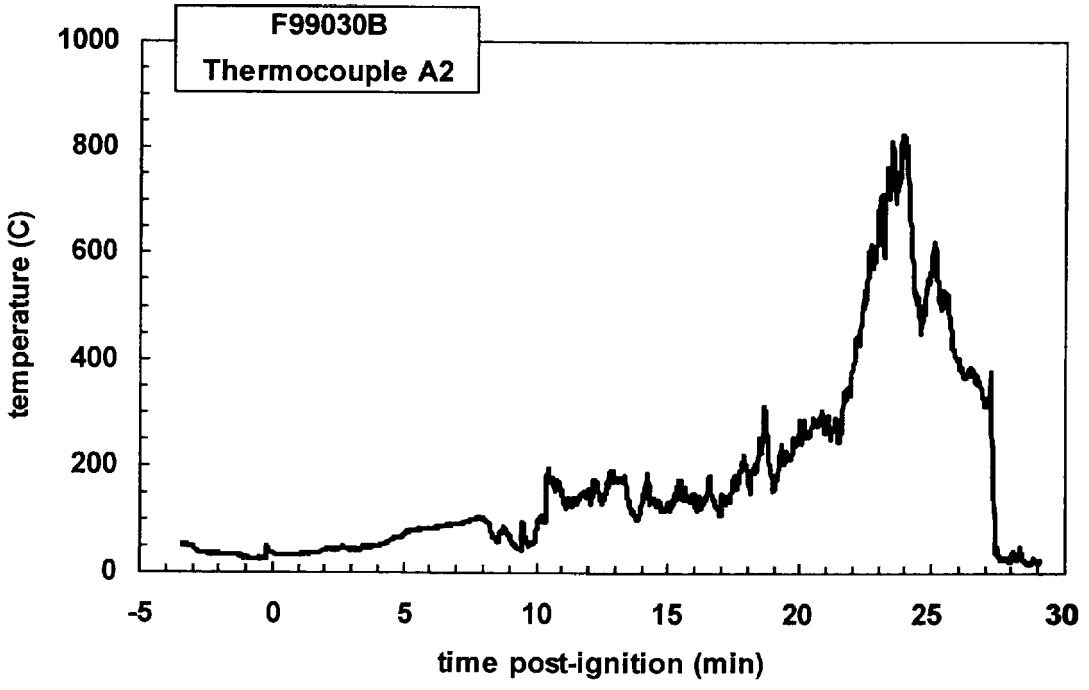

Plot C2. Fire Test F99030B. Data plot from thermocouple A 2.

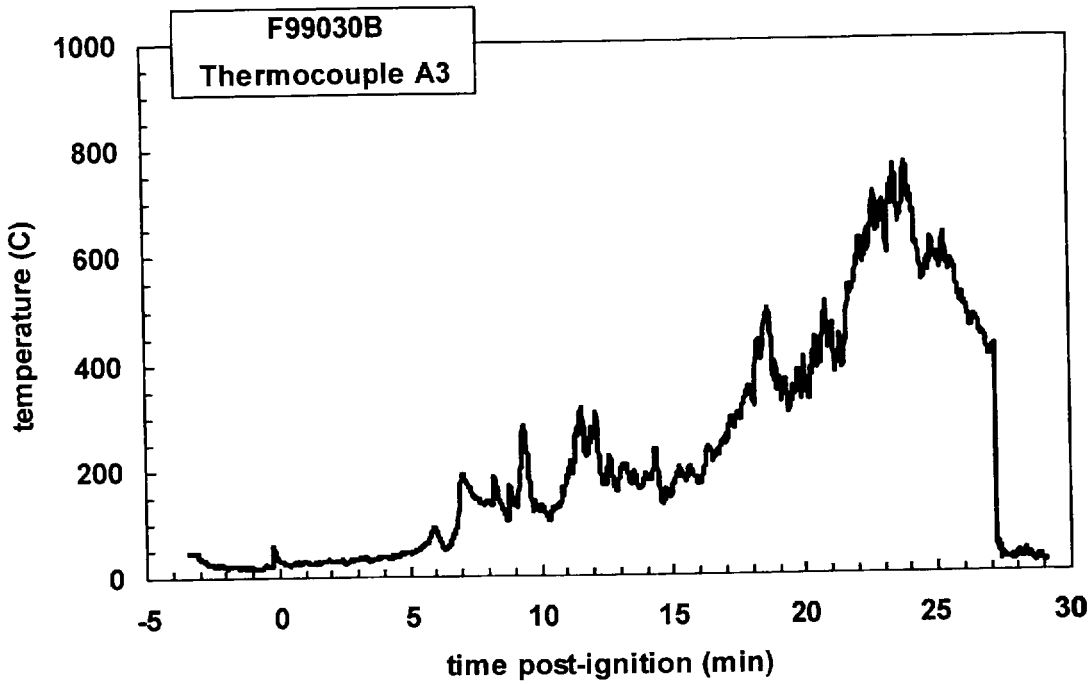

Plot C3. Fire Test F99030B. Data plot from thermocouple A 3.

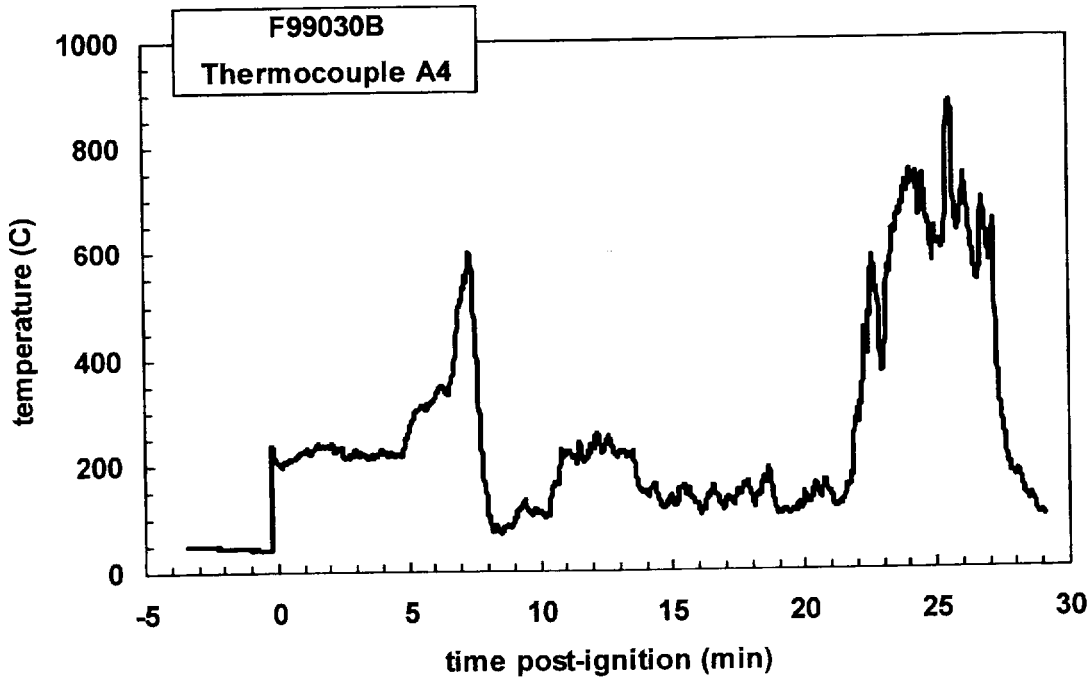

Plot C4. Fire Test F99030B. Data plot from thermocouple A 4.

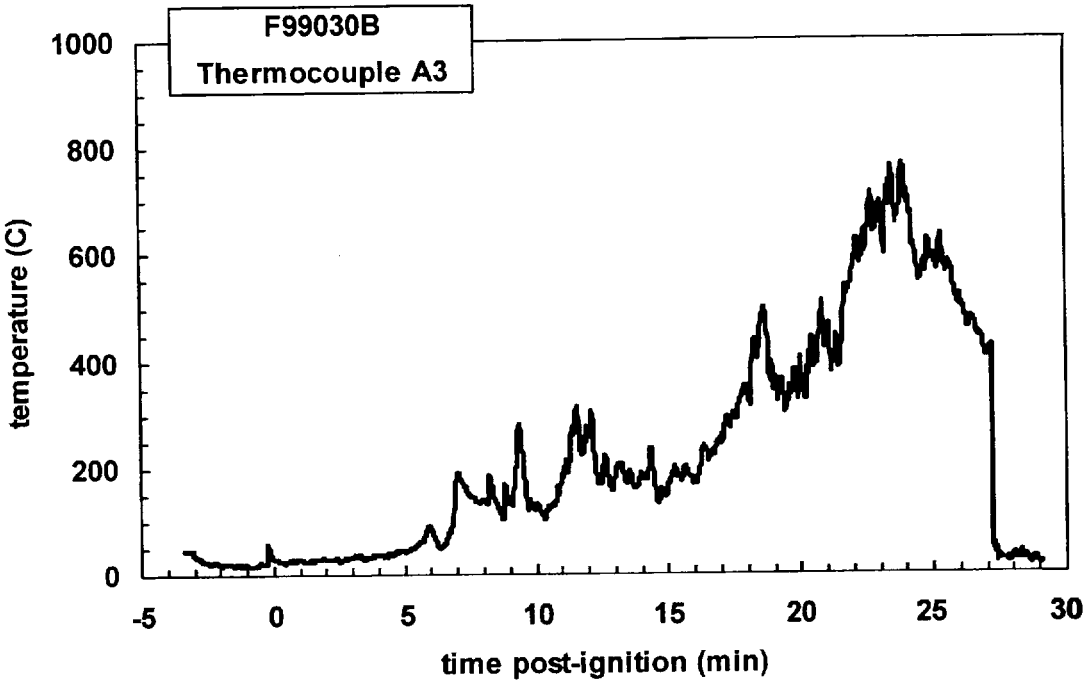

Plot C3. Fire Test F99030B. Data plot from thermocouple A 3.

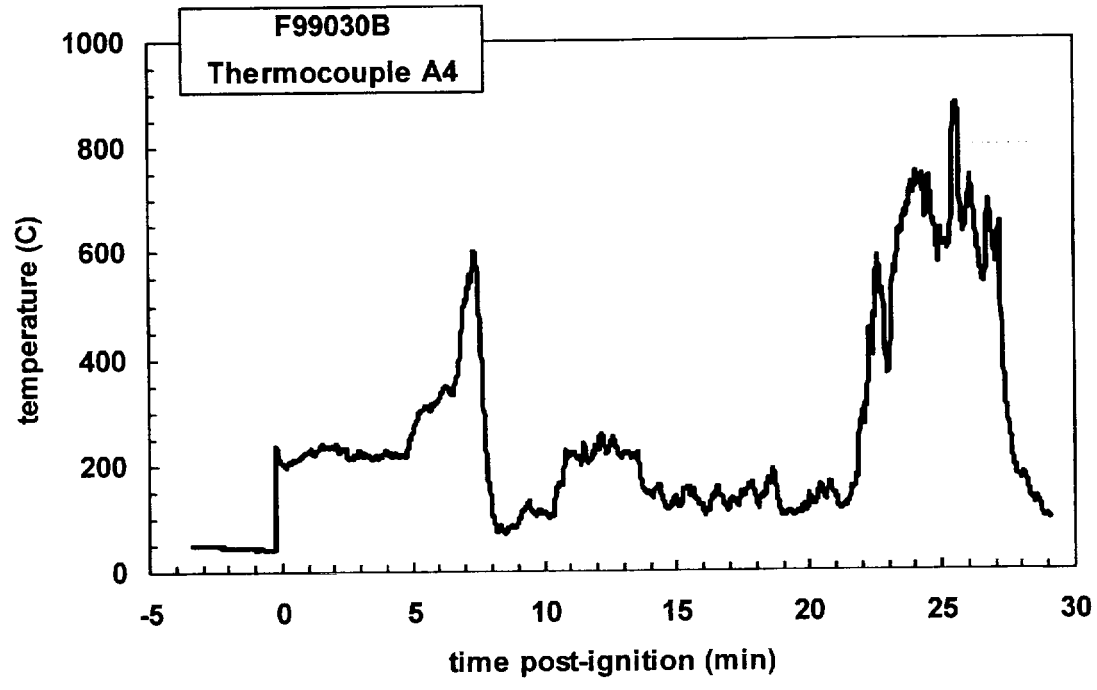

Plot C4. Fire Test F99030B. Data plot from thermocouple A 4.

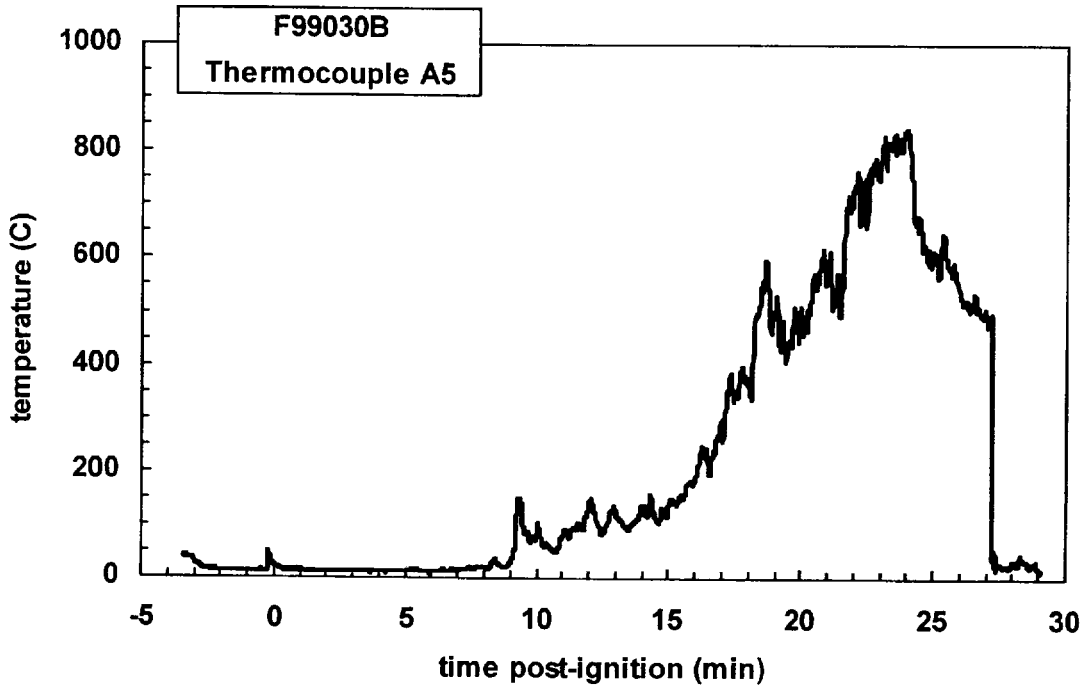

Plot C5. Fire Test F99030B. Data plot from thermocouple A 5.

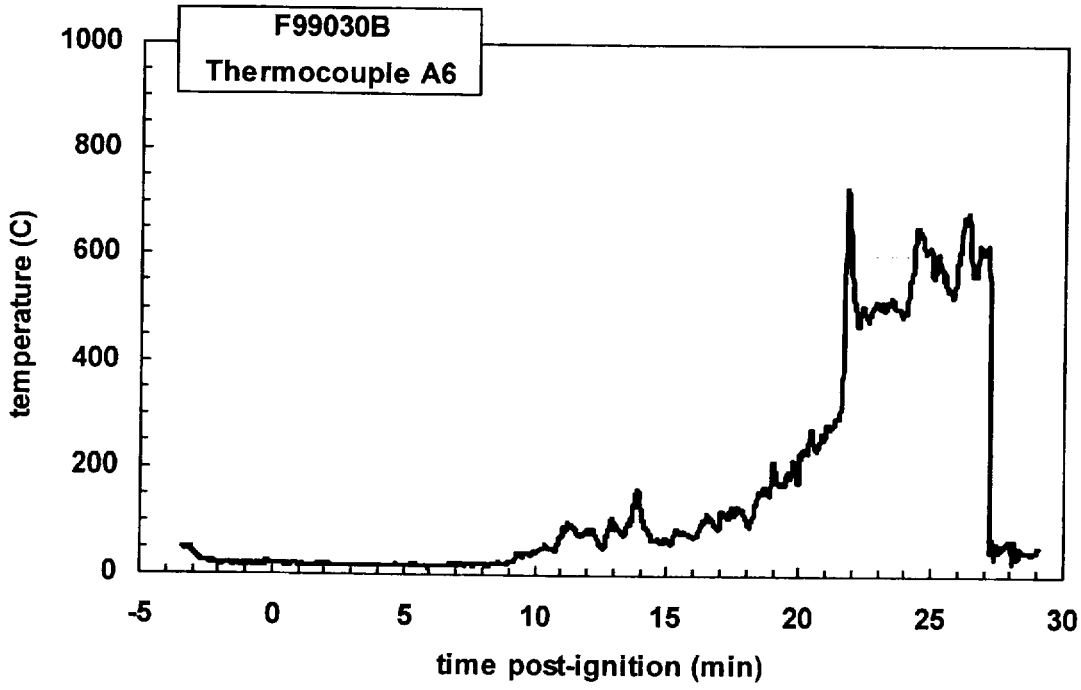

Plot C6. Fire Test F99030B. Data plot from thermocouple A 6.

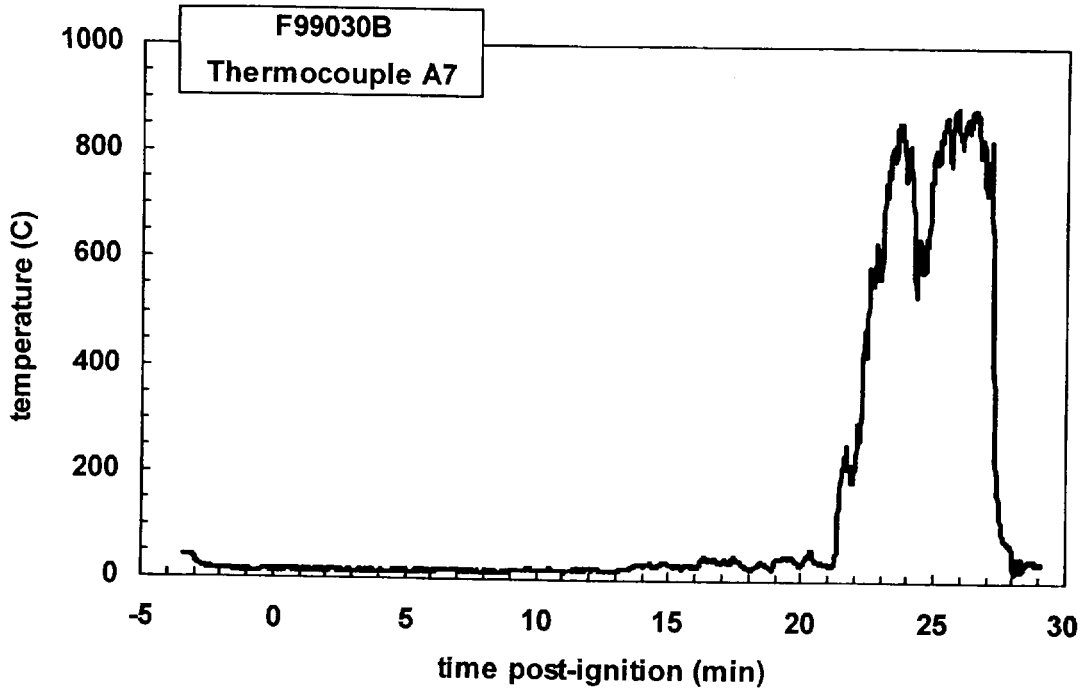

Plot C7. Fire Test F99030B. Data plot from thermocouple A 7.

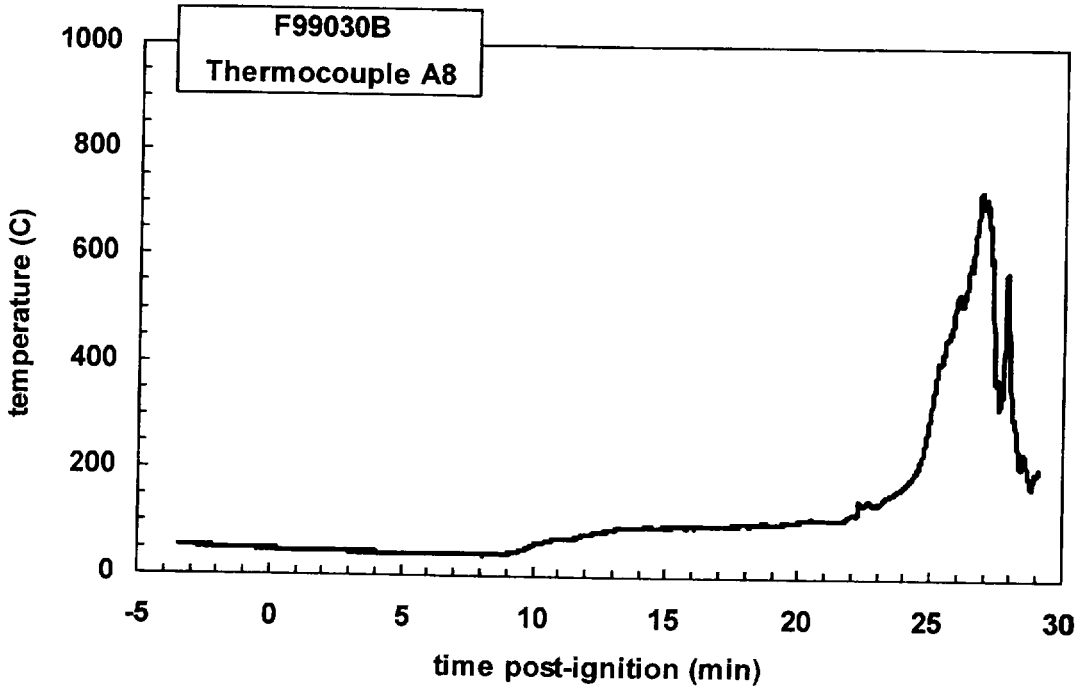

Plot C8. Fire Test F99030B. Data plot from thermocouple A 8.

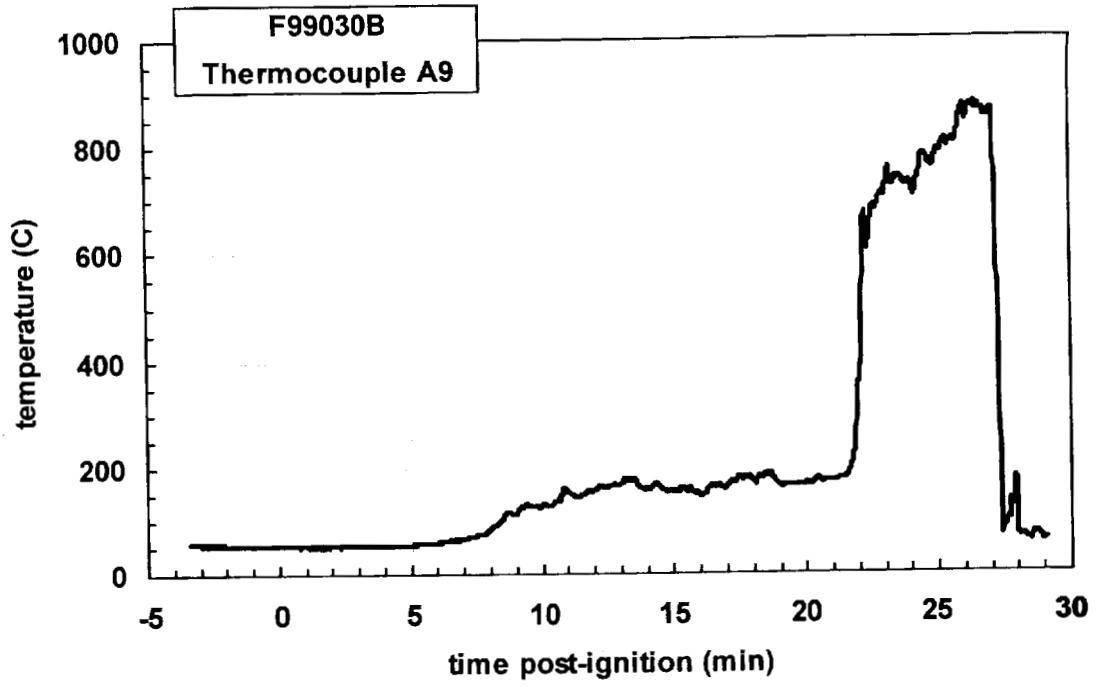

Plot C9. Fire Test F99030B. Data plot from thermocouple A 9.

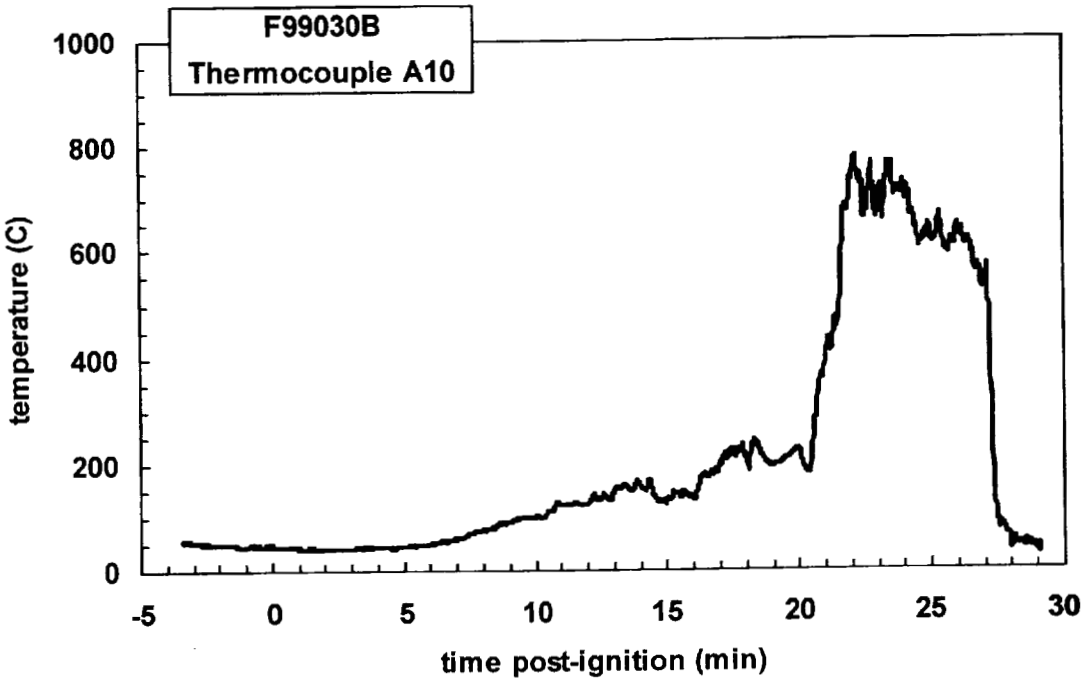

Plot C10. Fire Test F99030B. Data plot from thermocouple A10.

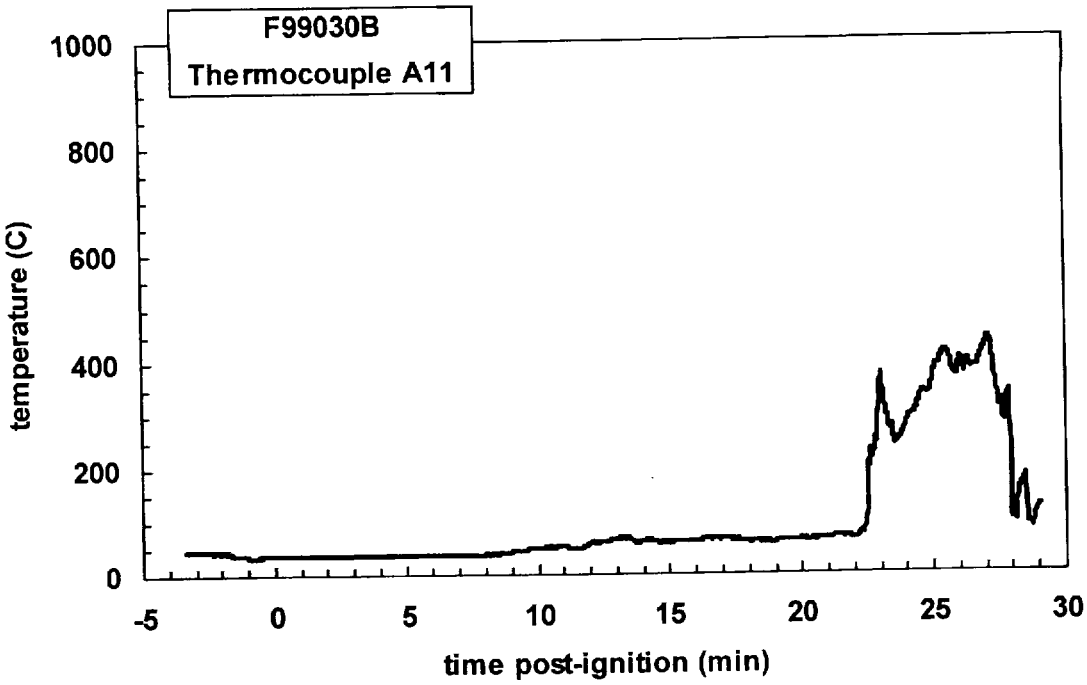

Plot C11. Fire Test F99030B. Data plot from thermocouple A11.

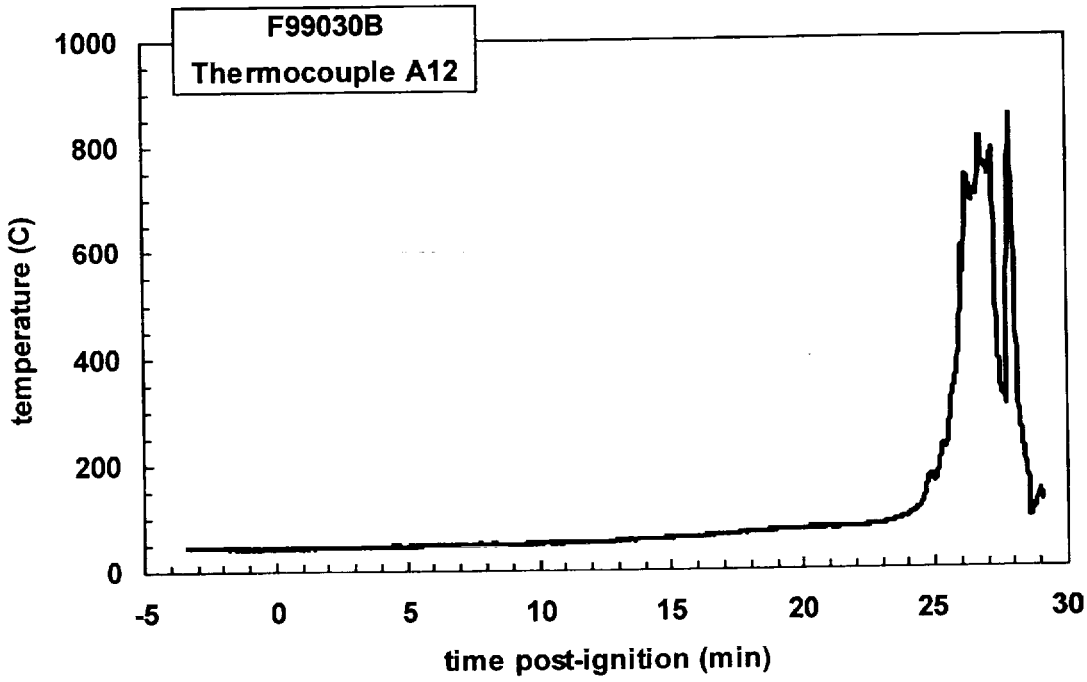

Plot C12. Fire Test F99030B. Data plot from thermocouple A12.

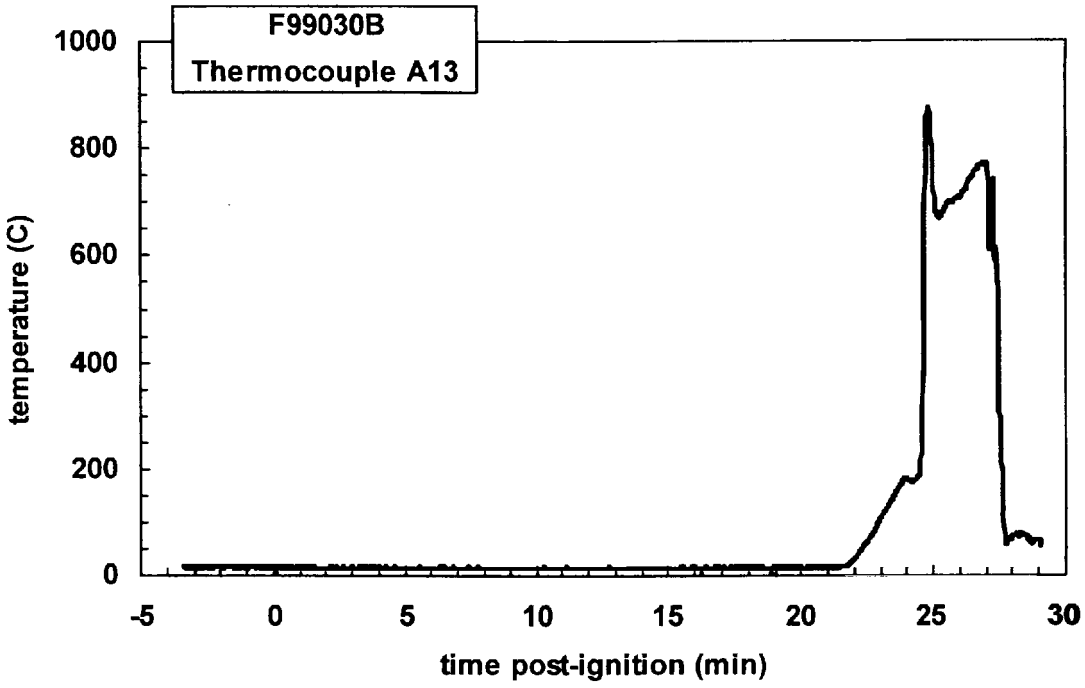

Plot C13. Fire Test F99030B. Data plot from thermocouple A13.

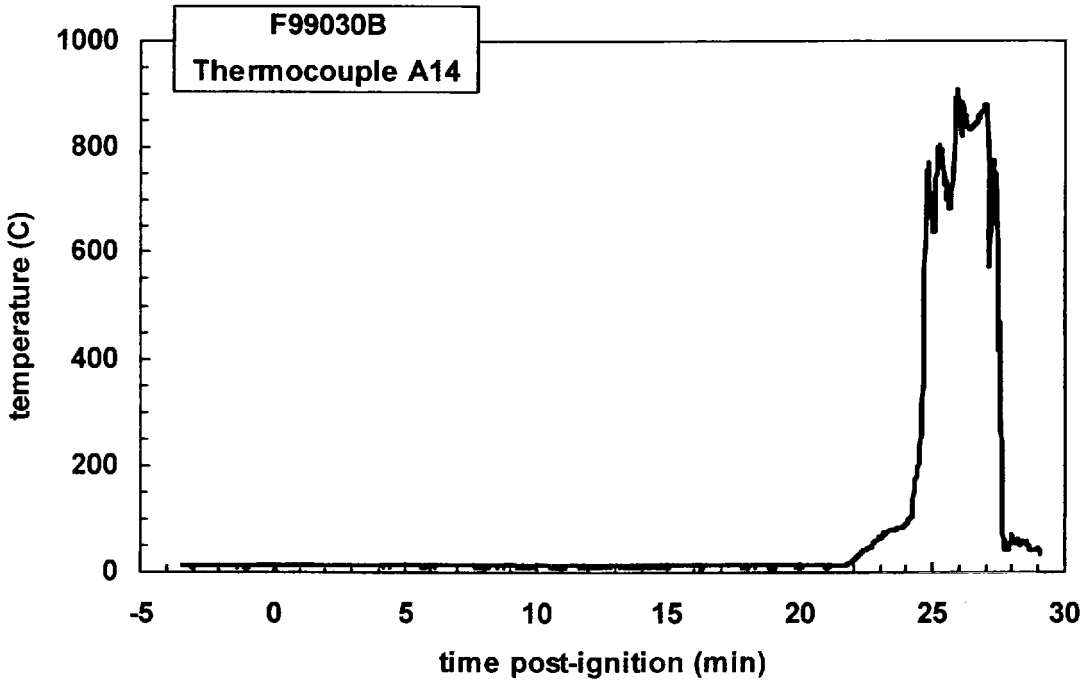

Plot C14. Fire Test F99030B. Data plot from thermocouple A14.

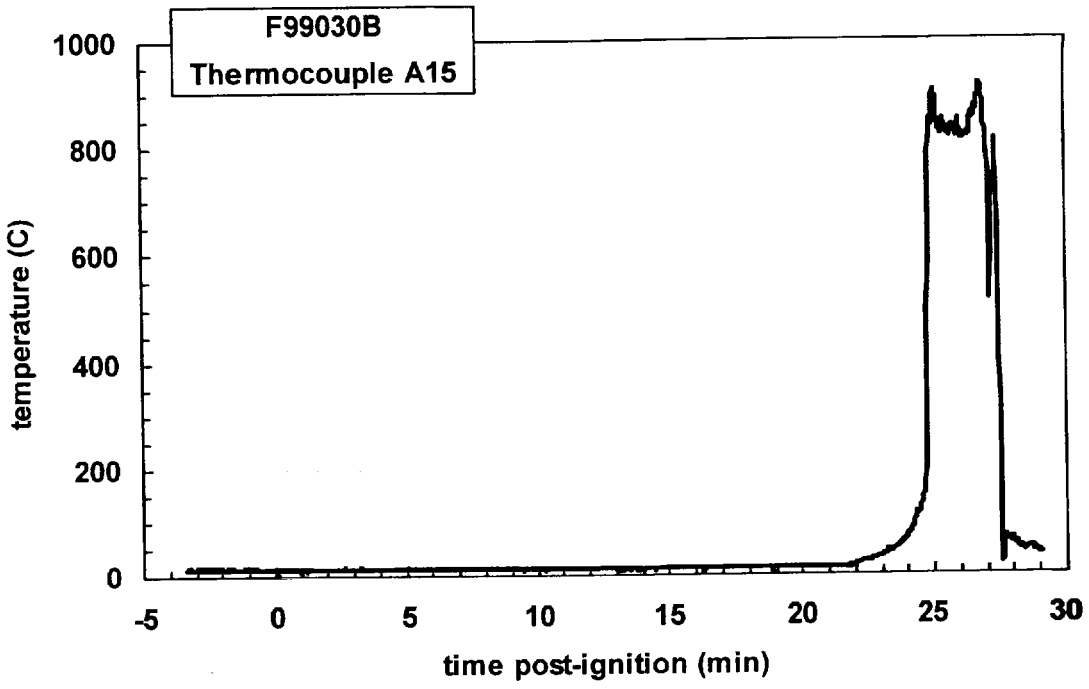

Plot C15. Fire Test F99030B. Data plot from thermocouple A15.

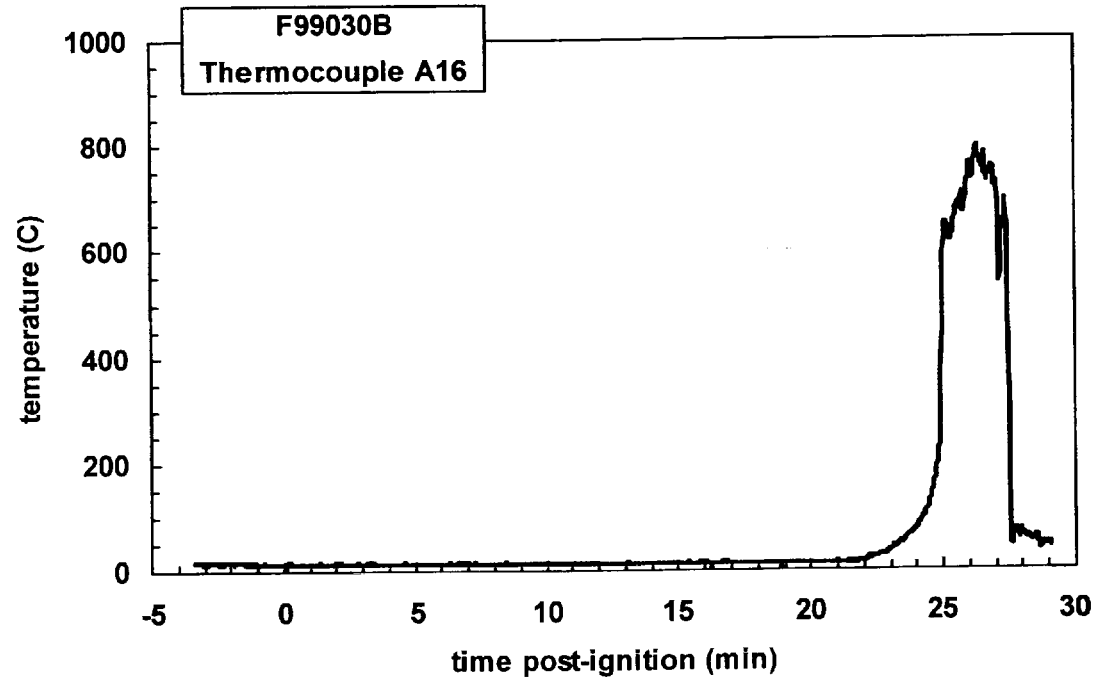

Plot C16. Fire Test F99030B. Data plot from thermocouple A16.

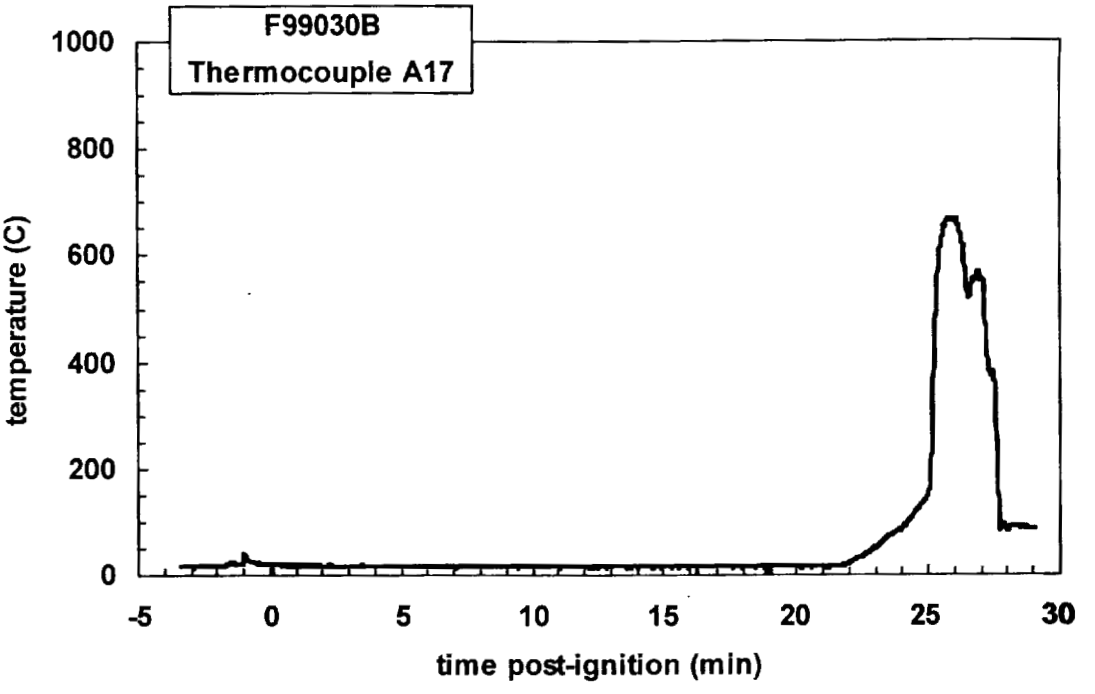

Plot C17. Fire Test F99030B. Data plot from thermocouple A17.

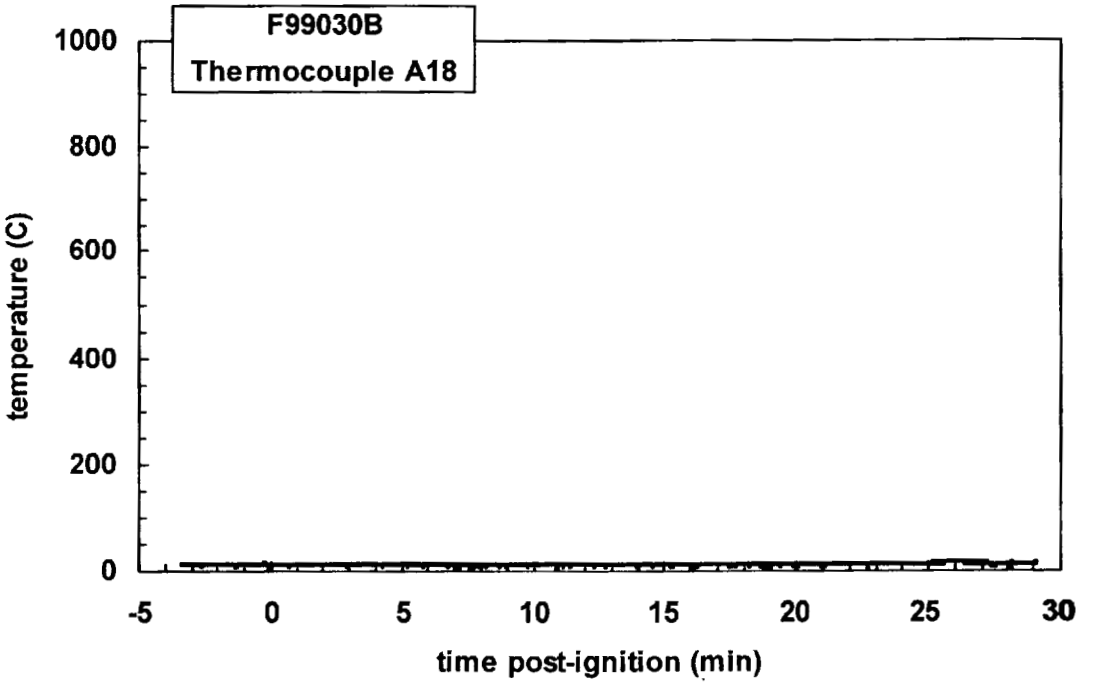

Plot C18. Fire Test F99030B. Data plot from thermocouple A18.

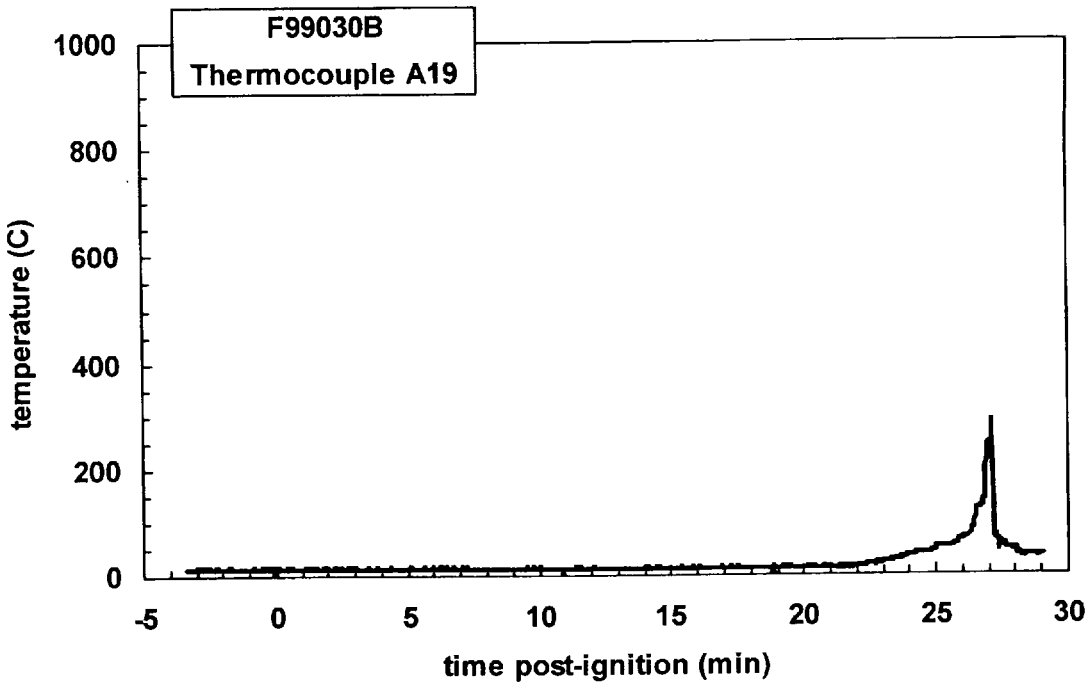

Plot C19. Fire Test F99030B. Data plot from thermocouple A19.

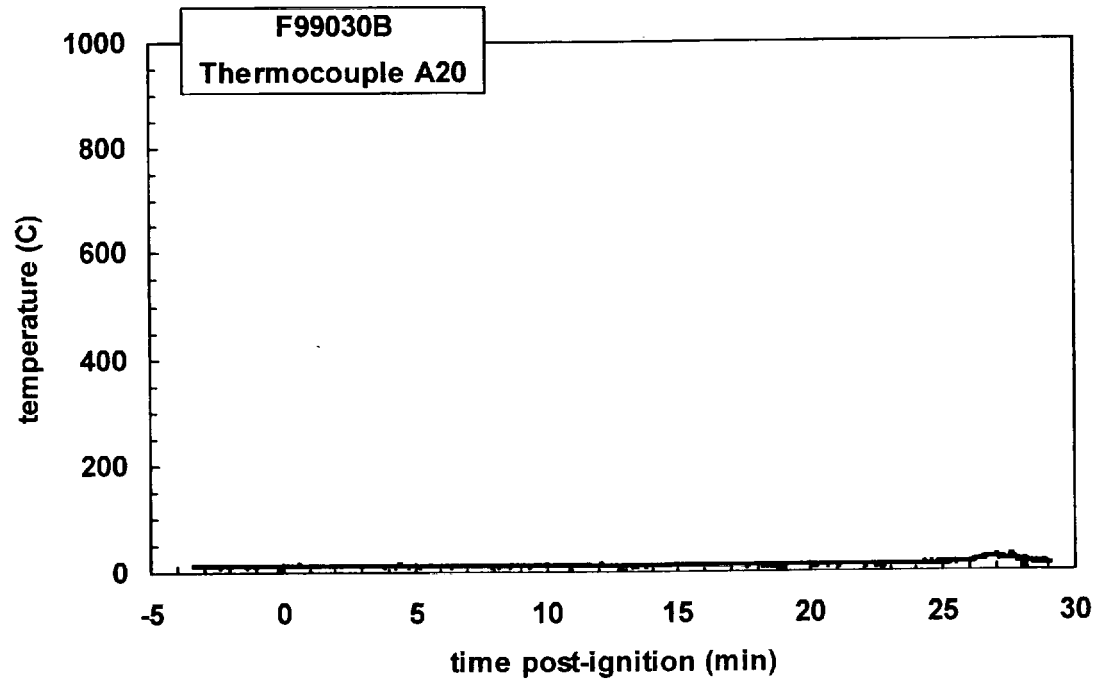

Plot C20. Fire Test F99030B. Data plot from thermocouple A 20.

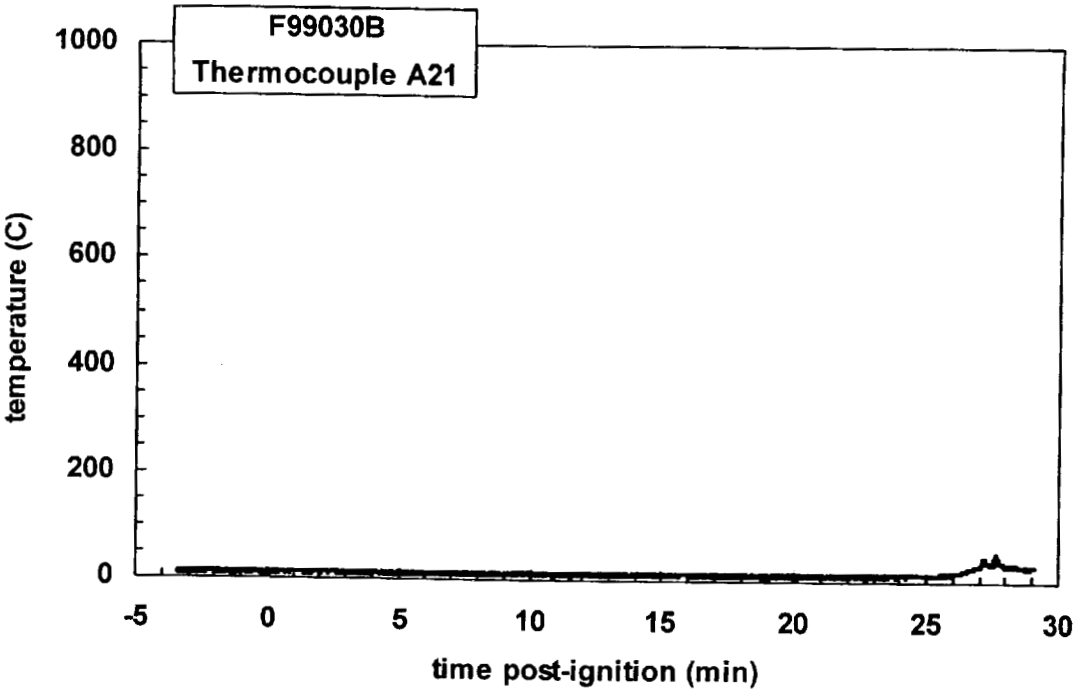

Plot C21. Fire Test F99030B. Data plot from thermocouple A21.

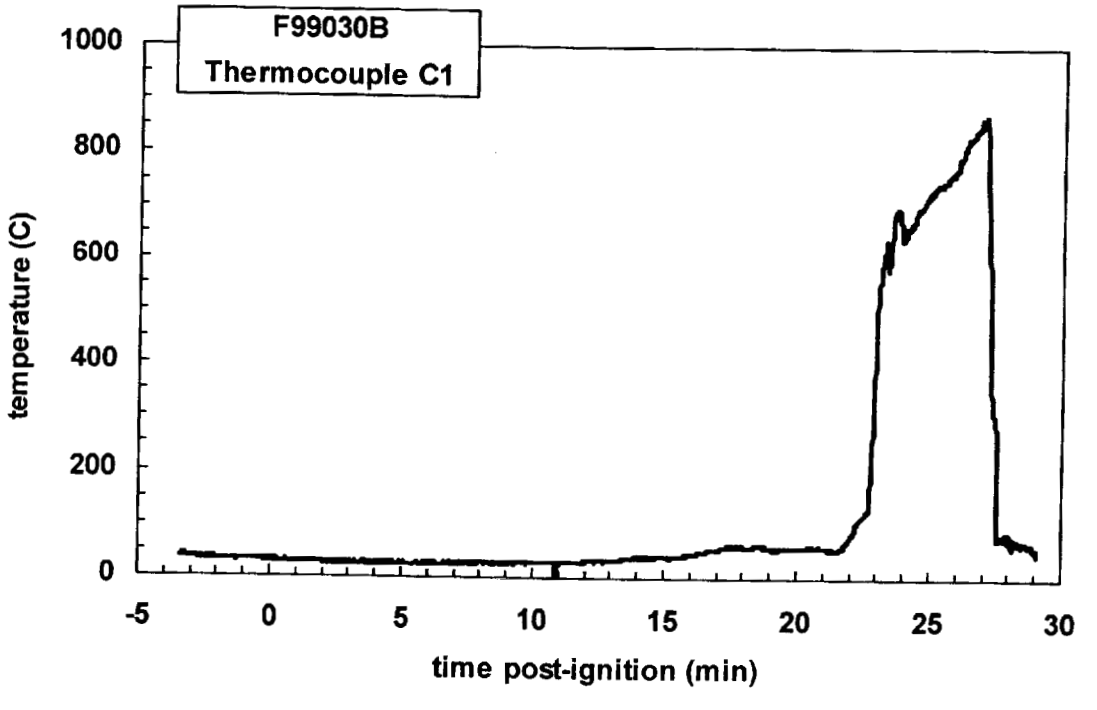

Plot C22. Fire Test F99030B. Data plot from thermocouple C1.

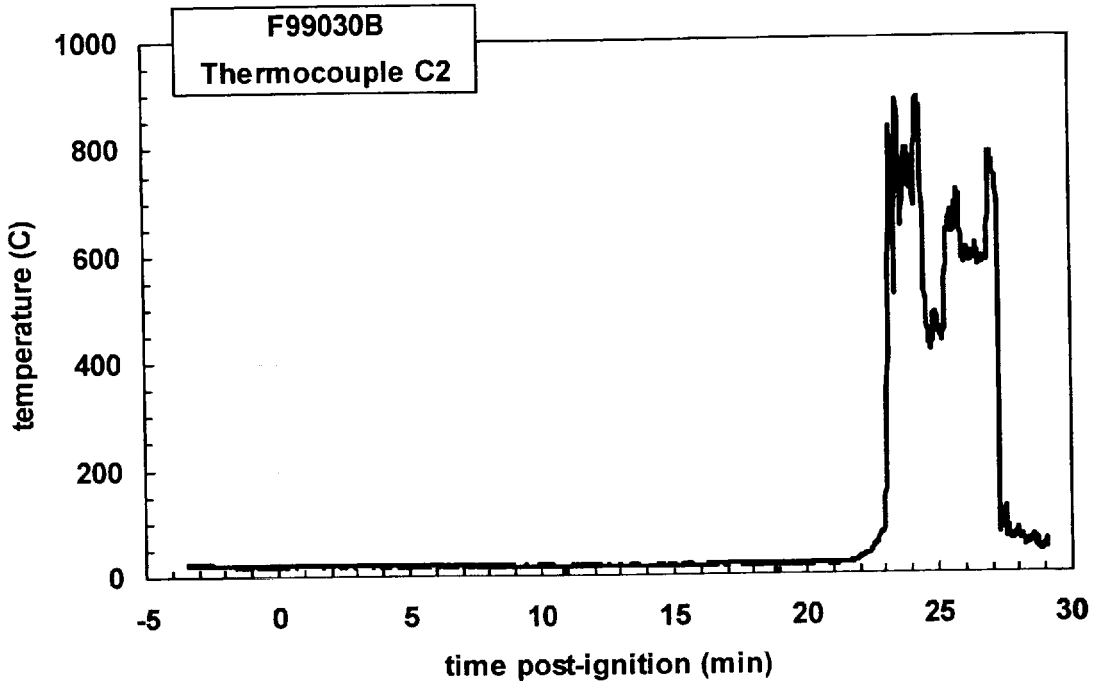

Plot C23. Fire Test F99030B. Data plot from thermocouple C2.

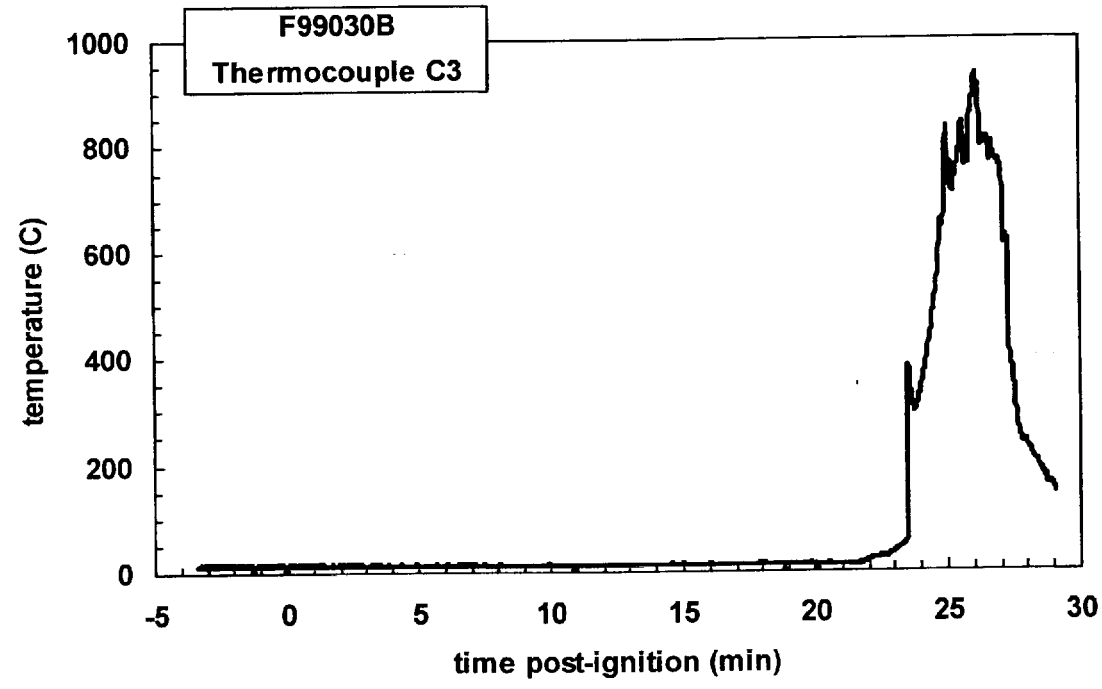

Plot C24. Fire Test F99030B. Data plot from thermocouple C3.

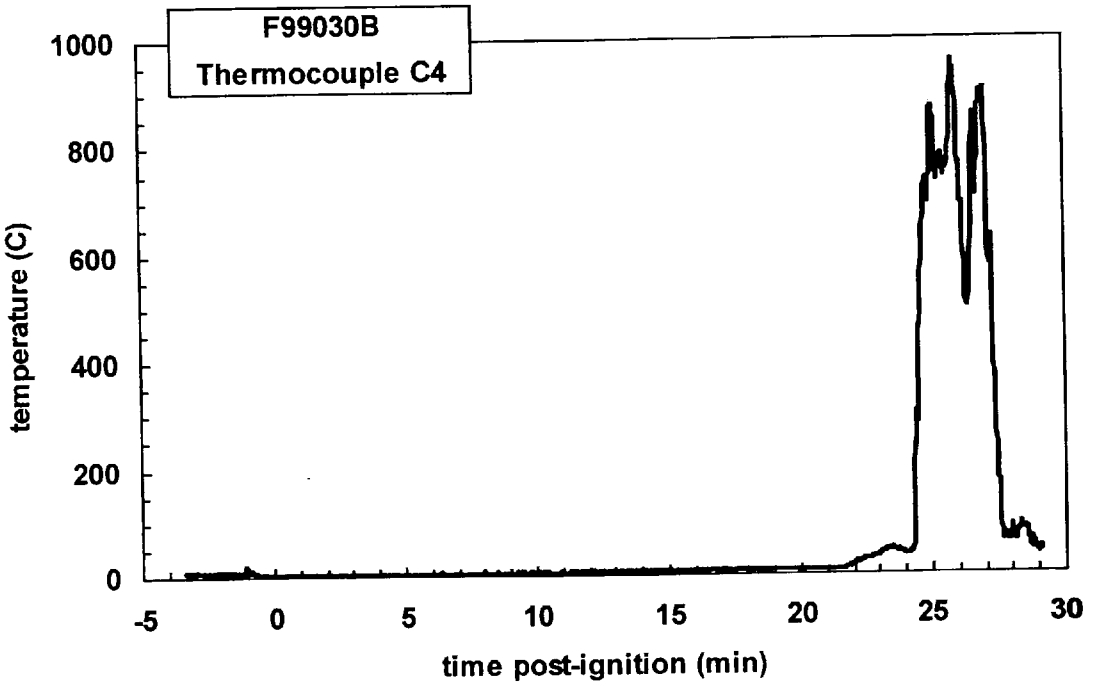

Plot C25. Fire Test F99030B. Data plot from thermocouple C4.

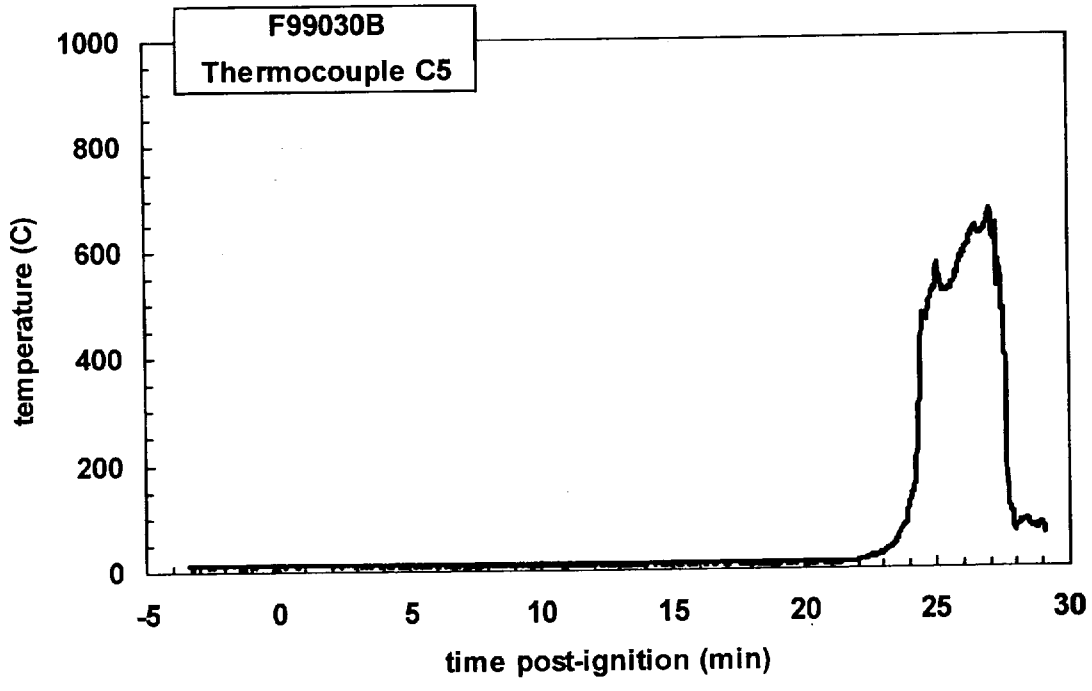

Plot C26. Fire Test F99030B. Data plot from thermocouple C5.

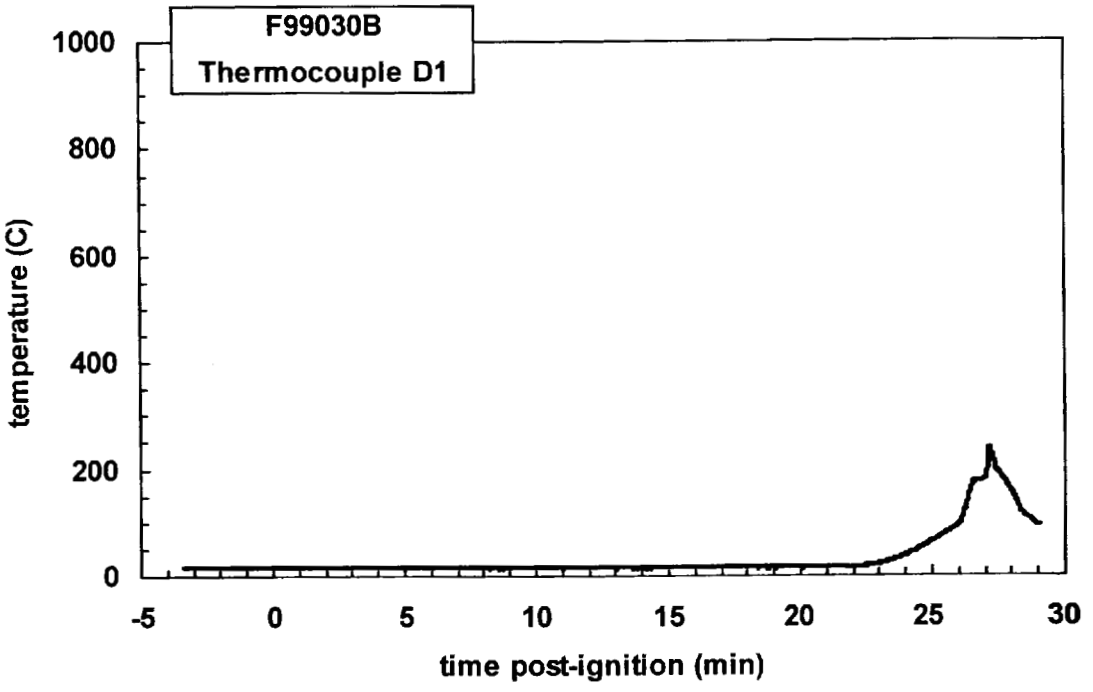

Plot C27. Fire Test F99030B. Data plot from thermocouple D1.

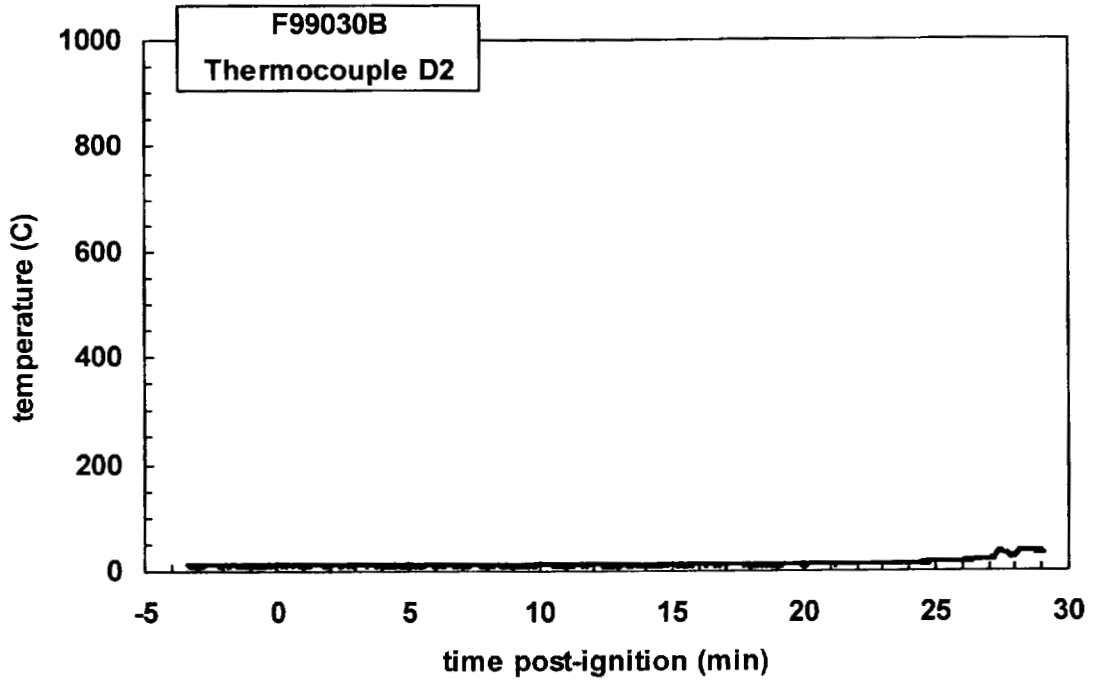

Plot C28. Fire Test F99030B. Data plot from thermocouple D2.

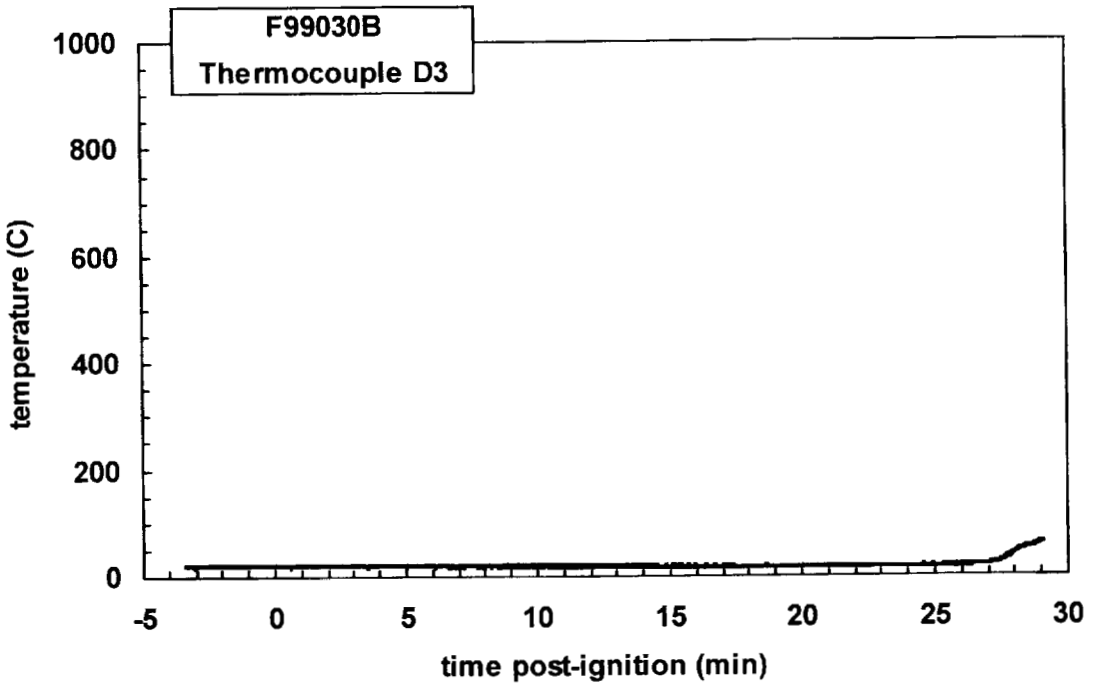

Plot C29. Fire Test F99030B. Data plot from thermocouple D3.

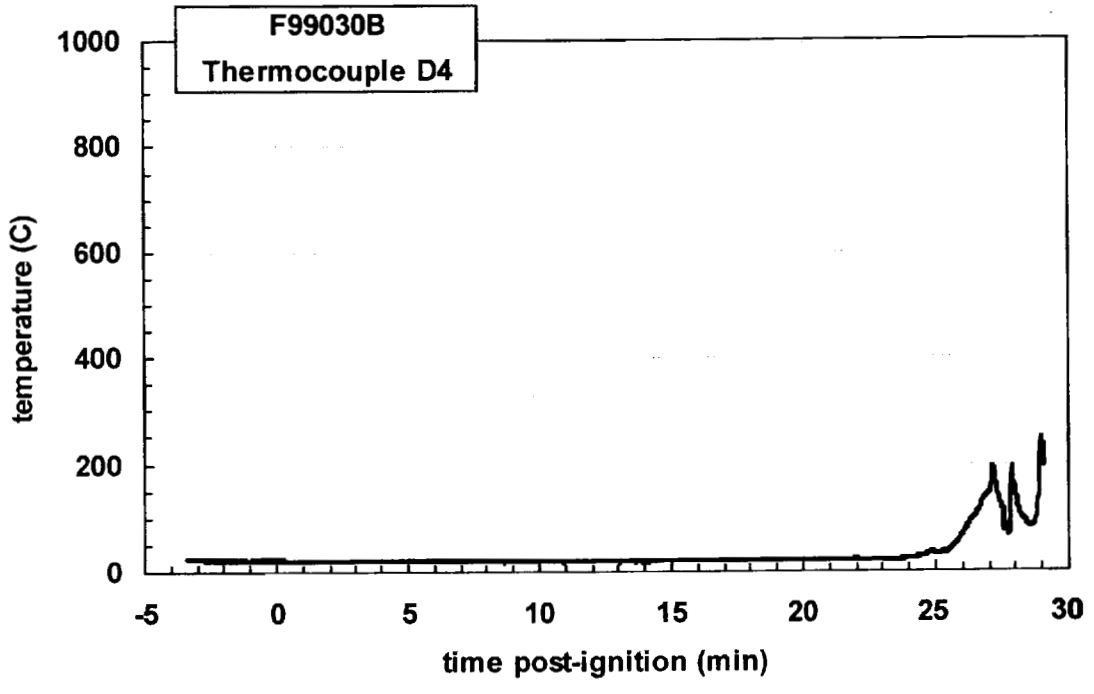

Plot C30. Fire Test F99030B. Data plot from thermocouple D4.

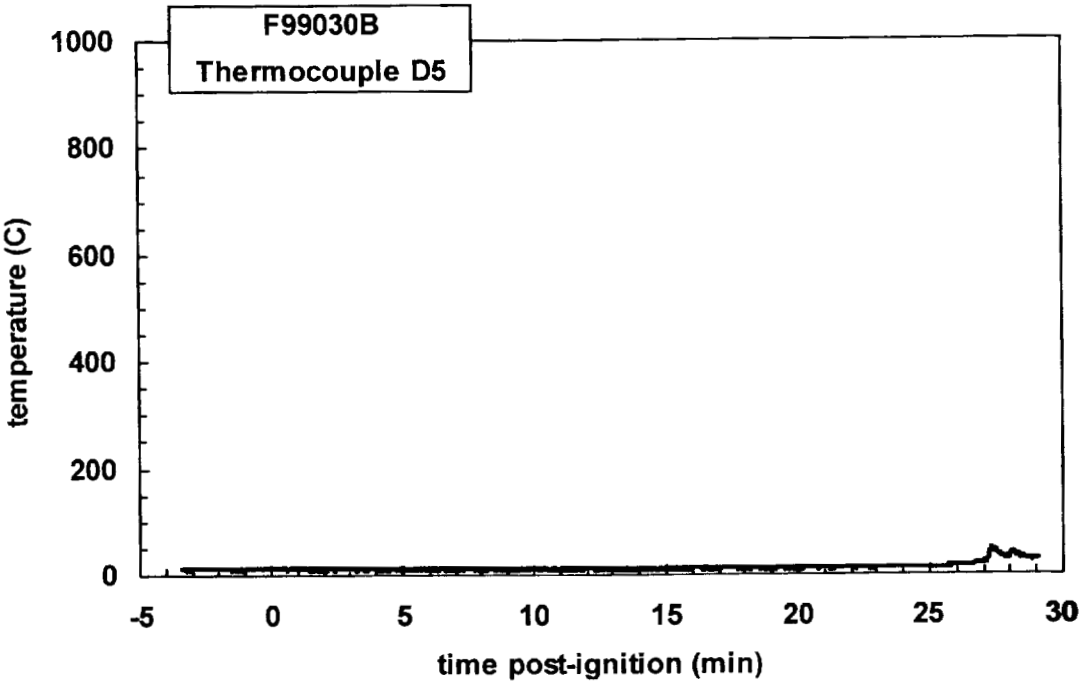

Plot C31. Fire Test F99030B. Data plot from thermocouple D5.

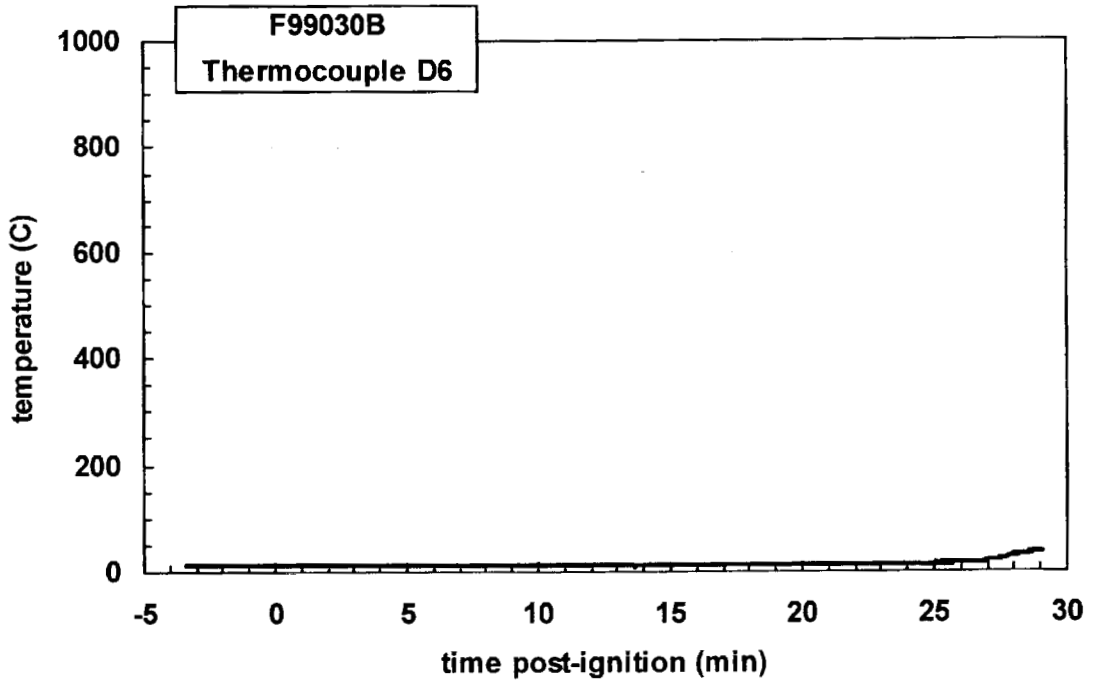

Plot C32. Fire Test F99030B. Data plot from thermocouple D6.

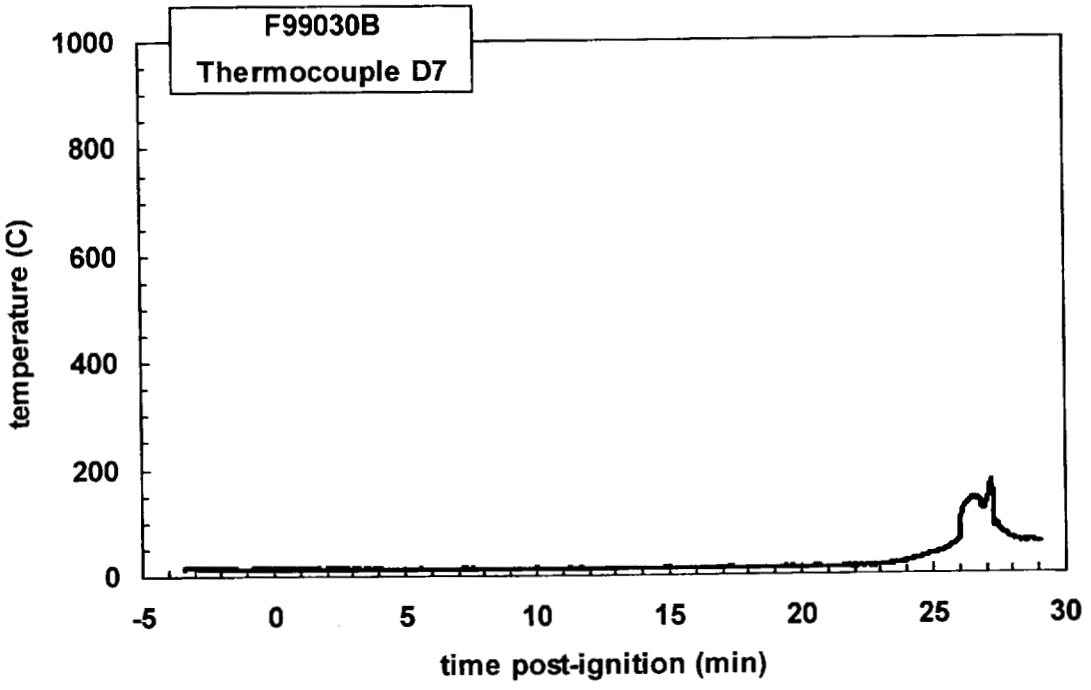

Plot C33. Fire Test F99030B. Data plot from thermocouple D7.

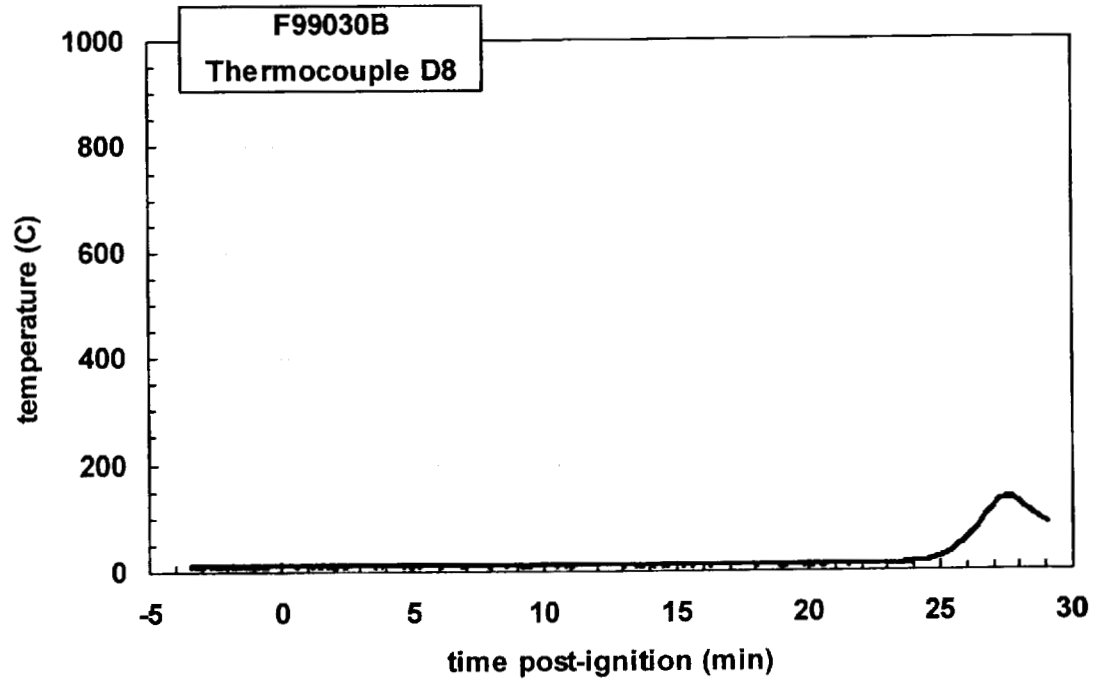

Plot C34. Fire Test F99030B. Data plot from thermocouple D8.

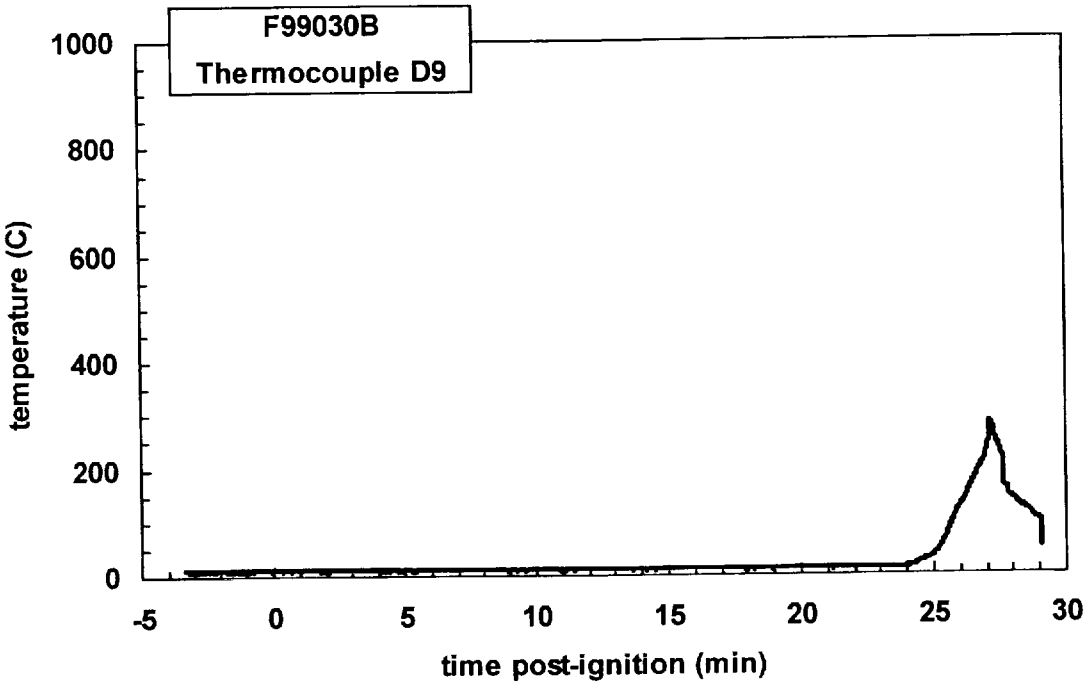

Plot C35. Fire Test F99030B. Data plot from thermocouple D9.

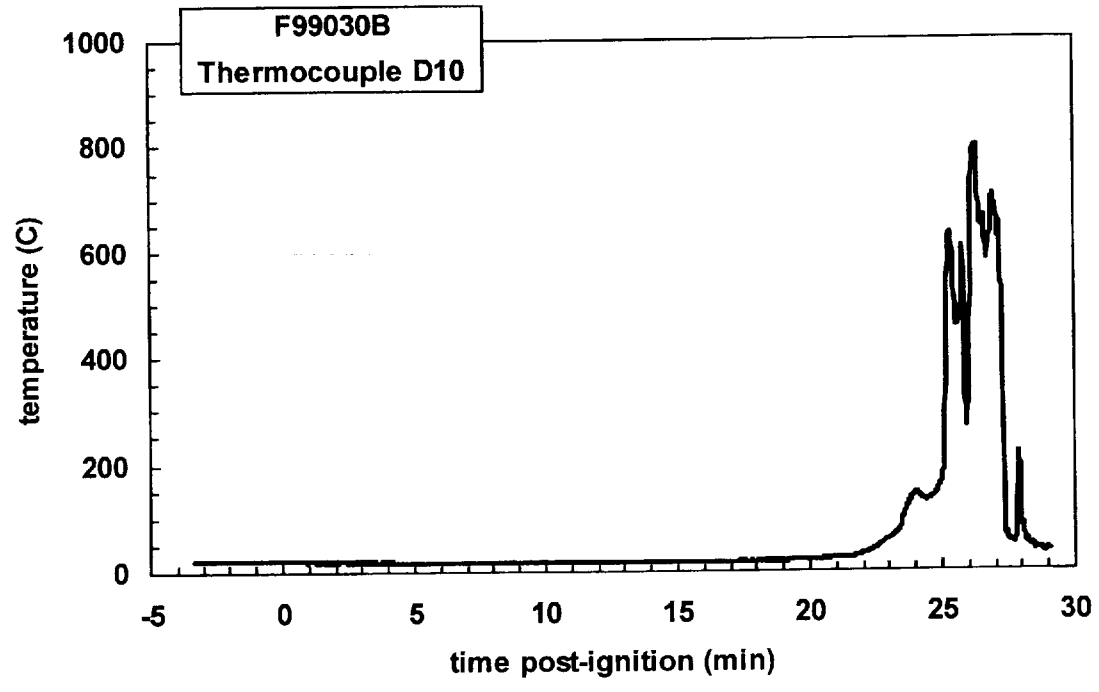

Plot C36. Fire Test F99030B. Data plot from thermocouple D10.

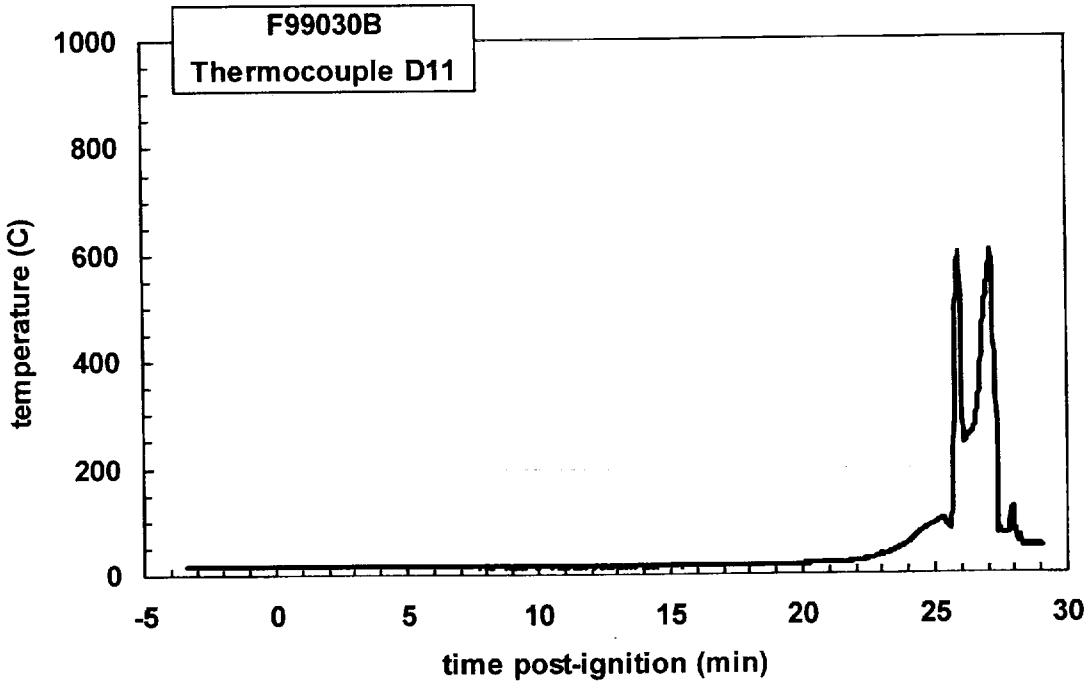

Plot C37. Fire Test F99030B. Data plot from thermocouple D11.

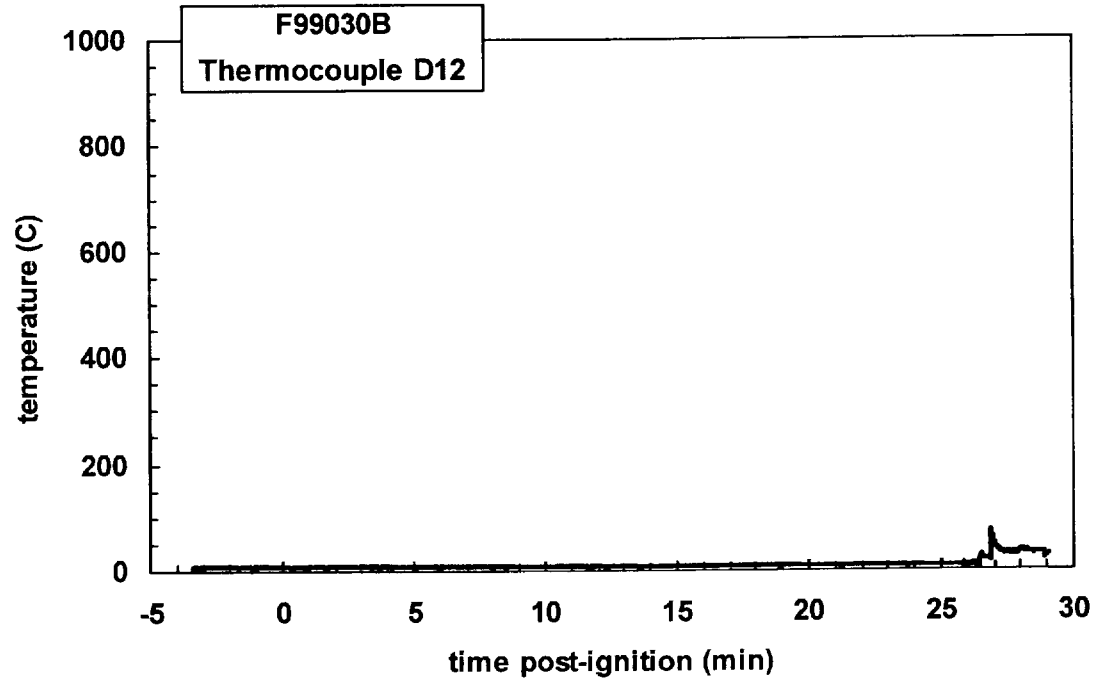

Plot C38. Fire Test F99030B. Data plot from thermocouple D12.

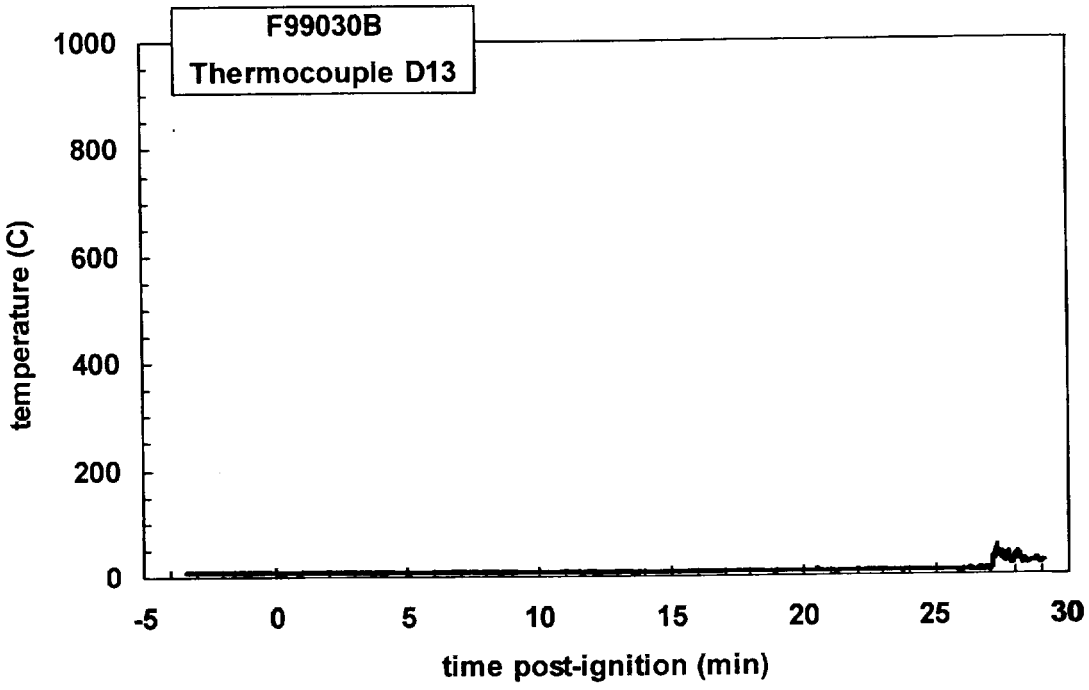

Plot C39. Fire Test F99030B. Data plot from thermocouple D13.

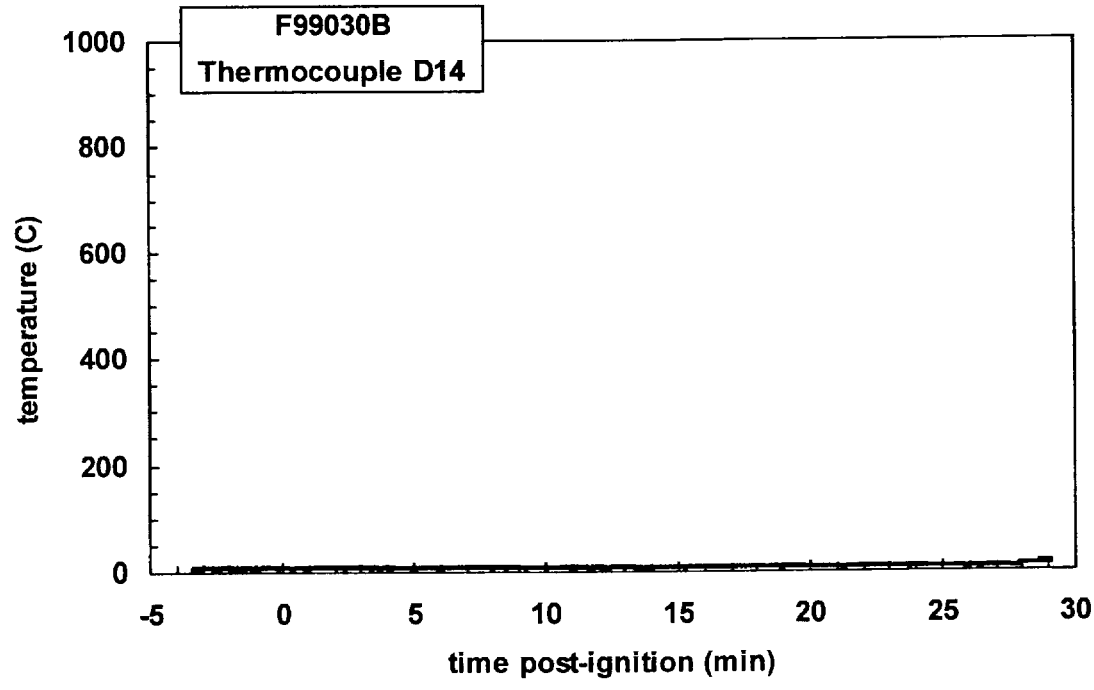

Plot C40. Fire Test F99030B. Data plot from thermocouple D14.

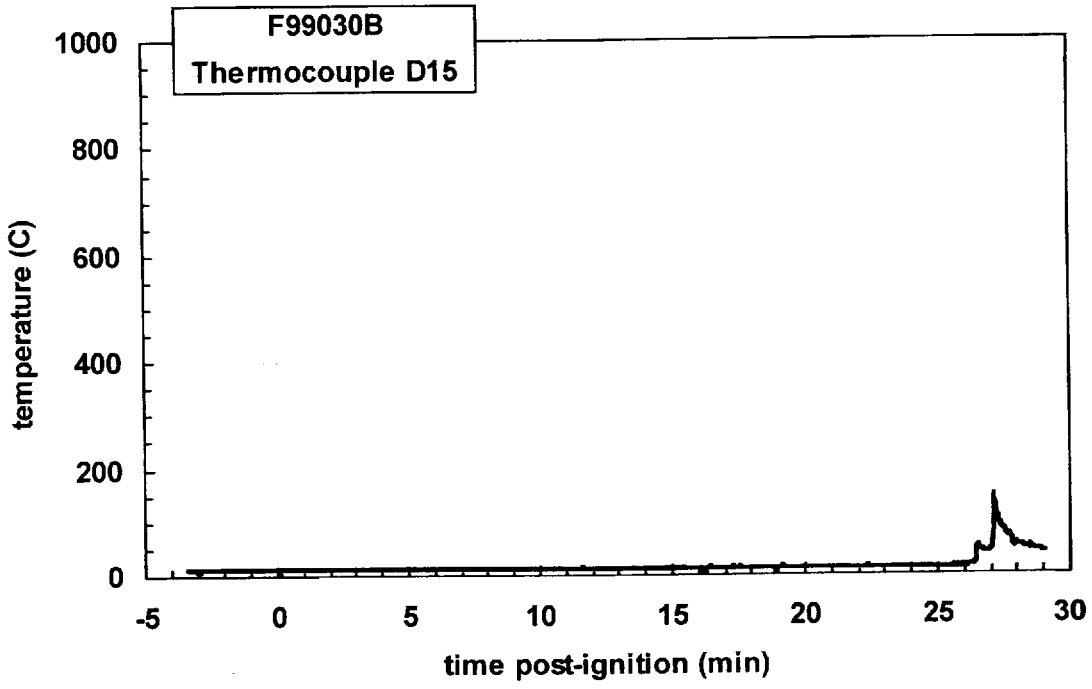

Plot C41. Fire Test F99030B. Data plot from thermocouple D15.

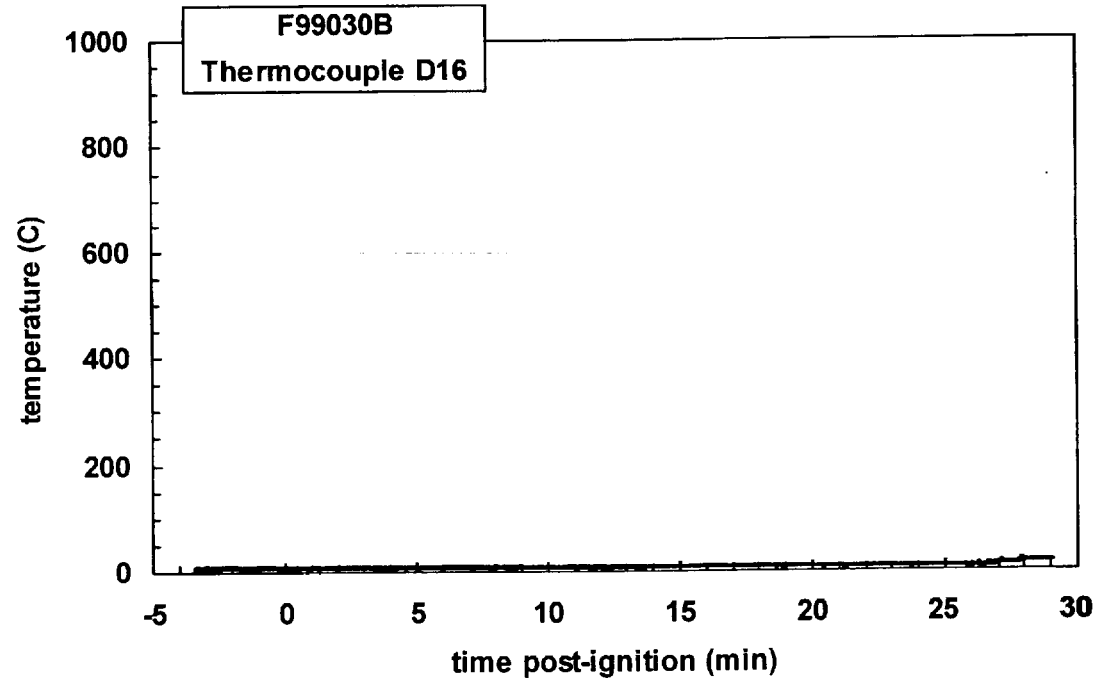

Plot C42. Fire Test F99030B. Data plot from thermocouple D16.

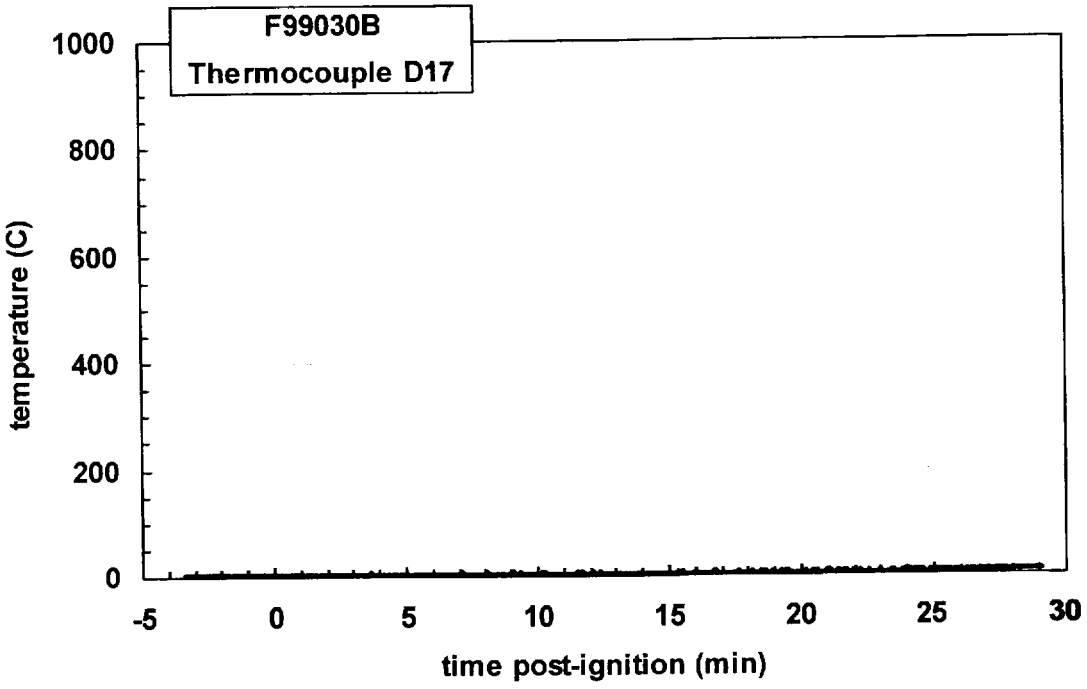

Plot C43. Fire Test F99030B. Data plot from thermocouple D17.

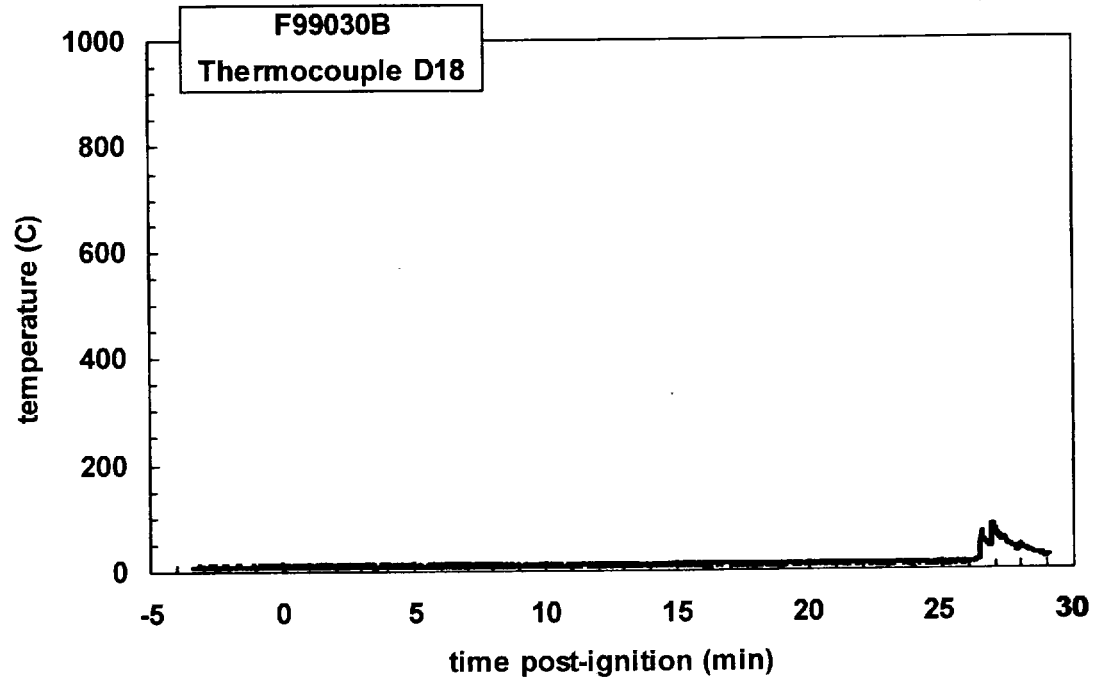

Plot C44. Fire Test F99030B. Data plot from thermocouple D18.

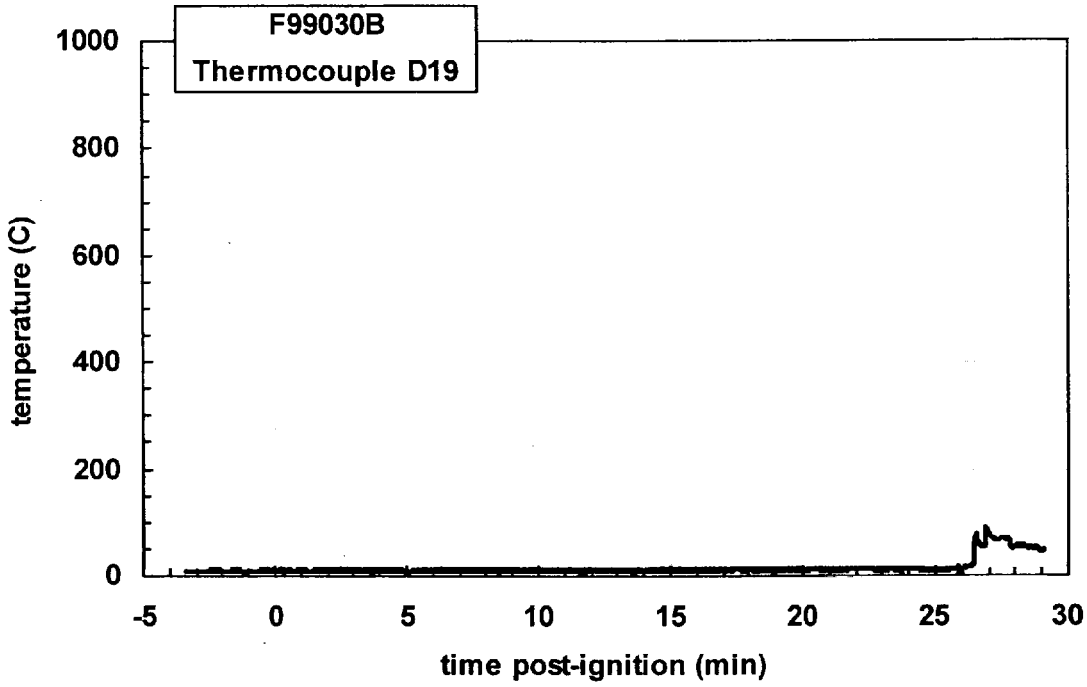

Plot C45. Fire Test F99030B. Data plot from thermocouple D19.

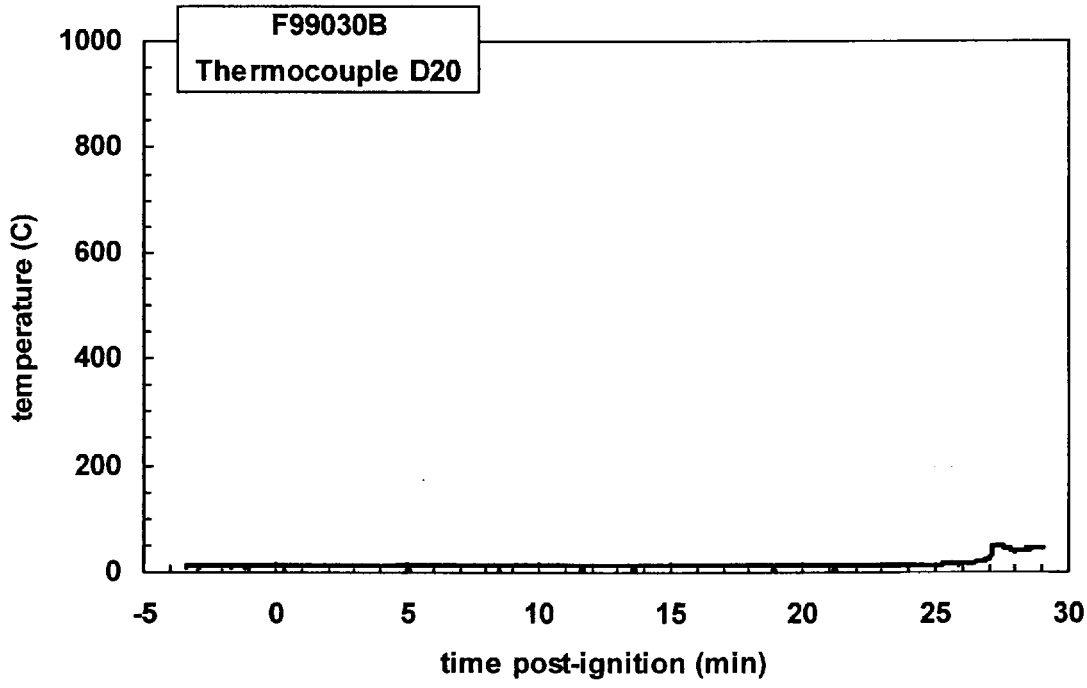

Plot C46. Fire Test F99030B. Data plot from thermocouple D20.

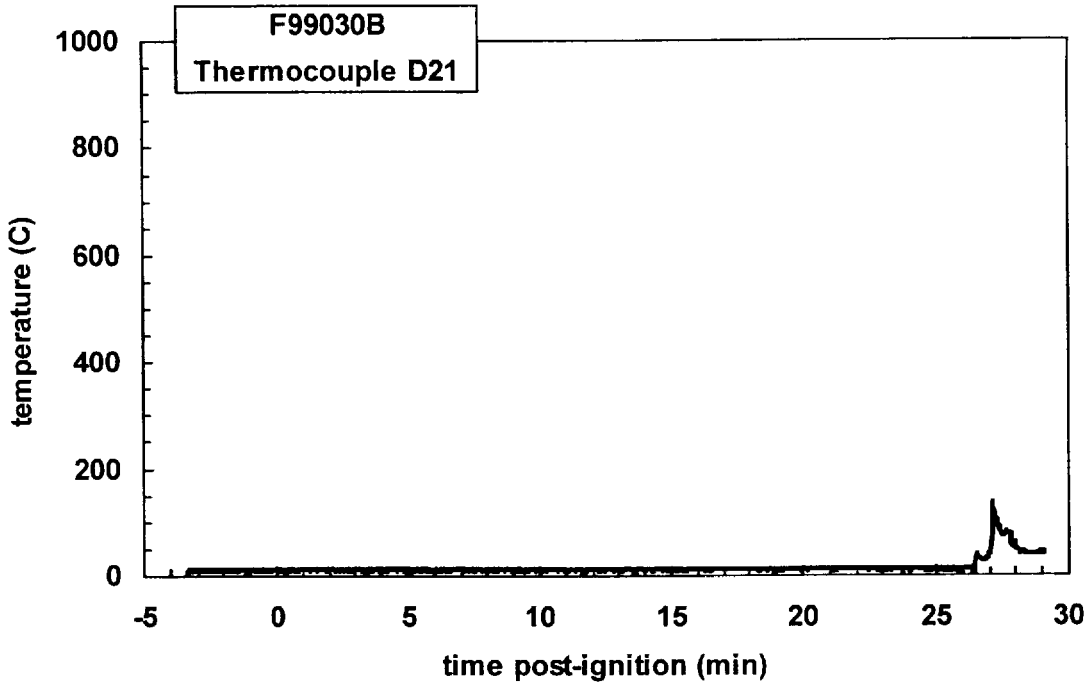

Plot C47. Fire Test F99030B. Data plot from thermocouple D21.

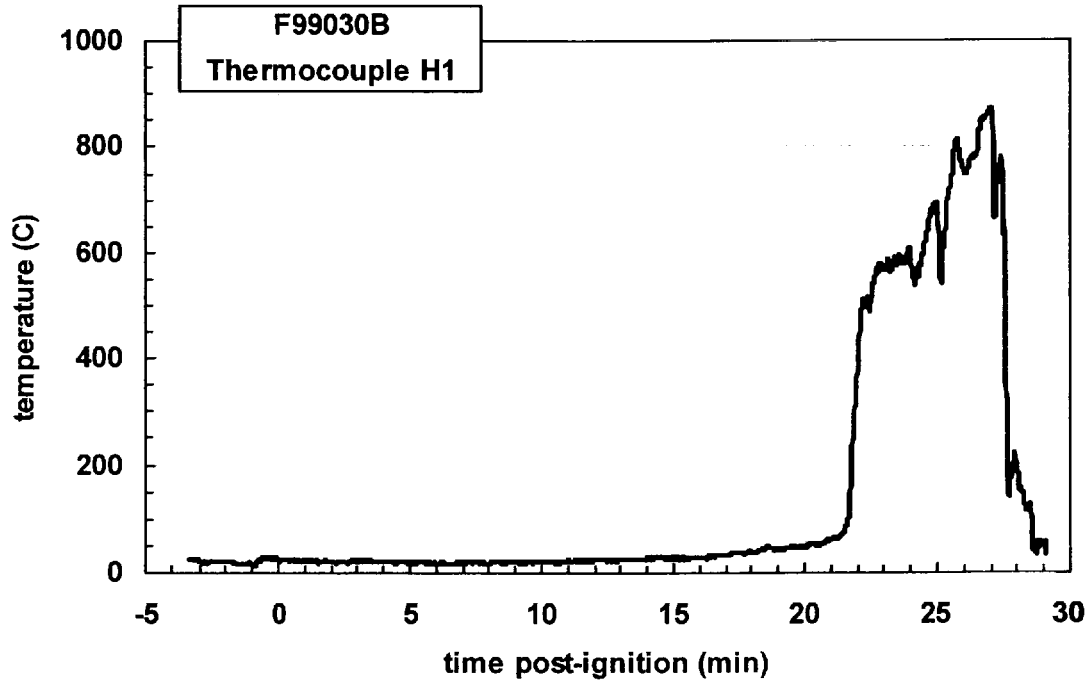

Plot C48. Fire Test F99030B. Data plot from thermocouple H1.

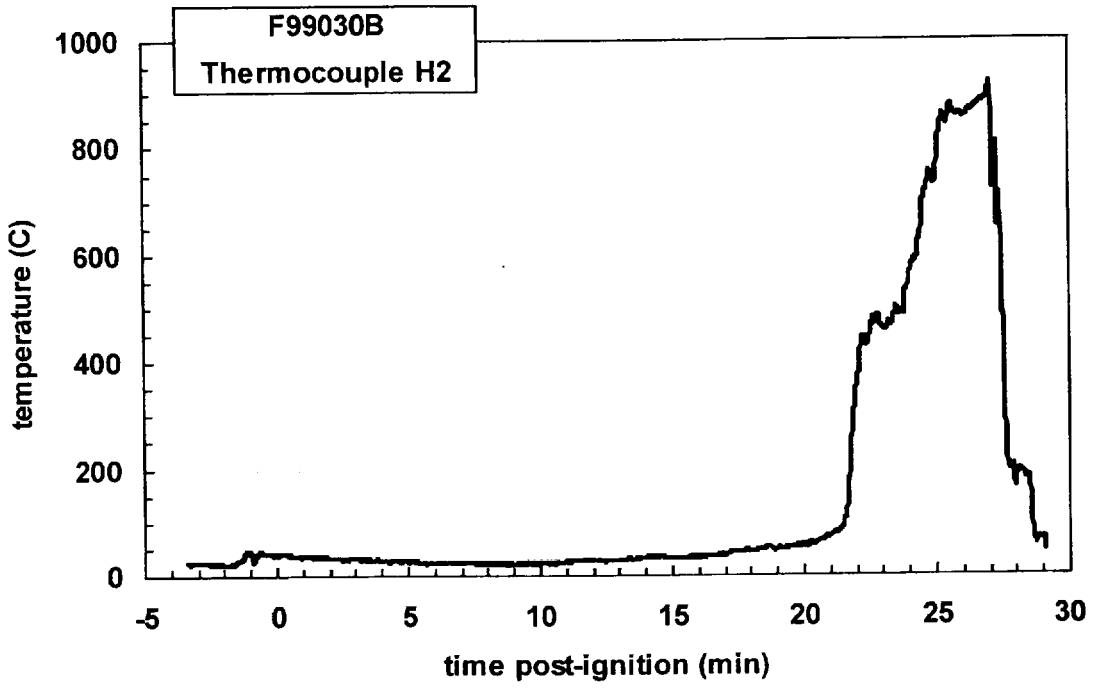

Plot C49. Fire Test F99030B. Data plot from thermocouple H2.

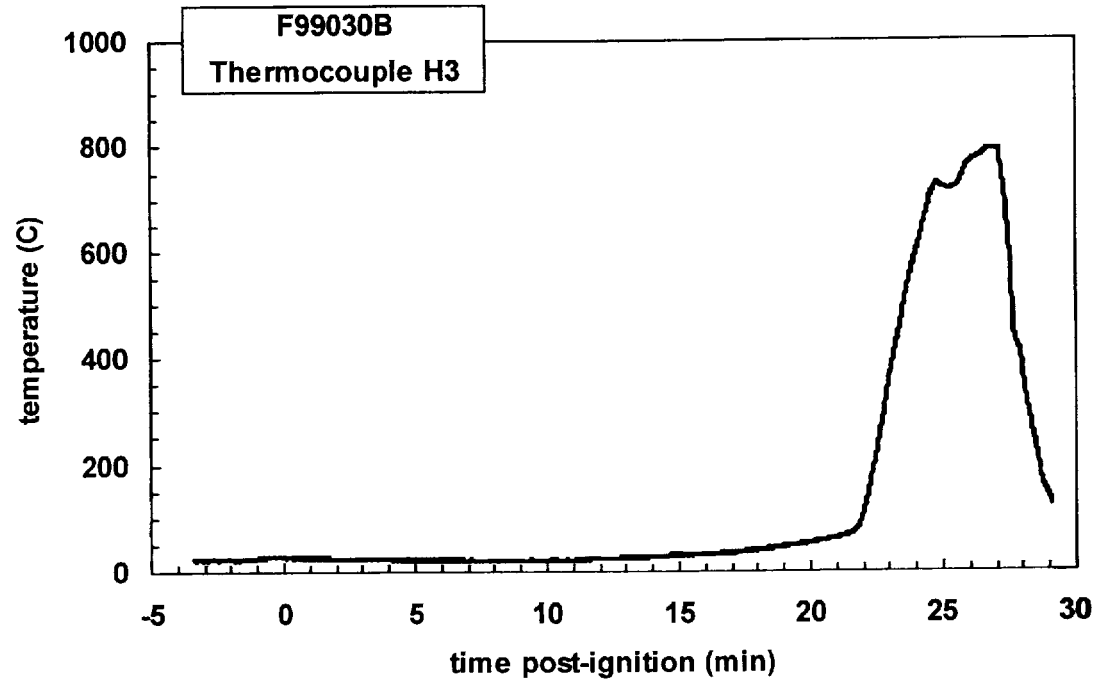

Plot C50. Fire Test F99030B. Data plot from thermocouple H3.

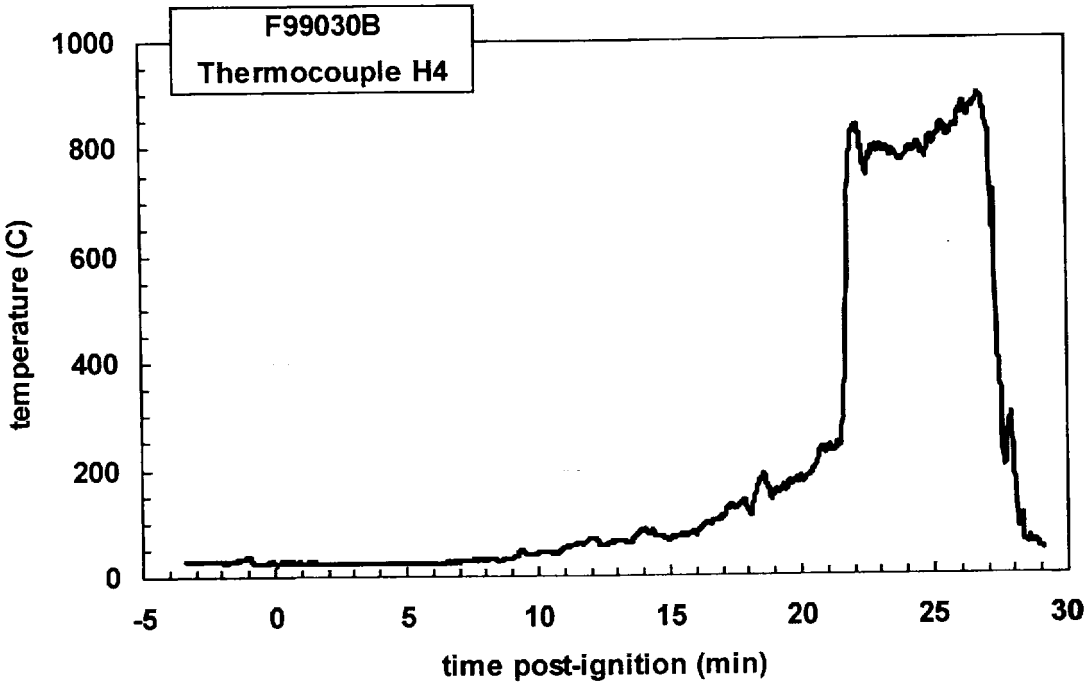

Plot C51. Fire Test F99030B. Data plot from thermocouple H4.

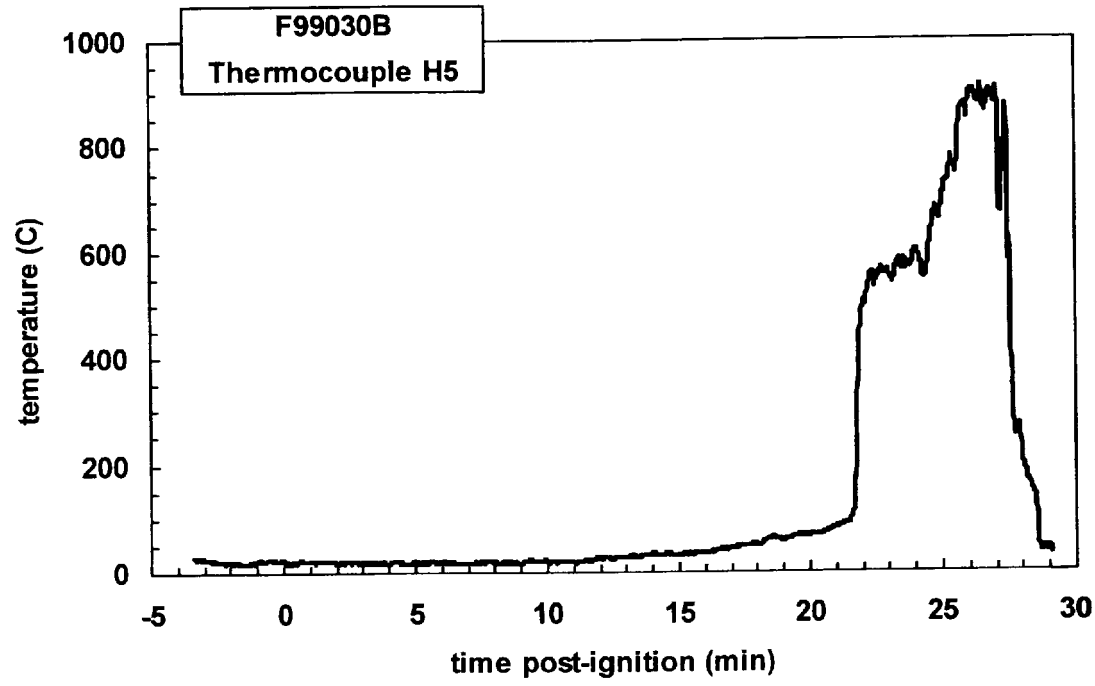

Plot C52. Fire Test F99030B. Data plot from thermocouple H5.

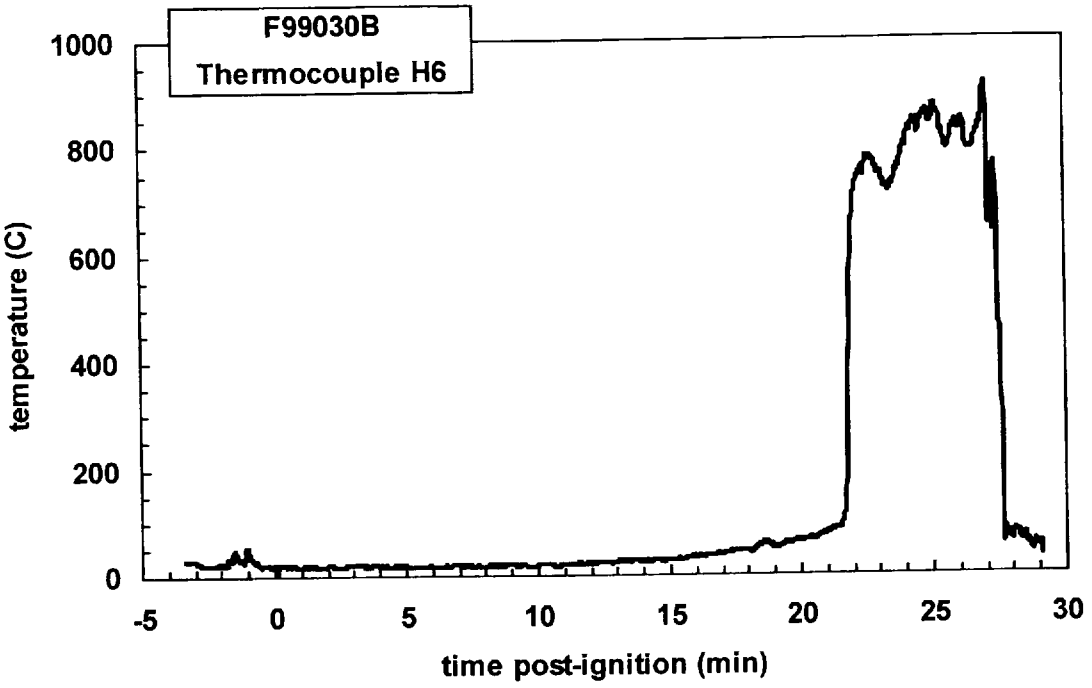

Plot C53. Fire Test F99030B. Data plot from thermocouple H6.

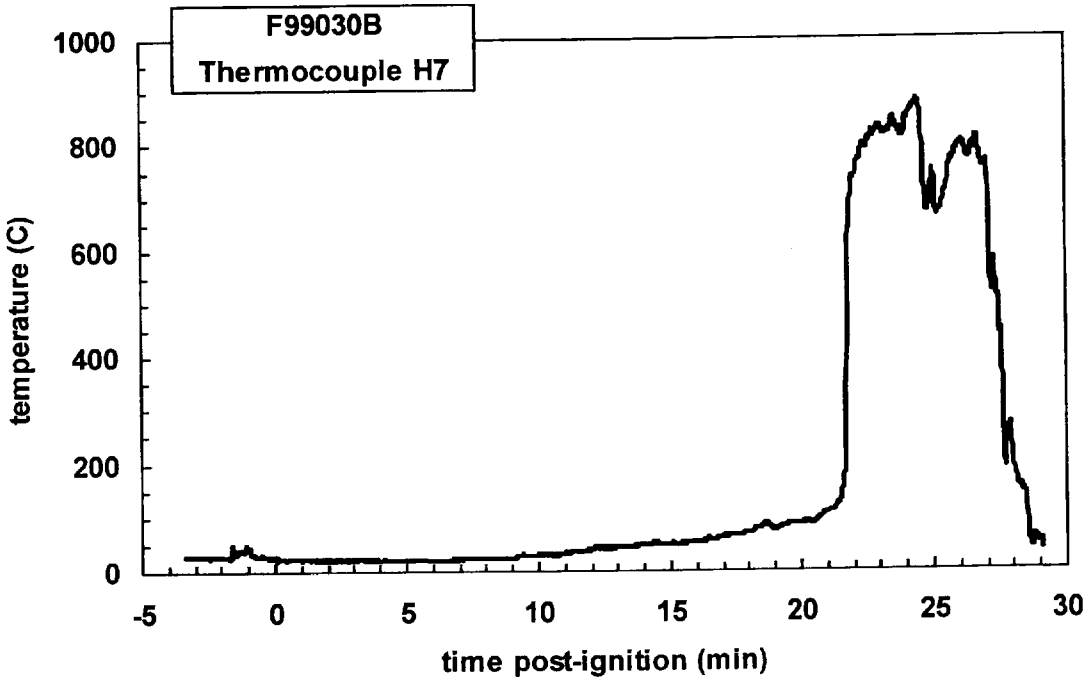

Plot C54. Fire Test F99030B. Data plot from thermocouple H7.

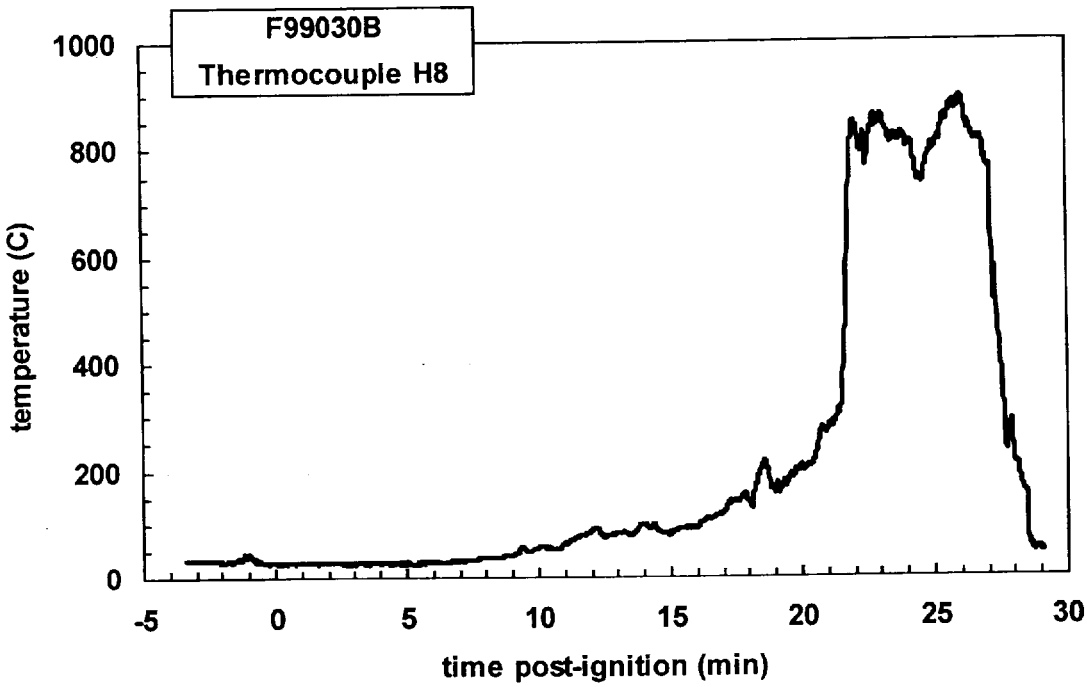

Plot C55. Fire Test F99030B. Data plot from thermocouple H8.

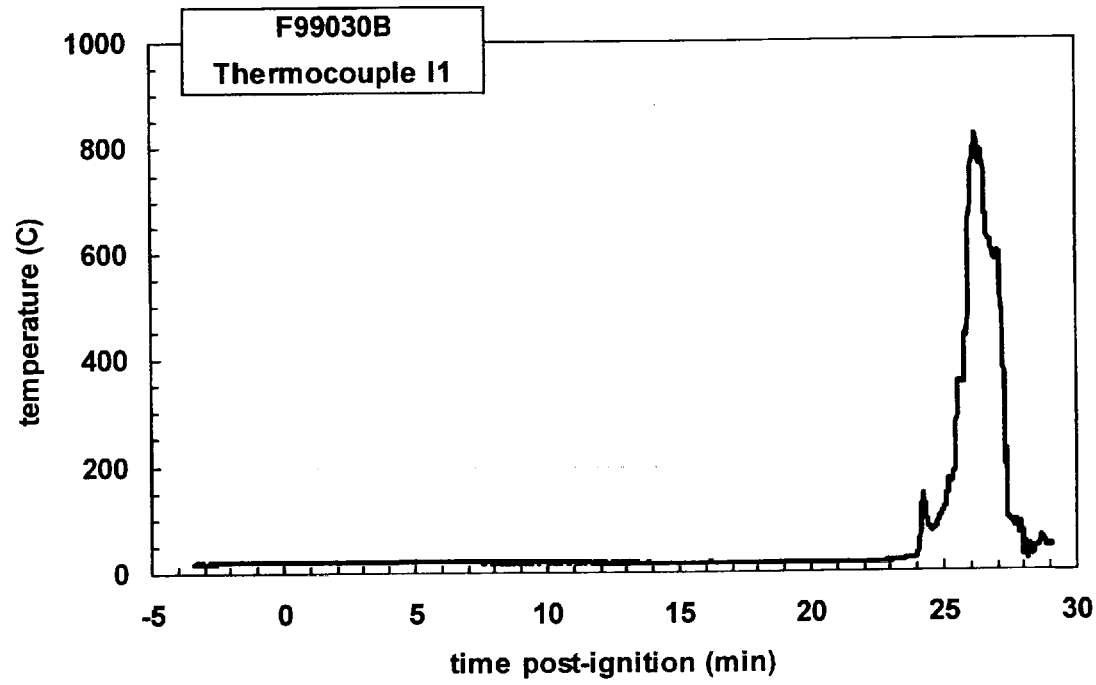

Plot C56. Fire Test F99030B. Data plot from thermocouple I1.

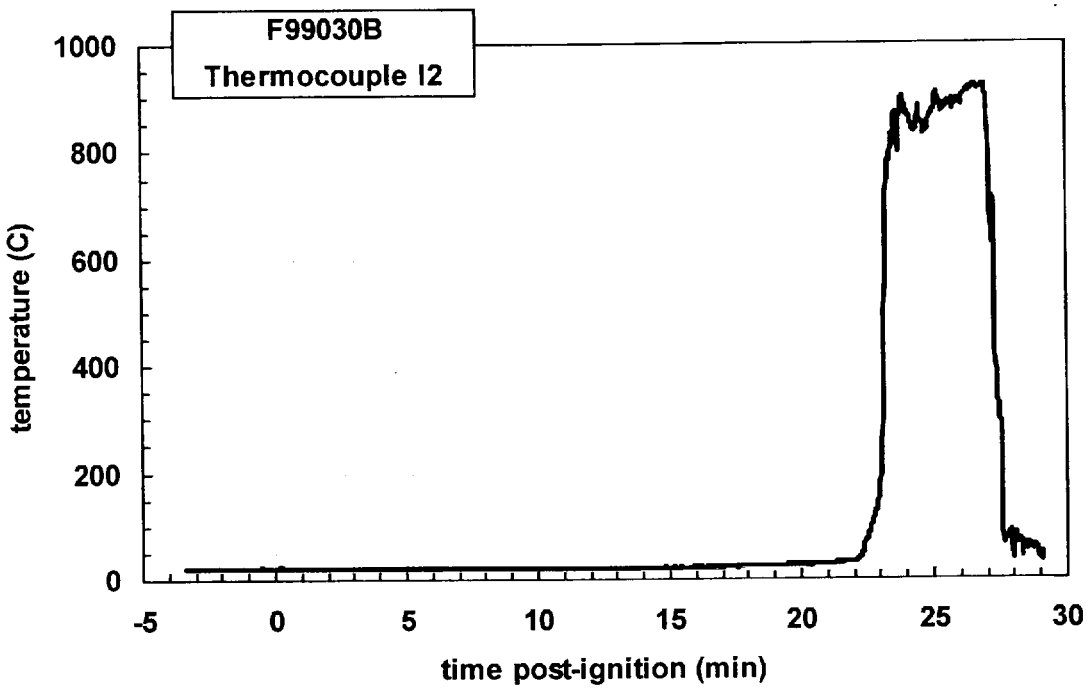

Plot C57. Fire Test F99030B. Data plot from thermocouple I2.

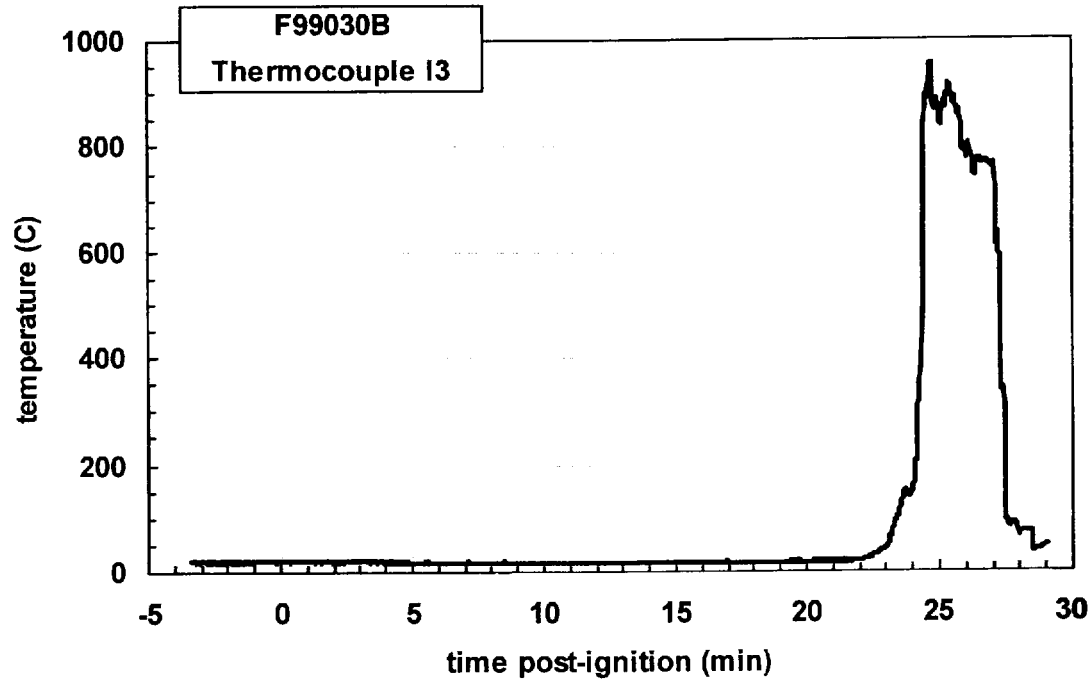

Plot C58. Fire Test F99030B. Data plot from thermocouple I3.

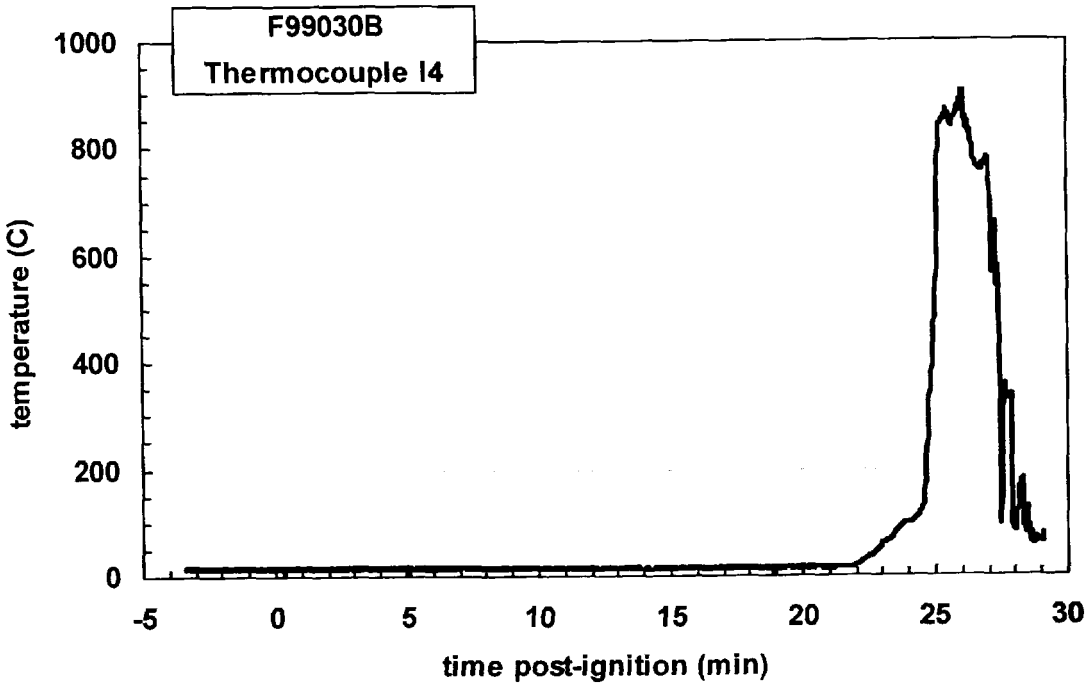

Plot C59. Fire Test F99030B. Data plot from thermocouple I4.

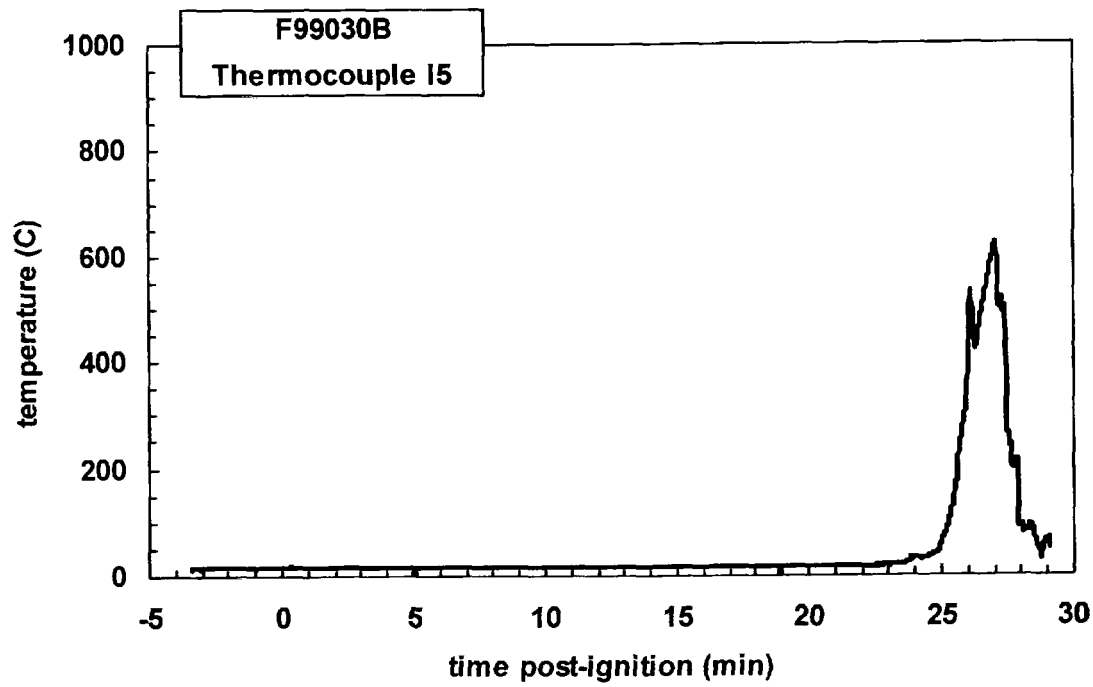

Plot C60. Fire Test F99030B. Data plot from thermocouple I5.

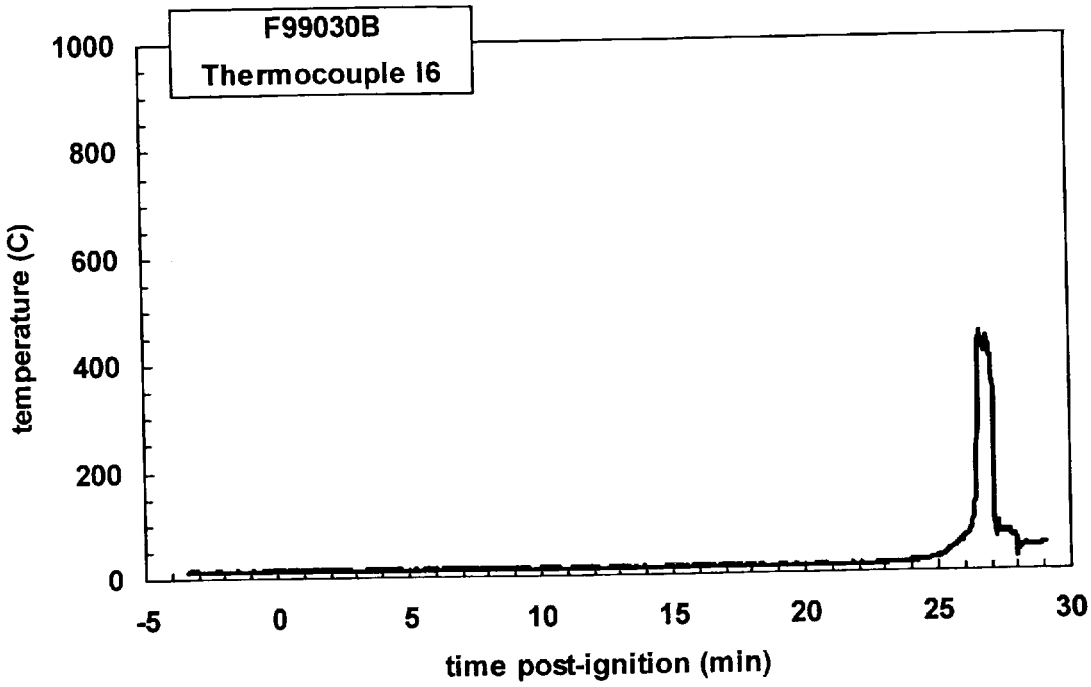

Plot C61. Fire Test F99030B. Data plot from thermocouple I6.

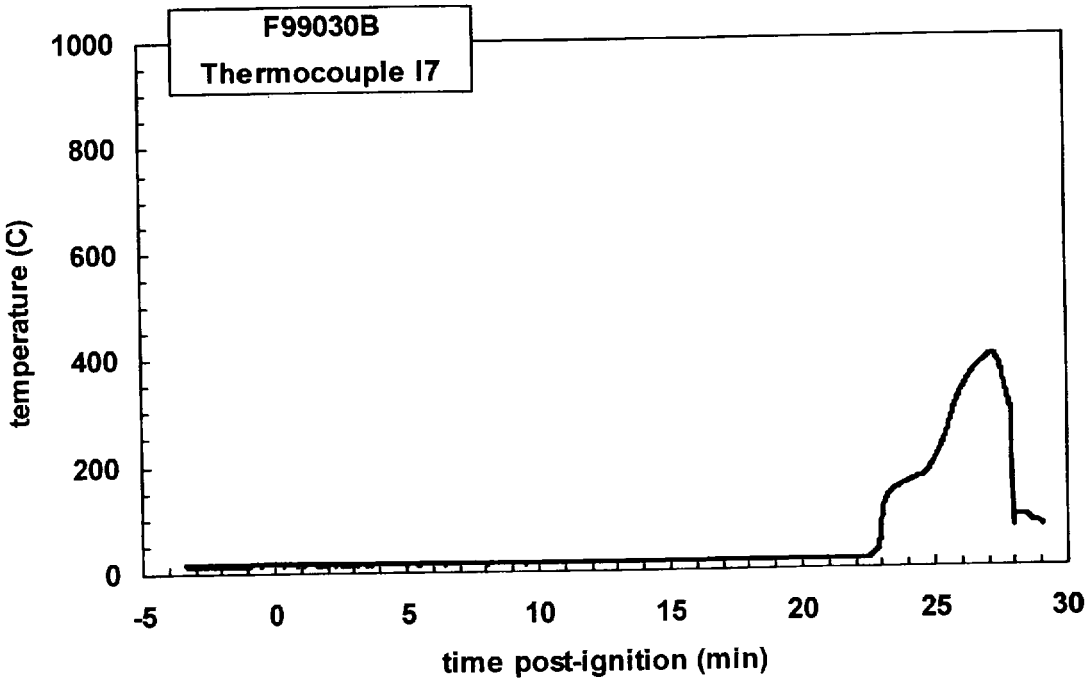

Plot C62. Fire Test F99030B. Data plot from thermocouple I7.

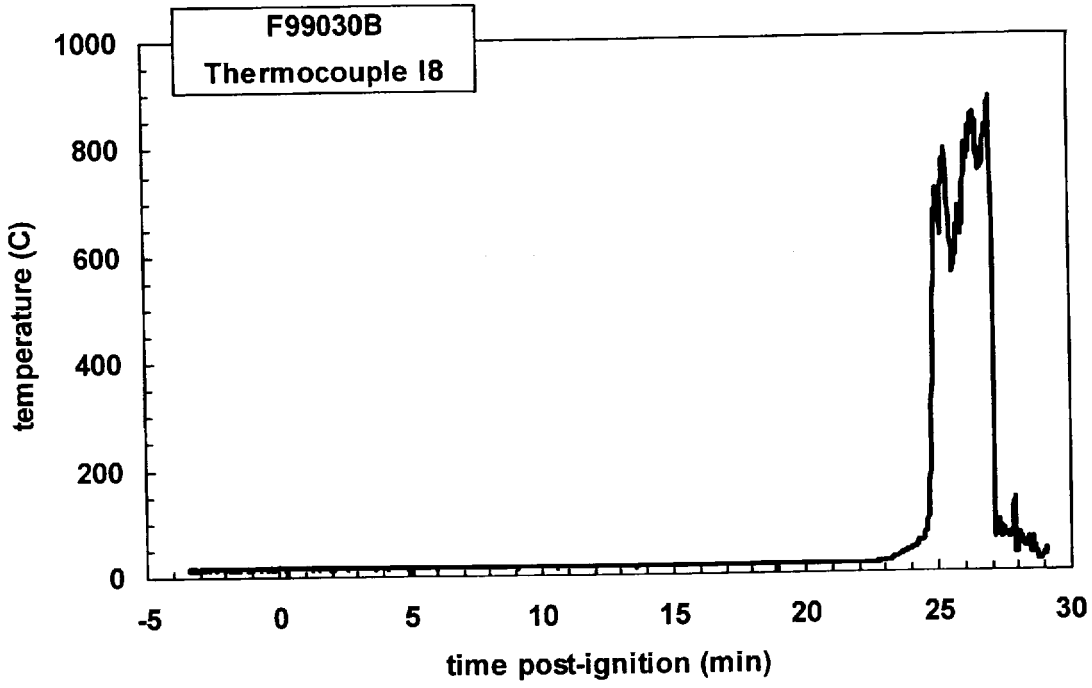

Plot C63. Fire Test F99030B. Data plot from thermocouple I8.

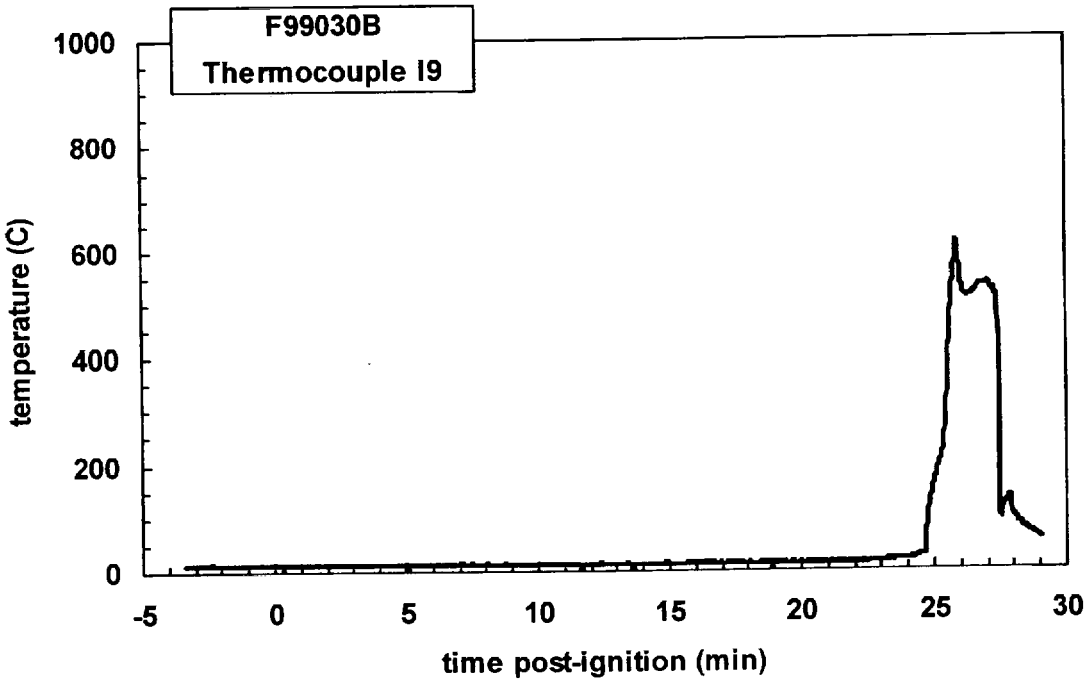

Plot C64. Fire Test F99030B. Data plot from thermocouple I9.

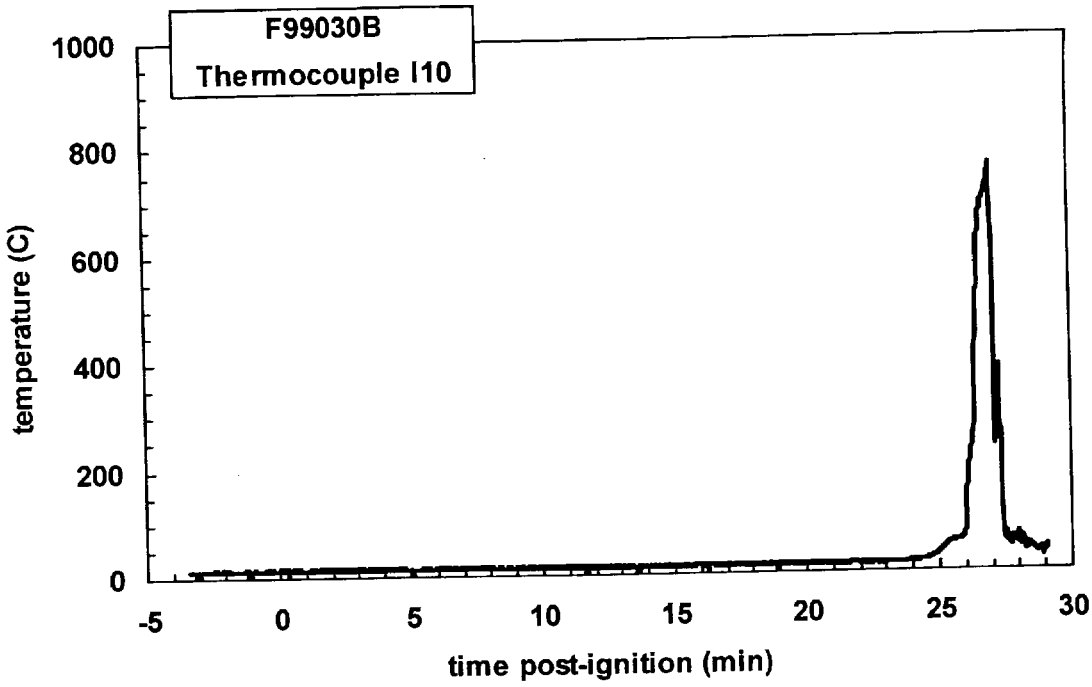

Plot C65. Fire Test F99030B. Data plot from thermocouple I10.

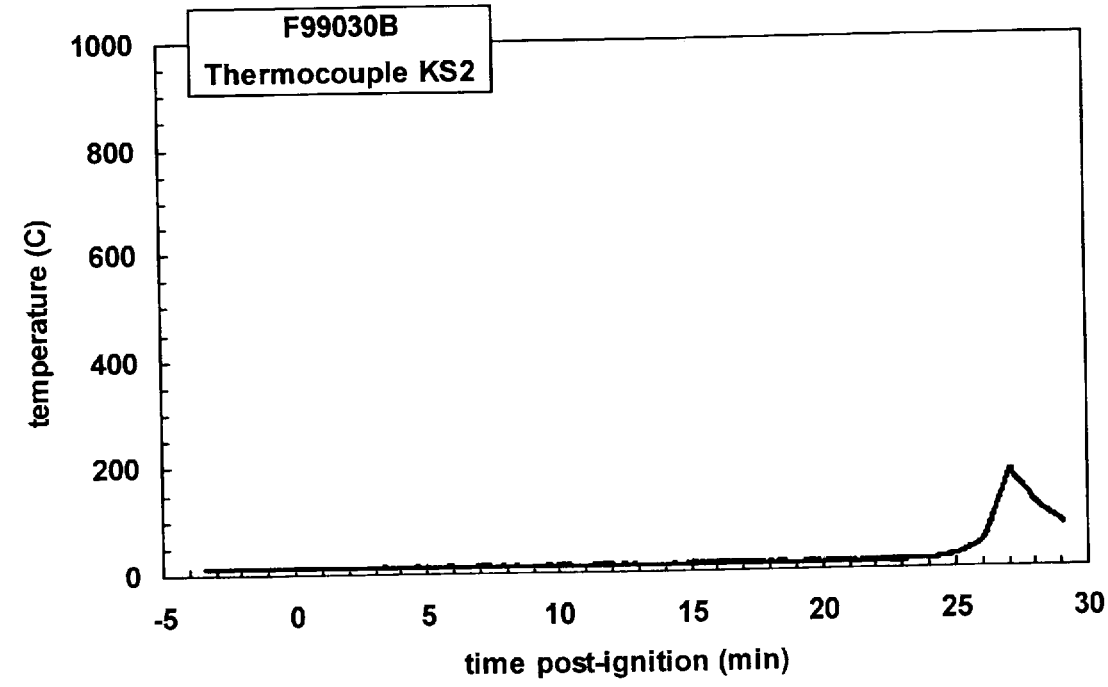

Plot C66. Fire Test F99030B. Data plot from thermocouple KS2.

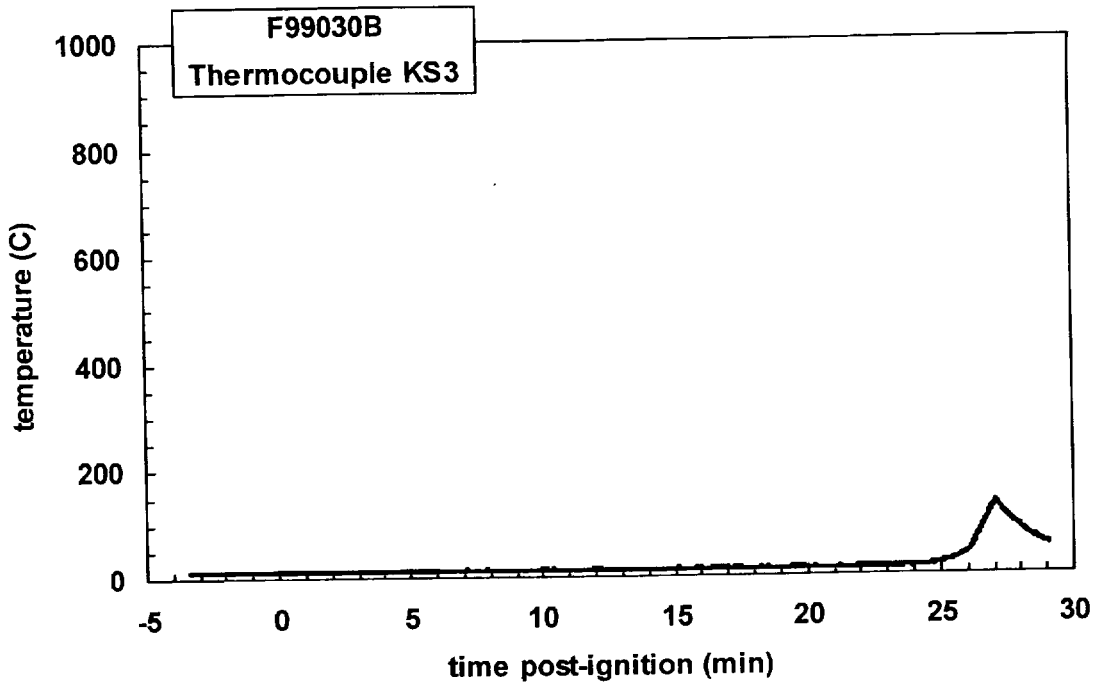

Plot C67. Fire Test F99030B. Data plot from thermocouple KS3.

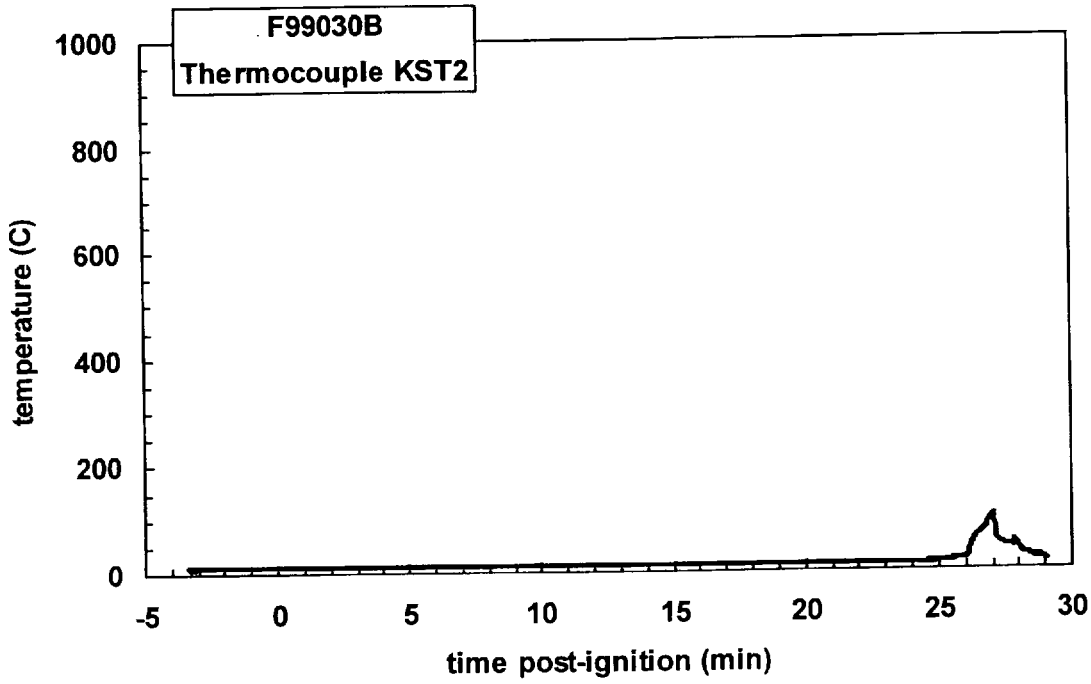

Plot C68. Fire Test F99030B. Data plot from thermocouple KST2.

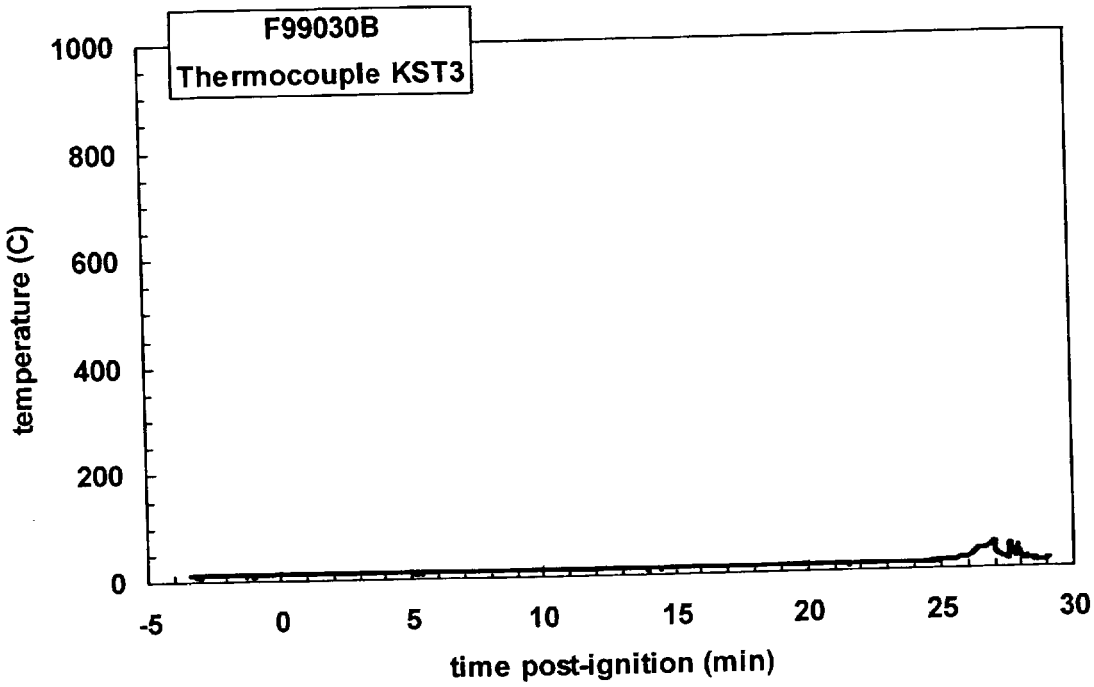

Plot C69. Fire Test F99030B. Data plot from thermocouple KST3.

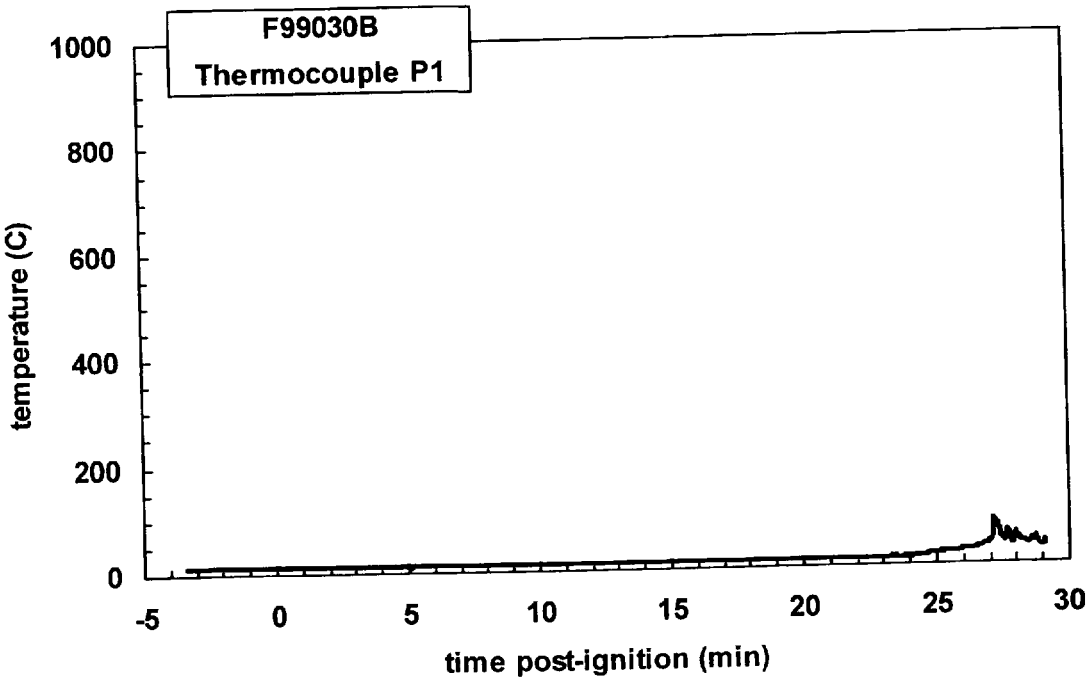

Plot C70. Fire Test F99030B. Data plot from thermocouple P1.

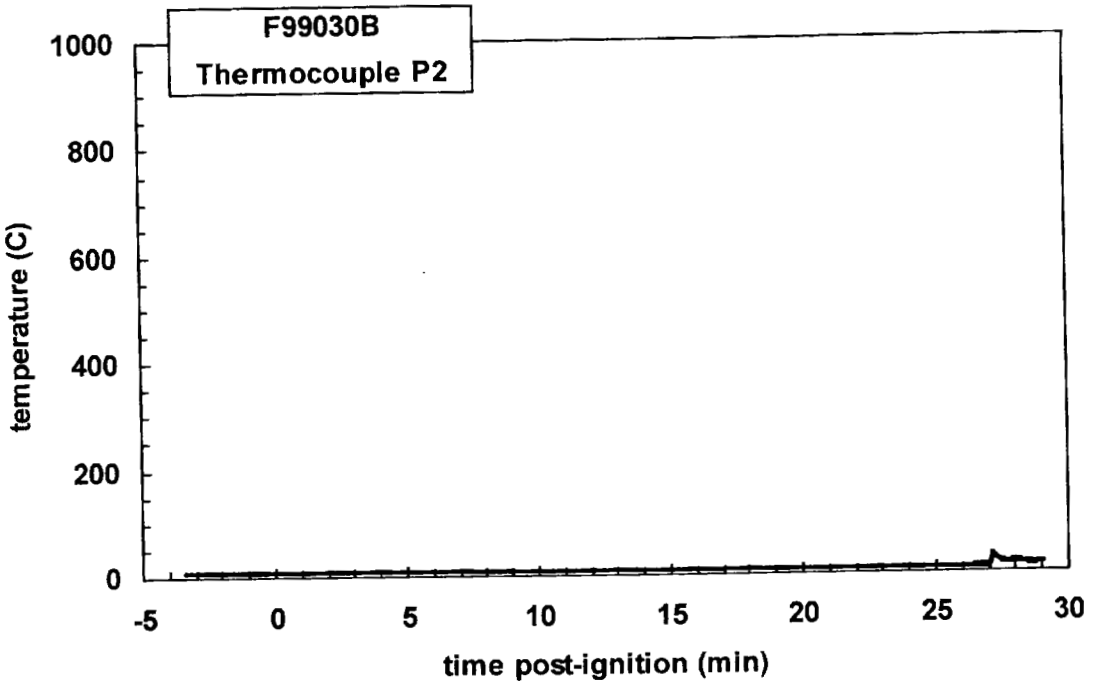

Plot C71. Fire Test F99030B. Data plot from thermocouple P2.

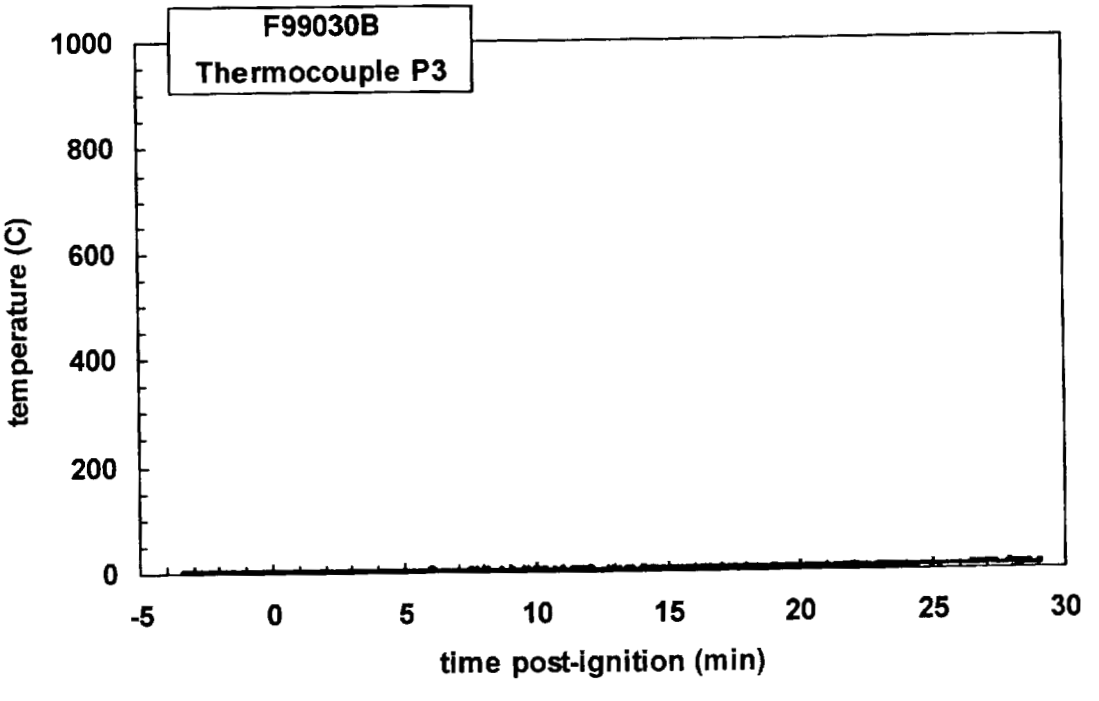

Plot C72. Fire Test F99030B. Data plot from thermocouple P3.

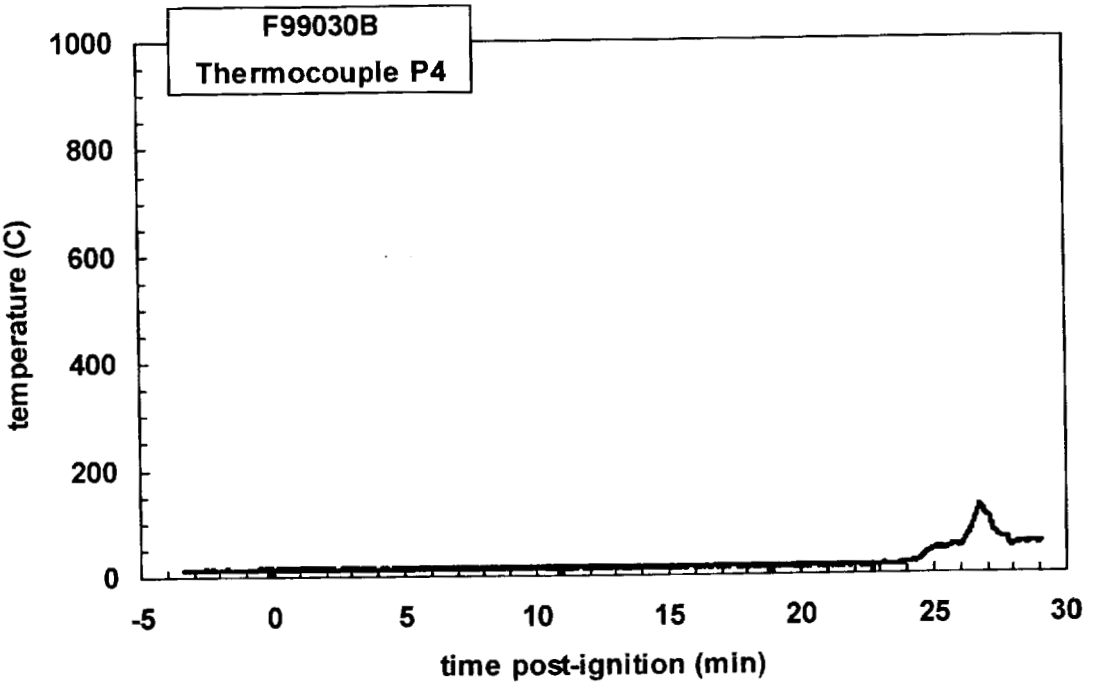

Plot C73. Fire Test F99030B. Data plot from thermocouple P4.

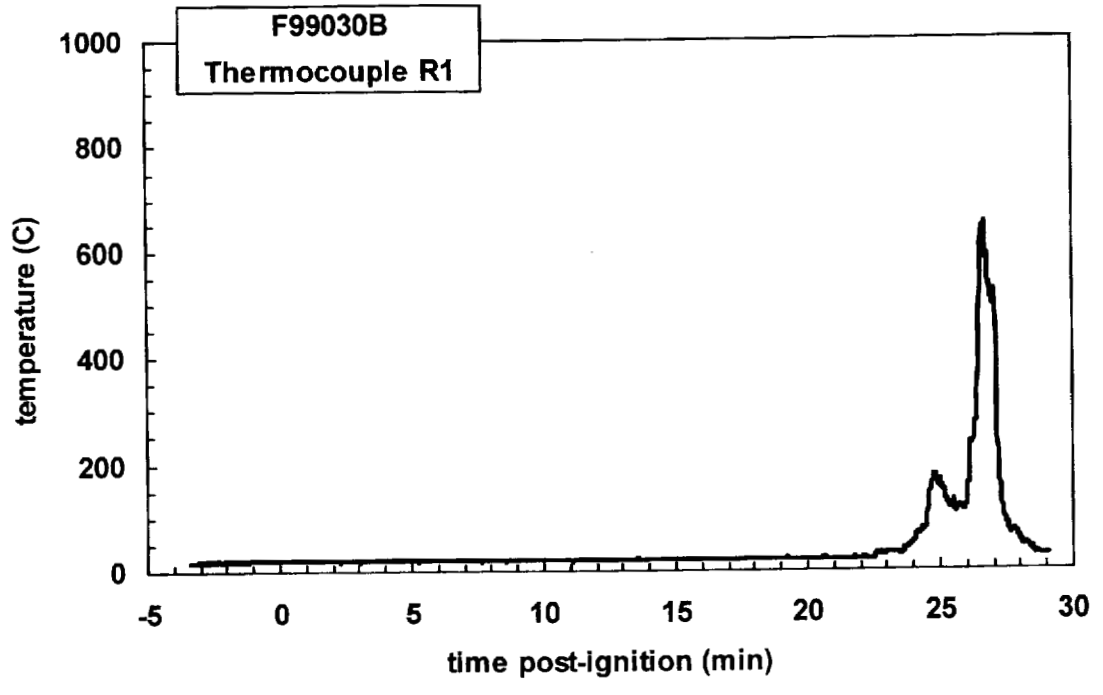

Plot C74. Fire Test F99030B. Data plot from thermocouple R1.

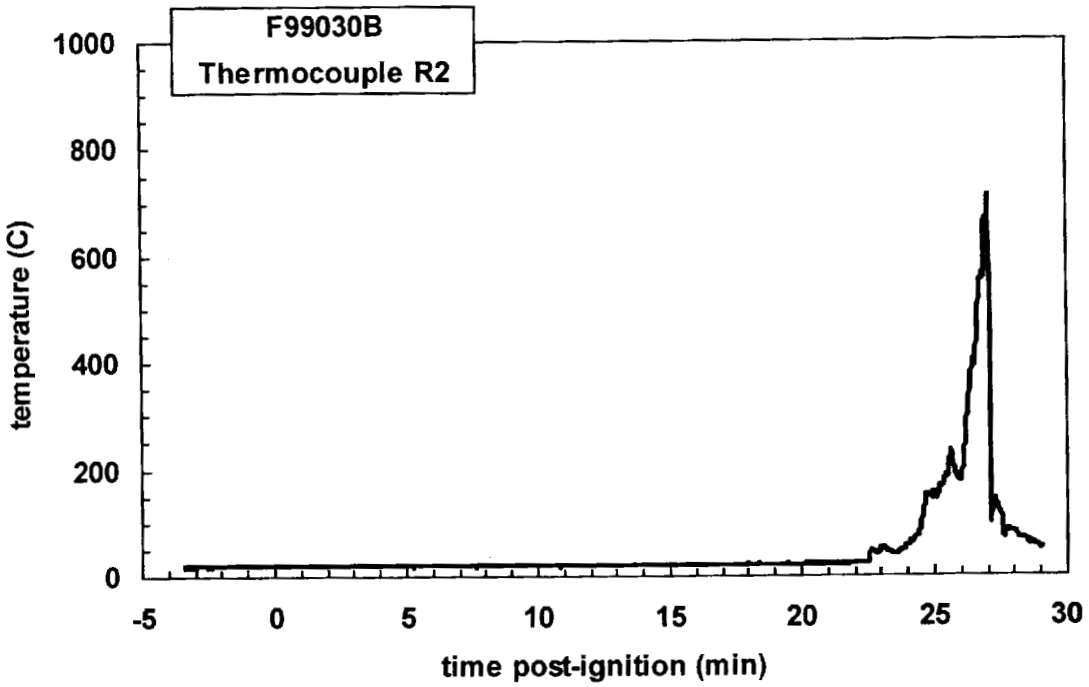

Plot C75. Fire Test F99030B. Data plot from thermocouple R2.

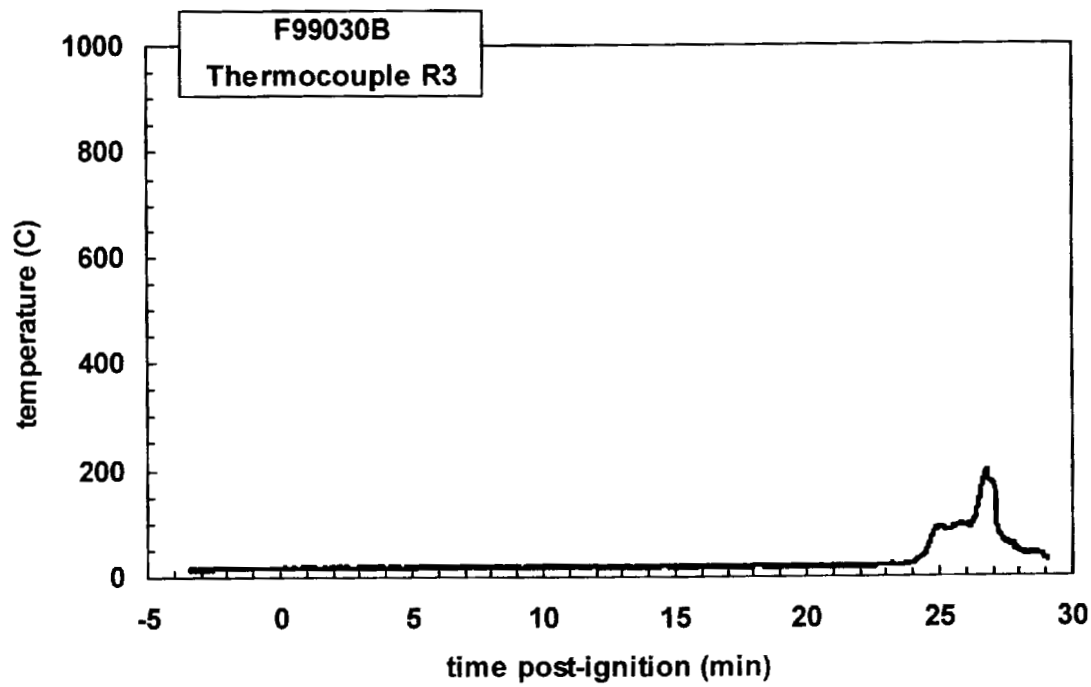

Plot C76. Fire Test F99030B. Data plot from thermocouple R3.

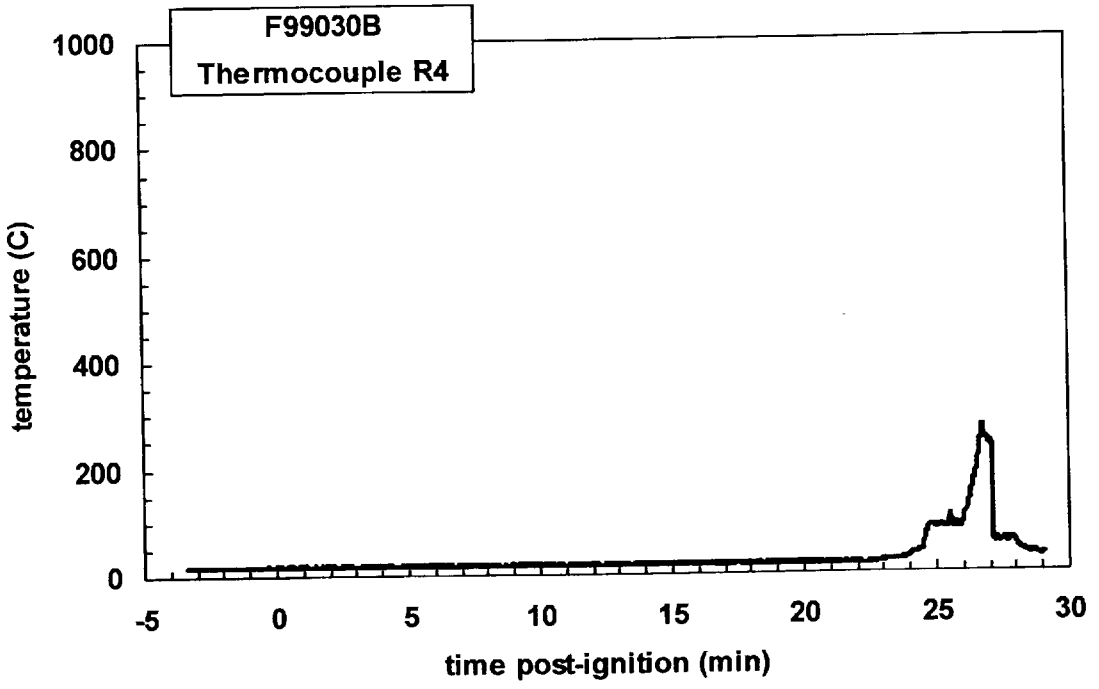

Plot C77. Fire Test F99030B. Data plot from thermocouple R4.

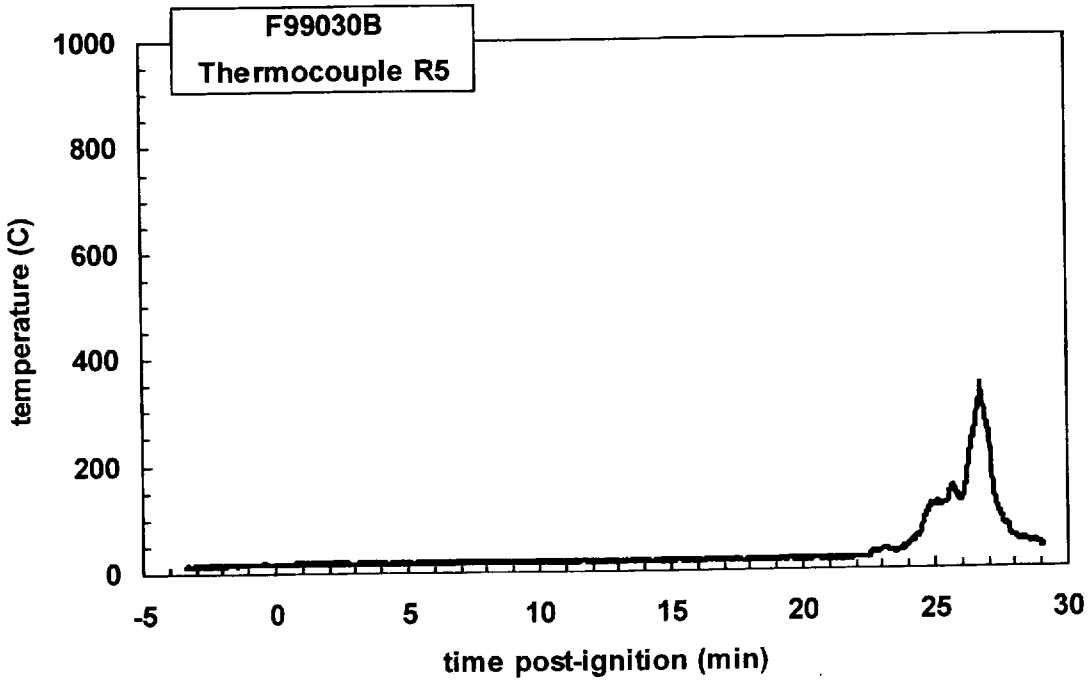

Plot C78. Fire Test F99030B. Data plot from thermocouple R5.

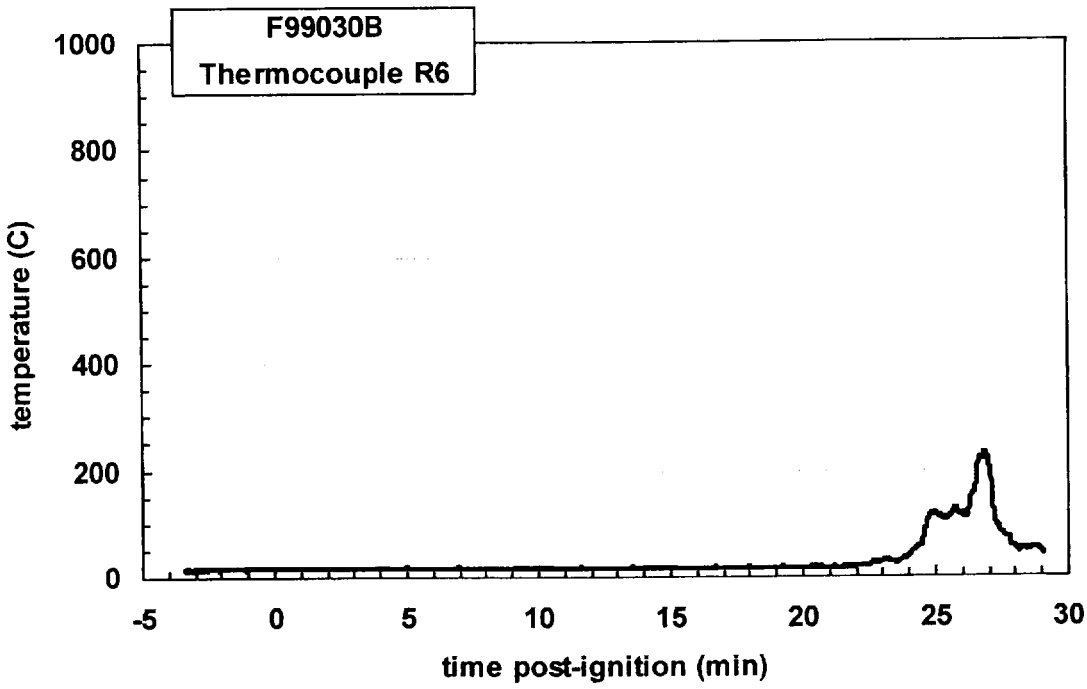

Plot C79. Fire Test F99030B. Data plot from thermocouple R6.

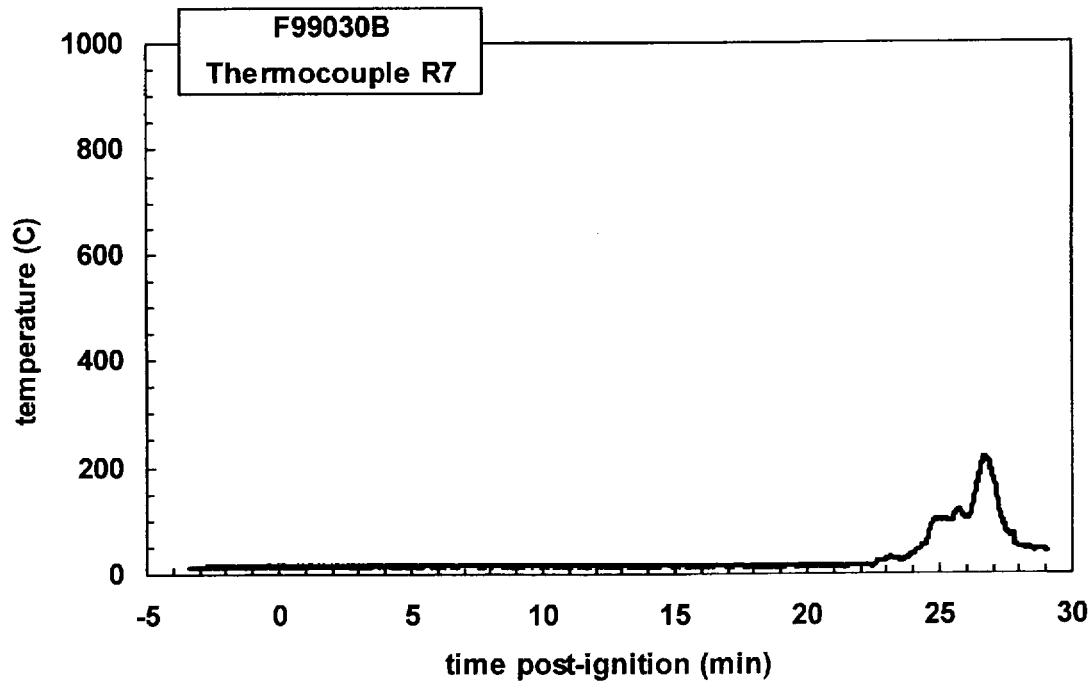

Plot C80. Fire Test F9806011. Data plot from thermocouple R7.

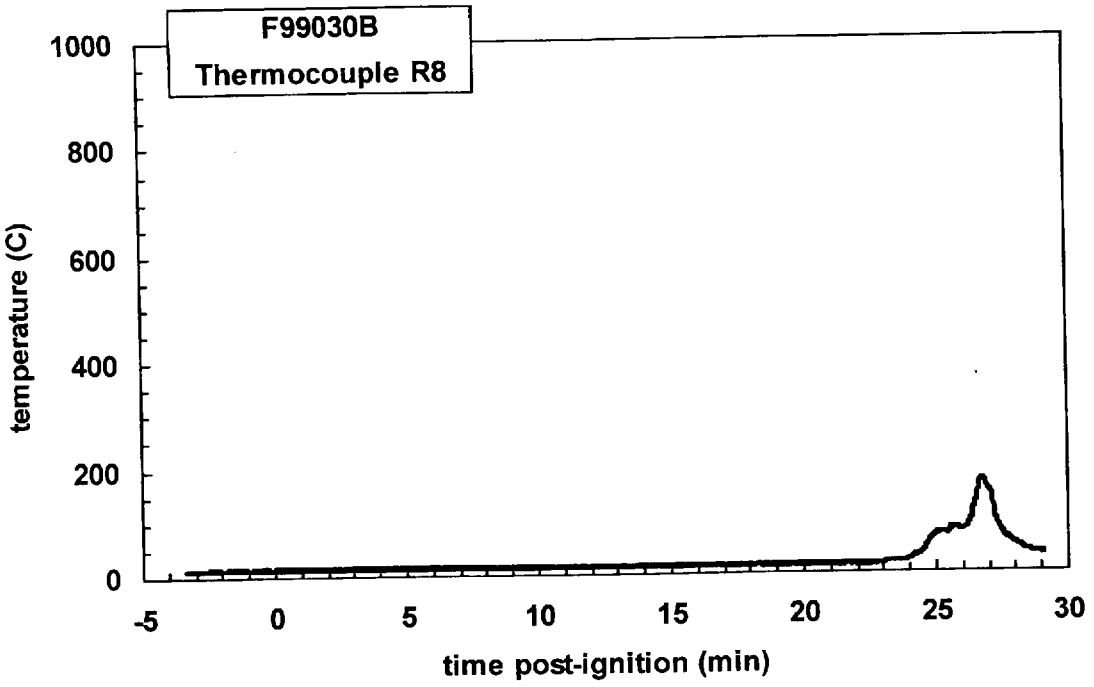

Plot C81. Fire Test F99030B. Data plot from thermocouple R8.

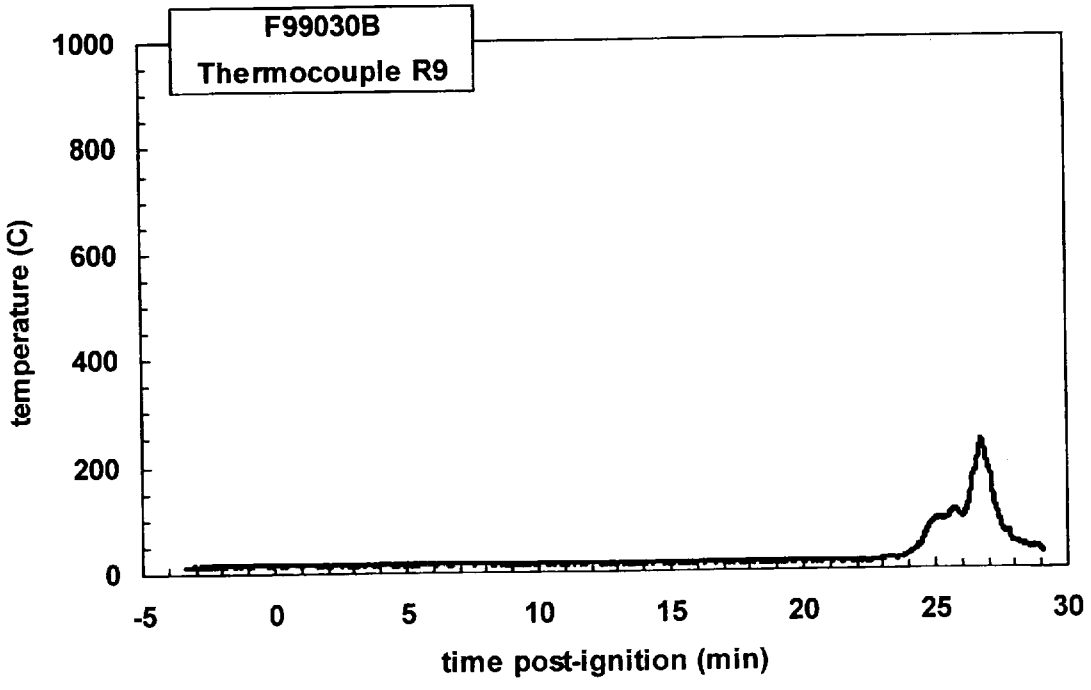

Plot C82. Fire Test F99030B. Data plot from thermocouple R9.

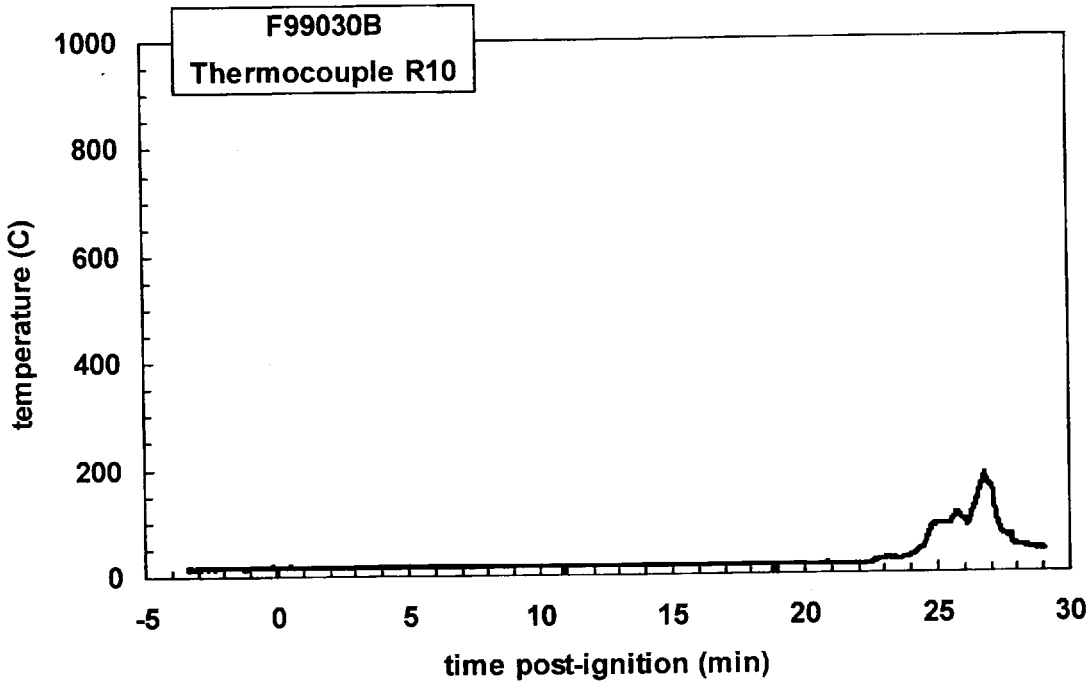

Plot C83. Fire Test F99030B. Data plot from thermocouple R10.

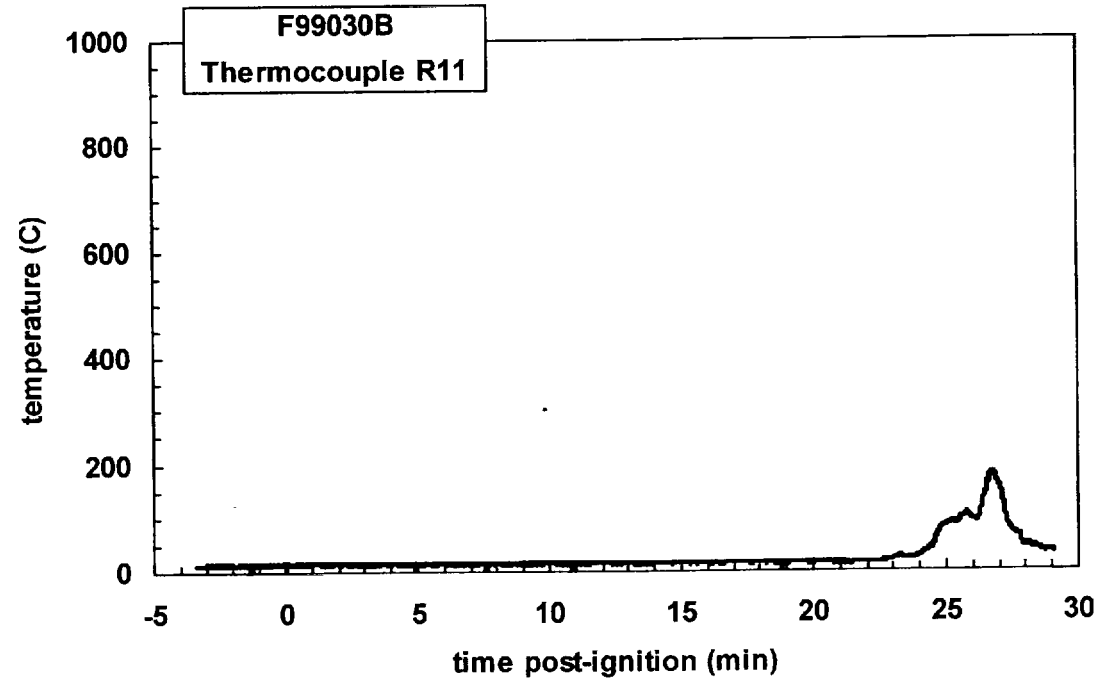

Plot C84. Fire Test F99030B. Data plot from thermocouple R11.

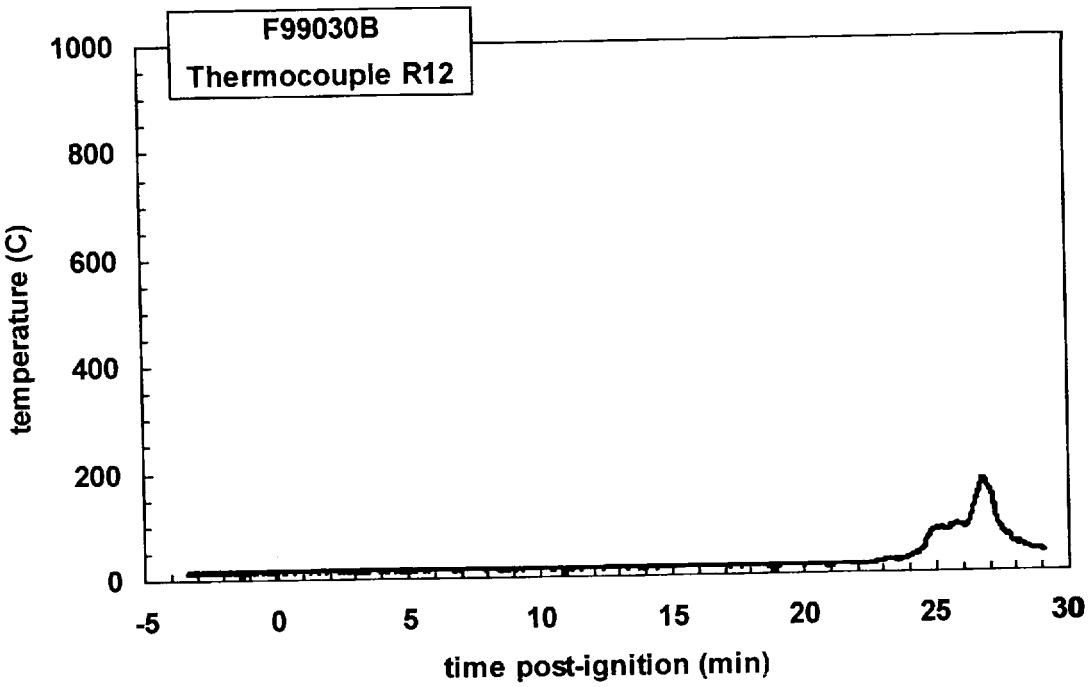

Plot C85. Fire Test F99030B. Data plot from thermocouple R12.

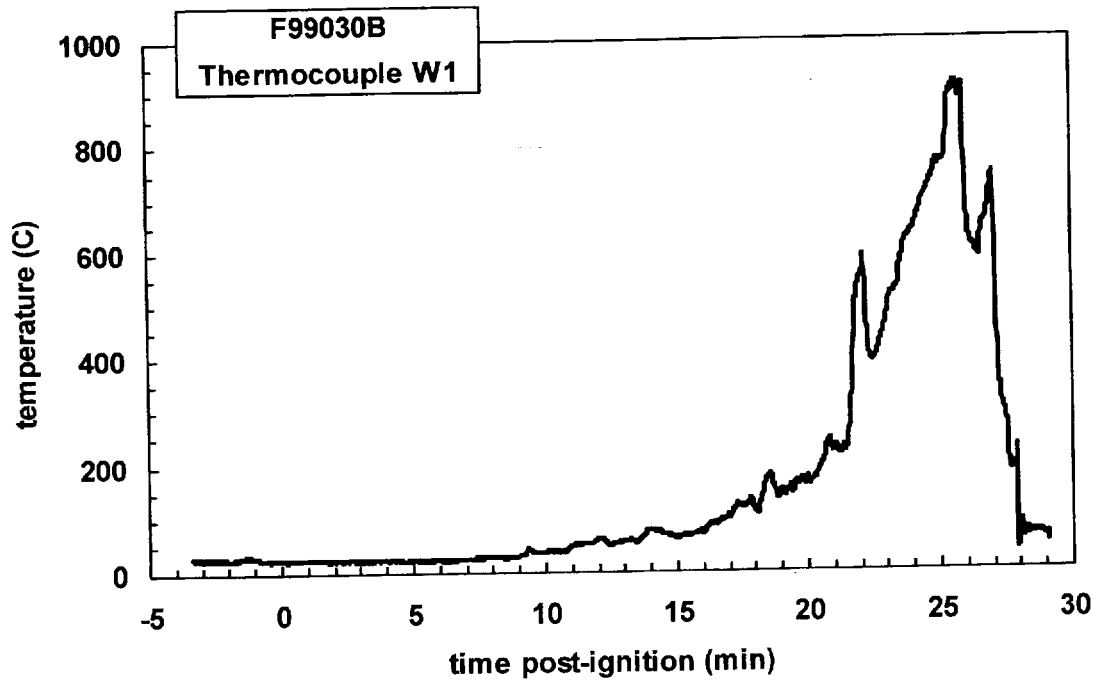

Plot C86. Fire Test F99030B. Data plot from thermocouple W1.

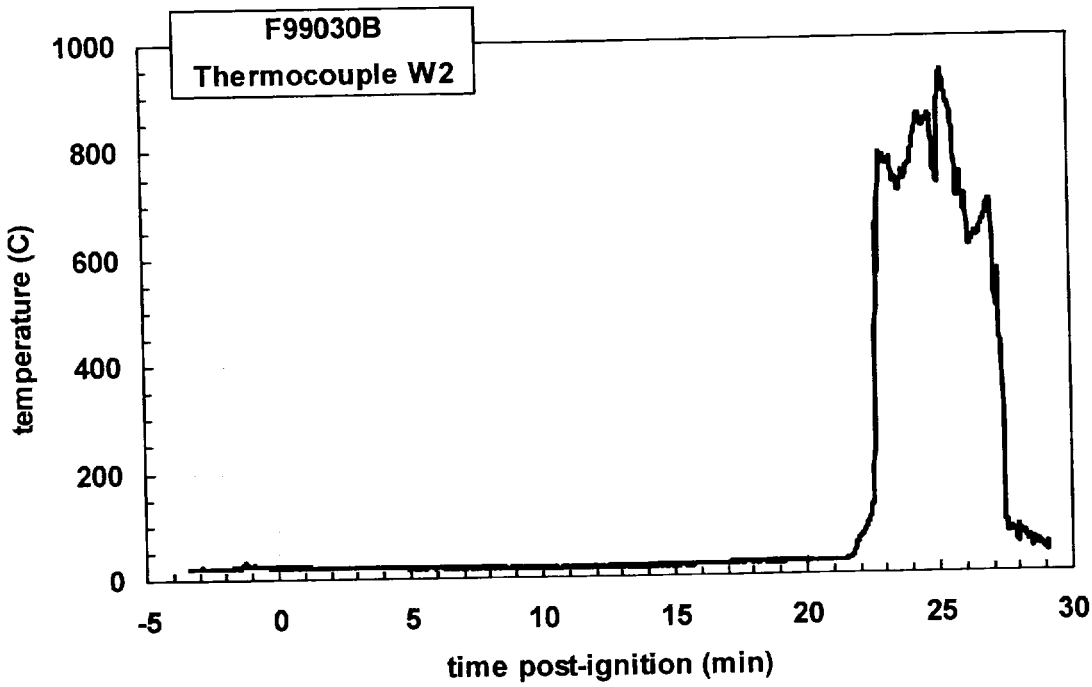

Plot C87. Fire Test F99030B. Data plot from thermocouple W2.

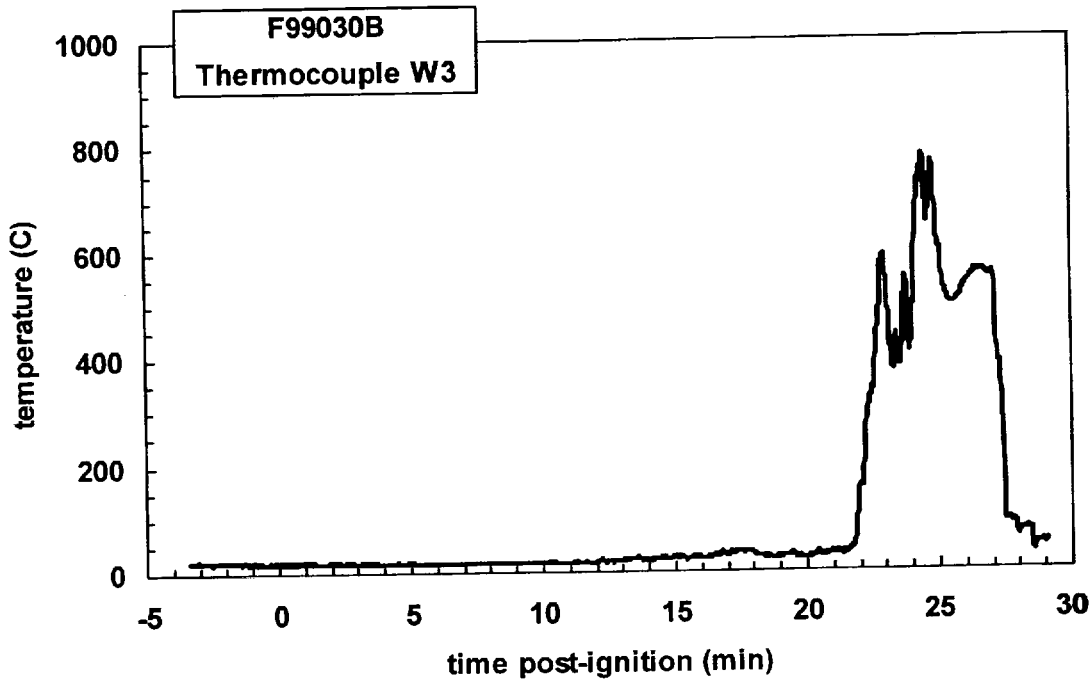

Plot C88. Fire Test F99030B. Data plot from thermocouple W3.

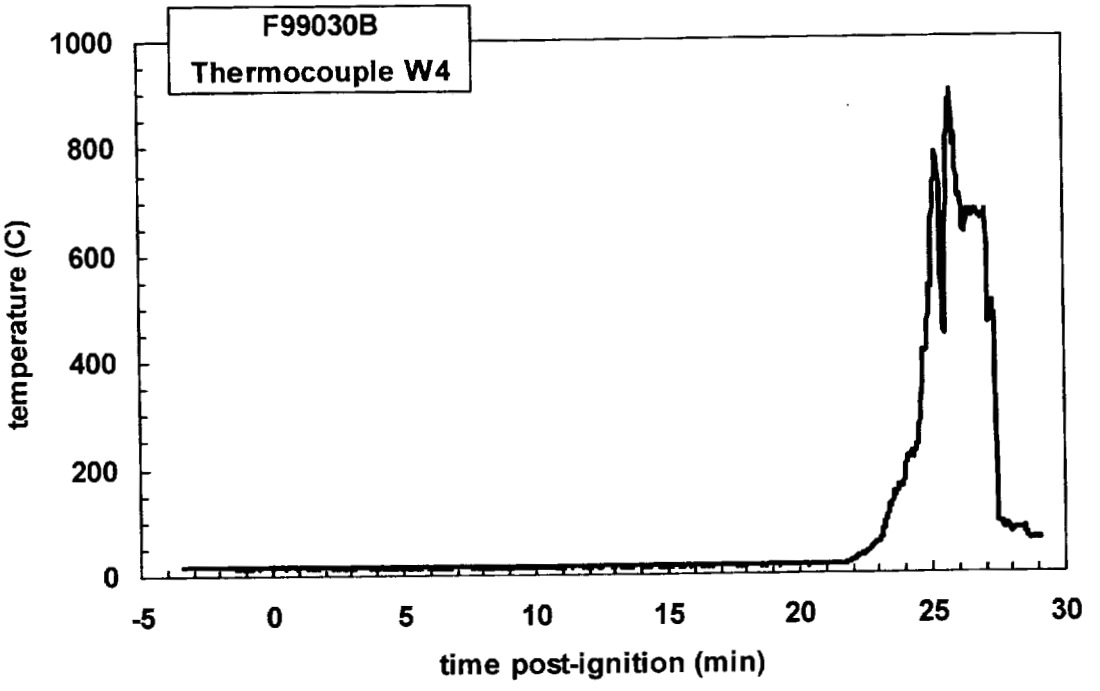

Plot C89. Fire Test F99030B. Data plot from thermocouple W4.

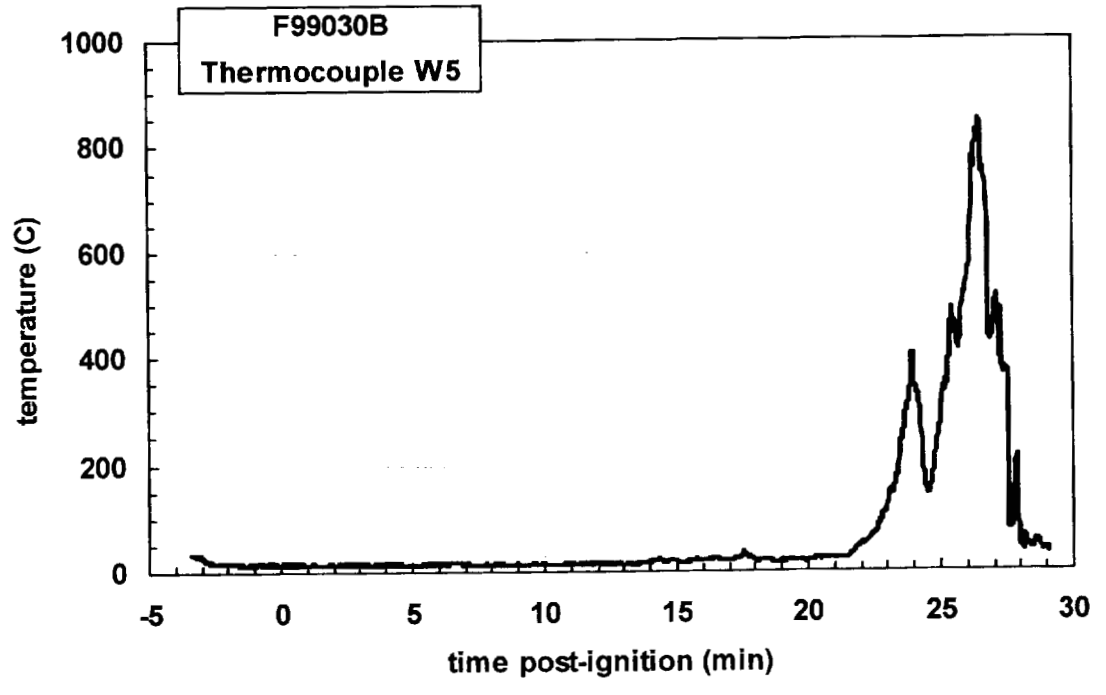

Plot C90. Fire Test F99030B. Data plot from thermocouple W5.

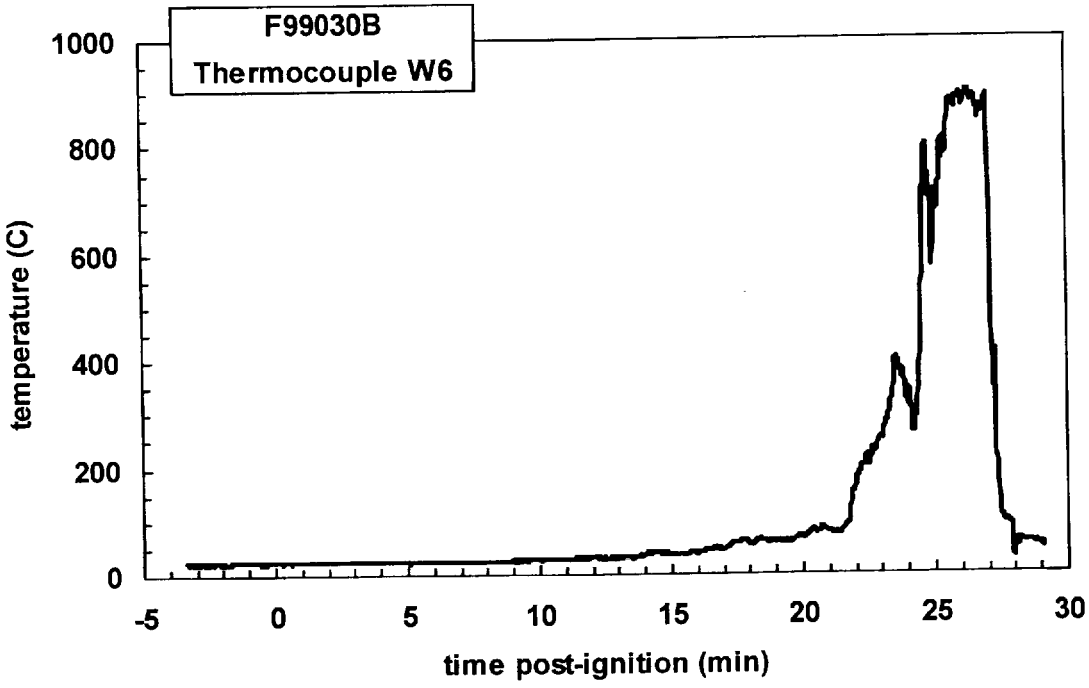

Plot C91. Fire Test F99030B. Data plot from thermocouple W6.

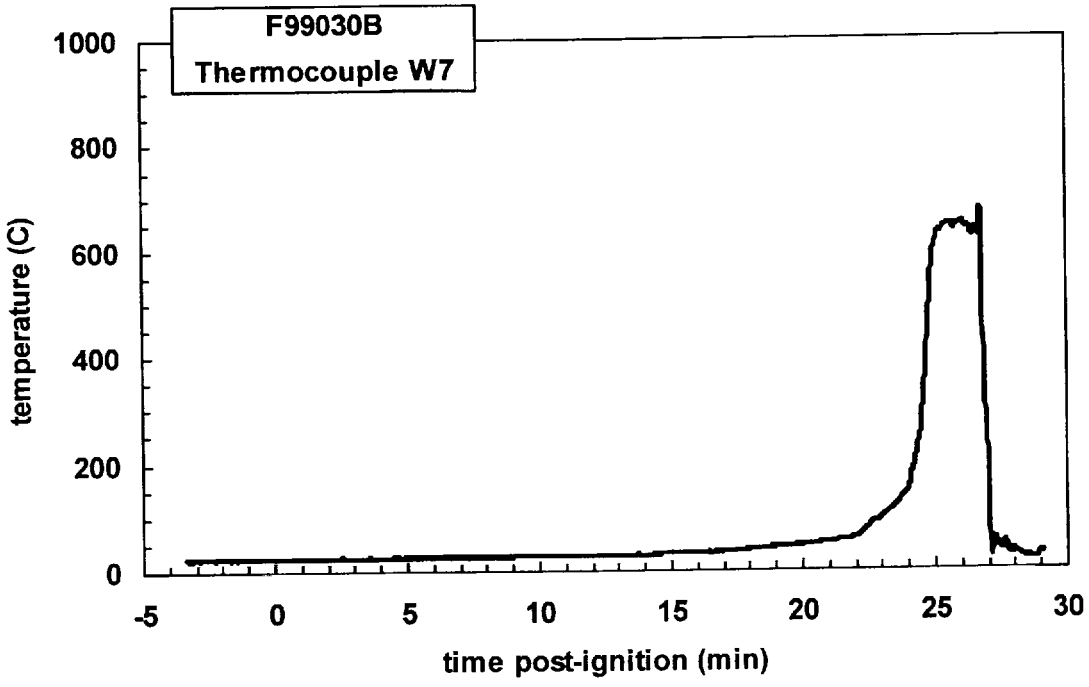

Plot C92. Fire Test F99030B. Data plot from thermocouple W7.

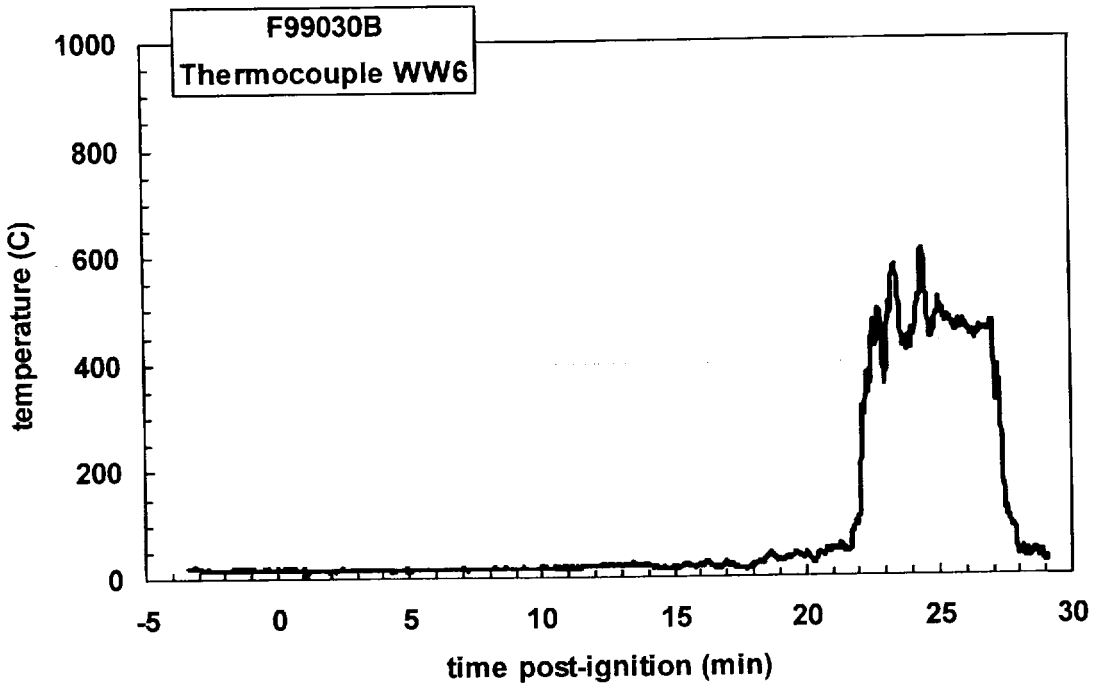

Plot C93. Fire Test F99030B. Data plot from thermocouple ww6.

APPENDIX D
ASPIRATED THERMOCOUPLE DATA

One aspirated thermocouple assembly (Medtherm Corporation) was installed in the test vehicle (Fig. D1). The aspirated thermocouple assembly was fabricated from Inconel 600 tubing. Each assembly consisted of a vertical manifold (o.d. = 0.375 in. (9.5 mm), i.d. = 0.25 in. (6.4 mm), length = 16 in. (406 mm)) with six horizontal radiation shields (o.d. = 0.25 in. (6.4 mm), i.d. = 0.19 in. (4.8 mm), length = 1.00 in. (25.4 mm)). The vertical spacing between the radiation shields along the manifold was 3 in. (75 mm). Three radial holes were drilled near the tip of each radiation shield. The holes were sized to approximately balance the airflow-rates over each thermocouple. Type-N thermocouples were inserted into each radiation shield so that the thermocouple junction was positioned approximately 0.2 in. (5.1 mm) down-stream from the inlet holes.

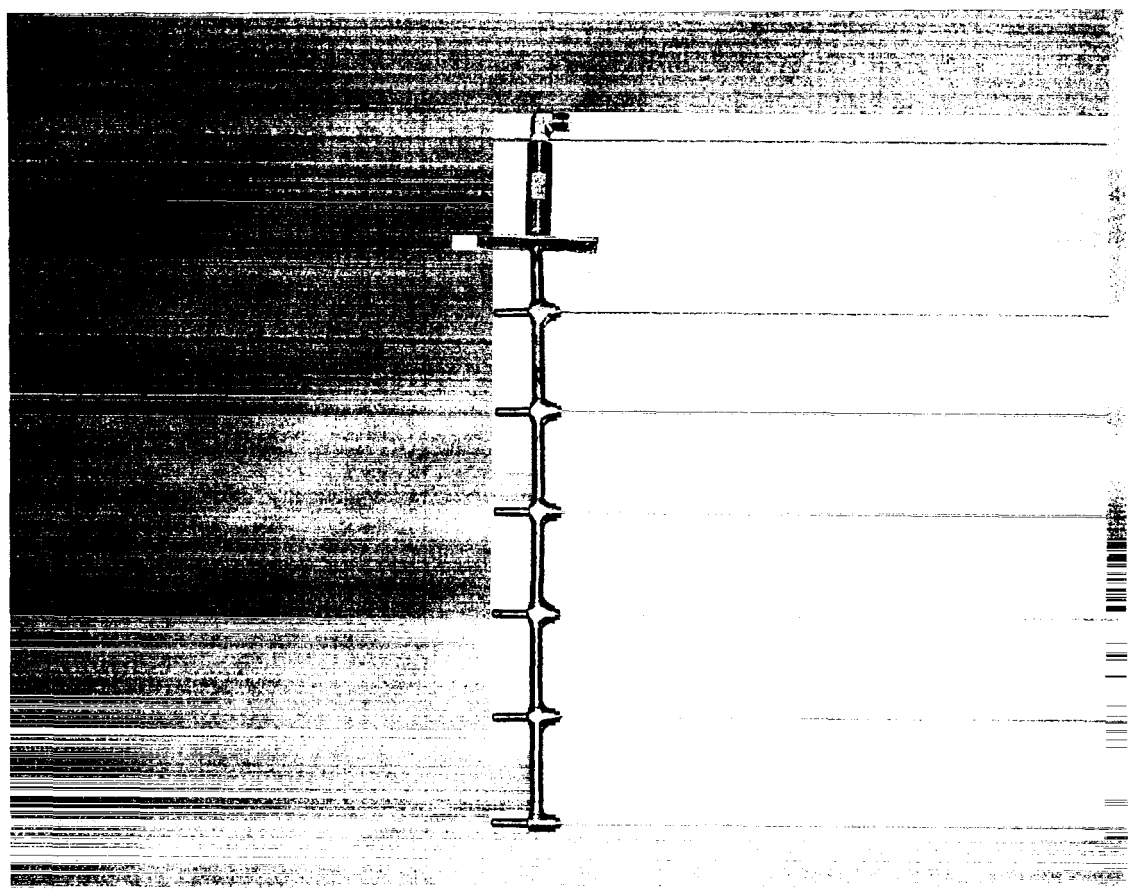

Figure D1. Fire Test F99030B. Photograph of the aspirated thermocouple assembly used in the passenger compartment of the test vehicle.

The mounting flange of the aspirated thermocouple probe assembly was attached to the roof of the vehicle. The probe extended into the passenger compartment through a hole in the roof so that all 6 thermocouples were located below the headliner. The probe was vertical and located

along the longitudinal mid-line of the vehicle approximately equidistant from the driver and passenger seat backs. The upper-most aspirated thermocouple was approximately 0.5 in. (12 mm) below the lower surface of the headliner. The manifold was connected to a rotary-vane pump with flexible copper tubing (o.d. = 0.5 in. (12 mm), length = 15 ft. (4.6 m)). The capacity of the pump was 50 L/min at atmospheric pressure.

Figures D2 and D3 show the approximate location of the aspirated thermocouple probe assembly in the test vehicle for this test. Data recorded from these aspirated thermocouples during this test is shown Plots D1 through D6. Thermocouple ASP 1-1 was at the top of the probe and ASP 1-6 was as the bottom of the probe as oriented in the test vehicle.

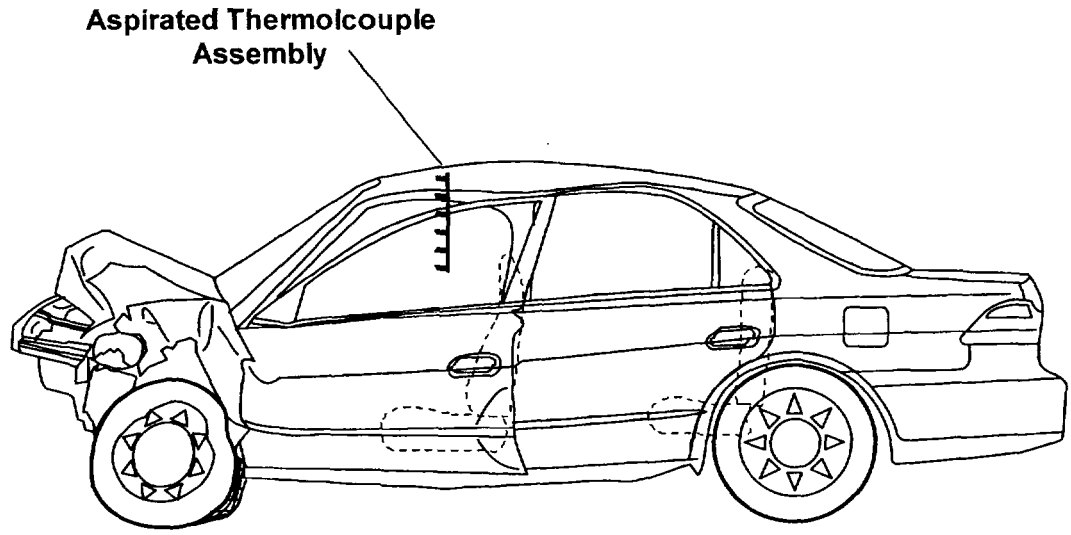

Figure D2. Fire Test F99030B. Side view of the test vehicle showing the approximate location of the aspirated thermocouple probe assembly in the passenger compartment.

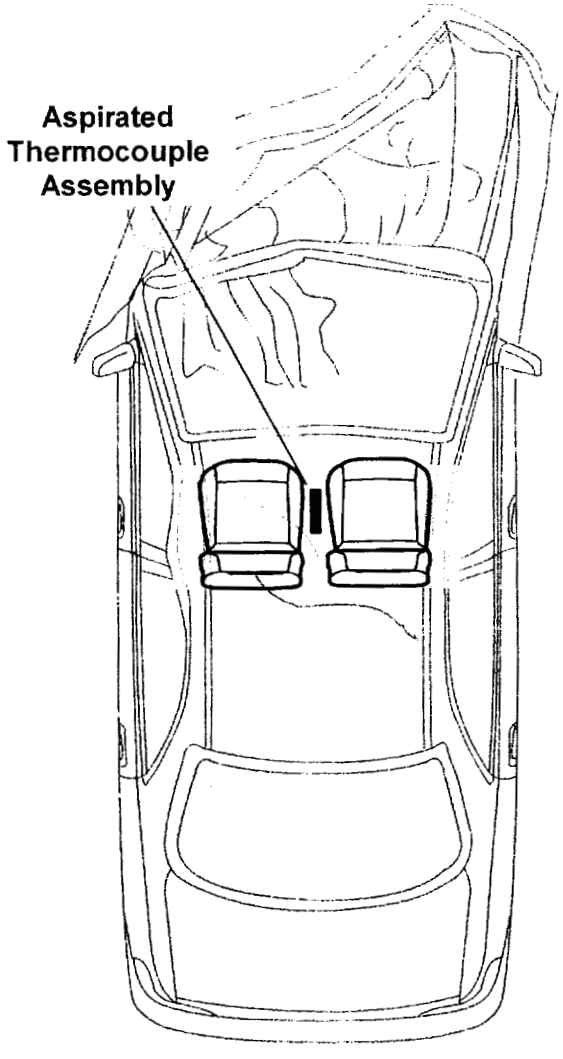

Figure D3. Fire Test F99030B. Top view of the test vehicle showing the approximate location of the aspirated thermocouple probe assembly in the passenger compartment.

REFERENCES

D1. J. S. Newman and P. A. Croce. A simple aspirated thermocouple for use in fires. *J. Fire Flamm.* **10**:326-336 (1979).

D2. N. R. Keltner and K. A. Strom. Thermal Measurement Uncertainty and Compensation. Paper in preparation.

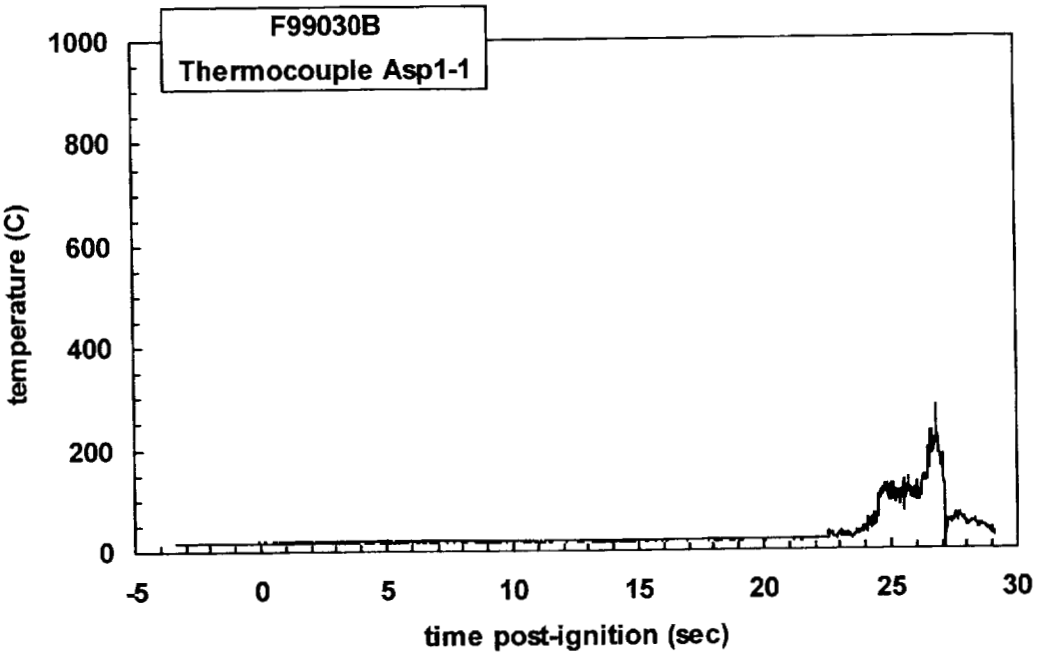

Plot D1. Fire Test F99030B. Data plot from thermocouple ASP1-1.

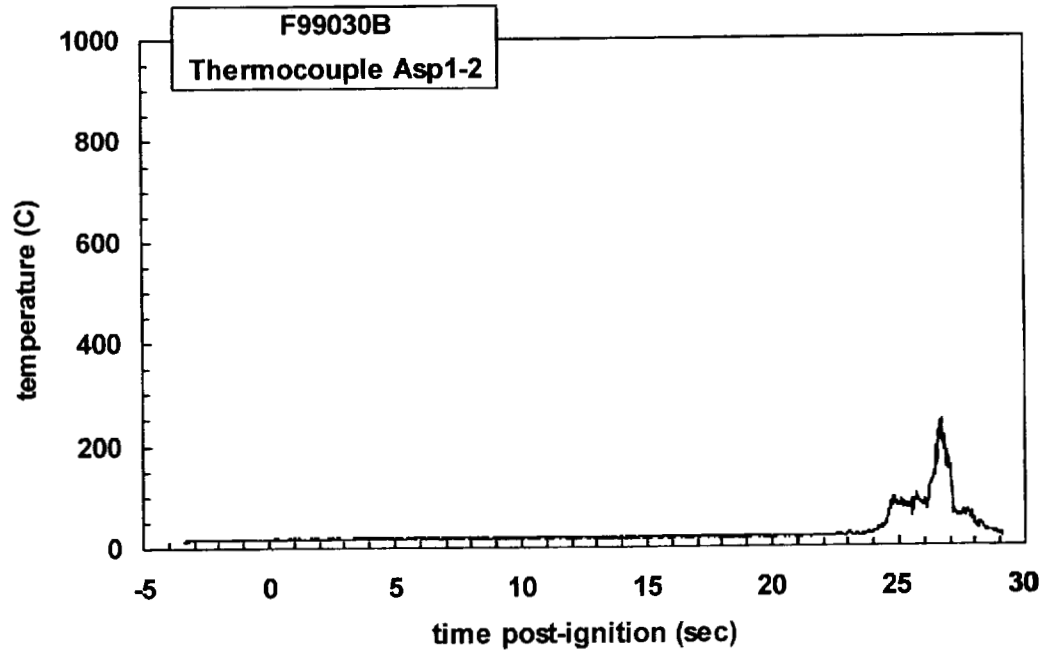

Plot D2. Fire Test F99030B. Data plot from thermocouple ASP1-2.

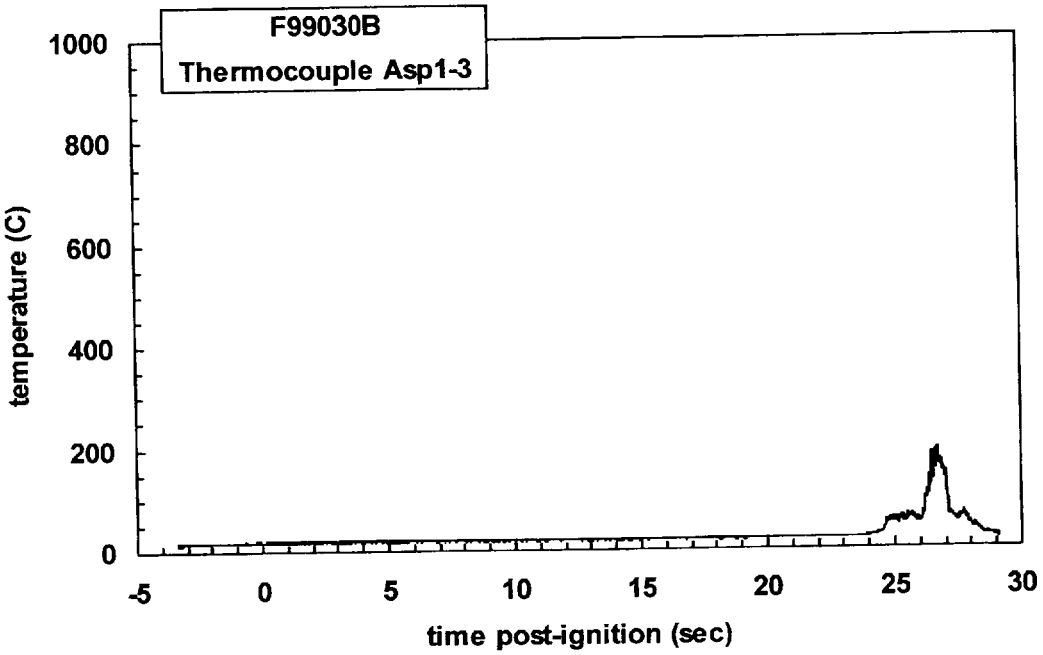

Plot D3. Fire Test F99030B. Data plot from thermocouple ASP1-3.

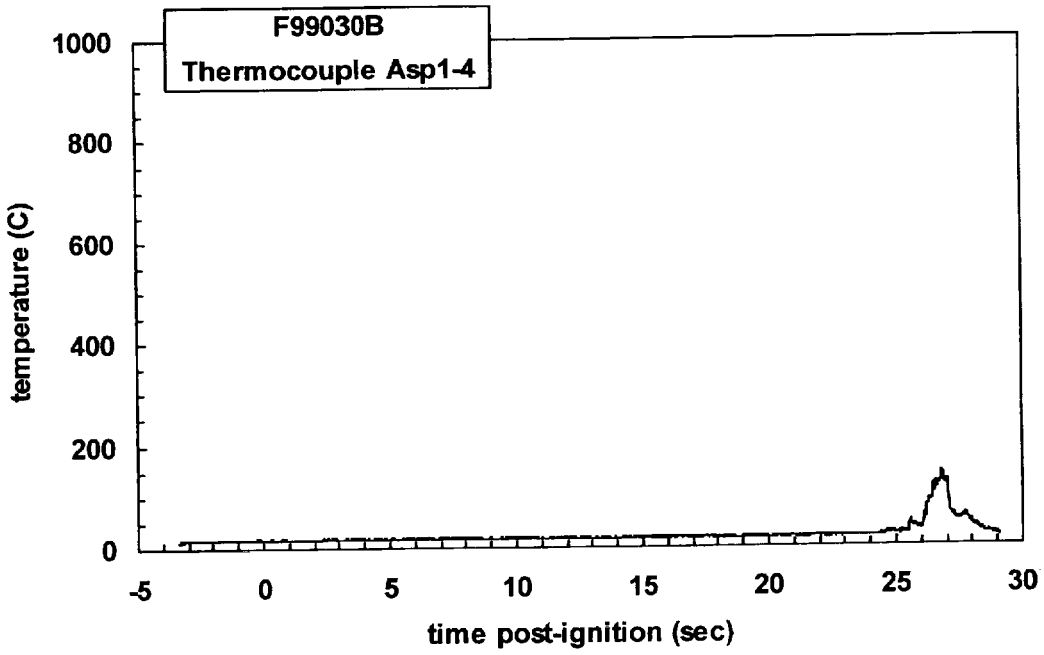

Plot D4. Fire Test F99030B. Data plot from thermocouple ASP1-4.

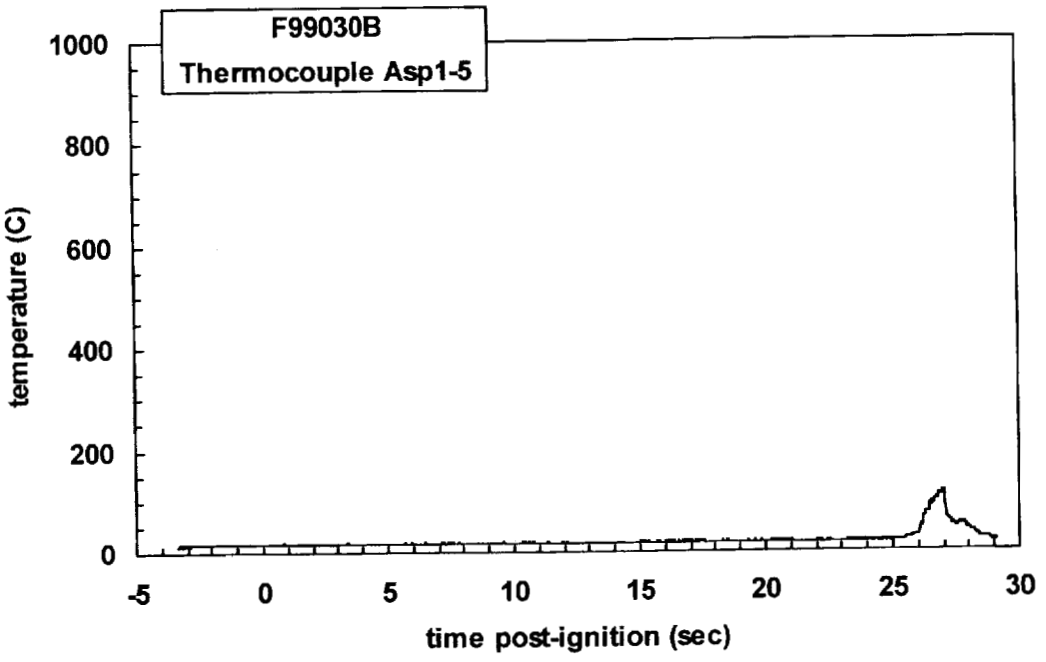

Plot D5. Fire Test F99030B. Data plot from thermocouple ASP1-5.

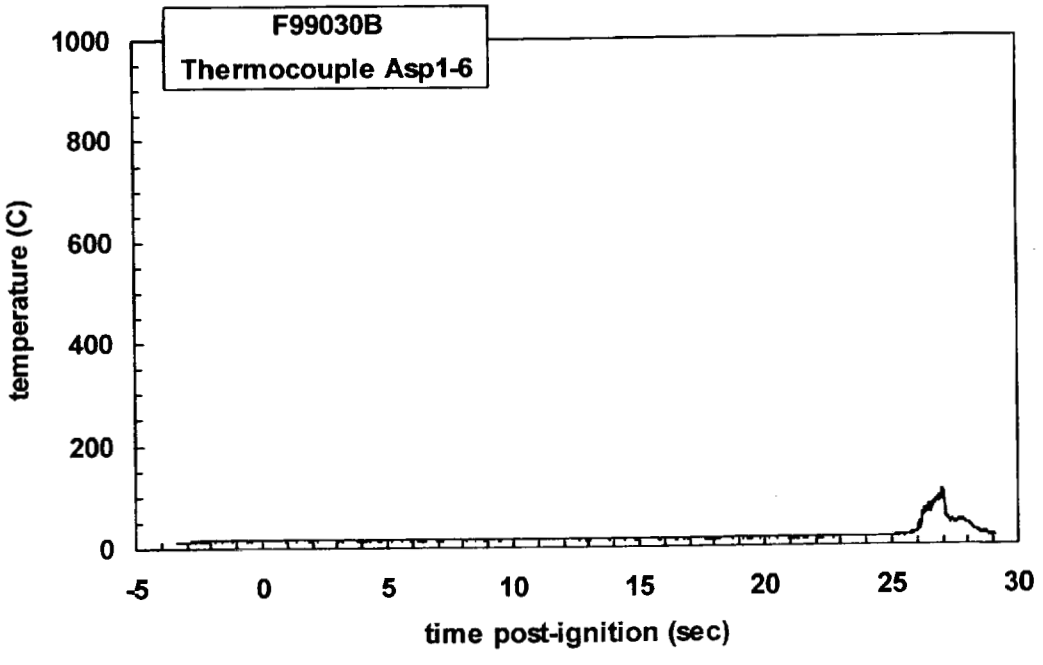

Plot D6. Fire Test F99030B. Data plot from thermocouple ASP1-6.

APPENDIX E
HEAT FLUX TRANSDUCER/RADIOMETER DATA

Heat-flux transducers (HFT) and heat flux transducer/radiometer (HFT/RAD) assemblies (64 Series, Medtherm Corporation) were used to measure convective and radiative heat transfer to selected objects in the vehicle. HFT1 was a heat flux transducers that contained one Schmidt-Boelter thermopile in a water-cooled copper body (diameter = 1 in. (25.4 mm), length = 1 in. (25.4 mm)). The face of this heat flux transducer was were coated with high-temperature optical black paint. This HFT was calibrated to 100 kW/m^2 at a reference temperature of 80°C.

HFT/RAD10 through HFT/RAD15 were heat flux transducer/radiometer assemblies. Each HFT/RAD contained two Schmidt-Boelter thermopiles in a water-cooled copper body (diameter = 1 in. (25.4 mm), length = 1 in. (25.4 mm)). The faces of the heat flux transducers were coated with high-temperature optical black paint. The radiometers had permanent sapphire windows (view-angle = 150°; optical transmittance range 0.4 to 4.2 μm). The HFTs and RADs in these assemblies were calibrated to 10 kW/m^2 at a reference temperature of 80°C.

The PC-based data system used to acquire data from the thermocouples (**APPENDIX C**) also was used to acquire data from the heat flux transducers and radiometers. The electrical signal wires from these transducers terminated in a 5-pin circular connector (165 Series, Amphenol). Each connector was plugged into a panel-mounted jack, which was hard wired to an analog-input multiplex expansion card (DBK-12, IOTech, Inc., Cleveland, OH). As with the thermocouples, the electrical shields on the signal cables were connected to the electronic chassis grounds on the analog-input expansion cards. The data acquisition software (DASYLab) was configured to sample each channel at a rate of 10 Hz and store the data in 10-point block averages.

Figure E1 shows the approximate location of HFT1 in the test vehicle. HFT1 was mounted to bracket attached to the top of the instrument panel. The transducer body was inserted into a circular clearance-hole in the windshield so that the transducer face was flush with the exterior glass outer layer. Thermocouple O1 was attached to the body of HFT1.

Figures E2 and E3 show the approximate locations of HFT/RAD10 through HFT/RAD15 in the test vehicle. HFT/RAD10, HFT/RAD11, and HFT/RAD12 were located above the left front seat as shown in Figures E1 and E2. HFT/RAD13, HFT/RAD14, and HFT/RAD15 were located above the right front seat as shown in Figures E1 and E2. Threaded rods (diameter = ½ in.) were inserted through holes in the roof above each of the front seats of the test vehicle. The lower end of each rod was secured to the seat cushion to stabilize the transducers during the test. HFT/RAD10 through HFT/RAD15 were mounted to one of these threaded rods. Thermocouples O10, O11, O12, O13, O14, and O15 were located in the bodies of each heat flux transducer or

heat flux transducer/radiometer assemblies HFT/RAD10,HFT/RAD11, HFT/RAD12, HFT/RAD13, HFT/RAD14, and HFT/RAD15, respectively.

One of the two fluid ports on each transducer was connected to the outlet manifold of a thermostated recirculating water bath, and the other fluid port was connected to the return manifold of the water bath using copper tubing (o.d. = 0.25 in.). The water in the water bath was equilibrated to 60°C before the test. Te flow rate of water through each body was approximately 100 mL/min during this test.

Data recorded from these transducers is shown in Plots E1 through E14.

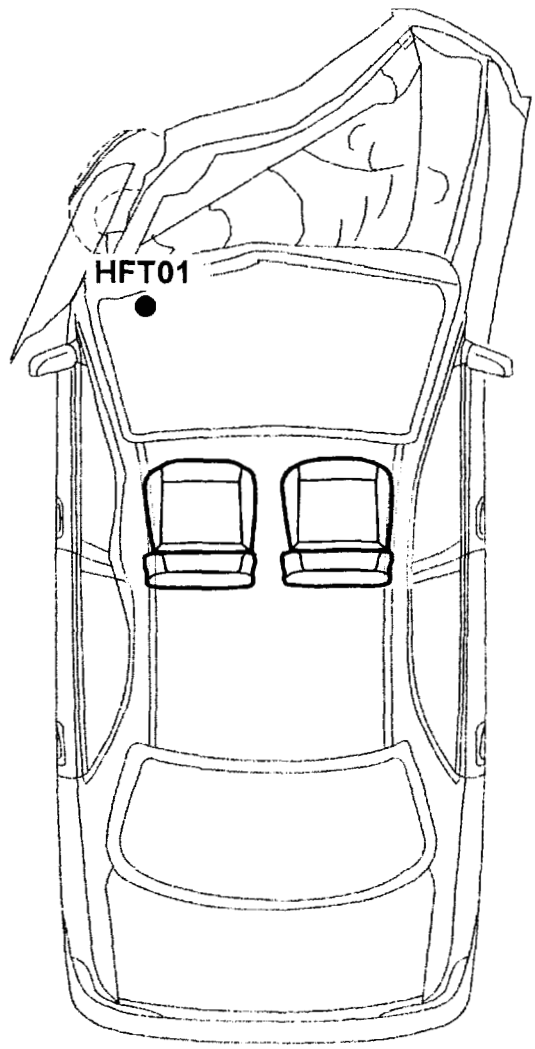

Figure E1. Fire Test F99030B. View showing the approximate locations of HFT01 in the test vehicle. HFT01 was mounted to a bracket attached to the top of the instrument panel with the transducer face facing forward through circular clearance hole cut in the windshield.

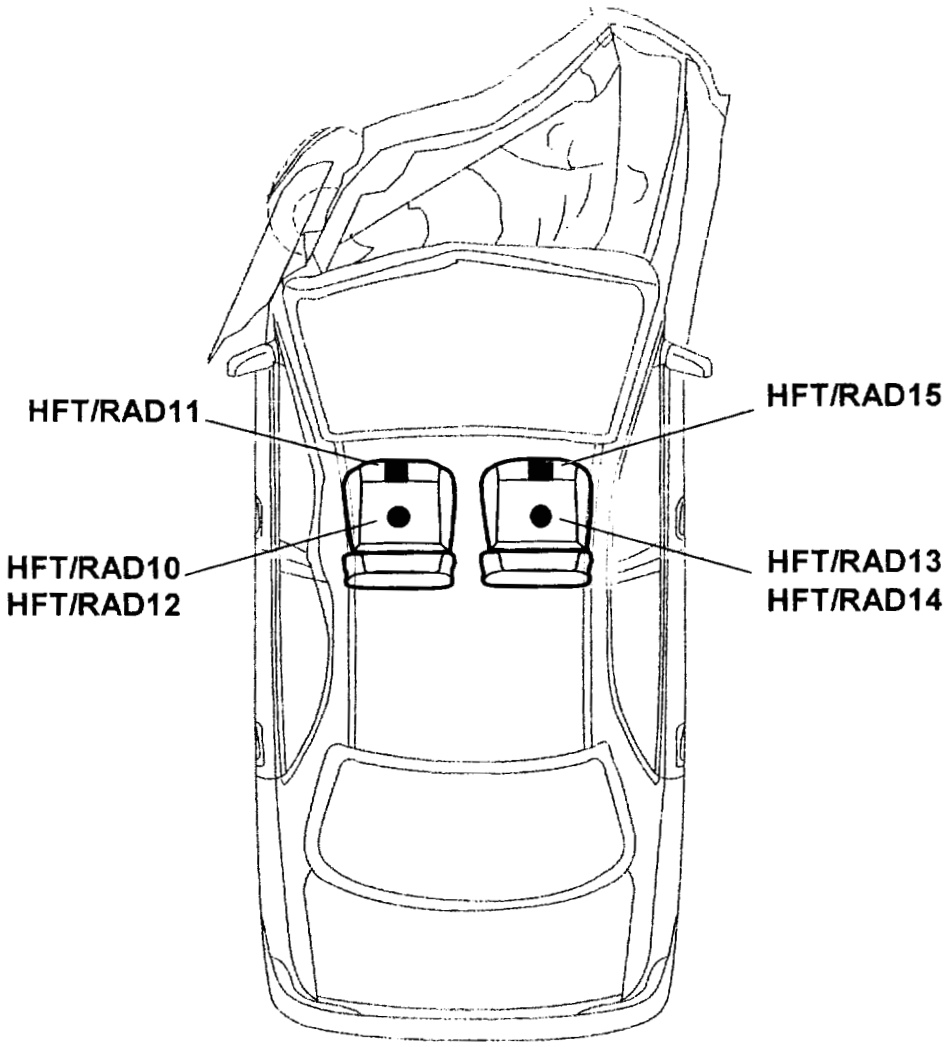

Figure E2. Fire Test F99030B. Top view of the test vehicle showing the approximate locations of heat flux transducer/radiometer (HFT/RAD) assemblies mounted in the test vehicle. HFT/RAD10 was located approximately 80 cm above the left front seat cushion facing upward. HFT/RAD11 was located on the left front seat cushion facing forward. HFT/RAD12 was located approximately 80 cm above the left front seat cushion facing forward. HFT/RAD13 was located approximately 80 cm above the right front seat cushion facing forward. HFT/RAD14 was located approximately 80 cm above the right front seat cushion facing upward. HFT/RAD15 was located on the right front seat cushion facing forward.

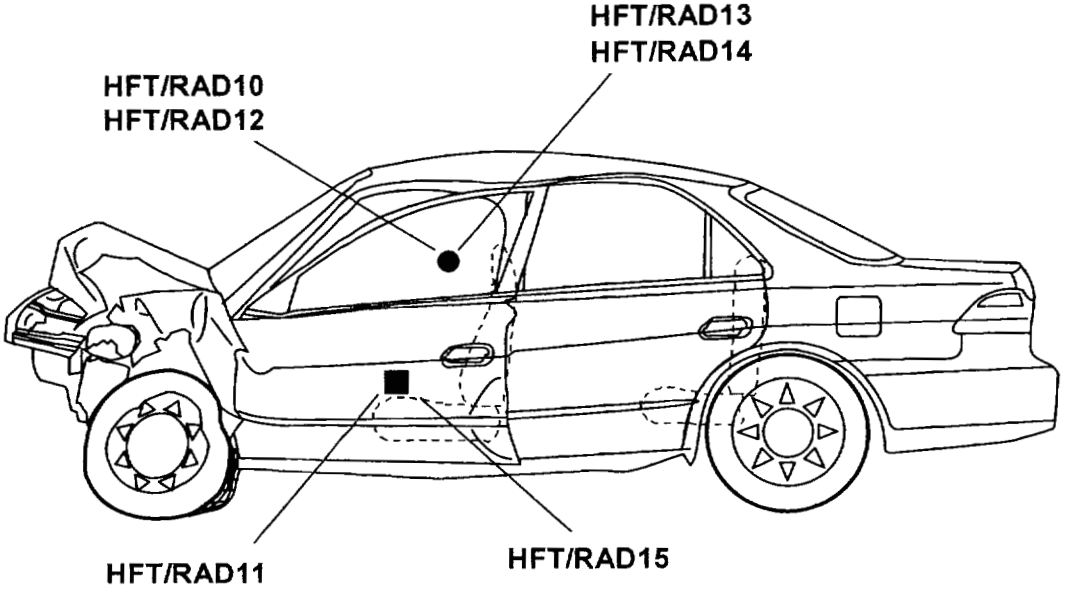

Figure E3. Fire Test F99030B. Side view of the test vehicle showing the approximate locations of heat flux transducer/radiometer (HFT/RAD) assemblies in the test vehicle. See the caption to Figure E2 for a description of the location of each transducer

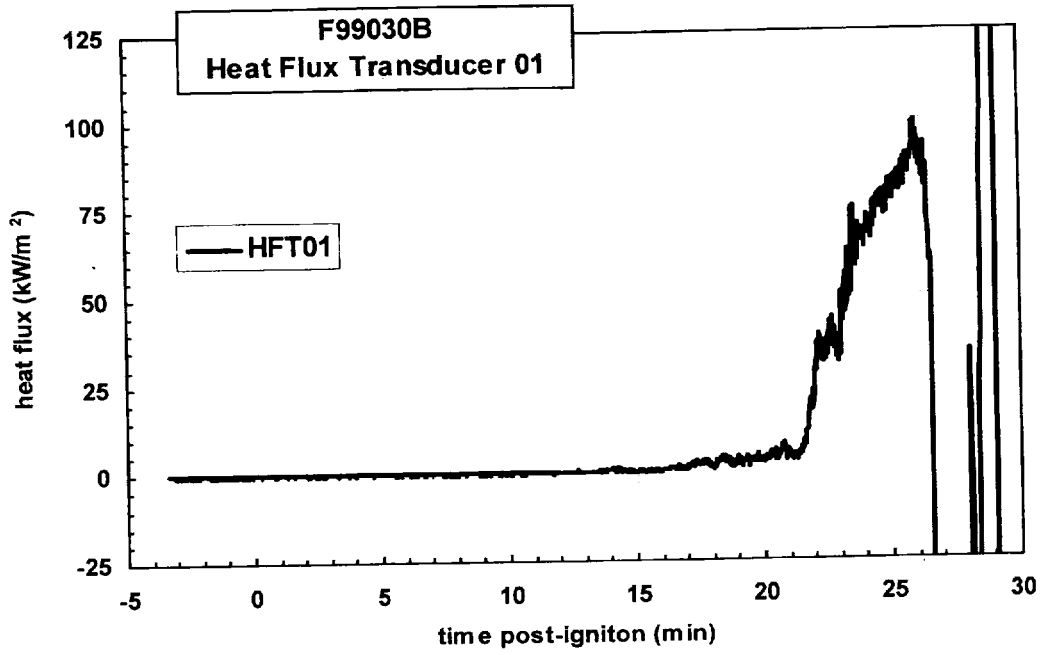

Plot E1. Fire Test F99030B. Data plot from Heat Flux Transducer 01. Thermocouple O1 malfunction during this test. No valid data was recorded from Thermocouple O1 during this test.

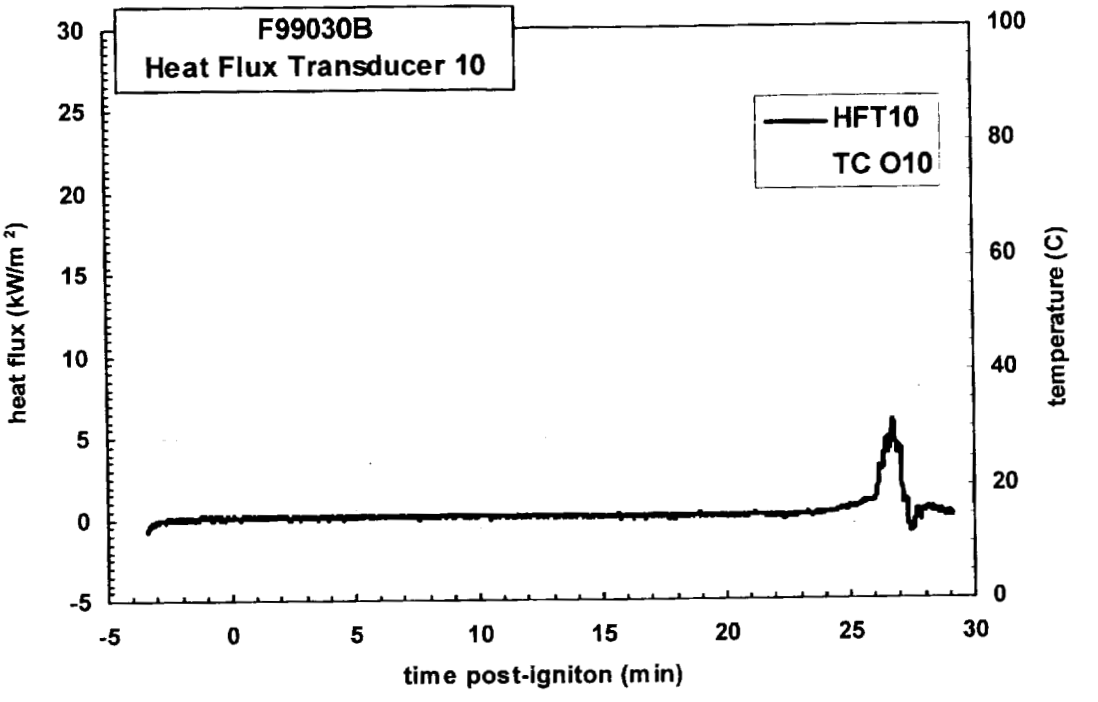

Plot E2. Fire Test F99030B. Data plot from Heat Flux Transducer 10.

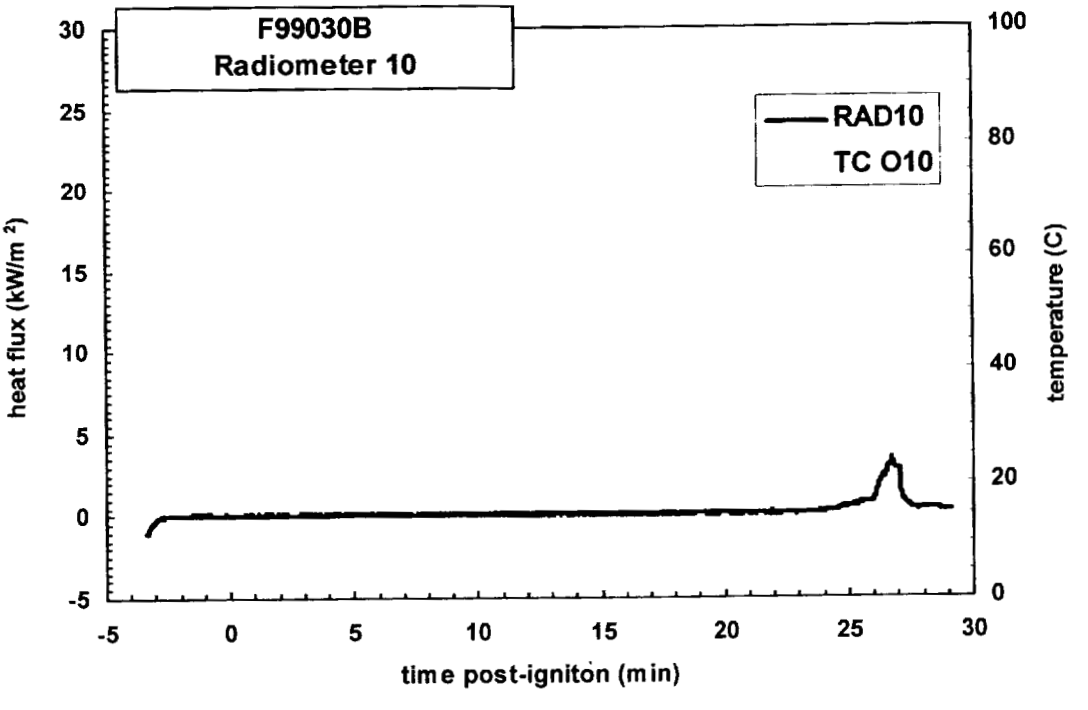

Plot E3. Fire Test F99030B. Data plot from Radiometer 10.

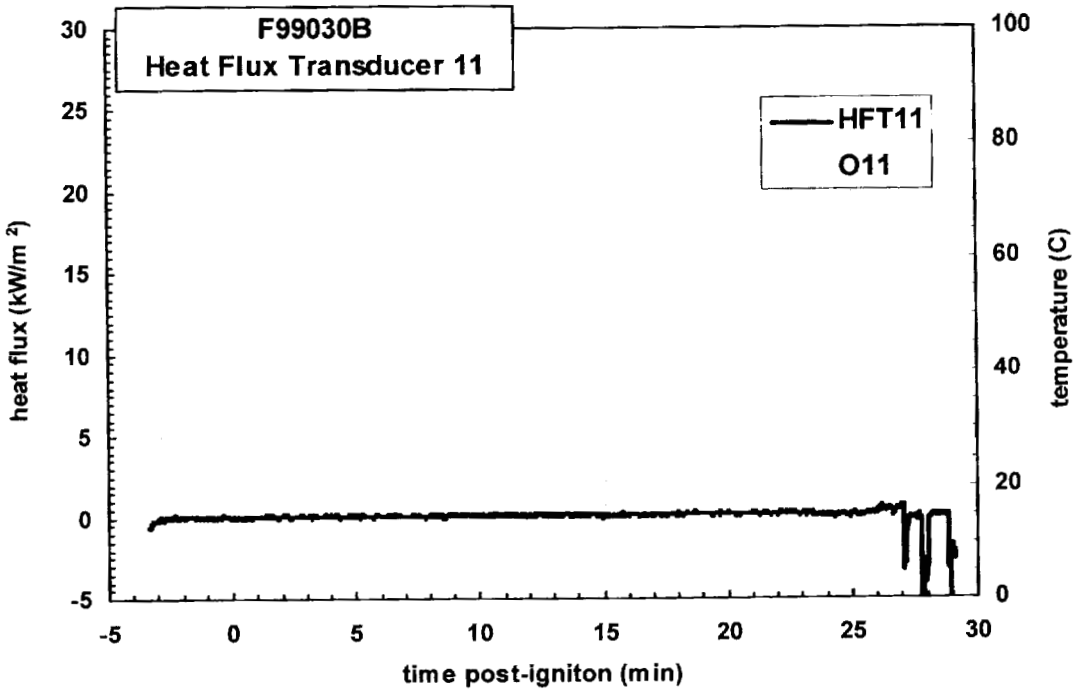

Plot E4. Fire Test F99030B. Data plot from Heat Flux Transducer 11.

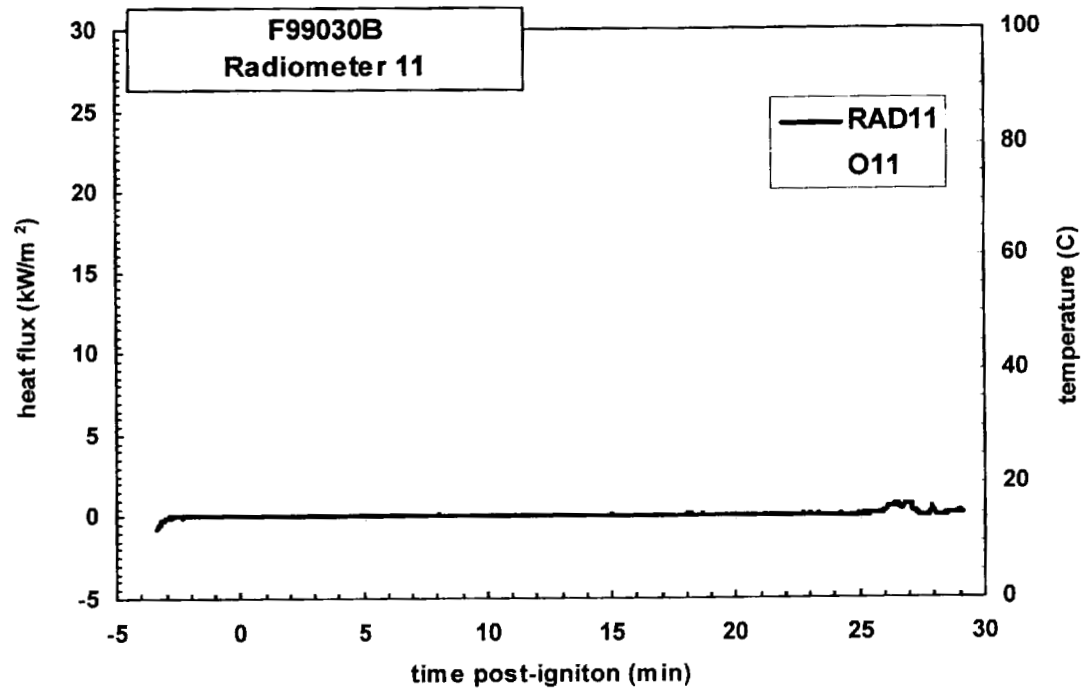

Plot E5. Fire Test F99030B. Data plot from Radiometer 11.

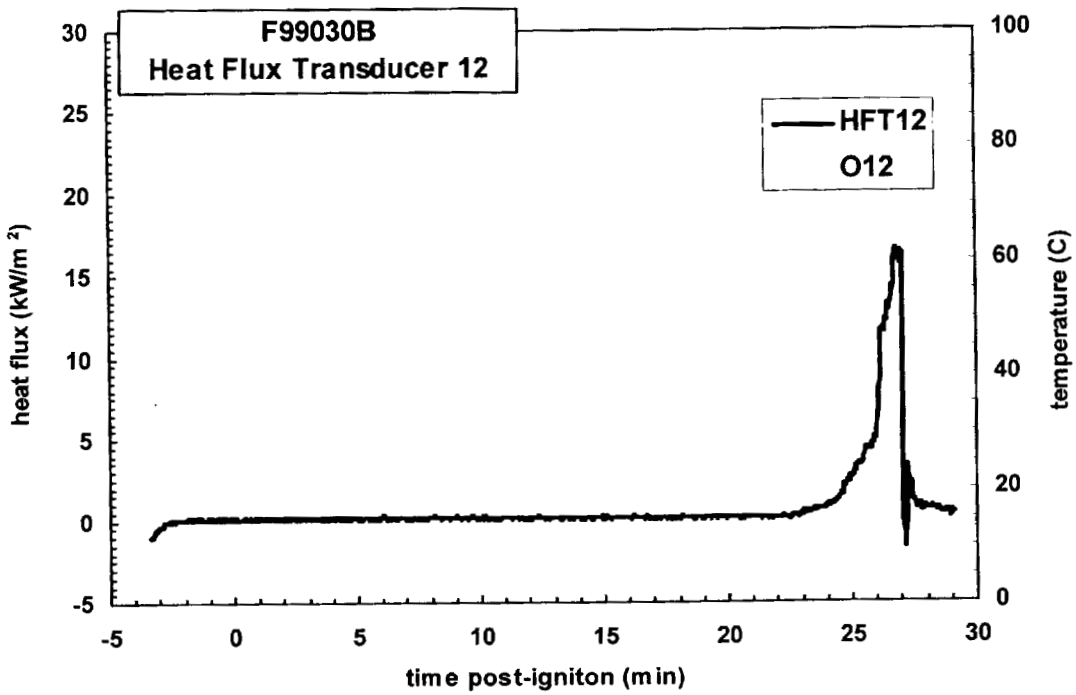

Plot E6. Fire Test F99030B. Data plot from Heat Flux Transducer 12.

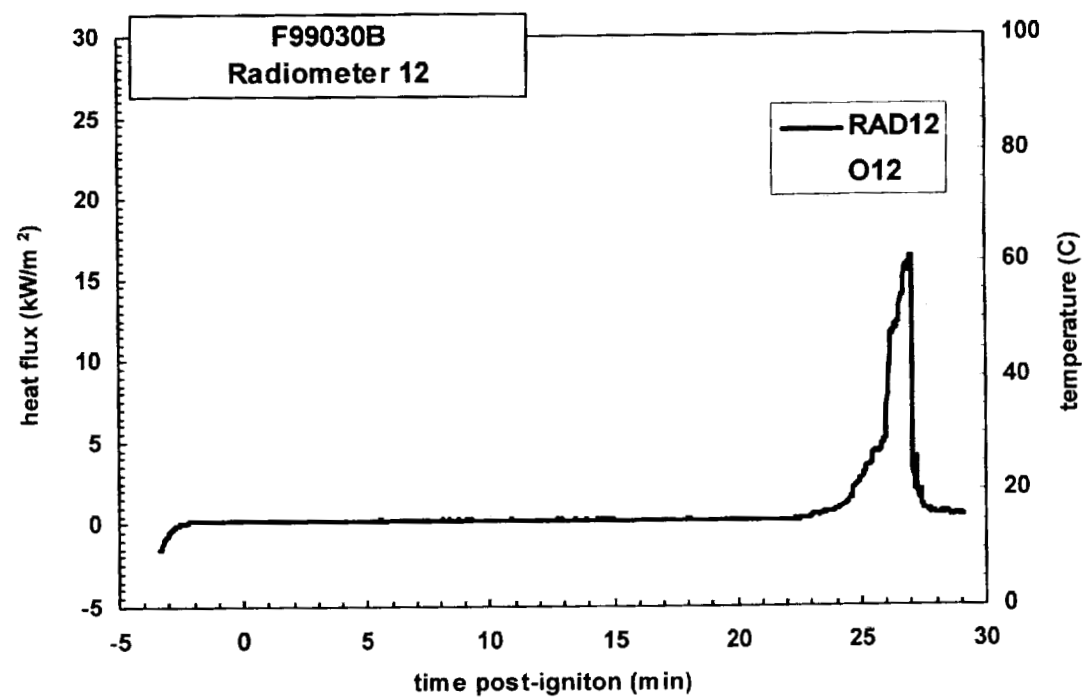

Plot E7. Fire Test F99030B. Data plot from Radiometer 12.

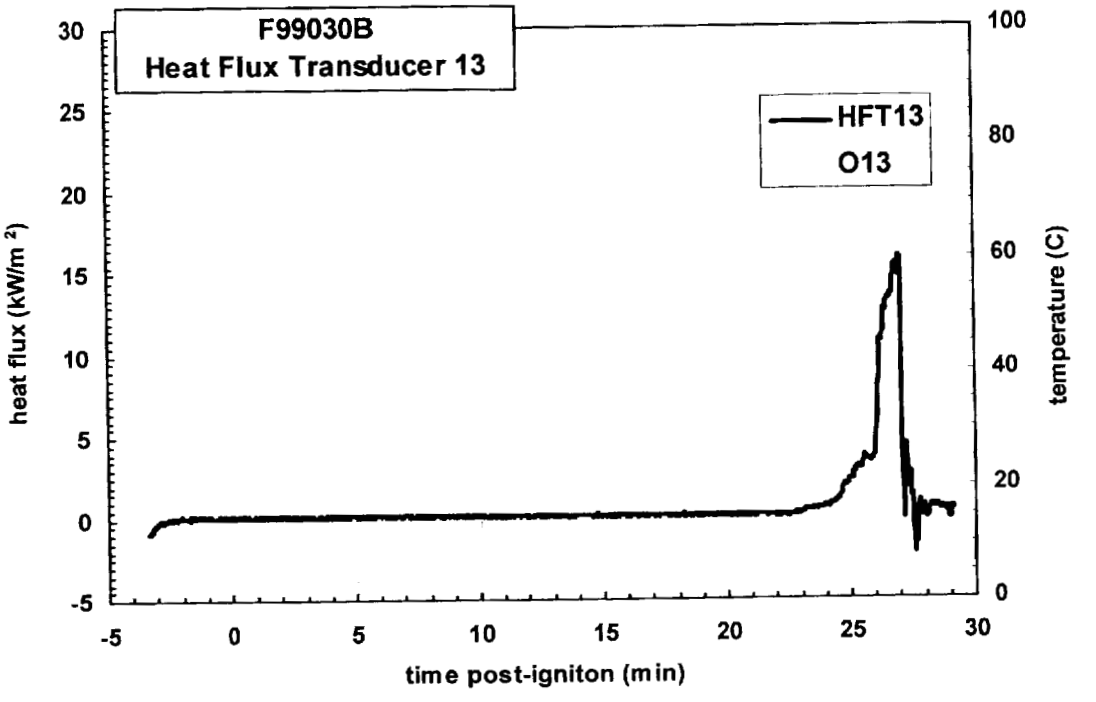

Plot E8. Fire Test F99030B. Data plot from Heat Flux Transducer 13.

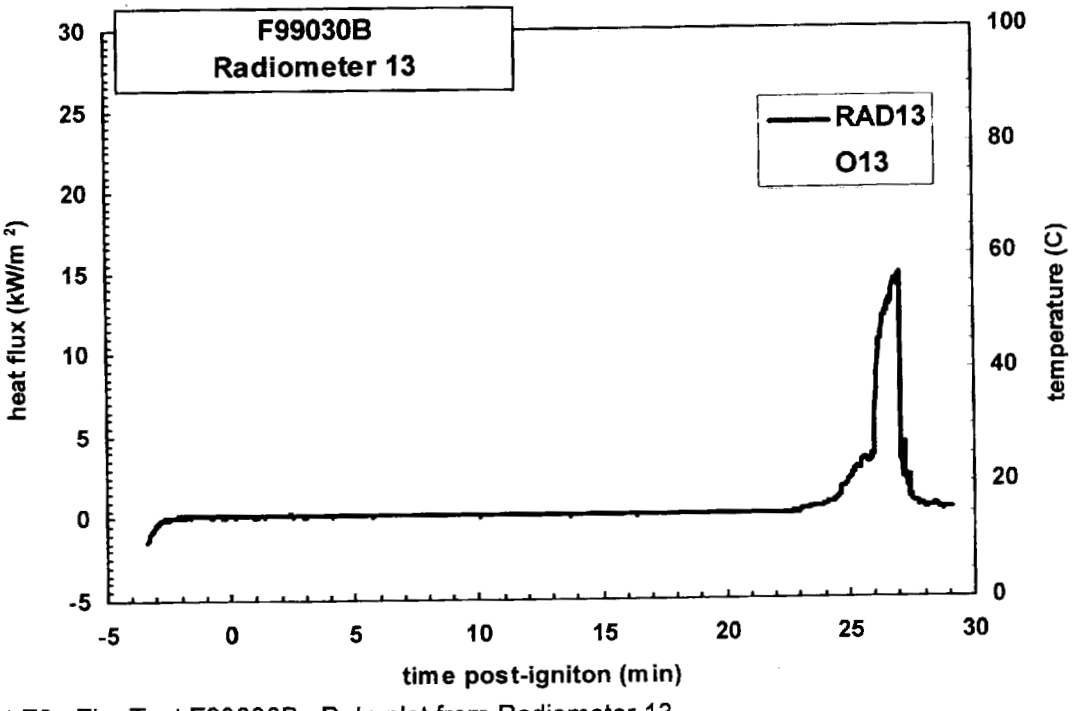

Plot E9. Fire Test F99030B. Data plot from Radiometer 13.

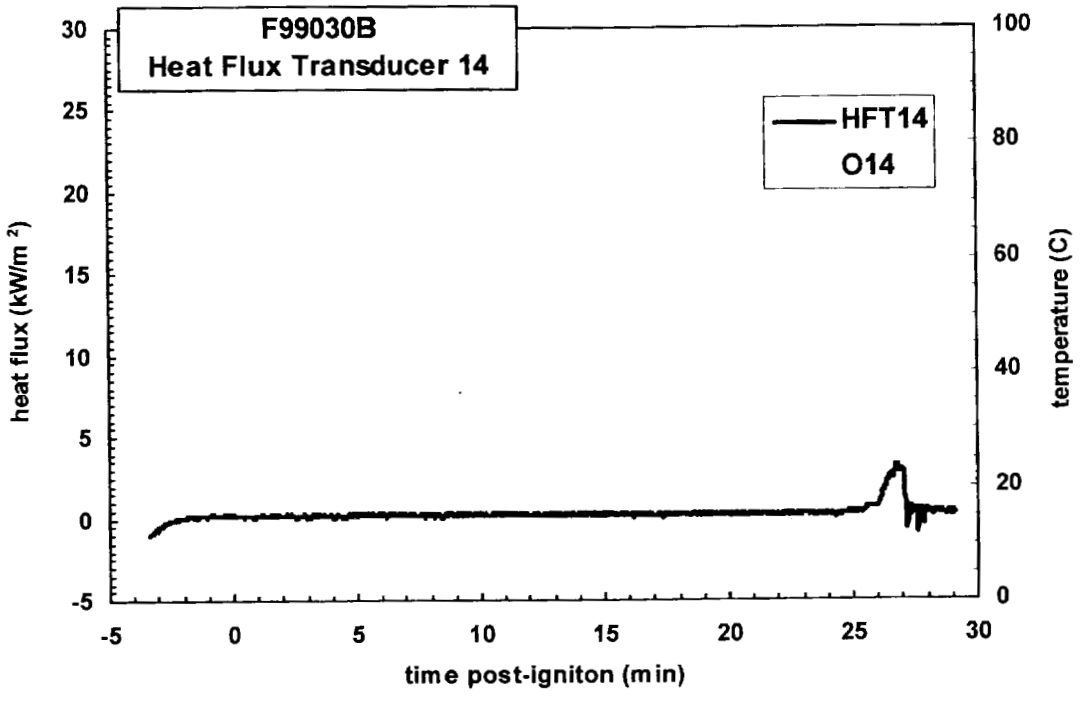

Plot E10. Fire Test F99030A. Data plot from Heat Flux Transducer 14.

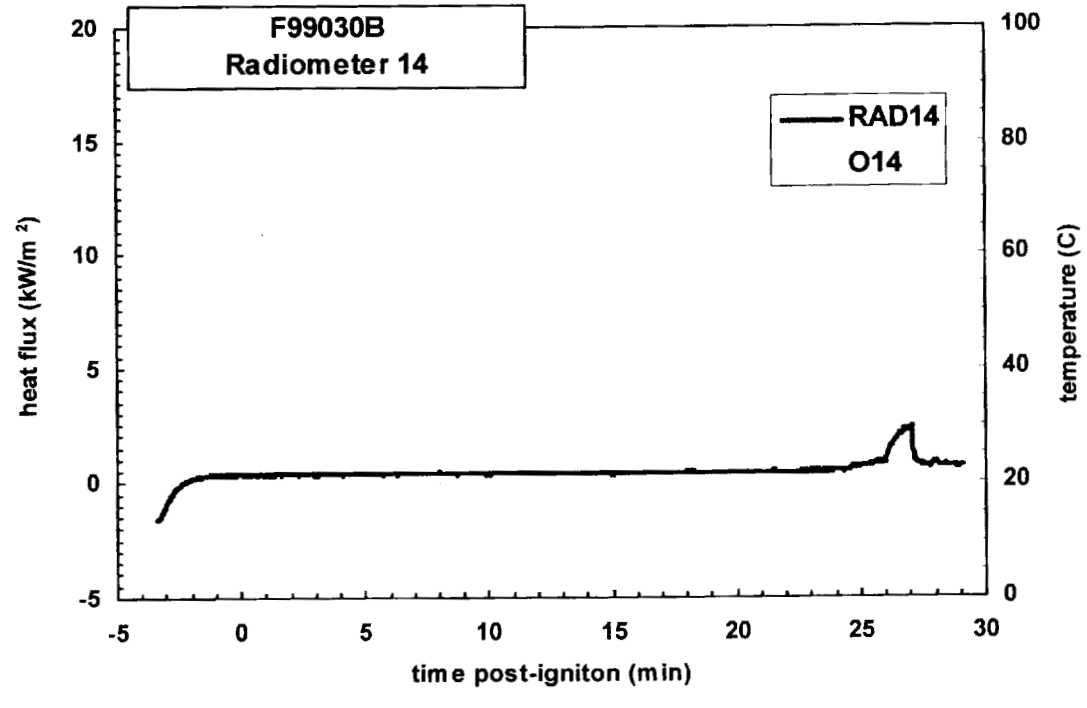

Plot E11. Fire Test F99030B. Data plot from Radiometer 14.

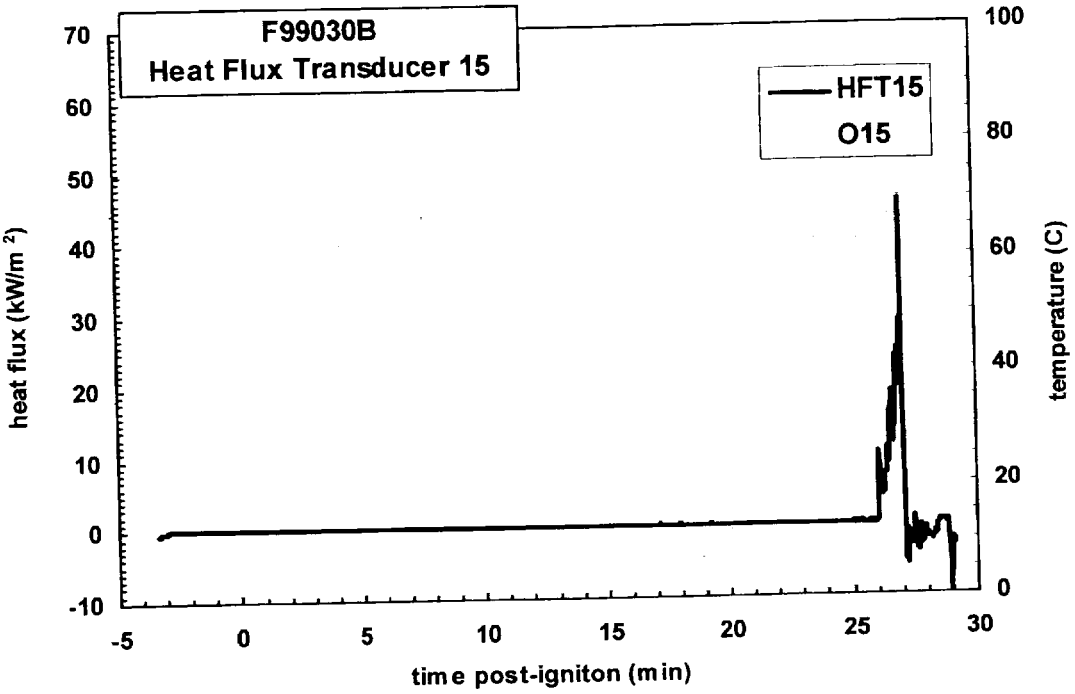

Plot E12. Fire Test F99030B. Data plot from Heat Flux Transducer 15.

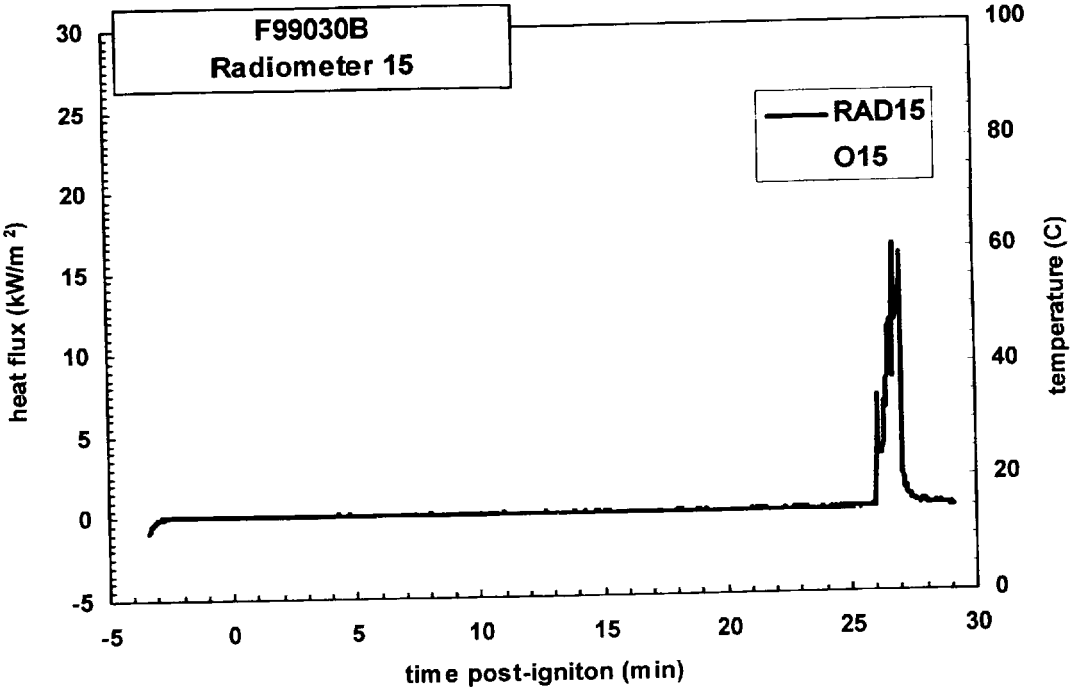

Plot E13. Fire Test F99030B. Data plot from Radiometer 15.

APPENDIX F
PRESSURE AND AIRFLOW MEASUREMENTS

Four pressure taps were installed in the test vehicle for this test in the following locations: at the exterior surface of the dash panel slightly right of center, at the interior surface of the dash panel slightly right of center, above the carpet in the foot area in front of the left side of the rear bench seat, and below the headlining panel above the foot area in front of the left side of the rear bench seat. A bi-directional flow probe was installed at the base of the windshield along the longitudinal center line of the test vehicle.

Figures F1 and F2 show the approximate locations of pressure taps at the inner and outer surfaces of the dash panel of the test vehicle.

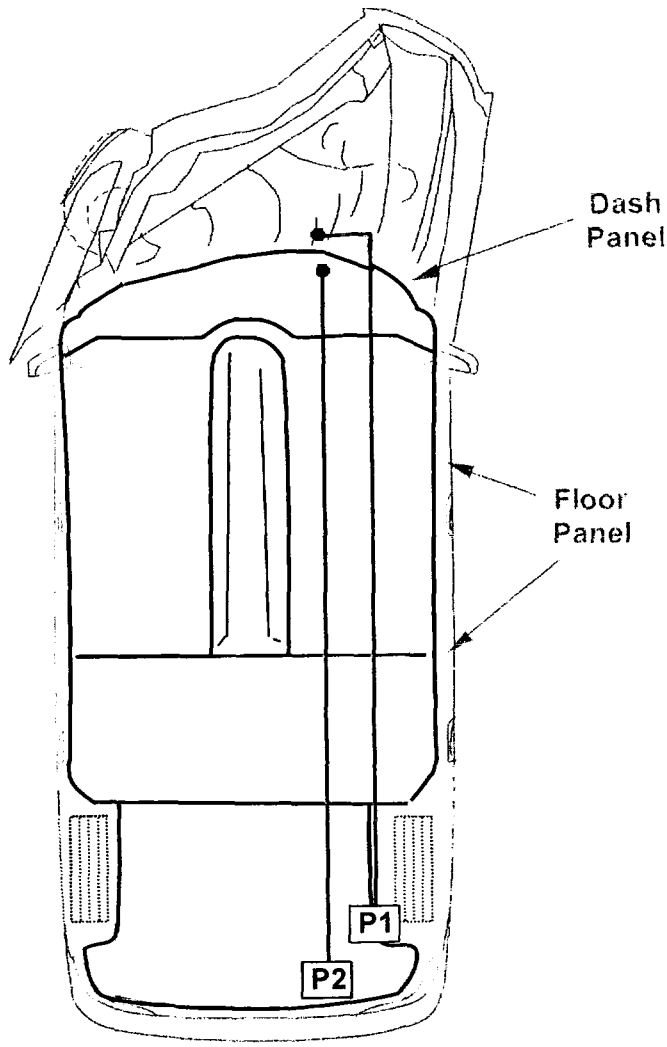

Figure F1. Fire Test F99030B. Top view showing the approximate locations of pressure taps at the inner and outer surfaces of the dash panel.

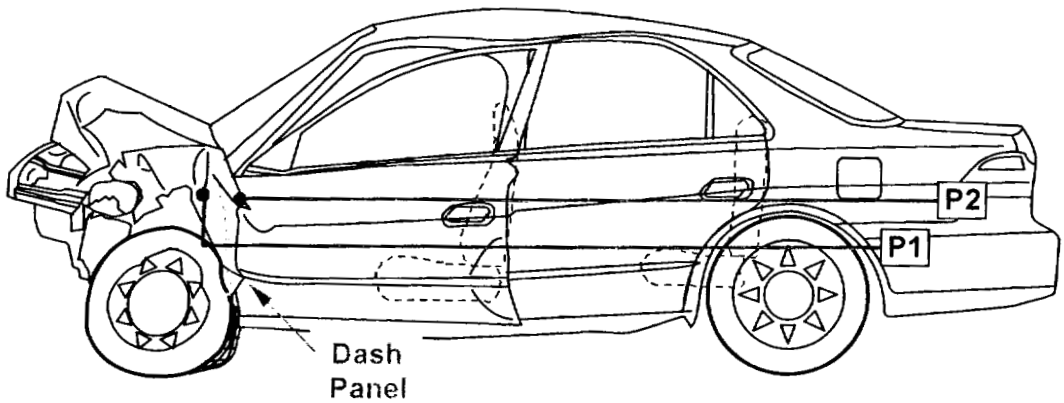

Figure F2. Fire Test F99030B. Side view showing the approximate locations of pressure taps at the inner and outer surfaces of the dash panel.

Figures F3 and F4 show the approximate locations of pressure taps on the roof and floor in the passenger compartment of the test vehicle, and a bi-directions flow probe at the base of the windshield of the test vehicle.

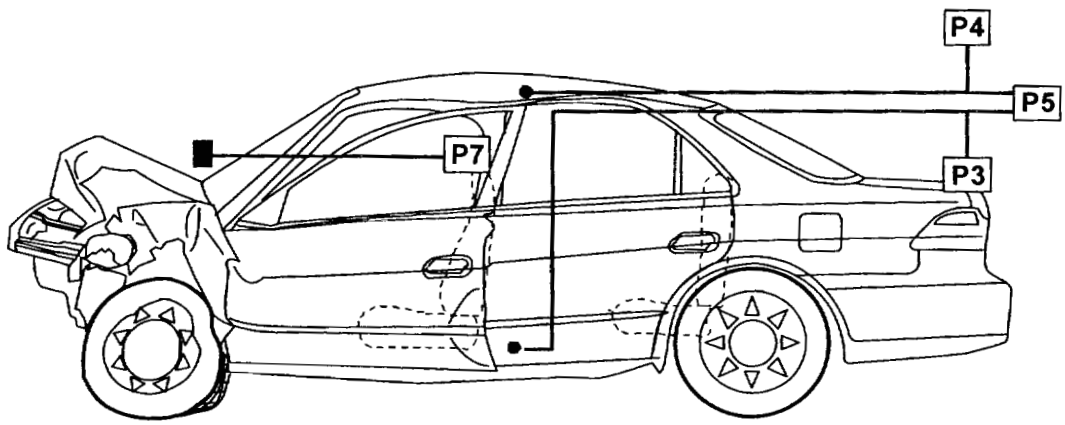

Figure F3. Fire Test F99030B. Side view showing the approximate locations of pressure taps at the inner and outer surfaces of the dash panel.

Each pressure tap was constructed from stainless steel tubing (o.d. = 0.250 in.). A union-T fitting with compression-type couplings (Parker) was attached to the inlet of the stainless steel tubing, with two of the three positions in the union-T fitting were left open. The other end of stainless steel tubing was connected to a pressure gauge with solvent-resistant flexible tubing (Tygon Masterflex® 6049; i.d. = 0.250 in.; o.d. = 0.438 in.). The total length of the stainless steel and flexible tubing was approximately 10 m.

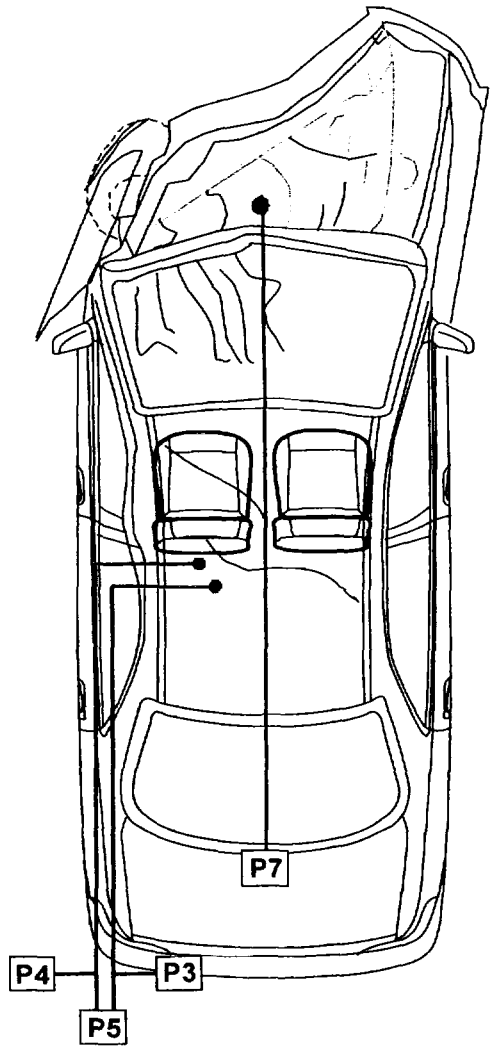

Figure F4. Fire Test F99030B. Top view showing the approximate locations of pressure taps at the roof and floor of the test vehicle, and of a bi-directional flow probe at the base of the windshield of the test vehicle.

A bi-directional flow probe was installed in the test vehicle so that it was located just outboard of the center of the upper edge of the left quarter opening. This probe was used to determine the velocity and direction of airflow through the window opening during the test. The stainless steel tubes leading from the flow probe were connected to pressure gauges with solvent-resistant resistant flexible tubing (Tygon Masterflex® 6049; i.d. = 0.250 in.; o.d. = 0.438 in.). The total length of tubing was approximately 10 m.

The velocity of gas flow through the window opening in the driver's door was calculated from the pressure difference measured across the bi-directional probe using the following relationship:

$$V = 0.070\sqrt{T\Delta p} \qquad \text{(F1)}$$

where V is the gas velocity in m/s, T is the gas temperature in degrees Kelvin, and Δp is the pressure difference in Pascals (N/m^2) [F1 and F2].

Pressure gauges (Model C-264, Setra Systems, Acton, MA) with two pressure ranges were used for this test: - 0.5 to 0.5 (± 0.0013) in. W.C. (-124.5 to 124.5 Pascal) and -0.1 to 0.1 (± 0.0003) in. W.C. (-24.9 to 24.9 Pascal). Both gauges were accurate to 0.25% full scale. The gages were powered with a 24 volt non-regulated power supply (Setra Systems).

The high-pressure inlet of Pressure Gauge P1 was connected to the pressure tap located at the outer surface of the dash panel. The low-pressure inlet of Pressure Gauge P1 was left open to the atmosphere. The high-pressure inlet of Pressure Gauge P2 was connected to the pressure tap located at the inner surface of the dash panel. The low-pressure inlet of Pressure Gauge P2 was left open to the atmosphere. The high-pressure inlet of Pressure Gauge P3 was connected to the pressure tap above the carpet in the foot area in front of the left side of the rear bench seat. The low-pressure inlet of Pressure Gauge P3 left open to the atmosphere. The high-pressure inlet of Pressure Gauge P4 was connected to the pressure tap located below the headlining panel above the foot area in front of the left side of the rear bench seat. The low-pressure inlet of Pressure Gauge P4 left open to the atmosphere. The high-pressure inlet of Pressure Gauge P5 was to the pressure tap located below the headlining panel above the foot area in front of the left side of the rear bench seat. The low-pressure inlet of Pressure Gauge P5 was connected to the pressure tap located above the carpet in the foot area in front of the left side of the rear bench seat. Pressure Gauge P6 was not used in this test. The low- and high-pressure inlets of pressure gauge P7 were connected to the bi-directional flow probe.

The PC-based data acquisition system described in **APPENDIX C** also was used to record the electronic signals from the pressure gauges during the test. The signal leads from the pressure gauges were plugged into panel-mounted connectors, which were hard-wired to a low-gain analog-input multiplex expansion card (DBK12, IOTech). The analog-input expansion card was interfaced to the main A/D card in the PC. The signal from each pressure gauge was sampled at a rate of 100 Hz. The analog data was stored to a data file in 100-point block-averages so that the effective sampling rate during the test was 1 Hz.

Plots of the pressures recorded with Pressure Gauges P1 through P7 are shown in Plots F1 through F6. Steam generated by the start of fire suppression and water entering the pressure

taps caused the positive- and negative-going pressure deflections at about 27 minutes post-ignition.

REFERENCERS

F1. N. R. Keltner and J. L. Moya. Defining the thermal environment in fire tests. *Fire and Materials* **14**: 133-138, 1989.

F2. B. J. McCaffrey and G. A. Heskestad. Robust bi-directional low-velocity probe for flame and fire application. *Combustion and Flame* **26**: 125-127, 1976.

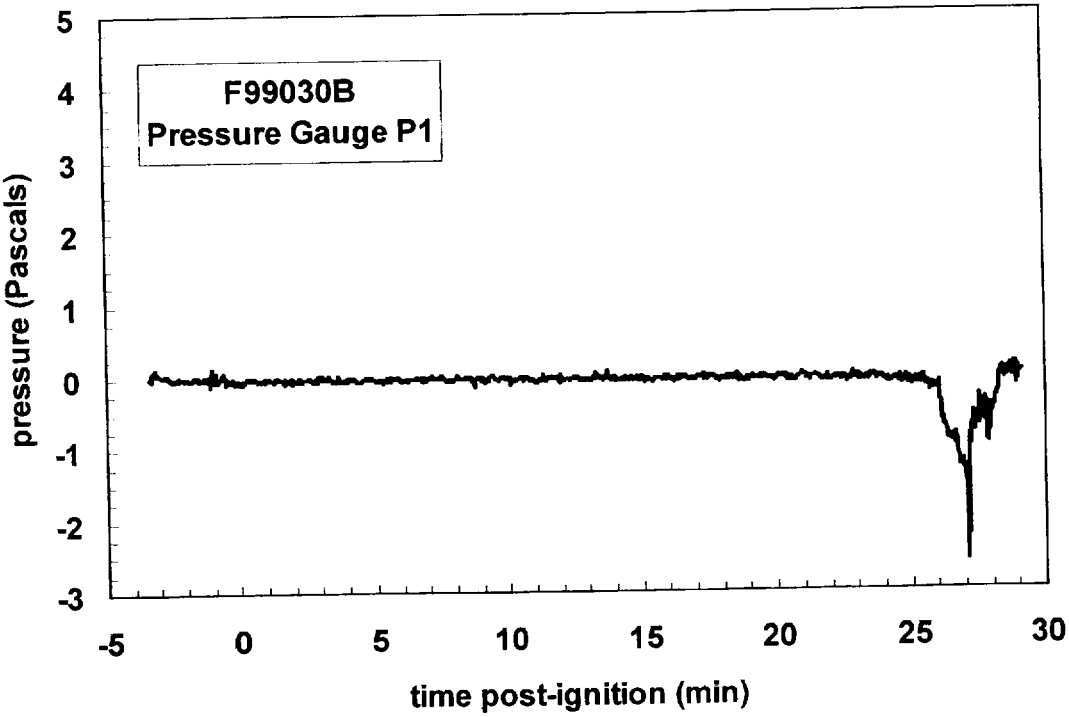

Plot F1. Fire Test F99030B. Absolute pressure at the exterior surface of the dash panel relative to atmospheric pressure measured with pressure gauge P1.

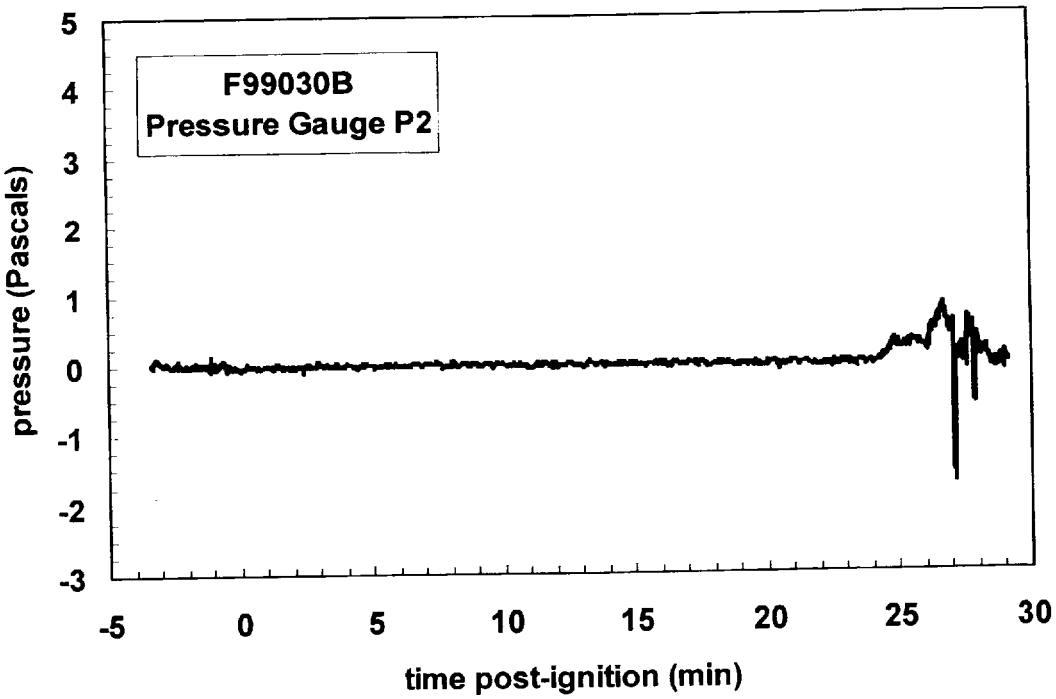

Plot F2. Fire Test F99030B. Absolute pressure at the interior surface of the dash panel relative to atmospheric pressure measured with pressure gauge P2.

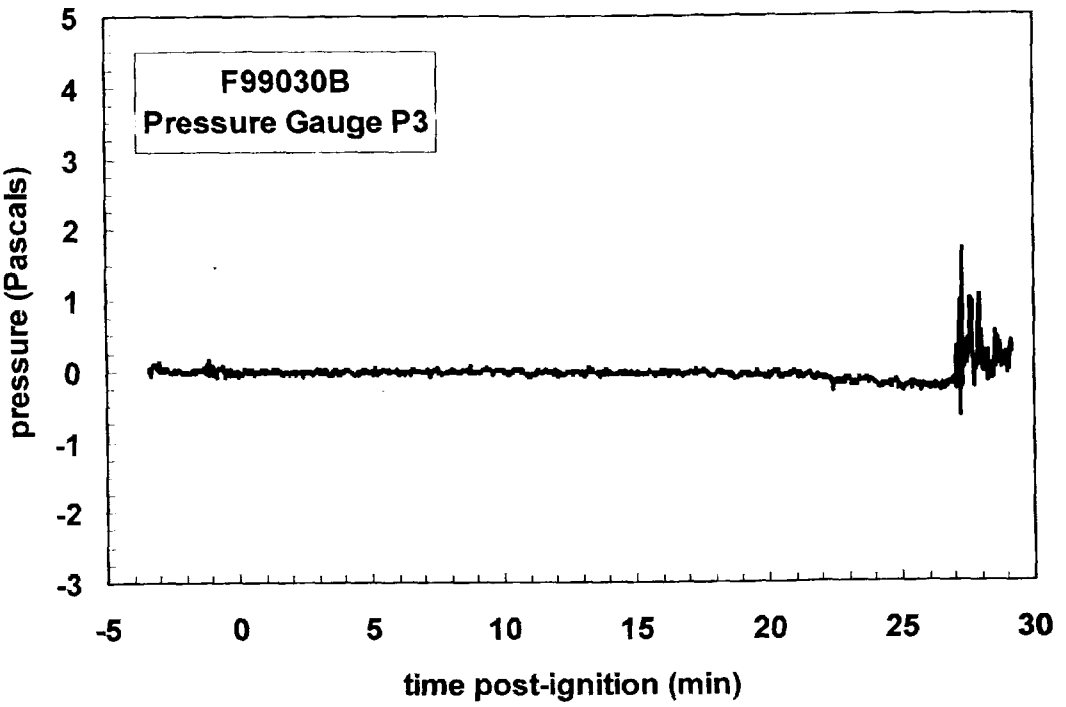

Plot F3. Fire Test F99030B. Absolute pressure above the carpet in front of the left side of the rear bench seat relative to atmospheric pressure measured with pressure gauge P3.

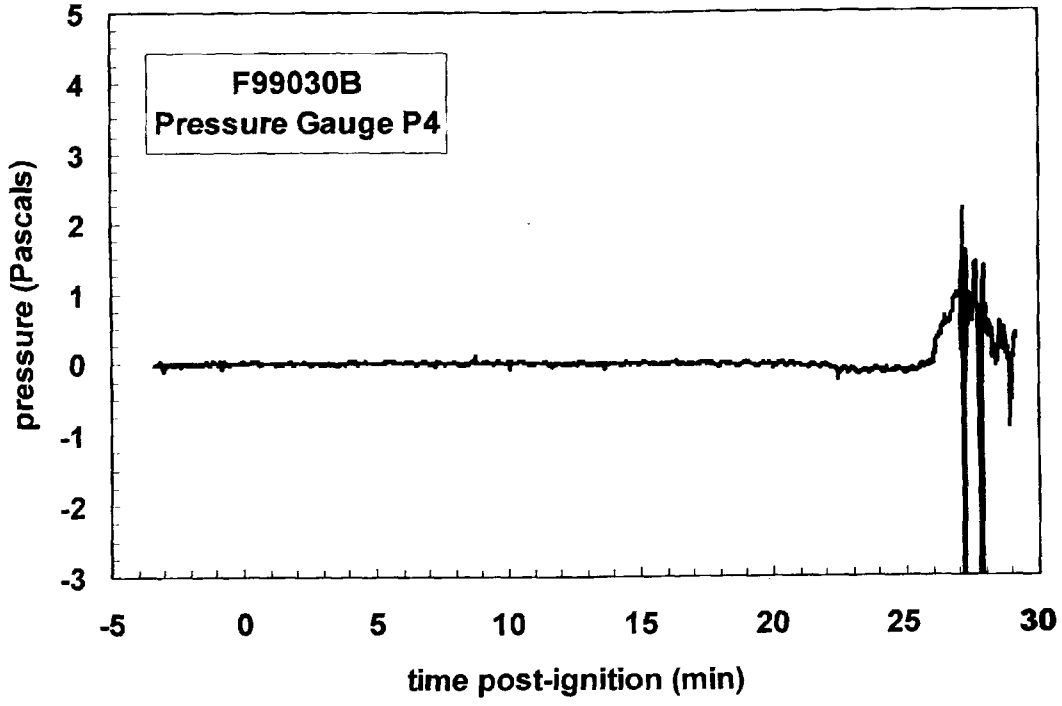

Plot F4. Fire Test F99030B. Absolute pressure below the headlining panel on the left side of the test vehicle relative to atmospheric pressure measured with pressure gauge P4.

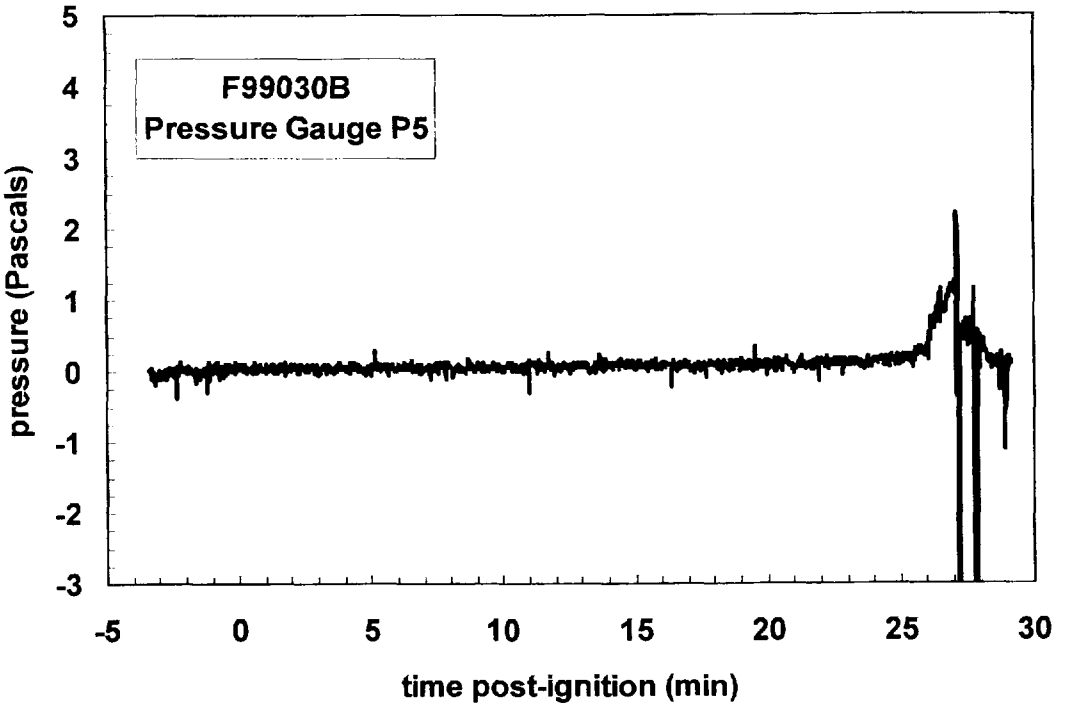

Plot F5. Fire Test F99030B. Differential pressure between the roof and floor behind the driver's seat measured with pressure gauge P5.

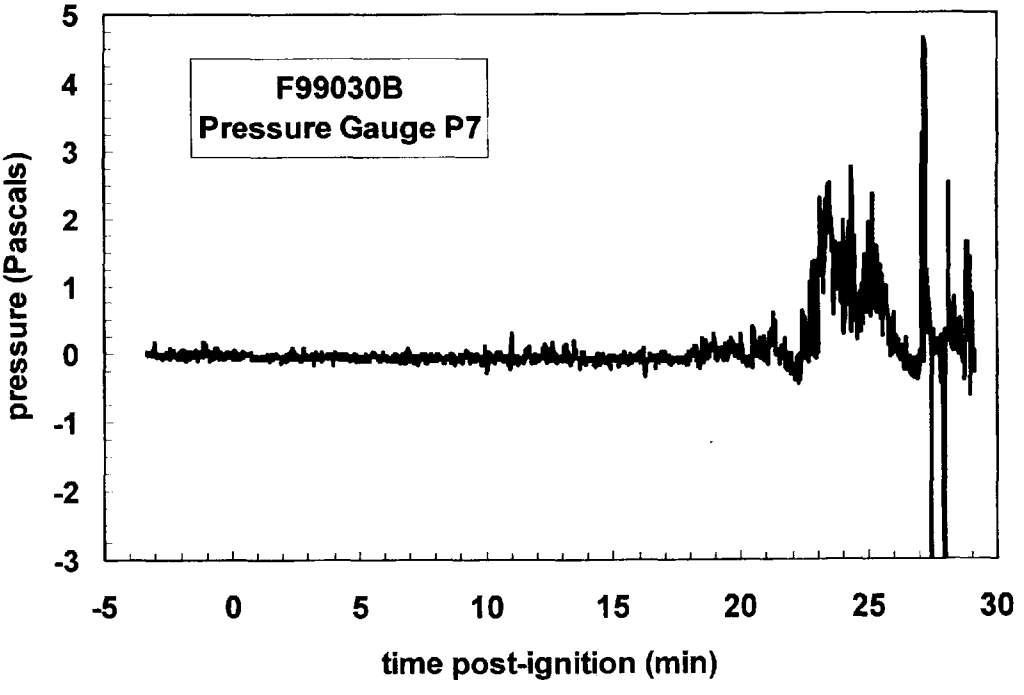

Plot F6. Fire Test F99030B. Differential pressure across the bi-directional flow probe measured with P7. Positive pressure indicated pressure was greater at the lower cup of the probe.

APPENDIX G
FIRE PRODUCTS COLLECTOR DATA

Scientific and technical personnel from Factory Mutual Research Corporation were primarily responsible for obtaining and analyzing data from the Fire Products Collector (FPC) at the Factory Mutual Test Center.

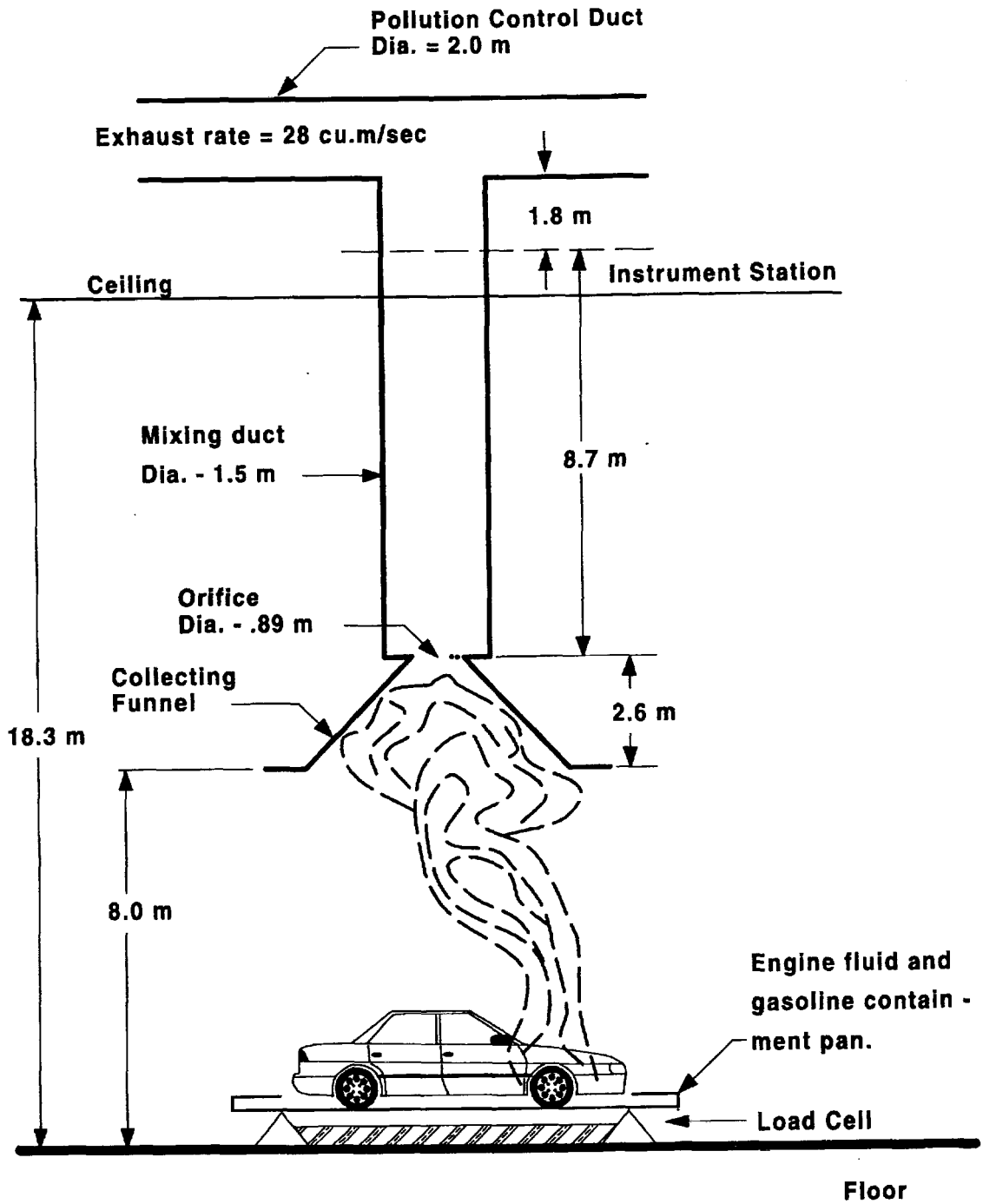

Figure G1. Fire Test F99030B. Diagram of the test vehicle under the fire products collector at the Factory Mutual Test Center.

A fire products collector was used to measure heat and combustion gases generated by the burning vehicle during this test (Fig. G1). The fire products collector consisted of a collection funnel (diameter = 6.1 m), an orifice plate (hole = 0.9 m), and a vertical stainless steel sampling duct (diameter = 1.5 m). The sampling duct was connected to the air pollution control system of the Test Center. The blower of the air pollution control system induces gas flow through the sampling duct. Air enters the sampling duct via the orifice plate. The temperature, linear velocity, optical transmission, and chemical composition of the entrained gas were measured in the center of the sampling duct 8.66 m (5.7 duct diameters) downstream from the orifice plate, ensuring a flat velocity profile at the sampling location. The data acquisition system consisted of a Hewlett Packard 2313B analog-to-digital conversion sub-system interfaced to a Hewlett Packard 1000 computer.

Gas temperature in the sampling duct was measured with two Type-K thermocouples (30 gage) with exposed bead-type junctions. The thermocouple leads were housed in stainless steel tubes (o.d. = 6.4 mm). Ambient air temperature in the facility was measured by five Type-K thermocouples attached to the external surface of the duct at 2.44, 5.49, 9.14, 12.8, and 15.9 m above the floor. These thermocouples were shielded from radiation from the fire.

The linear velocity of the gas entrained in the sampling duct was measured with a Pitot ring consisting of four Pitot tubes. A static pressure tap was mounted on the inside wall of the sampling duct. The pressure difference between the Pitot ring and the static wall tap was measured with an electronic manometer (Barocel Model 1173, CGS Scientific Corporation).

The particulate concentration in the entrained air was determined from the optical transmission across the duct measured at 0.4579 μm (blue), 0.6328 μm (red), and 1.06 μm (infrared). The optical path length across the duct was 1.524 m. Gas was withdrawn from the sampling duct through a stainless steel tube (o.d. = 3.9 mm) at a flow rate of 0.17×10^{-3} m^3/s for chemical analysis. The gas flowed through a particulate filter, a water condenser, and a drying agent before entering the analyzers. Carbon dioxide (CO_2) and carbon monoxide (CO) were measured with two dedicated non-disperse infrared analyzers (Beckman Model 864 Infrared Analyzers). Oxygen (O_2) was measured with a paramagnetic oxygen analyzer (Beckman Model 755 Paramagnetic Oxygen Analyzer). Total gaseous hydrocarbons were measured with a flame ionization analyzer (Beckman Model 400 Flame Ionization Analyzer).

The rate of product release was calculated using the following relationship:

$$\left(\frac{dR_j}{dt}\right) = f_j\left(\frac{dV}{dt}\right)\rho_j = f_j\left(\frac{dW}{dt}\right)\left(\frac{\rho_j}{\rho_g}\right) \qquad \text{(G1)}$$

where $d(R_j)/dt$ is the mass release rate of product j in kg/s; f_j is the volume fraction of product j; dV/dt is the total volume flow rate of the gas entrained in the sampling duct in m^3/s; dW/dt is the total mass flow rate of the gas entrained in the sampling duct in kg/s; ρ_j is the density of product j in g/m^3; and ρ_g is the density of the gas entrained in the concentration measurements. The rate of oxygen consumption was calculated using equation (G1), where the volume fraction of oxygen consumed was substituted for f_j.

The volume fraction of smoke particulate was calculated from the following relationship:

$$f_s = \frac{D\lambda \times 10^{-6}}{\Omega} \qquad \text{(G2)}$$

where f_s is the volume fraction of smoke, λ is the wavelength of the light source, Ω is the extinction coefficient of particulate (a value of 0.7 was used in these calculations), and D is the optical density at each of the three wavelengths at which measurements were made:

$$D = \frac{\ln\left(I_0/I\right)}{L} \qquad \text{(G3)}$$

where I_0 is the intensity of light transmitted through clean air, I is the intensity of light transmitted through air containing smoke particulate, and L is the optical pathlength, which was equal to 1.524 m. A value of 1.1×10^6 g/m^3 was used for the density of smoke particulate (ρ_j) in equation (G1).

The convective heat release rate was calculated using the following relationship:

$$\left(\frac{dE_{conv}}{dt}\right) = \left(\frac{dW}{dt}\right) \times c_p \times \left(T_g - T_a\right) \qquad \text{(G4)}$$

where $d(E_{conv})/dt$ is the convective heat release rate in kW; dW/dt is the mass flow rate of the gas entrained in the sampling duct in kg/s; c_p is the heat capacity of the gas entrained in the sampling

duct at the gas temperature in kJ/(kg×K); T_g is the temperature of the gas entrained in the sampling duct in K; and T_a is the ambient air temperature in K.

The chemical heat release rate was calculated from the release rates of carbon dioxide and carbon monoxide as follows:

$$\left(\frac{dE_{ch}}{dt}\right) = \Delta H^*_{CO_2} \times \left(\frac{dR_{CO_2}}{dt}\right) + \Delta H^*_{CO} \times \left(\frac{dR_{CO}}{dt}\right) \qquad \text{(G5)}$$

where $d(E_{ch})/dt$ is the chemical heat release rate in kW; ΔH^* is the net heat of complete combustion per unit mass of carbon dioxide or carbon monoxide released in the fire in kJ/g; and dR/dt is the mass release rate of carbon dioxide or carbon monoxide in kg/s. Values of ΔH^* for carbon dioxide and carbon monoxide were obtained from the literature [G1 and G2].

The chemical heat release rate also was calculated from the oxygen consumption rate as follows:

$$\left(\frac{dE_{ch}}{dt}\right) = \Delta H^*_O \left(\frac{dC_O}{dt}\right) \qquad \text{(G6)}$$

where $d(E_{ch})/dt$ is the chemical heat release rate in kW; ΔH^*_O is the net heat of complete combustion per unit mass of O_2 consumed in kJ/g; and $d(C_O)/dt$ is the consumption rate of oxygen in kg/s. The value for ΔH^*_O was obtained from the literature [G1 and G2].

The radiative heat release rate was the difference between the chemical heat release rate and the convective heat release rate:

$$\left(\frac{dE_{rad}}{dt}\right) = \left(\frac{dE_{ch}}{dt}\right) - \left(\frac{dE_{conv}}{dt}\right) \qquad \text{(G7)}$$

where $d(E_{rad})/dt$ is the radiative heat release rate; and $d(E_{ch})/dt$ is the average chemical heat release rate calculated using equations (G5) and (G6).

The vehicle was placed in a rectangular steel pan (length = 25 ft., width = 15 ft., height = 4 in.) to prevent spilled and leaking automotive fluids from spreading in the test facility. This fluid containment pan was fabricated from two sheets of carbon steel. Angle-braces were welded to

the under-side of the pan to keep it from flexing under the weight of the vehicle. The corners of the support frame rested on load cells. Mass loss was determined from data acquired from the load cells during the test.

The fluid containment pan was lined with a layer of fiberglass-reinforced cement construction board (DuraRock, USG Corporation). A thin layer of sand was used to level the concrete board so that the grade of the surface measured from the center to the edges along the major and minor axes was no greater than 1%. The joints between boards were sealed with latex caulking.

Mass loss from the burning vehicle and any burning fluids retained by the containment pan was measured with a load cell weigh-module system. The fluid containment pan was supported by an I-beam frame a load cell weight-module (KIS Series, BLH Electronics, Inc.) at each corner. These weight-modules contain cylindrical, double cantilever strain gauge transducers that are not generally affected by changes in mass distribution. The weight-module system was calibrated before this test by placing a series of standard weights on the fluid containment pan.

Data from the fire-products collector and load cell weight-module system are shown in Plots G1 through G5. The analyzer for measuring carbon monoxide in the fire plume malfunctioned during this test. The carbon monoxide release rate data in Plot G3 are invalid.

REFERENCES

G1. G. Heskestad. A Fire Products Collector for Calorimetry into the MW Range, Technical Report J.I. OC2E1.RA. Factory Mutual Research Corporation, Norwood, MA. June, 1981.

G2. Archibald Tewarson. "Generation of Heat and Chemical Compounds in Fires" Section 3/Chapter 4, SFPE Handbook of Fire Protection Engineering, 2nd Edition, 1995, pp. 3:53-124.

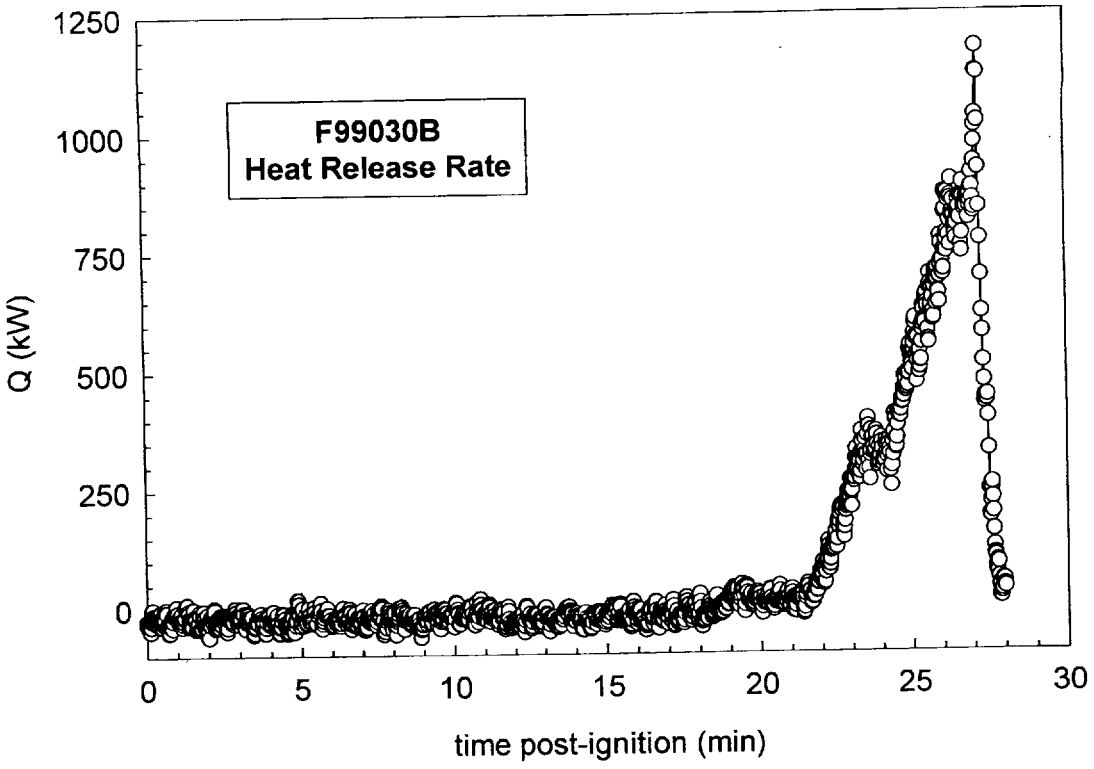

Plot G1. Fire Test F99030B. Heat release rate measured using the Fire Products Collector.

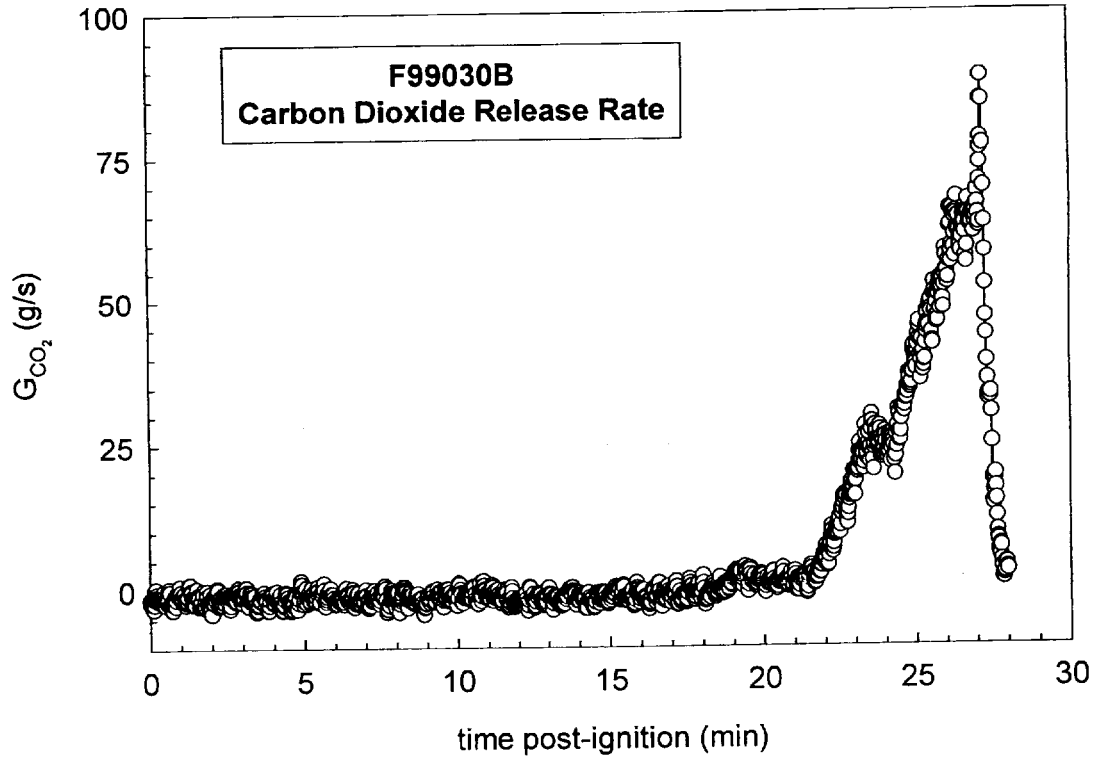

Plot G2. Fire Test F99030B. Carbon dioxide release rate measured using the Fire Products Collector.

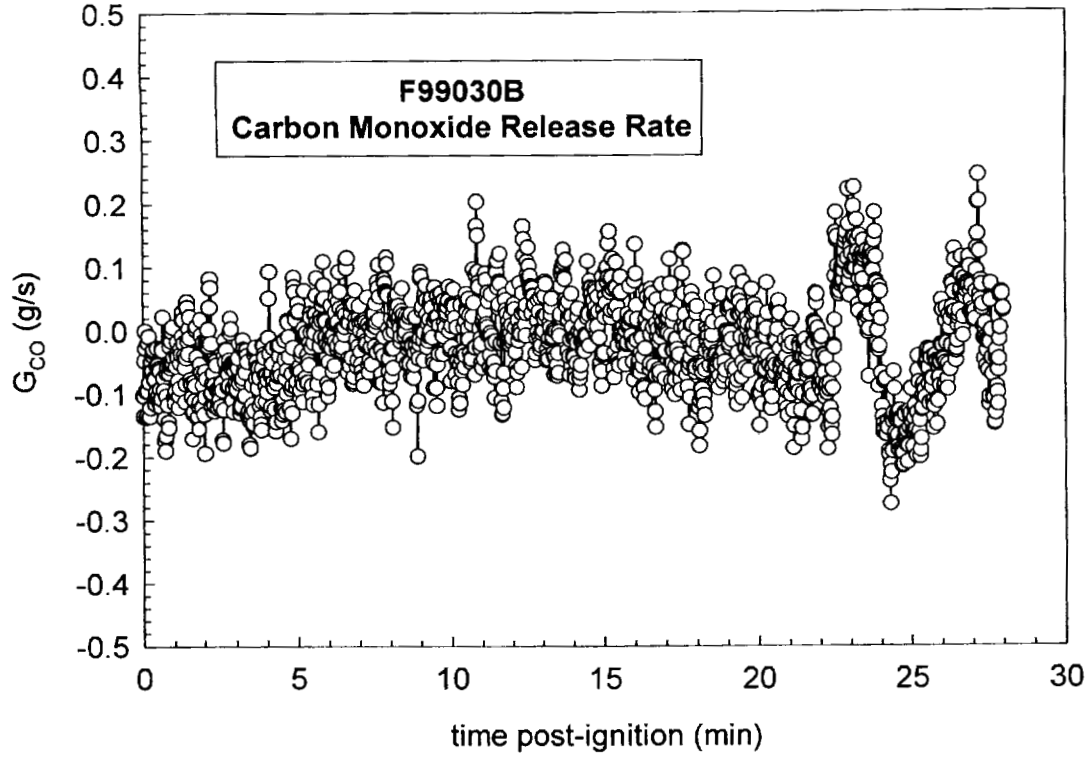

Plot G3. Fire Test F99030B. Carbon monoxide release rate measured using the Fire Products Collector.

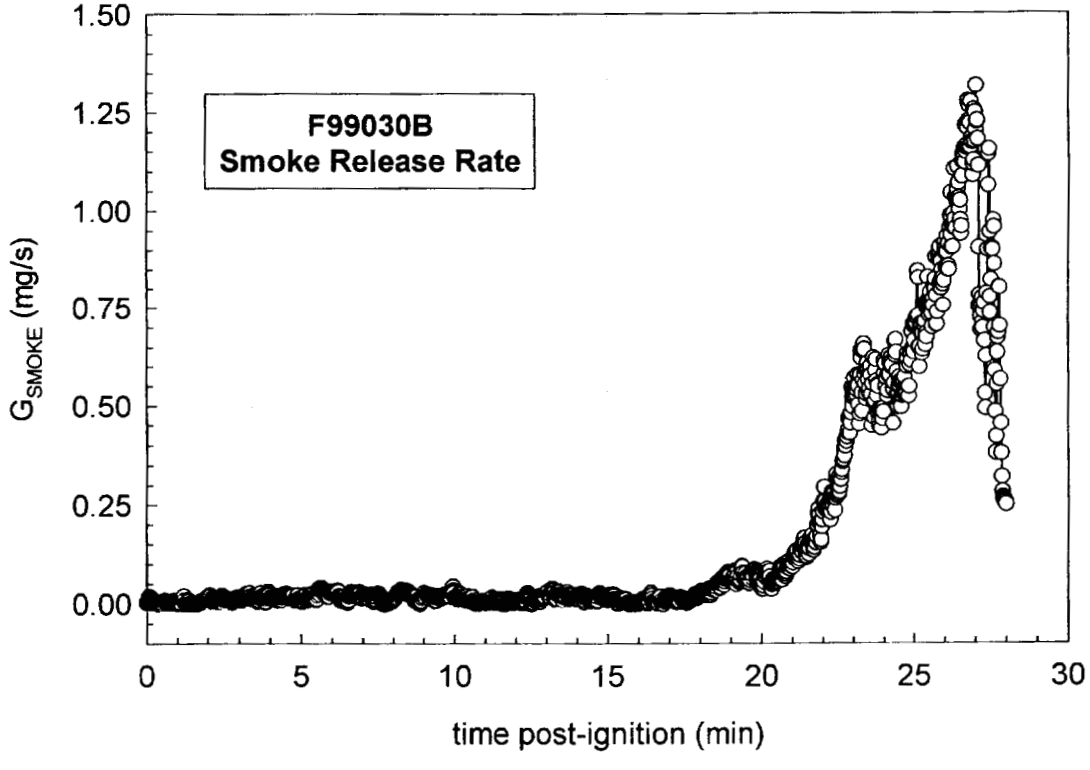

Plot G4. Fire Test F99030B. Smoke release rate measured using the Fire Products Collector.

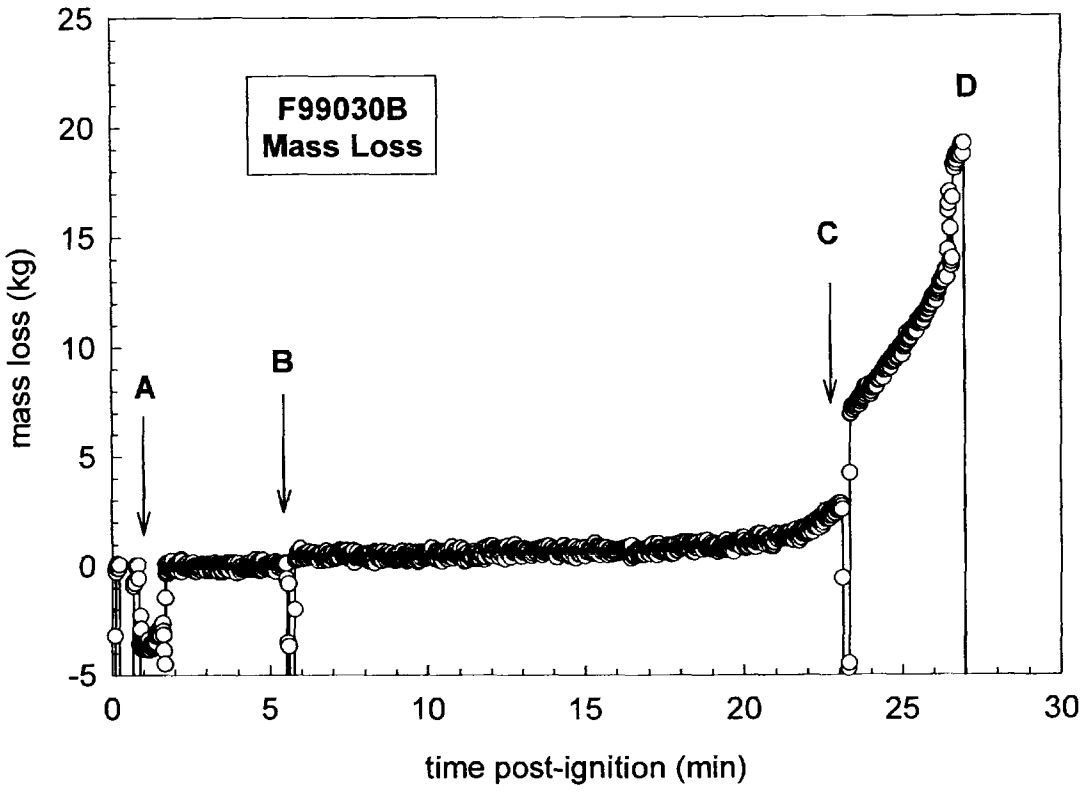

Plot G5. Fire Test F99030B. Mass Loss from the test vehicle during the fire test. Test personnel were leaning on the test surface to monitor the temperature of the thermocouple readout between the time of ignition and 2 minutes post-ignition (A), test personnel stepped onto the test surface to remove the thermocouple readout between 5½ and 5¾ minutes post-ignition (B), test personnel stepped onto the test surface to remove a video camera and tripod at between 23 and 23½ minutes post-ignition (C), and test personnel stepped onto the test surface to extinguish the fire at approximately 27 minutes post-ignition (D).

APPENDIX H
PASSENGER COMPARTMENT COMBUSTION GAS DATA
FOURIER TRANSFORM INFRARED SPECTROSCOPY

The sampling-line for FTIR analysis consisted of a stainless-steel tube (o.d. = 0.250 in. (6.4 mm), i.d. = 0.125 in. (3.2 mm), l = 20 ft (6.1 m)) inserted through the roof between the front seats along the longitudinal midline of the test vehicle (Fig.'s H1 and H2). The inlet of the sample-tube extended approximately 10 in. below the headlining. The tube was not heated. The outlet of the sample tube was connected to a heated Teflon® transfer-line (o.d. = 0.250 in. (6.4 mm), i.d. = 0.125 in. (3.2 mm), l = 75 ft. (23 m)), which was connected to the gas cell of the FTIR spectrometer. The transfer-line was heated to 105°C during the test to prevent condensation of water and water-soluble gases (*e.g.*, HCl, HCN, NO, and NO_2). An in-line stainless steel filter holder containing a quartz fiber filter (o.d. = 47 mm) was placed between the sample-tube and the transfer-line to prevent smoke particles from contaminating analytical instrumentation.

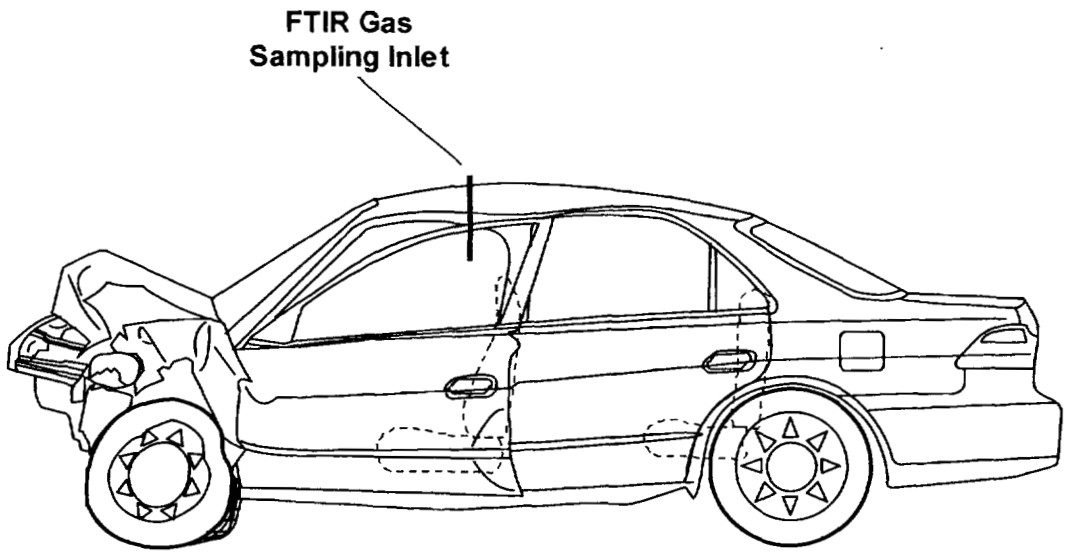

Figure H1. Fire Test F99030B. Side-view of the test vehicle show the approximate location of the FTIR gas sampling inlet in the passenger compartment.

The FTIR spectrometer was a Model I-1000 Series FTIR Spectrometer (MIDAC Corporation, Riverside, California), with a KBr beam-splitter; a liquid nitrogen-cooled Mercury-Cadmium-Telluride detector; and gold-surfaced aluminum optics. This instrument was fitted with a stainless steel, multiple-reflectance gas cell (path length = 10 m) with zinc selenide windows. The gas cell was heated to 105°C. The optical bench was filled with clean, dry argon and hermetically sealed. The usable spectral range of this instrument was approximately 7400-700 cm^{-1}. Pressure in the gas cell during the fire tests was measured with a Baratron pressure gauge (MKS Instruments, Burlington, MA). The spectrometer was operated at a spectral resolution of 0.5 cm^{-1}.

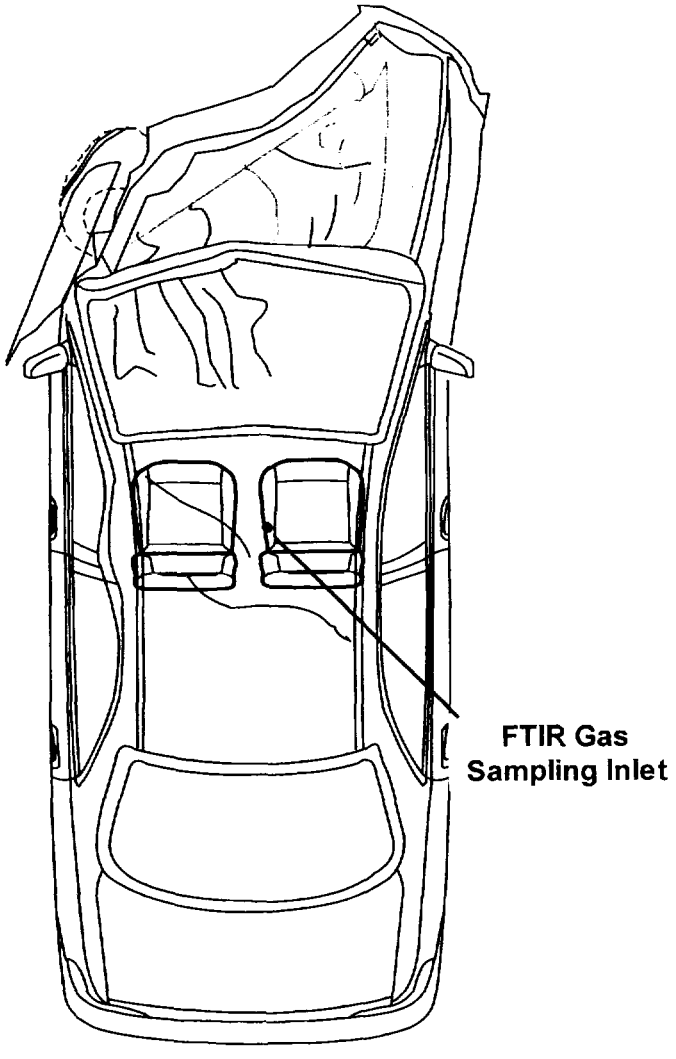

Figure H2. Fire Test F99030B. Top view of the test vehicle showing the approximate location of the FTIR gas sampling inlet in the passenger compartment.

The sampling line and gas cell were equilibrated to 105°C for at least 60 minutes before sample acquisition. A reference spectrum was acquired while the gas cell was evacuated. During the fire tests, the gas cell was purged continuously with air withdrawn from the passenger compartment at a flow rate of 7 L/min. Single-scan absorbance spectra were acquired and stored to disk at intervals of 10 s. After the test, the stored spectra were analyzed using the quantitative analysis software provided by the instrument manufacturer (AutoQuant, MIDAC). This software uses a Classical Least Squares algorithm to determine gas concentrations. The method developed for analysis of combustion gases was calibrated with gas standards (Scott Specialty

Gases, Inc., Troy, MI). The standards were either NIST-traceable or produced by a gravimetric blending process.

The gaseous combustion products measured by FTIR in the passenger compartment during this test included carbon dioxide, carbon monoxide, methane, ethylene, acetylene, hydrogen cyanide, nitric oxide, and hydrogen chloride (Plots H1 through H8). Except for carbon dioxide, which has a background concentration in air of approximately 0.05%, and hydrogen chloride, the concentrations of all of these gases were less than their respective lower limits of detection before ignition. The background concentration of carbon dioxide in air is approximately 0.04%. Noise in the Infrared spectra acquired before ignition resulted in an apparent hydrogen chloride concentration of < 1 ppm.

Carbon dioxide, carbon monoxide, methane, ethylene, and acetylene started to accumulate in the passenger compartment between 22 and 23 minutes post-ignition (Plots H1 through H5). The concentrations of these gases in the passenger compartment of the test vehicle increased until fire suppression began, and started to decrease between 27 and 28 minutes post-ignition (Plots H1 through H5).

A small amount of hydrogen chloride accumulated in the passenger compartment between approximately 24 and 28 minutes post-ignition (Plot I6).

A small amount of hydrogen cyanide appears to have accumulated in the passenger compartment between 26 and 27 minutes post-ignition (Plot I7). The hydrogen cyanide concentration data from this test contained a high degree of scatter (Plot I7).

Nitric oxide started to accumulate in the passenger compartment approximately 26 minutes post-ignition (Plot H8). The concentration of nitric oxide in the passenger compartment started to decreasebetween 27 and 28 minutes post-ignition.

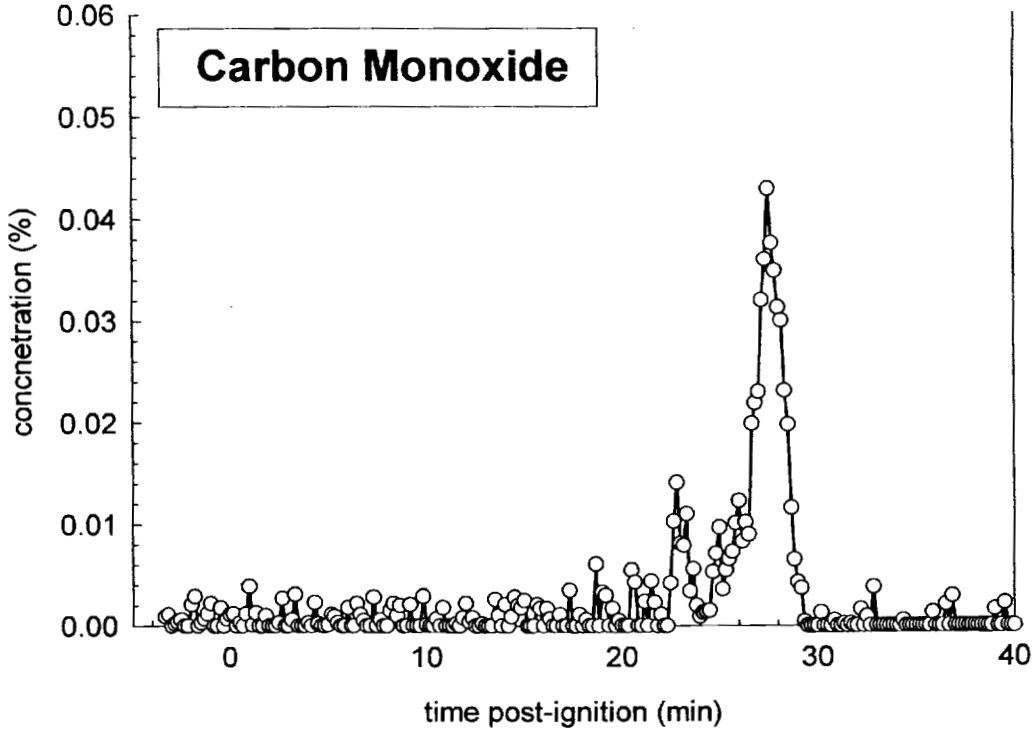

Plot H1. Fire Test F99030B. Concentration of carbon monoxide (CO) in the passenger compartment determined by FTIR analysis.

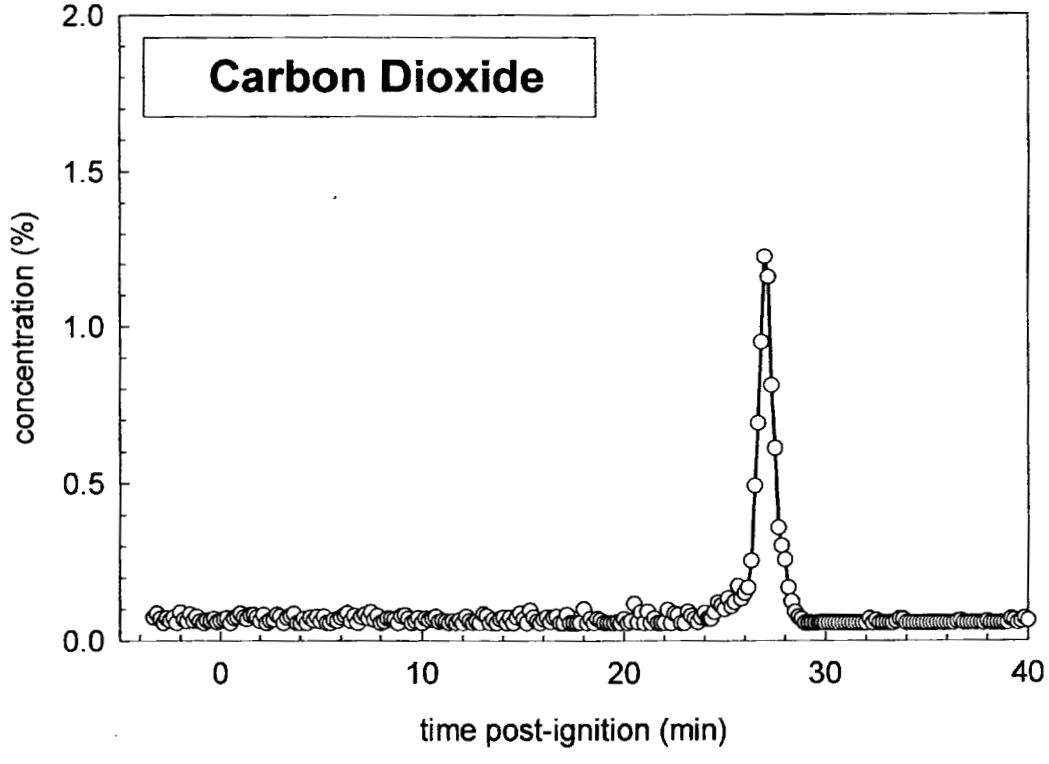

Plot H2. Fire Test F99030B. Concentration of carbon dioxide (CO_2) in the passenger compartment determined by FTIR analysis.

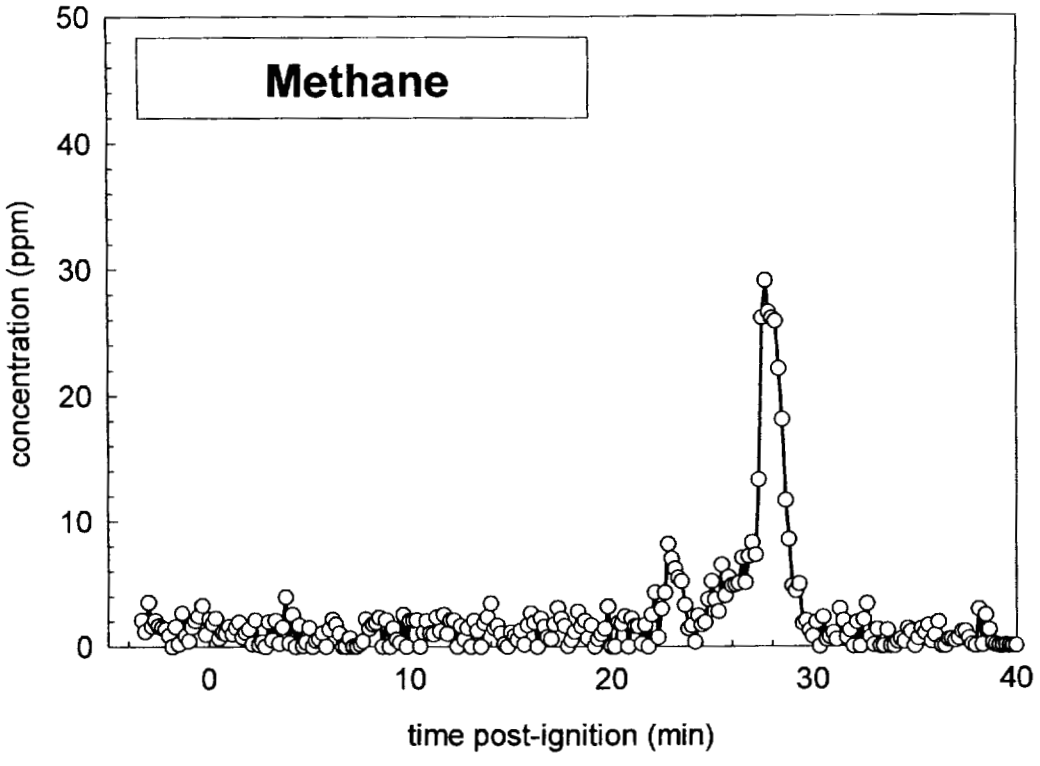

Plot H3. Fire Test F99030B. Concentration of methane (CH_4) in the passenger compartment determined by FTIR analysis.

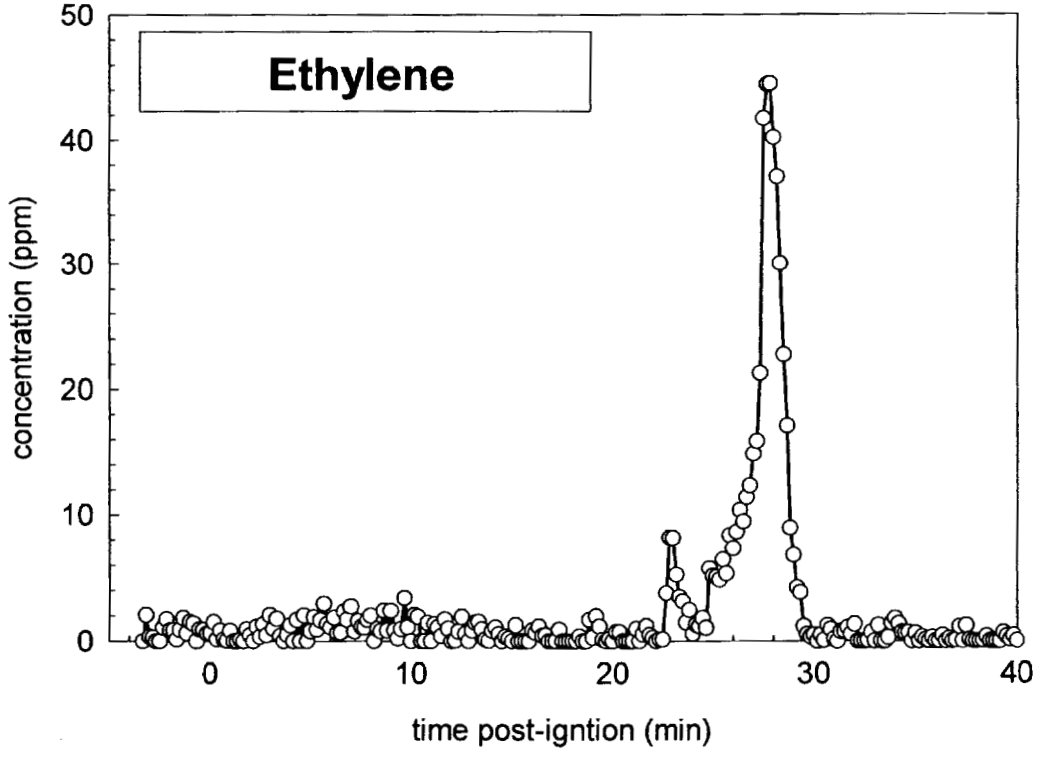

Plot H4. Fire Test F99030B. Concentration of ethylene (C_2H_4) in the passenger compartment determined by FTIR analysis.

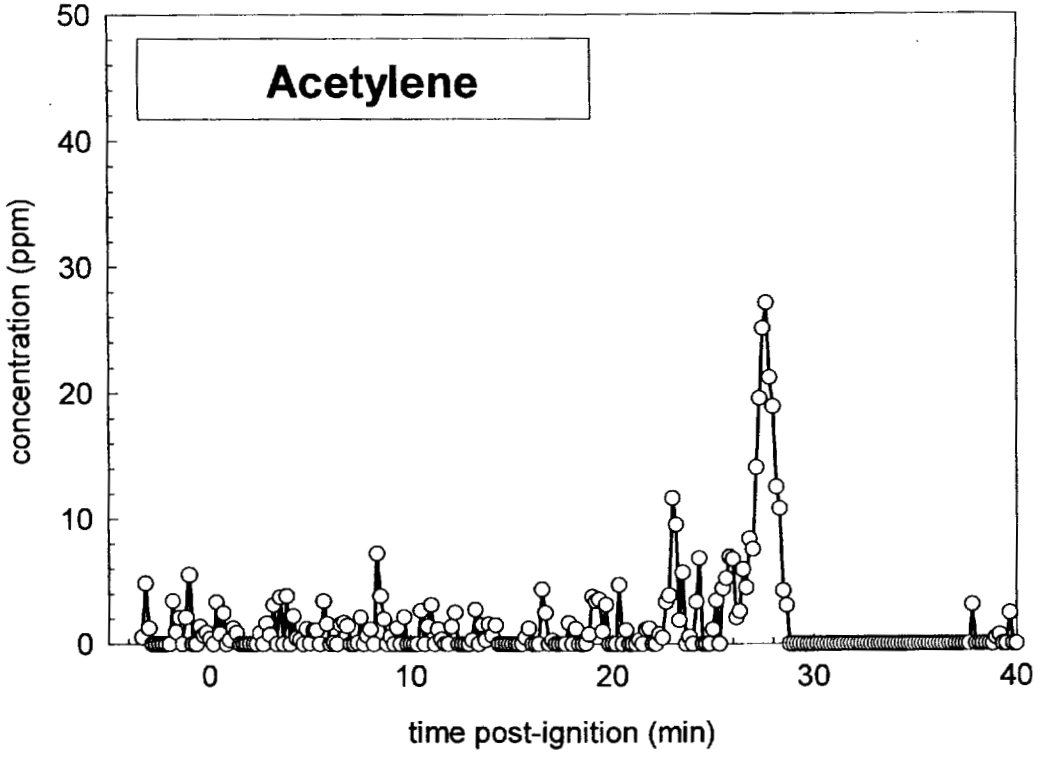

Plot H5. Fire Test F99030B. Concentration of acetylene (C_2H_2) in the passenger compartment determined by FTIR analysis.

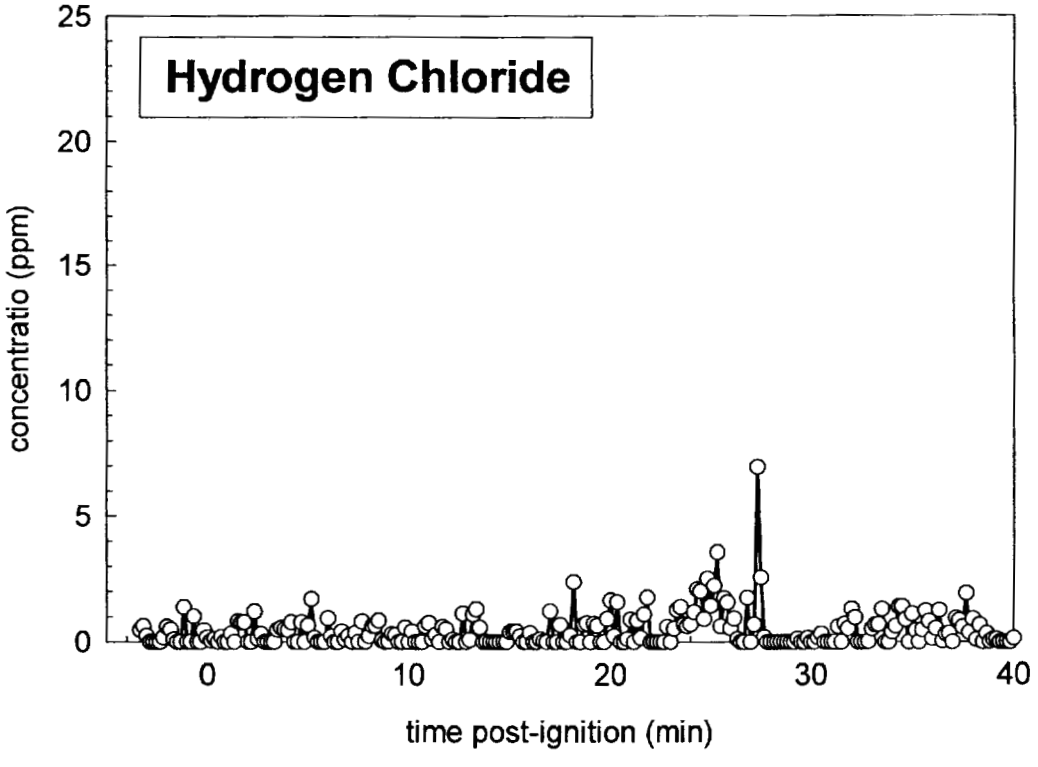

Plot H6. Fire Test F99030B. Concentration of hydrogen chloride (HCl) in the passenger compartment determined by FTIR analysis.

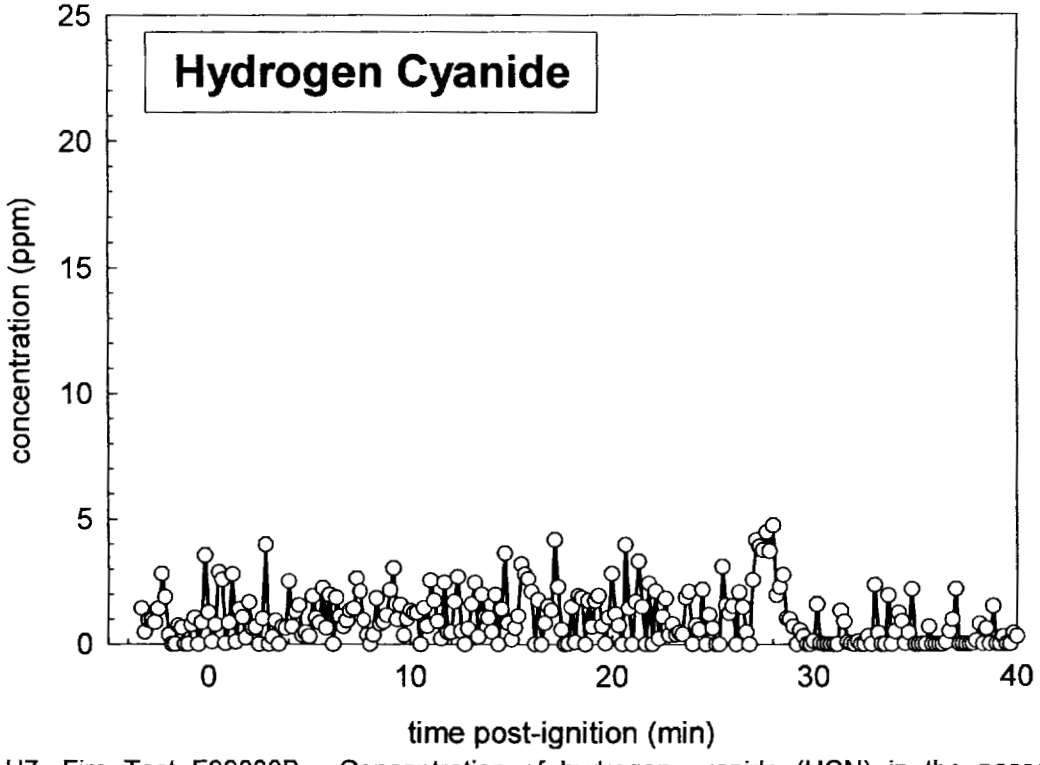

Plot H7. Fire Test F99030B. Concentration of hydrogen cyanide (HCN) in the passenger compartment determined by FTIR analysis.

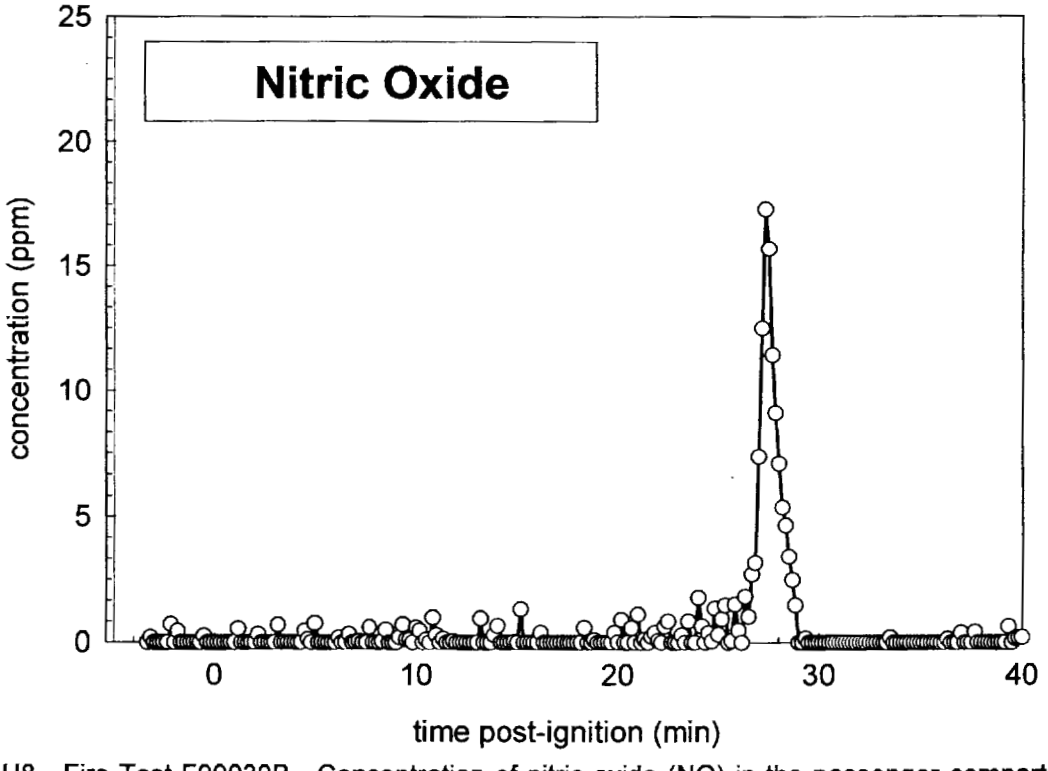

Plot H8. Fire Test F99030B. Concentration of nitric oxide (NO) in the passenger compartment determined by FTIR analysis.

APPENDIX I
PASSENGER COMPARTMENT COMBUSTION GAS DATA
GAS CHROMATOGRAPHY/MASS SPECTROSCOPY GAS ANALYSIS

The sampling-line for GC/MS samples consisted of a stainless-steel tube (o.d. = 0.250 in. (6.4 mm), i.d. = 0.125 in. (3.2 mm), l = 20 ft (6.1 m)) inserted through the roof between the front seats along the longitudinal midline of the test vehicle (Fig.'s I1 and I2). The inlet of the sample-tube extended approximately 10 in. below the headlining. The outlet of the sample tube was connected to sampling manifold by a length of stainless steel sampling tube (o.d. = ¼ in., length = 25 ft.). The sampling manifold contained five sample cartridges in parallel. Airflow was directed sequentially through the sample cartridges a solenoid-actuated gas-switching manifold. The airflow rate through the cartridges during sampling was adjusted 250 cm^3/min with a rotometer. None of the components of the GC/MS sampling line were heated.

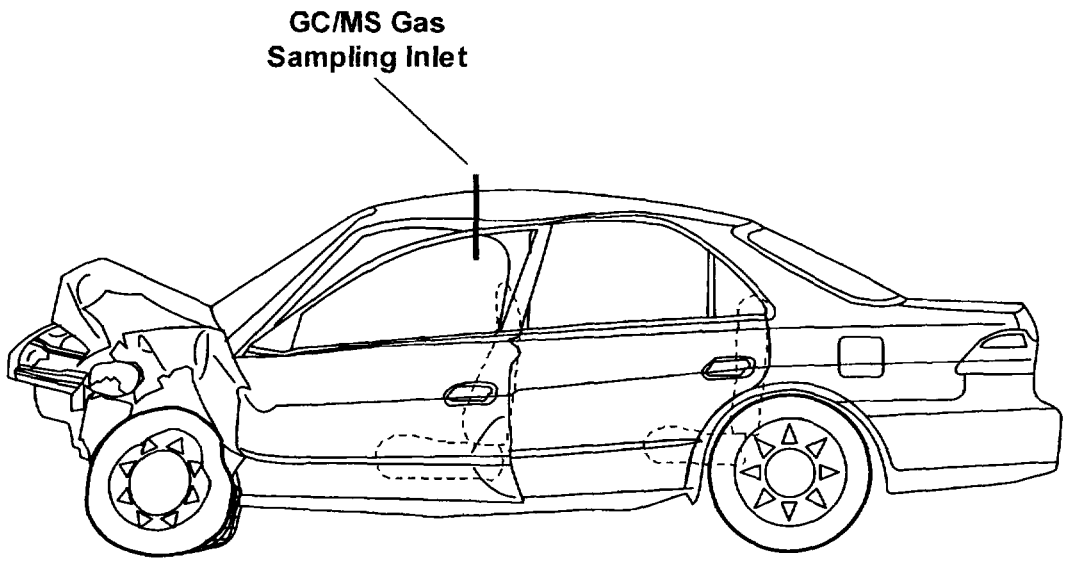

Figure I1. Fire Test F99030B. Side-view of the test vehicle show the approximate locations of the GC/MS gas sampling inlets in the passenger compartment.

Each cartridge was a glass-lined stainless steel tube (i.d. = 4 mm; length = 10 cm; Scientific Instrument Services, Inc, Ringoes, NJ) packed with 25 mg of Carbotrap™ C Graphitized Carbon Black (Supelco, Inc.; Bellefonte, PA) in series with 15 mg of Carbotrap™ Graphitized Carbon Black (Supelco).

After the test, the sample cartridges were analyzed by thermal desorption/gas chromatography/mass spectrometry. Deuterated standards dissolved in deuterated methanol were added to each sorbent cartridge to monitor sample recovery. A modified purge-and-trap concentrator was used for thermal desorption (Model 600 Purge-and-Trap Concentrator, CDS Analytical, Oxford, PA). The gas chromatograph was a Model 5890 Series II Plus Gas Chromatograph (Hewlet Packard, Palo Alto, CA). The mass spectrometer was a Hewlet Packard

Model 5989B Mass Spectrometer (Hewlett Packard). The thermal desorption unit was interfaced directly to the split/splitless injector of the gas chromatograph through a cryo-focusing unit. The injector was operated in the split mode with a split of approximately 10 mL/min. The chromatographic column was a fused silica capillary column coated with 100% methyl silicone (HP-1 ; length = 30 m; i.d. = 0.25 mm; film thickness = 0.25 μm).

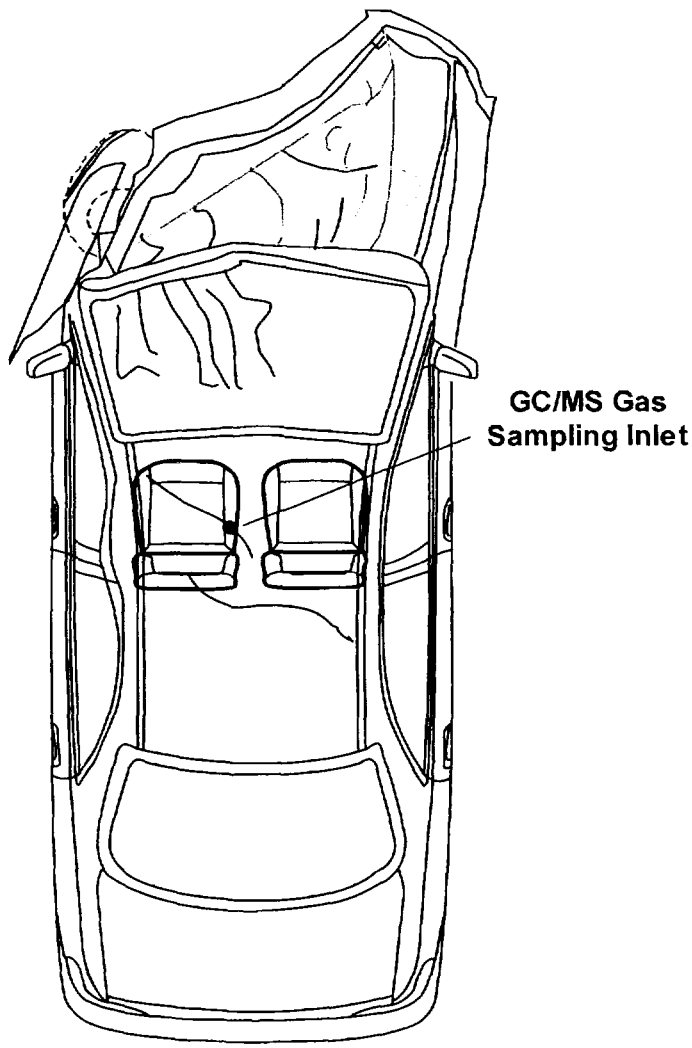

Figure I2. Fire Test F99030B. Top view of the test vehicle showing the approximate locations of the GC/MS gas sampling inlet in the passenger compartment.

The sample was desorbed at 320°C for 10 min, and cryofocused onto the head of the chromatographic column -80°C. The temperature of the analytical column was maintained at 0°C while the sample was desorbed and cryo-focused. To start the chromatographic analysis, the

cryo-focusing unit was heated bullistically to a temperature of 320°C. The column temperature was programmed from 0 to 325°C at a rate of 5°C/min. Mass spectra were obtained by scanning from m/z 40 to 600 at a rate of 1.2 scan/s.

Plots I1 through I7 show the mass chromatograms of the blank and samples acquired during this test. The sampling intervals in the figure captions were corrected for the time-delay for airflow through the sample-line, which was estimated to have been approximately 25 seconds.

Table I1 lists 83 components tentatively identified from analysis of the mass chromatograms of these samples and shows the abundance of each compound listed relative to the average of the deuterated n-alkanes added as internal standards. The components are listed in order of chromatographic retention time. Identifications were based on the results of a spectral search a commercial mass spectral library (Wiley 275K Mass Spectral Library).

Blanks 1 and 2 contained small amounts of aliphatic hydrocarbons in the range of C6 – C12 this contamination may have been from a kerosene heater used to heat area around test vehicle. The kerosene heater was turned off and moved away from the test vehicle before the start of this test.

Sample 1 was lost because of an equipment malfunction during its analysis. Samples 2 and 3 contained lesser amounts of the contaminants identified in Blanks 1 and 2, indicating the source of this contamination was no longer present. In addition to trace amounts of the contaminant hydrocarbons, Samples 4 and 5 contained aromatic compounds from combustion of styrene-containing polymers (ethenylbenzene, ethynylbenzene, 1-methylethenylbenzene, and 1,1'-(1,3-butadiyne-1,4-diyl)bis-benzene) and compounds generally associated with soot (indene, 1-methyl-1H-indene, naphthalene, 2-methylnaphthalene, and 3-methylnaphthalene).

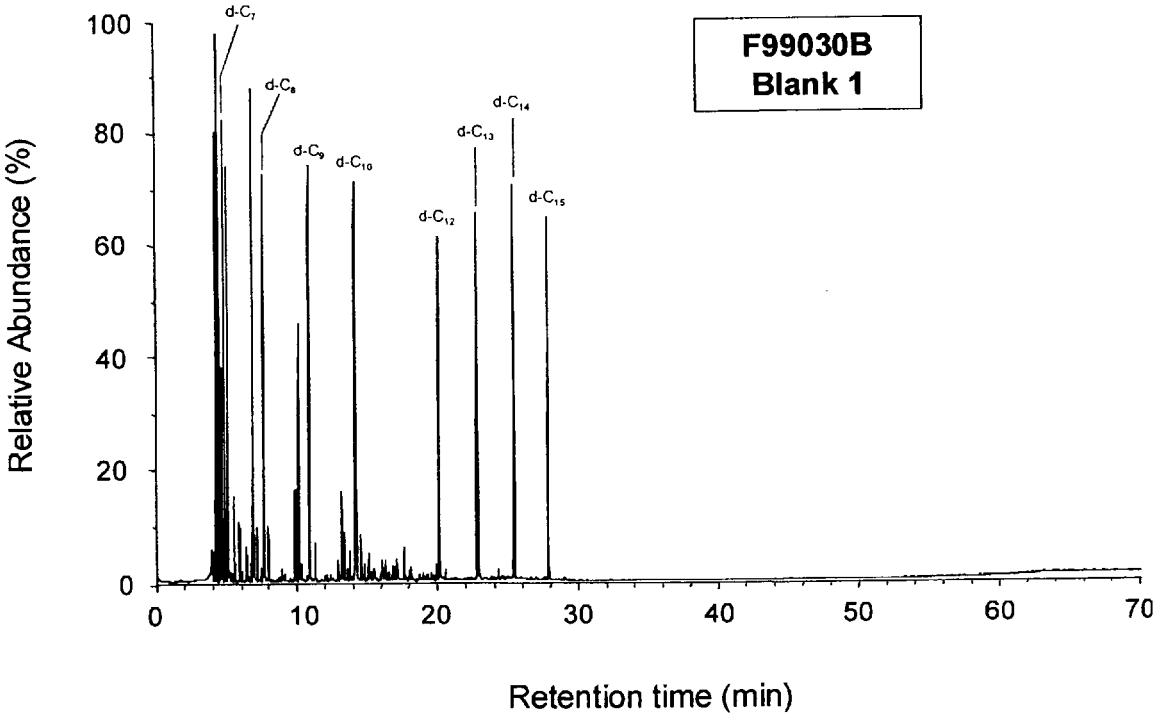

Plot I1. Fire Test F99030B. Mass chromatogram from GC/MS analysis of Blank 1 acquired for a period of 20 minutes before the test.

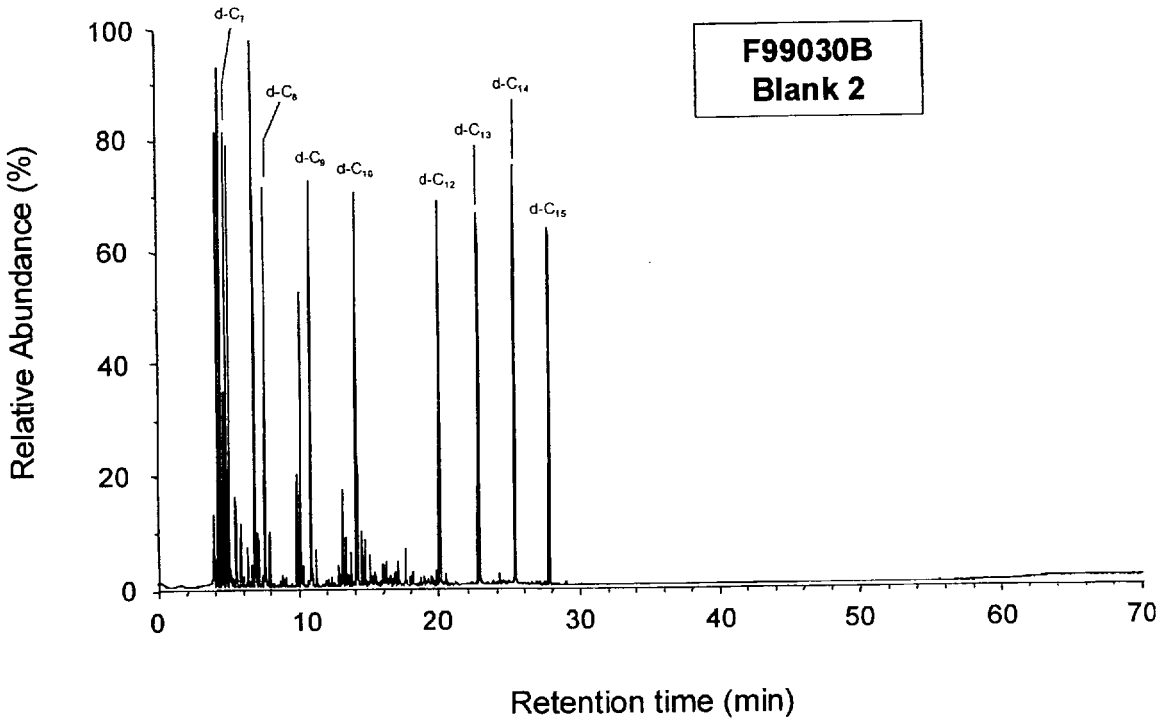

Plot I2. Fire Test F99030B. Mass chromatogram from GC/MS analysis of Blank 2 acquired for a period of 20 minutes before the test.

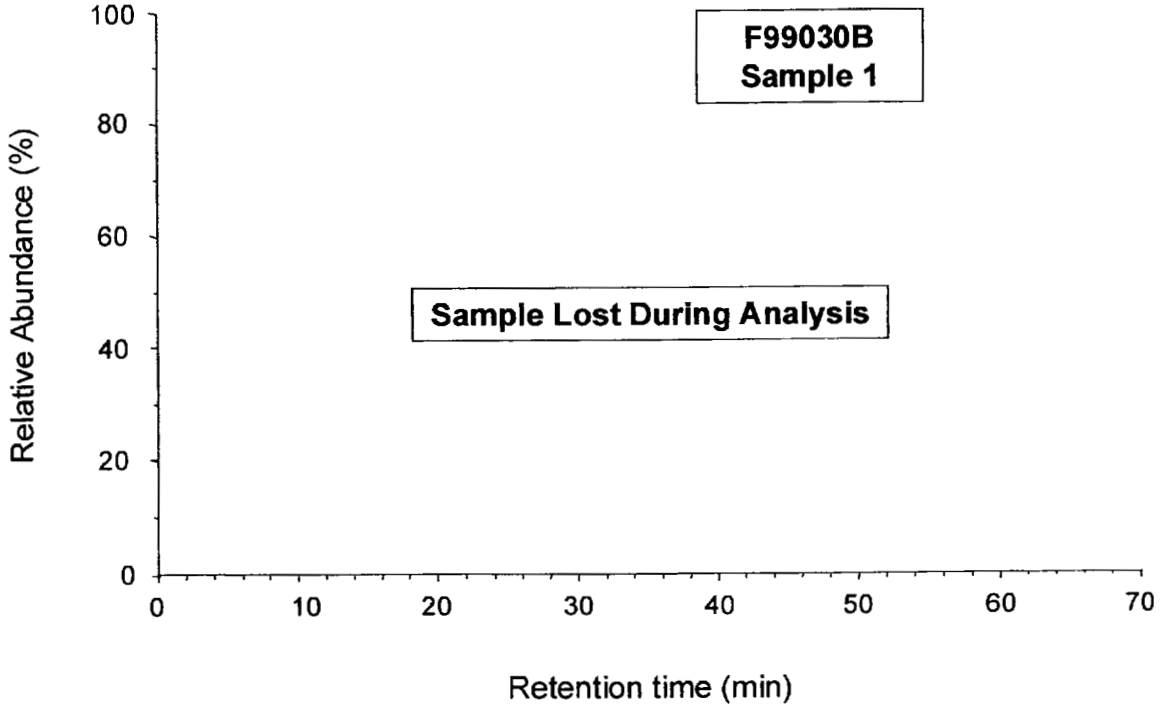

Plot I3. Fire Test F99030B. Mass Chromatogram of Sample 1 acquired from +00:00 to +22:30 min:sec post-ignition.

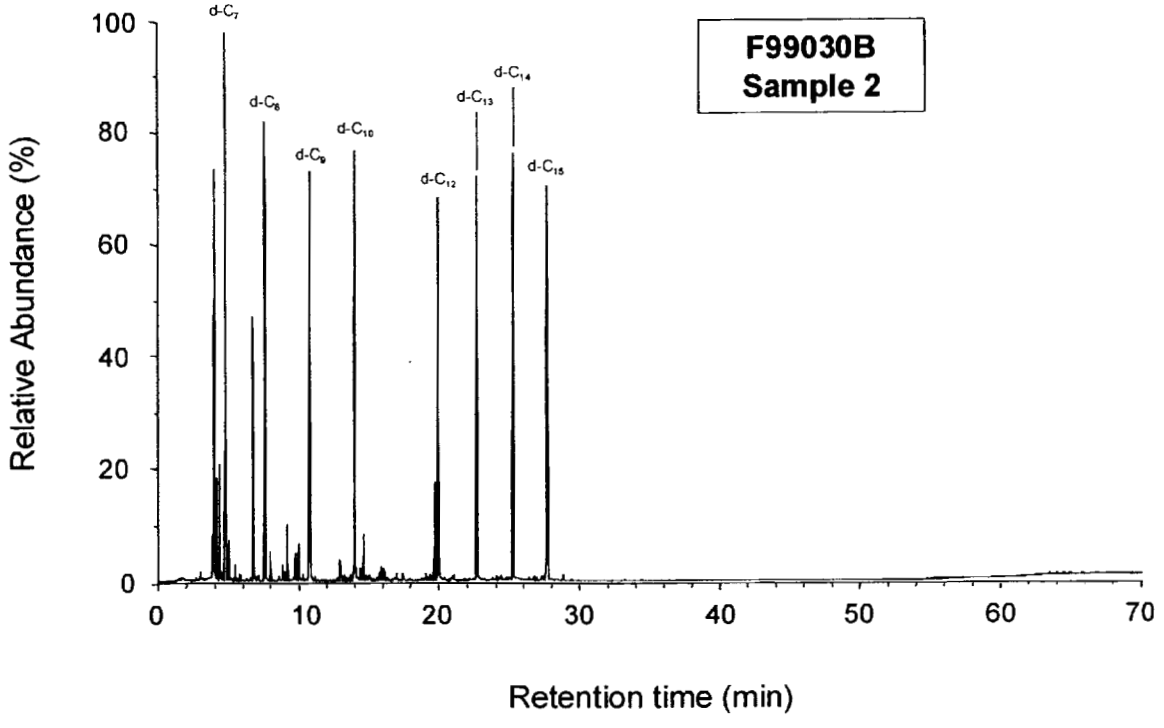

Plot I4. Fire Test F99030B. Mass Chromatogram of Sample 2 acquired from +22:30 to +25:22 min:sec post-ignition.

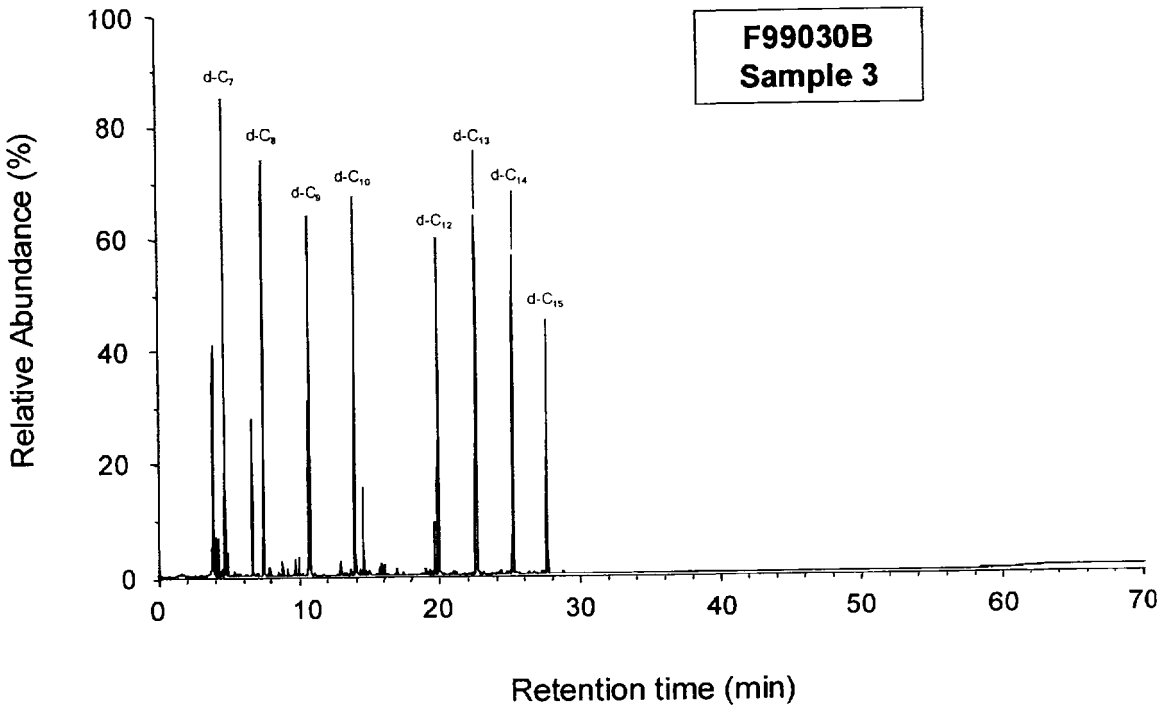

Plot I5. Fire Test F99030B. Mass Chromatogram of Sample 3 acquired from +25.22 to +26:14 min:sec post-ignition.

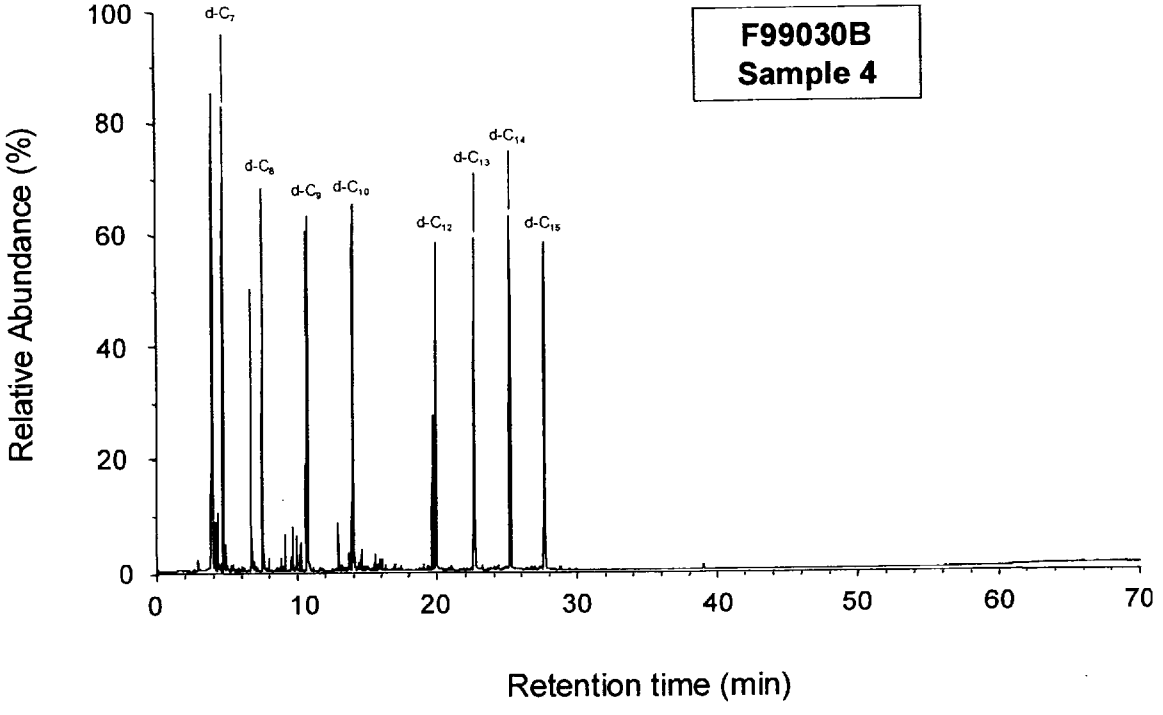

Plot I6. Fire Test F99030B. Mass Chromatogram of Sample 4 acquired from +26:14 to +27:02 min:sec post-ignition.

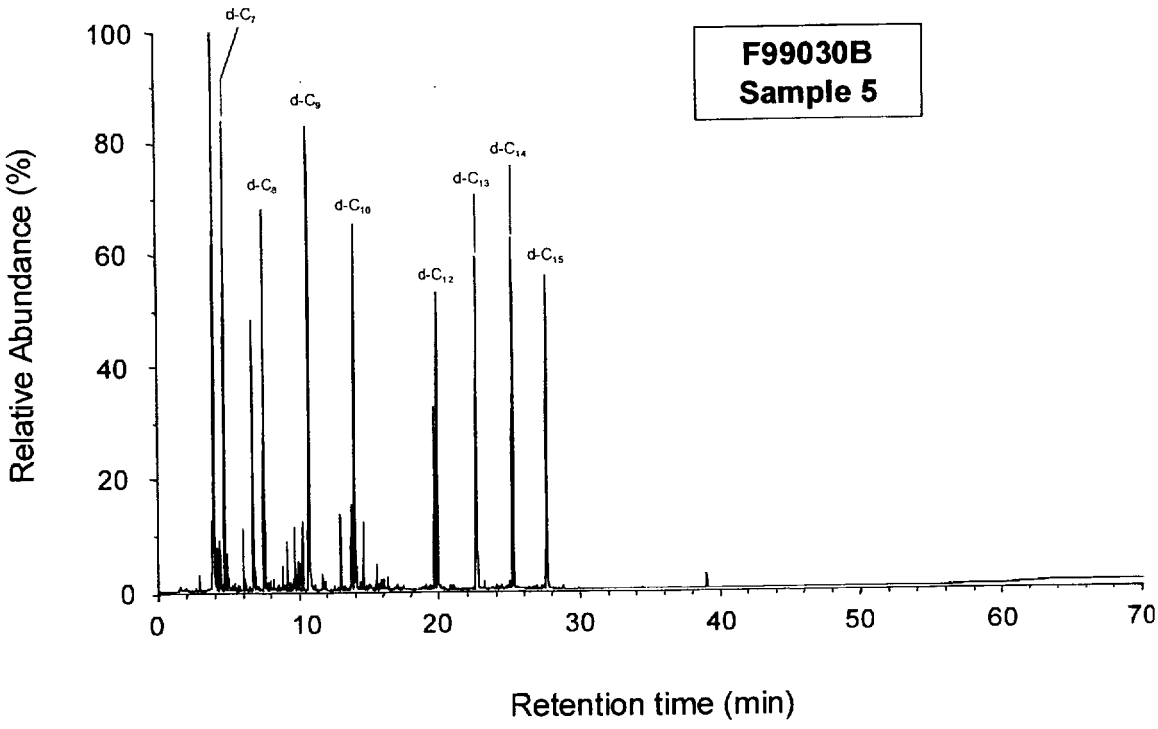

Plot I7. Fire Test F99030B. Mass Chromatogram of Sample 5 acquired from +27:02 to +27:05 min:sec post-ignition.

Table I1
GC/MS Peak Identification

t_R	Compound	Relative Abundance[1]						
		Blank 1	Blank 2	Sample 1	Sample 2	Sample 3	Sample 4	Sample 5
2.971	butanal	0.00	0.00	n/a	0.00	0.00	0.02	0.03
3.877	1-chlorobutane	0.00	0.00	n/a	0.00	0.00	0.00	0.07
4.081	benzene	0.12	0.85	n/a	0.87	0.59	1.29	1.63
4.248	2-methylhexane	0.94	0.76	n/a	0.09	0.05	0.06	0.05
4.376	3-methylhexane	0.82	0.00	n/a	0.09	0.05	0.05	0.04
4.430	1-butanol	0.00	0.00	n/a	0.00	0.00	0.00	0.04
4.614	dimethylcyclopentane isomer	0.06	0.06	n/a	0.00	0.00	0.00	0.00
4.690	dimethylcyclopentane isomer	0.03	0.03	n/a	0.00	0.00	0.00	0.00
4.733	C7 - alkane	0.26	0.25	n/a	0.00	0.00	0.00	0.00
4.823	d16-n-heptane (d-C7)	0.78	0.76	n/a	0.87	0.98	0.92	0.96
5.040	n-heptane	0.60	0.58	n/a	0.03	0.02	0.02	0.02
5.528	methylcyclohexane	0.11	0.12	n/a	0.01	0.00	0.00	0.00
5.944	C8 - alkane	0.06	0.05	n/a	0.00	0.00	0.00	0.00
5.991	2,4-dimethylheptane	0.03	0.03	n/a	0.00	0.00	0.00	0.00
6.132	1,2,3-trimethylcyclopentane	0.02	0.02	n/a	0.00	0.00	0.00	0.00
6.398	2,3,4-trimethylpentane	0.04	0.05	n/a	0.00	0.00	0.00	0.00

Table I1, continued
GC/MS Peak Identification

t_R	Compound	Relative Abundance[1]						
		Blank 1	Blank 2	Sample 1	Sample 2	Sample 3	Sample 4	Sample 5
6.437	dichloropropane isomer	0.00	0.00	n/a	0.00	0.19	0.00	0.07
6.493	C8 - alkane	0.03	0.03	n/a	0.00	0.00	0.00	0.00
6.775	C8 - alkane	0.03	0.03	n/a	0.00	0.00	0.00	0.00
6.825	methylbenzene	0.94	0.86	n/a	0.28	0.00	0.38	0.45
6.883	dichloropropane isomer	0.00	0.00	n/a	0.00	0.00	0.00	0.03
6.979	2-methylheptane	0.03	0.02	n/a	0.00	0.00	0.01	0.00
7.198	3-methylheptane	0.09	0.09	n/a	0.00	0.00	0.00	0.00
7.481	C8 - alkane	0.02	0.02	n/a	0.00	0.00	0.00	0.00
7.559	1-ethyl-3-methylcyclopentane	0.01	0.01	n/a	0.00	0.00	0.00	0.00
7.652	d18-n-octane (d-C8)	0.78	0.78	n/a	0.90	0.99	0.92	0.92
8.045	n-octane	0.08	0.08	n/a	0.03	0.01	0.02	0.00
8.751	C9 - alkane	0.01	0.02	n/a	0.00	0.00	0.00	0.00
8.970	C9 - alkane	0.02	0.02	n/a	0.00	0.00	0.00	0.00
9.049	propylcyclohexane	0.00	0.00	n/a	0.01	0.00	0.00	0.00
9.174	C9 - alkane	0.01	0.02	n/a	0.00	0.00	0.00	0.00

Table I1, continued
GC/MS Peak Identification

t_R	Compound	Relative Abundance[1]						
		Blank 1	Blank 2	Sample 1	Sample 2	Sample 3	Sample 4	Sample 5
9.224	2,4-dimethyl-1-heptene chlorobenzene	0.00	0.00	n/a	0.06	0.01	0.05	0.08
9.440	C9 - alkane	0.00	0.00	n/a	0.00	0.00	0.00	0.02
9.534	trimethylcyclohexane isomer	0.01	0.01	n/a	0.00	0.00	0.00	0.00
9.636	2-propyl-1,3-dioxolane	0.00	0.00	n/a	0.00	0.00	0.02	0.02
9.791	ethylbenzene	0.16	0.16	n/a	0.03	0.03	0.06	0.08
10.058	1,4-dimethylbenzene 1,3-diemthylbenzene	0.62	0.62	n/a	0.05	0.03	0.05	0.05
10.310	ethynylbenzene	0.00	0.00	n/a	0.00	0.00	0.04	0.11
10.381	C9 - alkane	0.03	0.02	n/a	0.00	0.00	0.00	0.00
10.757	ethenylbenzene	0.01	0.01	n/a	0.16	0.18	0.41	0.62
10.857	d20 -n-nonane (d-C9)	1.13	1.11	n/a	0.66	0.77	0.40	0.16
11.322	*n*-nonane	0.06	0.06	n/a	0.00	0.00	0.00	0.00
11.729	1,2,3-dichloropropane	0.00	0.00	n/a	0.00	0.00	0.00	0.02
12.137	C10 - alkane	0.01	0.01	n/a	0.00	0.00	0.00	0.00
12.420	C10 - alkane	0.01	0.01	n/a	0.00	0.00	0.00	0.00
12.623	C10 - alkane	0.01	0.01	n/a	0.00	0.00	0.00	0.00

Table I1, continued
GC/MS Peak Identification

t_R	Compound	Relative Abundance[1]						
		Blank 1	Blank 2	Sample 1	Sample 2	Sample 3	Sample 4	Sample 5
12.968	propylbenzene	0.03	0.04	n/a	0.00	0.00	0.00	0.00
12.987	benzaldehyde	0.00	0.00	n/a	0.02	0.03	0.06	0.12
13.235	C3 - benzene	0.21	0.22	n/a	0.00	0.00	0.00	0.00
13.344	C10 - alkane	0.00	0.01	n/a	0.00	0.00	0.00	0.00
13.439	C3 - benzene	0.09	0.09	n/a	0.00	0.00	0.00	0.00
13.627	C10 - alkane	0.02	0.02	n/a	0.00	0.00	0.00	0.00
13.720	1-methylethenylbenzene	0.00	0.00	n/a	0.01	0.01	0.02	0.08
13.799	benzonitrile	0.00	0.00	n/a	0.00	0.00	0.01	0.16
13.800	C3 - benzene	0.05	0.05	n/a	0.00	0.00	0.00	0.00
14.072	d22-n-decane (d-C10)	0.86	0.83	n/a	1.05	1.16	1.07	1.10
14.120	benzofuran	0.00	0.00	n/a	0.00	0.00	0.02	0.03
14.240	C3 - benzene	0.13	0.00	n/a	0.00	0.00	0.00	0.00
14.442	n-decane	0.08	0.08	n/a	0.01	0.01	0.01	0.00
15.132	C3 - benzene	0.04	0.04	n/a	0.00	0.00	0.00	0.00
15.289	C11 - alkane	0.01	0.02	n/a	0.00	0.00	0.00	0.00
15.560	1H - indene	0.01	0.01	n/a	0.00	0.00	0.02	0.04

Table I1, continued
GC/MS Peak Identification

t_R	Compound	Relative Abundance[1]						
		Blank 1	Blank 2	Sample 1	Sample 2	Sample 3	Sample 4	Sample 5
16.042	C4 - benzene	0.02	0.01	n/a	0.00	0.00	0.00	0.00
16.104	C4 - benzene	0.04	0.03	n/a	0.00	0.00	0.00	0.00
16.199	C4 - benzene	0.03	0.03	n/a	0.00	0.00	0.00	0.00
16.324	C4 - benzene	0.05	0.03	n/a	0.00	0.00	0.00	0.00
16.354	1-phenylethanone	0.00	0.00	n/a	0.00	0.00	0.01	0.03
16.559	C4 - benzene	0.03	0.03	n/a	0.00	0.00	0.00	0.00
16.763	C11 - alkane	0.01	0.01	n/a	0.00	0.00	0.00	0.00
16.873	C4 - benzene	0.01	0.02	n/a	0.00	0.00	0.00	0.00
17.123	C4 - benzene	0.04	0.04	n/a	0.00	0.00	0.00	0.00
17.672	n-undecane	0.05	0.05	n/a	0.00	0.00	0.00	0.00
18.017	C4 - benzene	0.02	0.02	n/a	0.00	0.00	0.00	0.00
18.143	C4 - benzene	0.02	0.02	n/a	0.00	0.00	0.00	0.00
18.676	methyl dihydro-1H-indene isomer	0.02	0.02	n/a	0.00	0.00	0.00	0.00
18.990	methyl dihydro-1H-indene isomer	0.02	0.02	n/a	0.00	0.00	0.00	0.00
19.770	naphthalene	0.03	0.03	n/a	0.12	0.09	0.29	0.39

Table I1, continued
GC/MS Peak Identification

t_R	Compound	Relative Abundance[1]						
		Blank 1	Blank 2	Sample 1	Sample 2	Sample 3	Sample 4	Sample 5
20.026	d26-n-dodecane (d-C12)	1.08	1.08	n/a	0.95	1.03	0.99	0.99
20.575	n-dodecane	0.02	0.02	n/a	0.00	0.00	0.00	0.00
22.759	d28-n-tridecane (d-C13)	1.14	1.17	n/a	1.20	1.28	1.24	1.31
24.318	C13 - alkene isomer	0.02	0.02	n/a	0.02	0.00	0.00	0.00
24.549	C13 - alkane isomer	0.01	0.01	n/a	0.01	0.00	0.00	0.00
25.325	d30-n-tetradecane (d-C14)	1.13	1.18	n/a	1.23	1.09	1.27	1.33
27.748	d32-n-pentadecane (d-C15)	1.10	1.10	n/a	1.14	0.70	1.19	1.23
39.048	1,1'-(1,3-butadiyne-1,4-diyl)bis-benzene	0.00	0.00	n/a	0.00	0.00	0.01	0.03

[1] The abundance values shown in this table are the ratio of the peak area of the compound of interest to the average peak area of the deuterated n-alkanes (internal standards) in each sample.

APPENDIX J
PASSENGER COMPARTMENT
AIRBORNE PARTICULATE ANALYSIS

Five samples of airborne particulate were samples from the passenger compartment during this test. The approximate locations of the inlets particulate samplers are shown in Figures J1 and J2.

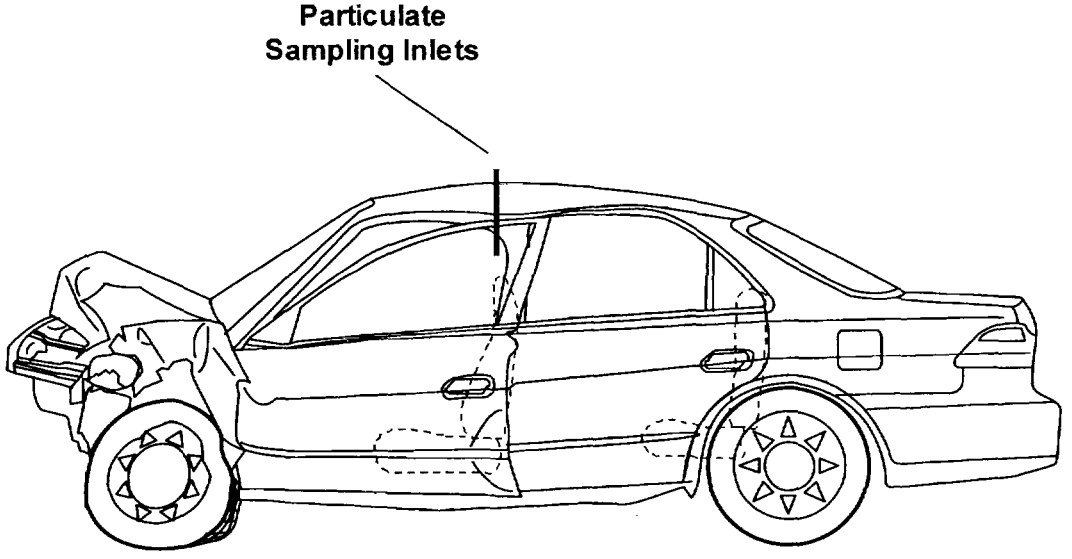

Figure J1. Fire Test F99030B. Side-view of the test vehicle showing the approximate locations of the particulate sampling inlets in the passenger compartment.

Each particulate sampling apparatus consisted of an in-line stainless steel filter holder (filter diameter = 47 mm, Gelman Scientific). The inlet of each filter holder was fitted with a straight length of stainless steel tubing (o.d. = ¼ in., o.d. = $^{5}/_{16}$ in., length = 12 in.) using a compression fitting (¼ in., Swagelok). The inlet tube was inserted through the roof of the test vehicle so that it extended below the headlining approximately 10 in.. The outlet of each filer holder was connected to a vacuum manifold using flexible copper tubing (o.d. = $^{5}/_{16}$ in., length = 25 ft.). The vacuum manifold was connected to a pumping system configured to maintain constant flow through the filter holder as the pressure drop across the filter increased due to particulate loading. Qartz-fiber filters were used to collect particulate from the passenger compartment. The filters were placed in an electric furnace at 650°C in air overnight and pre-weighed. The pumping system was adjusted to maintain a volume flow rate of 30 L/min. through a single filter holder. This produced a linear velocity of approximately 29 cm/sec. of airflow perpendicular the face of the filter.

Two blanks were collected for 10 minutes before the test. Samples were collected during the test. In-line solenoid valves fitted to each port of the vacuum manifold and were actuated manually during the test to direct flow through the filter holders sequentially. The time intervals for sample acquisition were the same as those for acquiring GC/MS samples.

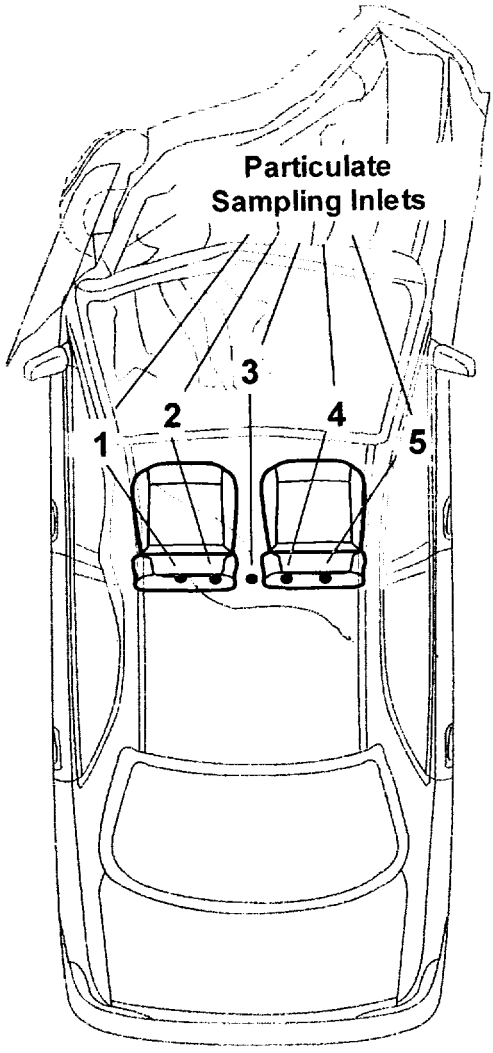

Figure J2. Fire Test F99030B. Top-view of the test vehicle showing the approximate locations of the particulate sampling inlets in the passenger compartment.

After the test, the filters placed in a dissector cabinet overnight to remove water absorbed by the filter media and particulate. The weight of each filter was recorded only after constant weight was achieved. The average concentrations of airborne particulate during each sample interval were determined from the mass of particulate collected, the volume flow rate, and the elapsed time.

A quarter was cut from each filter, weighted, and extracted for quantitative ion chromatographic analysis. The extracting solution was the mobile phase buffer. The chromatography column was an IC-Pak A HC column (Waters, Milford, MA). The mobile phase was a sodium borate/gluconate buffer at a flow rate of 1.8 mL/min [J1]. The chromatographic system consisted

of a Model 616 Pump, a Model 717 Autosampler, and a Model 431 Conductivity Detector (Waters). The following anions were measured in the ion chromatographic analysis: fluoride (F^-), bicarbonate (HCO_3^-), chloride (Cl^-), nitrite (NO_2^-), bromide (Br^-), hypochlorite ($HClO_3^-$), nitrate (NO_3^-), phosphate (HPO_4^-), sulfate (SO_4^-), and oxalate ($C_2O_4^-$).

Table JI shows the concentration of airborne particulate in the passenger compartment during this test.

Table J1
Average Airborne Particulate Concentration

Sample	Sampling Interval (min:sec.)	Sampling Time (min:sec.)	Airborne Concentration (mg/m^3)
Blank	n/a	20:00	-2
Sample 1	00:00 to 22:30	22:30	2
Sample 2	22:30 to 25:22	02:52	14
Sample 3	25:22 to 26:14	00:52	22
Sample 4	26:14 to 27:02	00:48	189
Sample 5	27:02 to 27:05	00:03	6222

Table J2 shows the results of the average anion concentration in the airborne particulate. The results shown in Table J2 were corrected for bicarbonate, nitrate, phosphate, sulfate, and oxalate detected in the blanks. Samples 2, 3, 4, and 5 contained chloride. Samples 4 and 5 contained bromide. Samples 2 and 3 contained sulfate.

Table J2

Average Anion Concentration in the Airborne Particulate

Sample	Anion Concentration in Airborne Particulate (μg/mg)[1]									
	F^-	HCO_3^-	Cl^-	NO_2^-	Br^-	$HClO_3^-$	NO_3^-	HPO_4^-	SO_4^-	$C_2O_4^-$
Sample 1	n/d[1]	n/d	n/d	n/d	n/d	n/d	n/d	n/d	n/d	n/d
Sample 2	n/d	n/d	101	n/d	n/d	n/d	n/d	n/d	134	n/d
Sample 3	n/d	n/d	242	n/d	n/d	n/d	n/d	n/d	252	n/d
Sample 4	n/d	n/d	25	n/d	165	n/d	n/d	n/d	n/d	n/d
Sample 5	n/d	n/d	52	n/d	83	n/d	n/d	n/d	n/d	n/d

[1] n/d = not detected

REFERENCES FOR APPENDIX J

J1. Method A-102, Waters Innovative Methods for Ion Analysis, Manual Number 22340, Waters Corporation, Milford, MA.